Electronic and Transport Characteristics of Low-dimensional Materials: Effect of Structural Imperfection, Metal Inclusion and Spin-crossover

A Thesis

Submitted for the Degree of

DOCTOR OF PHILOSOPHY

in the Faculty of Science

by

Dibyajyoti Ghosh

CHEMISTRY AND PHYSICS OF MATERIALS UNIT
JAWAHARLAL NEHRU CENTRE FOR ADVANCED SCIENTIFIC RESEARCH
Bangalore – 560 064

JUNE 2016

To My Family

DECLARATION

I hereby declare that the matter embodied in the thesis entitled "**Electronic and Transport Characteristics of Low-dimensional Materials: Effect of Structural Imperfection, Metal Inclusion and Spin-crossover**" is the result of investigations carried out by me at the Chemistry and Physics of Materials Unit, Jawaharlal Nehru Centre for Advanced Scientific Research, Bangalore, India under the supervision of Prof. Swapan K. Pati and that it has not been submitted elsewhere for the award of any degree or diploma.

In keeping with the general practice in reporting scientific observations, due acknowledgement has been made whenever the work described is based on the findings of other investigators.

Dibyajyoti Ghosh

CERTIFICATE

I hereby certify that the matter embodied in this thesis entitled "**Electronic and Transport Characteristics of Low-dimensional Materials: Effect of Structural Imperfection, Metal Inclusion and Spin-crossover**" has been carried out by Mr. Dibyajyoti Ghosh at the Chemistry and Physics of Materials Unit, Jawaharlal Nehru Centre for Advanced Scientific Research, Bangalore, India under my supervision and that it has not been submitted elsewhere for the award of any degree or diploma.

Prof. Swapan K. Pati
(Research Supervisor)

Acknowledgements

As Rose Kennedy once said, "Life isn't a matter of milestones, but of moments.", I feel that every moment in JNC, every person I met, taught me something about life and I owe my gratitude to all those people who have made this thesis possible. Because of whom my journey has been the one that I will cherish forever.

First and foremost I wish to thank my research supervisor, Prof. Swapan K. Pati. He has been very encouraging and understanding since my Masters days, when I first began to work in his group. Working with him has been a thoroughly enjoyable experience. Ever since he has supported me not only by providing all the academic insights I needed, but also emotionally through the not-always-so-smooth road to finish my Ph.D. Thanks to him I had the opportunity to work in different scientific areas. He has always given me the support, encouragement, enthusiasm and the freedom whenever I needed. He made me ready for tomorrow's challenges.

I must thank Anusooya Ma'am and Sohan for their love and affection. Sir and Ma'am never allowed me to feel that I am far away from home, they have always been my family in Bangalore.

It has been an honour for me to work with the wonderful collaborators, Prof. Anna Painelli from University of Parma and Anindita and Prof. T. K. Maji from JNCASR. I thank them for all the scientific discussions we had.

I thank all my course instructors in JNCASR for the useful courses. Many thanks to Prof. Shobhana Narasimhan, Prof. H. Ila, , Prof. S. Balasubramanian, Prof. T. K. Maji, Prof. Aloknath Chakraborty (IISc), Prof. Shivaprasad, Prof. Narayan, Prof. Umesh waghmare, Prof. Eswaramoorthy, Prof. Chandrabhas Narayana, Dr. Ranjan Dutta, Dr. Rajesh Ganapathy, Prof. Sundaresan, Prof. Vidhyadhiraja,

Prof. Jayanta Haldar and Prof. Swapan K. Pati. I thank Prof. Subir K. Das for many helps. I am very gratefull to all the CPMU and TSU faculties. Being around them has been a learning experience for me.

My thesis would be incomplete without thanking my labmates. I cannot even imagine my life in lab without them. I would like to acknowledge Dr. Sudipta Dutta and Dr. Sasmita Mohakud for treating me as their younger brother. I don't have enough words to thank Dr. Prakash, my "friend, philosopher and guide". He helped me through all the scientific problems, took pain to answer all my queries. Without him probably I would not have become what I am today. Thank you for making time for me even in the busiest of your times. Thank you! Dr. Arun helped me from the first day in this lab. Dr. Pralok never let me feel that he is elder than me, without his lively presence the Italy trip would not have been enjoyable. The life at JNC would not have been this much lively, exciting and replete with food without one companion, Arkamita. Thanks for all her far-reaching supports in each day of my JNC-life. Alex, Dr. Siam, Dr. Meera and Ershaad were always good friends, with whom I share many fun moments. Thank you Palllavi for the endless chats. JNC would not have been the same without Somananda and Swastika, they also helped me in my tough times. Work is never dull with the laughter and conversations with Bradraj (for all the jokes!) and Asvini. Shubhajit and Abhiroop should specially be mentioned because of their singing sessions in lab. I am also thankful to Dr. Ganga Periyasamy for the guidance. Thanks to Dr. Sharma, Wasim, Silvia, Nisheal, Neha and Dr. Madhuri, whom I always enjoyed being around and discussed different topics. I should also mention all the visiting students, Francesco, Francesca, Nabanita, Cristina, Divya, Anisha and Elizabeth for their company. Prof. Ayan Dutta also helped me in understanding some basics.

I am grateful to my high school and undergraduate teachers, they have instilled a love for learning and left a life-long impact. Thank you Pranab Da, Bidhan Da and Motin Da for helping me in understanding the basics of science and clarifying my doubts.

I would like to thank my Integrated PhD batchmates Prashant, Anindita, Ajmala and Darshana for their constant support and encouragement. I will prize this friendship lifelong.

I will always be indebted to Mighfar Bhai, Sananda, Kanchan and Sudeshna for

all the academic helps. From selfies to parties and from gossips to movies, thanks for being there for me Sudeshna, Debdipto, Koushik, Arkamita and Rajib. Weekends were fun because of you only. Thanks to my seniors Pranab, Prakash K., Sudip, Barun, Gautam, Babhru, and Partha for their company. Sachi da, Arup da, Debu da, Ritesh da, Arpan da, Pralok da and Suman da, thank you. You made me feel at home in JNC. I also thank Subhajit, Saikat, Jia, Anshul and Pawan for the little enjoyable breaks. Thanks to all my friends in JNC, who made my life less stressful. Sutapa, Sandeep, Rana, Dasari, Avinash, Shiva, Nagarjun, Gayatri, Chidambar, Sisir, Anirban, Ramana, Bivas, Amrit, Dhanya, Srinu, Soumik, Jiaul, Rajdeep, Manoj, Vasu, Meha, Priyanka, Ananya, Anjali, Sohini, Soumyabrata, Mohini, Shreyan, Manodeep, Niloy, Gangaiah, Satya, Debopreeti, Pallabi, Dibyasree, Anaranya, Sunita, Nivedita, Tarak, Moumita, Somnath, Arpan, Chandan K, Syamantak, CD, Negi, Sudip, Chaitali, Karthik, Papri, Vinutha, Ruksan, Sourav, Raktim, Somesh, Saikat, Nisha, Urmi, Nitesh, Vini, Varun, Piyush, Pandu, Dileep, Vikas, Sharmila, Nishith, Anirudh, Sutanuka, Devina, Sona, Ananthu, Uttam, Suchitra, Abhijit, Avijit, Debasree, Shruti, Rajkumar, Sumanta, Mohit, Bhawani, Pavan, Viswas, Shiladitya, Kim, Lowkya, Bharath, Guin, Krishnendu, Sumayya, Murthy, you all made my stay here easier. I will certainly miss the football and cricket matches in JNC. I have made some very good friends there.

I would like to thank all my school and college friends Chinmay, Soumyajyoti, Sabyasachi, Sayani, Payel, Soumen, Tathagata, Ranjan, Atreyee, Arpita, Debparna, Bappaditya, Abhijit, Sohel, Pratik, Sugata, Rudra, Subrata and many more, who made my college-life memorable. Banabir, Rima and Nabadyuti, though we don't meet every day, will always remain very close to me. Appreciation also goes out to Pritha, whose support has been unique in many ways. Special thanks to my closest friends, Javed and Sabina who gave me moral support when I needed it the most.

I am also grateful to JNCASR for providing a world class environment to pursue research. I am thankful to all the administrative, technical, security, Complab, TUE-CMS and Dhanvantari staffs who try their best to make our life smooth at the campus.

Finally and most importantly, I would like to thank my parents for all the supports and for always having the sympathetic ear which I needed the most in my difficult times. You are always there for me. Also, my sister, whom I cannot thank

enough for being my best friend, for knowing me through my goods and bads and for helping me to handle problems of life with a smiling face. My brother in law Sabyasachi is also always very supportive.

JNC always will be a whiff of nostalgia for me. Thank You All for being there.

Synopsis

Systems with low-dimensionality show the restriction in the motion of microscopic degrees-of-freedom, resulting in appearance of various exciting properties, most of which are absent in three-dimensional bulk materials. In recent times, a revolutionary advancement in nanotechnology can be experienced due to the parallel progress both in experimental techniques and theoretical understanding. Fundamentally, with reducing the dimensionality of systems, the electrons experience the constraint in their motions, namely quantum confinement. Due to the quantum nature of these emerging properties, it is quite challenging to understand their microscopic properties. In this thesis, electronic, magnetic, optical and quantum transport in different kinds of low-dimensional materials have been explored. Real time dynamics, static electronic structures as well as non-equilibrium transport phenomena have been studied with the help of quantum many-body and density functional theory based approaches.

The thesis is divided into nine chapters.

In the **first chapter**, a brief discussion about a few recently obtained low-dimensional systems such as graphene and few analogous two dimensional sheets of it is given. An overview of molecular junctions from both experimental as well as theoretical point of view is depicted. Different transport regimes, depending upon the length and energy scale have been reviewed briefly. A general description of theoretical models and computational approaches which extensively used in following chapters, have been explored.

Using constant-temperature Born-Oppenheimer molecular dynamics (BOMD) simulation, a way to insert extended line defects (ELDs) at the grain boundary in

hybrid graphene and boron nitride nanoribbons (BNCNRs) have been demonstrated in the **second chapter**. Systematic studies have shown that different kinds of extended line defects can be stabilized by depositing different adatoms such as carbon, boron, and nitrogen at the grain boundaries of graphene - boron nitride junctions. It has been found that the electronic and magnetic structures of these nanoribbons can highly be modulated in presence of these ELDs. Depending upon the interfacial structures, these nanoribbons show a wide range of electronic properties ranging from semiconducting to spin polarized metallic behaviours.

In the **third chapter**, emergence of different kinds of stable line defects in silicene have been discussed by performing BOMD simulations. Our results show that depending upon the presence of silicon adatoms, edge shape of grain boundaries (i.e. armchair or zigzag), stable line-defects can be introduced in a controlled manner. Further studies demonstrate the stability of these line-defects containing sheets on Ag(111) surface at room-temperature. Importantly, 5-5-8 line defects modify the non-magnetic semimetallic pristine silicene sheet to spin-polarized metal. As ferromagnetically ordered magnetic moments remain strongly localized at the line-defect, an one-dimensional spin-channel gets created in silicene. Zigzag silicene nanoribbons with 5-5-8 line defect also shows various interesting magnetic and electronic properties depending on the nature of magnetic coupling between edge and defect spin-states.

In the **fourth chapter**, electronic, magnetic and optical properties of 3d-transition metal embedded graphitic carbon nitride sheets with and without graphene support have been explored using density functional theory-based calculations. Bare carbon nitride sheets, which is a wide-gap semiconductor, becomes metallic upon transition metal inclusion. Studies show that depending upon the 3d-metal atoms, different kinds of magnetic ground state can appear in these systems. Stacking with graphene layer, composite systems demonstrate increase in structural stability and magnetic interactions with respect to transition metal deposited carbon nitride sheets. Performing Heisenberg model based Monte Carlo simulations, the Curie temperatures are calculated for different ferromagnetically stable systems. These sheets also demonstrate prominent visible light response, which gives a clue about their probable photocatalytic activity.

Nitrogen substituted point-defects containing graphene sheet have been explored

in the **fifth chapter** for their potential application towards trapping of pollutant gases. BOMD studies demonstrate that, electron-rich point-defect sites can selectively and efficiently trap different kinds of poisonous and greeenhouse polar gas molecules. Moderately strong hydrogen-bond formation between the hydrogen atom of the gas molecules and nitrogen of defect-sites stabilized the adsorbed molecules. Desorption of gases from these sheets at higher temperature have also been studied. Interestingly, increased defect concentration in the sheets can enhance the adsorption capacity of these adsorbents.

In the **sixth chapter**, using ab-initio numerical methods, the spin-dependent transport and thermoelectric properties of a spin-crossover molecule based nanojunction have been explored. A large magnetoresistance, efficient conductance-switching, and spin-filter activity in this molecule-based two-terminal device has been demonstrated. The spin-crossover process also modulates the thermoelectric entities. It can efficiently switch the magnitude as well as spin-polarization of the thermocurrent. Moreover, it also substantially affects the thermopower and consequently, the device shows extremely efficient spin-crossover magnetothermopower generation. Furthermore, by tuning the chemical potential of electrodes into a certain range, a pure spin-thermopower can be achieved for the high-spin state. Finally, the reasonably large values of figure-of-merit in the presence and absence of phonon demonstrate a large heat-to-voltage conversion efficiency of the device.

In the **seventh chapter**, reversible spin-state switching of NO-adsorbed manganese porphyrin (MnP) on top of gold (111) surface has been explored using on-site Coulomb interaction incorporated density functional theory. The spin-state switching can be achieved by inducing conformational change in the molecular geometry. Mechanical manipulation of conformation by a STM tip in this regard has been studied. Transport and thermoelectric characteristics in the two-terminal device architecture embedding these molecular systems, have been studied thoroughly.

Electronic transport in molecular nanojunction based on heteronuclear six-membered rings have been discussed in the **eighth chapter**. The master (rate) equation approach has been used to treat the system which stays within Coulomb blockade regime. The results show how the chemical nature of site, attached to electrodes, can influence the response of this nano-system to an external source-drain bias. Depending on attachment of electrodes at various atomic sites, we have been able

to obtain a host of exotic current-voltage characteristics, from negative differential conductance to rectification to Coulomb blockade behaviors. We have analyzed the microscopic reasons behind these exotic phenomena in details.

The **last chapter** summarizes the present thesis. It also discusses about the various new directions of research, appear as the future outlooks of the thesis.

List of Publications

Publications Related to the Thesis Work

1. *"Adsorption of HF Pollutant on Single Vacant 2D Nanosheets: Ab Initio Molecular Dynamics Study"*
   Dibyajyoti Ghosh, Ganga Periyasamy and Swapan K. Pati,
   J. Phys. Chem. C, **117**, 21700 - 21705 (2013).

2. *"Line Defects at the Heterojunction of Hybrid Boron Nitride/Graphene Nanoribbons"*
   Dibyajyoti Ghosh, Prakash Parida and Swapan K. Pati,
   J. Mater. Chem. C **2**, 392 - 398 (2014).

3. *" Insertion of Line Defect in Nanoribbons of Graphene, Boron Nitride and Hybrid of them: An AIMD study"*
   Dibyajyoti Ghosh, Prakash Parida and Swapan K. Pati,
   J. Phys. Chem. C, **118**, 14670 - 14676 (2014).

4. *"Transition Metal Embedded Two-Dimensional C3N4-graphene Nanocomposite: A Multifunctional Material"*
   Dibyajyoti Ghosh, Ganga Periyasamy and Swapan K. Pati,
   J. Phys. Chem. C, **118**, 15487 - 15494 (2014).

5. *"Computational Studies on Magnetism and Optical Properties of Transition Metal Embedded Graphitic Carbon Nitride Sheet"*
   Dibyajyoti Ghosh, Ganga Periyasamy, Bradraj Pandey and Swapan K. Pati,
   J. Mater. Chem. C, **2**, 7943 - 7951 (2014).

6. *"Spin Crossover Molecule based Thermoelectric Junction"*
   Dibyajyoti Ghosh, Prakash Parida, and Swapan K. Pati,
   Appl. Phys. Lett, **106**, 193105 (2015).

7. *"Stable Line Defects in Silicene"*
   Dibyajyoti Ghosh, Prakash Parida, and Swapan K. Pati,
   Phys. Rev. B, **92**, 195136 (2015).

8. *"Spin-state Switching of Manganese Porphyrin by Conformationan Modification"*
   Dibyajyoti Ghosh, Prakash Parida, and Swapan K. Pati,
   J. Phys. Chem. C, Just Accepted (2016).

9. *"Reversible Gas Trapping in Defective N-doped Graphene"*
   Dibyajyoti Ghosh and Swapan K. Pati,
   (Under preparation)

10. *"Electron Transport through Small Heterocyclic Molecules: A Quantum Many-body Approach"*
    Dibyajyoti Ghosh, Prakash Parida, and Swapan K. Pati,
    (Under preparation)

Other Publications by the Author

11. *"2D coordination polymer composed of 1D NiII(mu-O)(mu-H2O)NiIIn ferromagnetic chains: Modulation of magnetic properties based on dehydration and rehydration"*
    Stephen Adie Adalikwu, Anindita Chakraborty, Arpan Hazra, **Dibyajyoti Ghosh**, Swapan K. Pati and Tapas Kumar Maji,
    (Submitted)

12. *"Electronic, Magnetic and Transport Properties of Fe_n-bis(n-acene) and Fe_n-bis(n-BNacene) (n=1,2): A Theoretical Study"*
    Dibyajyoti Ghosh, Prakash Parida and Swapan K. Pati,
    J. Phys. Chem. C, **116**, 18487 - 18494 (2012).

13. *"Density Functional Theoretical investigation of the aromatic nature of the BN substituted Benzene and four ring polyaromatic hydrocarbons"*

Dibyajyoti Ghosh, Ganga Periyasamy and Swapan K. Pati,
Phys. Chem. Chem. Phys., **13**, 20627 - 20636 (2011).

List of Figures

List of Tables

Contents

Chapter 1

Introduction

Low-dimensional materials are of booming interest to both experimental as well as theoretical research [1]. Reduction of one or more spatial dimension(s) to nanometer range, makes these materials quite different in terms of various properties compared to their bulk counterpart. Fundamentally, quantum confinement effects are very prominent in these systems where the motion of electrons is strongly constrained along the reduced dimensions. Effect of electron-electron correlation becomes very much important and quite decisive for the properties of these classes of materials. As the system-size remains in the range of electron wave length here, understanding the emerging phenomena in these materials, eventually needs the concept of quantum mechanics.

In this thesis, we have studied a class of low-dimensional systems and explored their different fascinating properties, arising from various interactions.

To begin with, in this introductory chapter, we give a brief overview of low-dimensional materials, particularly, various graphitic two-dimensional (2D) systems and different theoretical models and numerical techniques that are used to investigate the structural, electronic and transport properties. In the following section, we discuss about the two-dimensional materials, majorly focusing on graphene, hexagonal boron nitride, silicene and graphitic carbon nitride and their quasi one-dimensional nanoribbons. Thereafter, we explore various kinds of defects and interfaces, generally appear in these low-dimensional materials. In third section, we move to the topic of quantum transport in molecular nano-junctions where we discuss experimental and theoretical progress of this field in short. In section 1.4,

thermoelectric properties of various materials are discussed. Subsequently, we review various theoretical models and numerical methods which have been adopted in the present thesis to study the low-dimensional materials. Finally, we conclude the chapter with brief outline of successive other chapters of the thesis.

1.1 Low-dimensional Materials

Though the extraordinary properties of low-dimensional materials have long been explored by theoretical studies, experimental realizations remained challenging for long time. Recent discovery of various experimental approaches to perform controlled synthesis and reliable characterizations have produced tremendous impetus for research of low-dimensional materials. Here, we are discussing some of these materials, relevant for the present thesis.

1.1.1 From Carbon Atom to Graphene

Carbon (C) is the second most abundant element by mass in human body. It is the key element in all the living systems and form maximum compounds except hydrogen. The wide range of carbon compounds and its diverse and unique characters have generated a separate field of research, the area of which keeps on increasing every day. Looking in its primary properties, carbon is a p-block element and is tetravalent. The compounds of it are mostly covalent with very few (relatively) exceptions where ionic character of bonds predominate. Most importantly, carbon forms innumerable number of compounds and polymer systems, as it is the only element which forms systems with all the three hybridization, namely sp, sp^2 and sp^3. In fact, it is due to its catenation character that systems formed by carbon is versatile in nature. Coming to the crystalline allotropic forms of carbon, two of the allotropes are very common, diamond and graphite. However, a set of allotropes are recently added to the list, nanocarbons. Some of the known allotropes are (1) fullerenes, which are molecular clusters and contain closed hollow cage of sixty or more carbon atoms; [2] (2) nanotubes, where carbon atoms show long cylindrical arrangement [3] and (3) nanobuds, which are combination of fullerenes and nanotubes [4]. In this allotrope, fullerenes remain covalently attached to the outer surface

of nanotubes. Another highly explored all-carbon material is graphene which is nothing but a single layer of graphite [5].

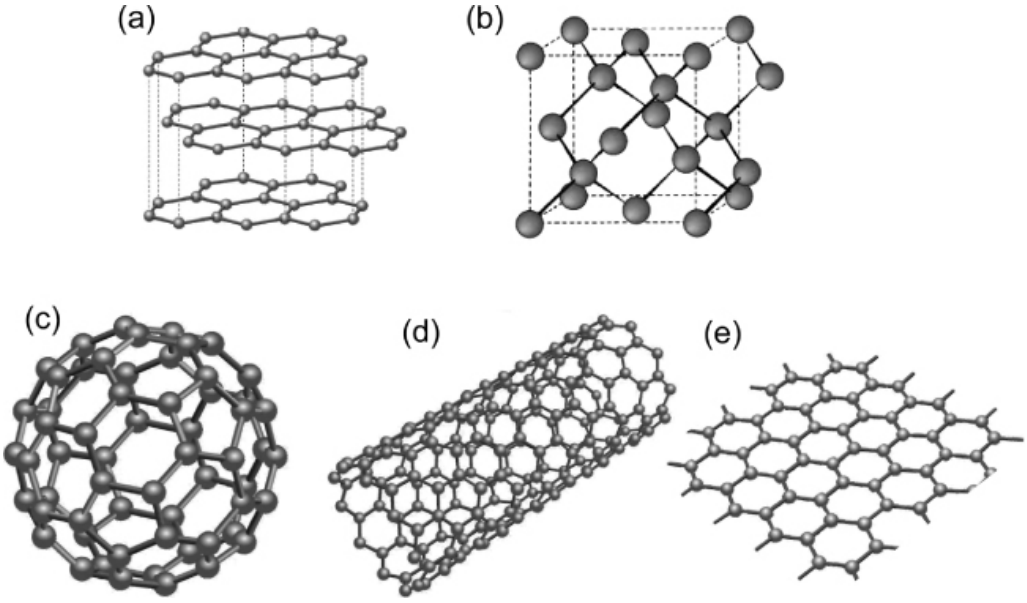

Figure 1.1: Ordered carbon structures, (a) graphite, (b) diamond, (c) buckminsterfullerene (C60), (d) nanotube and (e) graphene. The gray sphere represents carbon atoms. Adopted from Ref. [6].

Looking into the atomistic structures of the allotropes in Fig. 1.1(b), all C-atoms in diamond remain tetrahedrally surrounded by other four carbon atoms (i.e. form sp^3 hybridization). However, graphite is composed of layers of hexagonally arranged C-atoms, each of which remains sp^2 hybridized, forming planar 2D-sheets (See Fig. 1.1(a)). Note that, in the present thesis, we have majorly focused on the graphite form of carbon and discussed about it in detail.

As can be seen in Fig. 1.1(a), the basic building block of the single graphite layer is six-membered planar benzene ring, without any H atoms. Here, each C atom forms two kinds of bonds, (1) three σ bonds with three neighbouring C atoms, using sp^2 hybridized orbitals and (2) one π-bond where the $2p_z$ orbital gets involved. Importantly, appearance of well known resonance between the structures which contain alternative modes of single and double bonds, results in identical C - C bonds, with a length of 1.415 Å. The cyclic localization of the π-electrons in benzene ring results in extra stabilization, which in general is described as gaining of aromaticity. Looking closely at the graphite structure, it becomes evident that these aromatic

benzene rings fused to each other, forming single layer of two-dimensional sheet of carbon atoms. And this single layer stack to other identical layers in third dimension with an interlayer separation of 3.35 Å, by weak van der Waals forces. Depending upon the nature of stacking, graphite can be of different types. Most common form is α-graphite, where every alternative layers stay in same phase and create so called AB-stacking (See Fig. 1.2). Graphite conducts electricity due to the delocalization of π-electrons which remain free on the plane of the layers. For its conducting nature, graphite is used in arc lamp electrodes, carbon microphone etc.

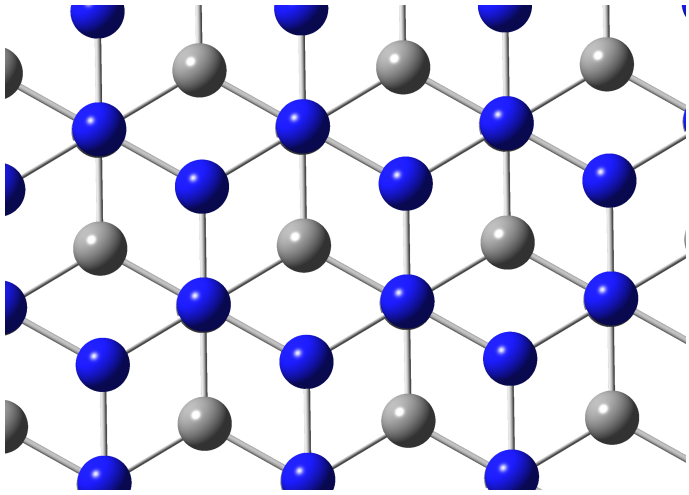

Figure 1.2: Positional relationship between two identical planes, A and B in α-graphite. Carbon atoms of A and B planes are represented in gray and blue colored spheres, respectively.

As mentioned earlier, graphene is a single layer of graphite i.e. one atom thick two dimensional sheet with carbon atoms arranged in honey-comb lattice [5]. This allotrope was isolated in 2004, which revolutionized the material science research with its number of extraordinary properties [5, 7]. Graphene can be considered as the "missing link" between the nanocarbon systems i.e. zero- and one-dimensional materials and three dimensional bulk graphite. One can also think of making all other carbon materials of any dimensionality from graphene. As an example, wrapping with additional formation of pentagonal rings in between and rolling up of graphene sheet can produce fullerenes and nanotubes. Whereas, stacking of graphene layers eventually gives us graphite.

Although, graphene has been discovered recently, the properties of it has been investigated theoretically quite long time ago, in 1947, by P. R. Wallace [8]. However, it had been believed that free standing graphene can't exist in nature. In their seminal papers, Landau and Peierls argued that due to the thermodynamic instability, a pure free standing two-dimensional crystalline material can't be realized at finite temperatures [9, 10]. Even at zero temperature, the quantum fluctuation was predicted to destroy true long range order in honeycomb lattice. Surprising discovery of two-dimensional graphene by K. Novoselov and A. Geim at Manchester University proved this long standing believe not to be correct [11]. Nonetheless, earlier theoretical predictions still remain true as close investigation of structure reveals that graphene is not completely two-dimensional as it has intrinsic ripples in the non-periodic direction [12]. Apart from all these, another surprising fact perhaps is the simplicity of isolation of graphene. As demonstrated by Geim and Novoselov, simple adhesive tape can pull out graphene layers from highly oriented pyrolytic graphite [11]. This particular process is known as micromechanical exfoliation technique. Note that, generally in this process, single layer of graphene is formed along with other graphite sheets, containing different number of graphene layers. One needs to identify graphene with single and few-layers by transferring all the peeled out materials onto a thin layer of SiO_2 on a silicon wafer [13]. Followed by that, particular single layered area can be found using combination of different microscopy techniques, such as optical, electron-beam and atomic force microscopes. The colour difference between the wafers, containing thick- and thin layers of graphite, can easily distinguish between these two kinds of graphite. Moreover, to differentiate between few- and multi-layer graphene, optical and scanning tunneling microscope had been used. Finally, the single layer of graphene has been identified by using atomic force microscopy technique. Importantly, as demonstrated by this group of Manchester University, all these graphene layers are stacked on top of the substrate by weak van der Waals interactions and consequently free-standing layers can be obtained by applying precise etching of the substrate [14]. With that, one can efficiently reduce the substrate-effect and study the intrinsic properties of single and a few-layer graphenes. After this path-breaking work, graphene came to the limelight of research and immediately a large number of papers started appearing in the literature. For their outstanding work in the field of graphene, Geim and Novoselov

have been awarded the Nobel prize in Physics in 2010. The press release from Nobel committee reads the prize given to these two researchers for "for groundbreaking experiments regarding the two-dimensional material graphene".

The experimental realization of graphene has given the access to an enormous number of interesting physics in this material. Various extraordinary properties such as, ambipolar field effect [11], integer quantum Hall effect at room temperature [15], huge carrier mobility [11, 13], detection of single molecules [16], metal-free magnetism [17], long phase coherent lengths[18], Berry phase [15] and Klein paradox [19] have been found almost immediately. With these discoveries, it had been realized that graphene is quite promising in various technological applications, such as, ultrahigh-frequency transistors [20], thermally and electrically conductive reinforced composites, optical electronics [21], sensors [16], biological engineering [22], photovoltaic cells [23] etc.

The rhombic two-atom unit cell of graphene is bipartite in nature i.e. it consists of two interpenetrating sublattices, each of which forms a triangular Bravais lattice (see Fig. 1.3(a)). [24] In reciprocal space, as shown in Fig. 1.3(b), graphene has a honeycomb lattice. As shown in Fig. 1.3 (c), the band structure of it shows zero-gap semiconducting nature, where, linearly dispersed π-bands touch each other at the K and K'-points of the hexagonal Brillouin zone. Consequently, the charge carrier density as well as nature can be tuned by electrical gating [24].

1.1.2 Hexagonal Boron Nitride sheets

With the explosion of interest on graphene, other two-dimensional materials also have become prime focus of material science research [25]. One such material is two-dimensional sheet of hexagonal boron nitride (h-BN), which is isoelectronic to graphene and called as "white graphene"[26]. As shown in Fig. 1.4 (a), a sheet of h-BN is consists of alternating boron and nitrogen atoms in a honeycomb arrangement, where all the atoms are sp^2 hybridized. Following same analogy between benzene and graphene, one can demonstrate borazine ($B_3N_3H_6$) ring as the building block of h-BN sheet. For synthesis of h-BN layers, two commonly used processes are mechanical and liquid-phase exfoliations [27]. Applying these methods, individual sheets of h-BN can be peeled out from stacked 2D crystals of it by breaking the weak interlayer van der Waals forces.

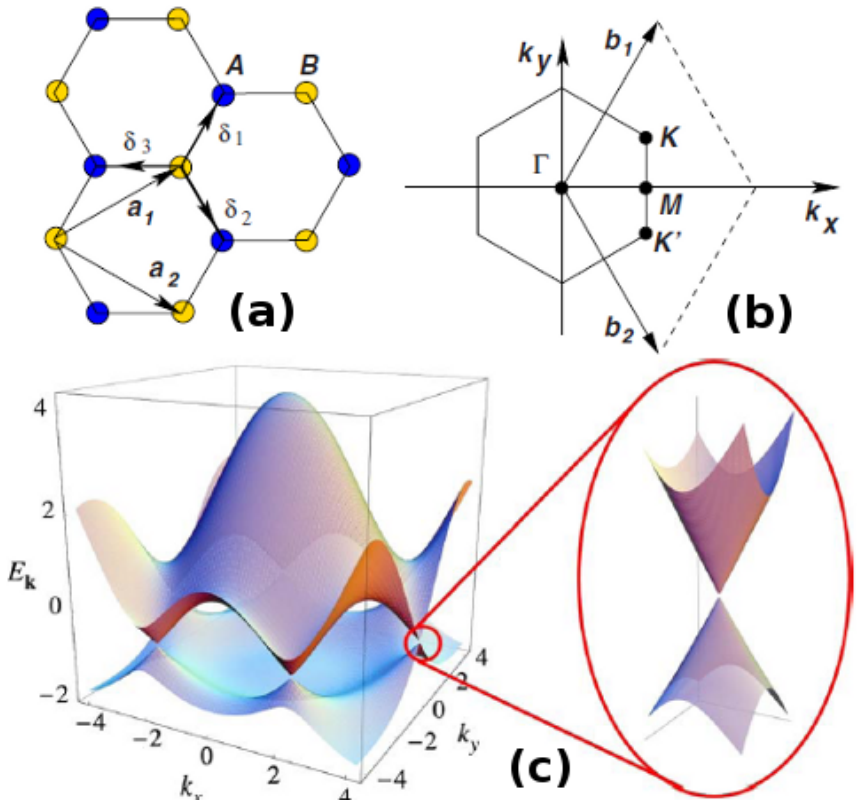

Figure 1.3: (a) Honeycomb lattice of graphene and (b) its Brillouin zone. In (a), a_1 and a_2 are the lattice unit vectors of graphene, and δ_i where i=1,2,3 are the nearest-neighbor vectors. (c) Electronic dispersion in the Brillouin zone of graphene; right side shows zoomed energy bands close to one of the Dirac points. Adopted from Ref. [24].

Though it has similarity with graphene in structural aspects, electronic and optical properties differ quite largely. The h-BN is an insulator with a band gap of 5.9 eV [25]. And consequently, it has been used as an efficient charge leakage barrier layer in various electronic equipments [25]. Moreover, due to its chemical stability and strong insulating nature, h-BN layer is incorporated in the graphene-transistor, where it serves two-fold purposes, (1) atomically thin top dielectric layer and (2) inert flat substrate [25]. The composite device of graphene - h-BN layer shows significantly improved device performance. Fundamentally, the difference between graphene and h-BN arises from the electronegativity difference between B and N atoms, making the B-N bond quite ionic in nature. Unlike graphene, where delocalization of π-electrons results in structural stability, for h-BN, the two dimensional structure gets stabilized by the p_π-p_π charge transfer from N to B.

1.1.3 Silicene Sheets

Another extensively explored two-dimensional graphene-like material is a single layer of Si atoms, namely silicene (see Fig. 1.4 (b,c)) [25, 28]. Fundamental physical and chemical properties as well as technological applications of silicene have created considerable research interest. This 2D material is quite promising to enhance the performance as well as scalability of existing silicon-based electronics due to its compatibility-issue. From the extensive first-principle calculations, it was predicted that monolayer of Si atoms can be stabilized in the low-buckled hexagonal structures where the equilibrium buckling appears as 0.44 Å (see Fig. 1.4(c)) [28]. The presence of this buckling evidently proves the preference for sp^3-like hybridization over a pure sp^2 one for the silicene sheet. Fundamentally, the large Si-Si distance in silicene (i.e. 2.28 Å) weakens the π-π overlaps and makes the realization of pure sp^2-hybridized planar silicene impossible. Further study revealed the stabilization of silicene by partial hybridization between s and p_z-orbitals of Si atoms. In general, the Si atoms in silicene are considered as in intermediate hybridization, in between sp^2 and sp^3. Interestingly, despite of structural differences, the band structure of silicene strongly resemble with that of graphene [25, 28]. The linear dispersion of π and π^* bands at the K and K′-points demonstrate the massless Dirac fermionic behaviour of ambipolar charge carrier in the silicene [25].

Although silicene appeared to be quite promising for next-generation electronics,

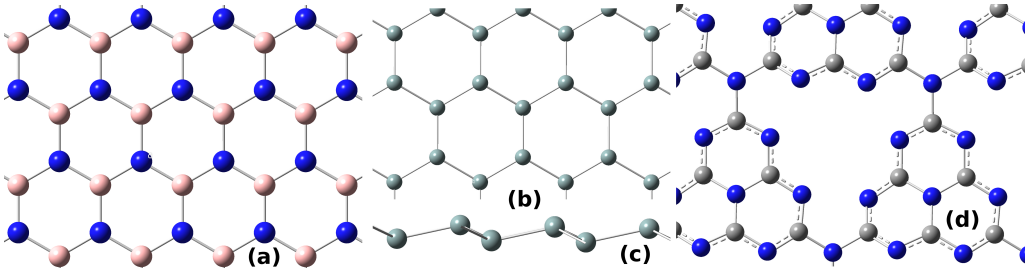

Figure 1.4: (a) Honeycomb lattice of h-BN sheet. The (b) top-view and (c) side-view of silicene. And (d) top view of monolayer of buckled g-C_3N_4 sheet. Blue, yellow and gray coloured spheres represent nitrogen, boron and silicon atoms, respectively.

high-quality synthesis of it is still challenging. The major problem arises due to the non-existence of van der Waals layered bulk-phase solid of silicene. Silicon remains in its bulk-phase by forming Si-Si sp^3-hybridized covalent bonds. Thus, up to now, only reliable method to realize this elemental monolayer is the substrate assisted epitaxial growth of it under ultra-high vacuum condition. As demonstrated by different experimental groups, atomically clean and highly ordered plane of Ag(111), Ir(111), $ZrB_2(0001)$ serve as efficient growth assisting substrates. [29–31] Among all these, Ag(111) plane has been explored mostly where Si atoms are deposited from a piece of Si wafer on the substrate which remains heated at 220-260 °C. [30] It can be noted, despite all these investigations, there is no evidence of free-standing silicene layer so far.

1.1.4 Graphitic Carbon Nitride Sheets

Graphitic carbon nitride (g-C_3N_4), which is the most stable phase of carbon nitride in ambient environment, has attracted a considerable research interest due to its fascinating mechanical, electronic and photophysical properties . It's quite different in structural aspect than that of graphene and its other analogous systems. As shown in Fig. 1.4(d), tri-s-triazine units get connected by planar amino groups and construct plane with cavities. Generally, these planes get stacked in the third dimension via weak van der Waals forces during the synthesis process. There are number of processes employed for the synthesis of g-C_3N_4 such as physical vapor deposition, chemical vapor deposition, solvothermal method, thermal condensation

etc. From ultraviolet-visible absorption spectrum and extensive theoretical calculations, this material appears to be a semiconductor with a bandgap of 2.7 eV [32]. Due to these special structural and electronic properties, pristine and doped g-C_3N_4 have shown efficient applications towards catalysis(for Friedel-Crafts reactions, oxygen reduction reaction, water splitting etc.) batteries, light emitting devices, fuel cells, solar cells etc [33].

1.1.5 Nanoribbons: Quasi One-dimensional Systems

Up to now, we majorly discussed infinite sheet of various two-dimensional materials. However, considering their possible applications in nano-electronics, these sheets are quite unsuitable and needed to be precisely terminated. These sheets can be cut down into elongated strips, having small but finite width. By that way, one can find quasi one-dimensional ribbon like systems, where the width is very very smaller than the length [34–36]. Due to finite-size, quantum confinement and structural boundaries, the electronic and magnetic properties of these nanoribbons (NRs) differ a lot from their two-dimensional counterparts [37, 38]. Depending upon the direction of truncation, there can be two kinds of NRs, zigzag NRs (ZNRs, see Fig. 1.5 (a)) and armchair NRs (ANRs, see Fig. 1.5 (b)) [37]. Interestingly, due to their different boundary conditions, these two NRs show quite different electronic and magnetic properties [37–39]. Note that, the atoms of zigzag and armchair edges appear from same and different sublattices of bipartite lattice, respectively. In general, width of the nanoribbons strongly influences their various properties. Thus, precise control over the ribbon-width is necessary during their fabrication. As shown in Fig. 1.5 (a), the width of ZNRs are specified by counting the number of zigzag chains (n) in the truncated direction and named as n-ZNRs. For ANRs, the number of atoms (m) along the terminated zigzag edge in cross ribbon direction signifies the width and named as m-ANRs (see Fig. 1.5 (b). In the present thesis, we have considered nanoribbons of three 2D-materials, graphene (ZG/AG), boron-nitride (ZBN/ABN) and silicene (ZSi/ASi) nanoribbons (NR).

With finite termination, edge dangling states appear in these NRs due to the unsatisfied valency. Consequently, these edges remain quite reactive and generally show different kinds of structural reconstruction processes [40–42]. To minimize this stabilization problem, most general approach has been to passivate the edges with

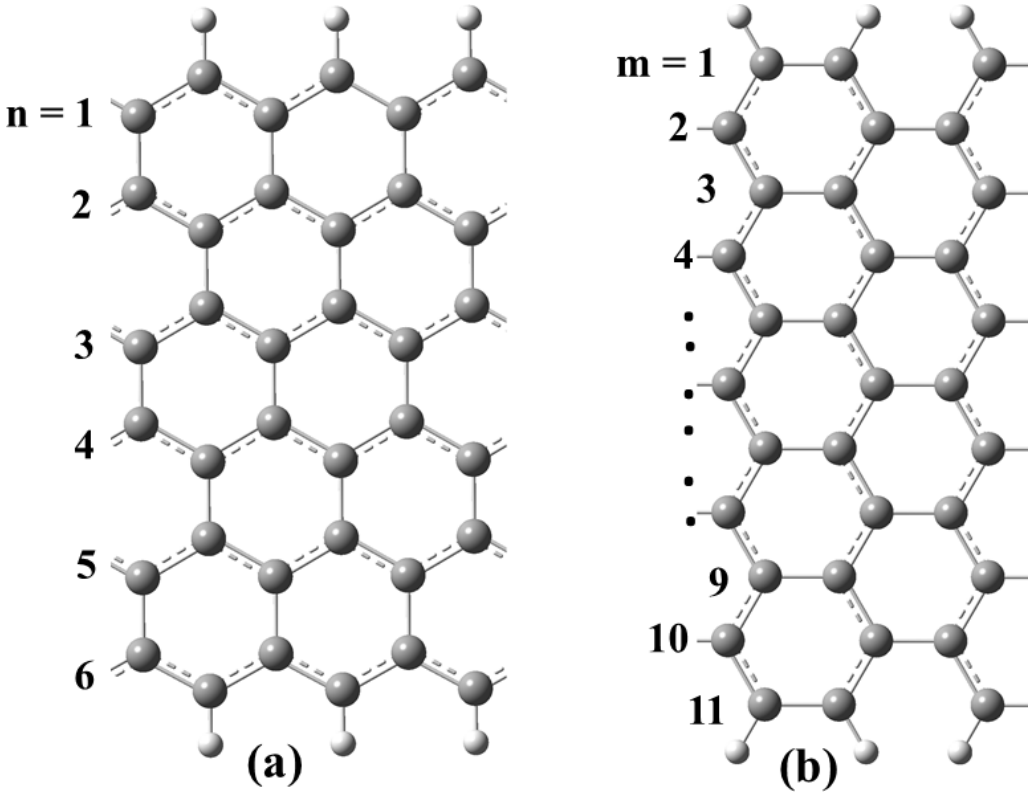

Figure 1.5: Schematic representation of the GNRs. The cells of zigzag (a) and armchair (b) graphene nanoribbons (GNRs) are given. The GNRs are periodic along the x axis. The n and m indices specify the width of zigzag and armchair GNRs, respectively.

different atoms, majorly hydrogen (see Fig. 1.5 (a, b)). Various studies have already considered different kinds of H-passivation of these nanoribbons and explored their rich variation in electronic and magnetic properties [43–45]. In their ground state, H-passivated ZGNRs appears as spin-symmetric semiconductor, where parallelly arranged magnetic moments at two edges couple antiferromagnetically (AFM) across the edges [37]. The ZNRs of silicene behave quite similar to the ZGNRs, i.e. H-passivated ZSiNRs show antiferromagnetic semiconducting ground state [39]. Furthermore, other excited magnetic configurations i.e. ferromagnetic and nonmagnetic states of ZSiNRs are metallic. Note that, in these ZNRs, nature of the magnetic ground state depends on the width of the ribbons [39, 46]. The energy difference between AFM and FM states decreases as the width of ZNRs increases. As the ribbon width becomes greater than spin-decay length, these two magnetic states

become energy-degenerate. Unlike these two, H-passivated ZBNNRs are wide band gap insulator with a nonmagnetic ground state [47]. For AGNRs and ABNNRs, the ribbons show nonmagnetic semiconducting nature for all widths [37, 38]. Whereas, for ASiNRs, depending on the value of "m", ribbons behave as either metallic or semiconducting [39]. Due to their interesting properties, appearing from peculiar localized edge-states, in the thesis, we have extensively investigated the electronic and magnetic properties of ZNRs.

One of the most challenging issues in patterning nanoribbons is the control over their width at the nanometer scale. However, recent experimental developments have made it possible to realize the ribbons with precise widths as well as almost well-defined edges [48]. A number of techniques, such as, electron-beam lithography, metallic nanoparticle etching, microscope lithography, chemical method have extensively been used to pattern these sheet materials in nano-scale devices [49–52]. Apart from these top down approaches, for GNRs, bottom up approaches are also quite well-explored [53, 54]. In these approaches, giant graphene structures form by attaching small molecular building blocks using reliable chemical synthetic route. Following this, one can have graphene nanoribbons with complete control over the exact nature of edge structures. Another method, implemented recently is to unzip and unroll the corresponding nanotubes to achieve GNRs/BNNRs with smooth edges [55, 56]. Recent experiments have demonstrated detailed edge geometries of both armchair and zigzag ribbons, synthesized by this novel method.

1.2 Defects and In-plane Interfaces in Graphitic Systems

Appearance of disorders in pure crystalline materials is quite inevitable due to the second law of thermodynamics. Apart from this fundamental law, defects can also form in the regular lattice during its preparation. These defects are of different kinds, such as, zero-dimensional point defects i.e. vacancies, interstitial atoms; one-dimensional dislocation line defects; two-dimensional grain-boundaries or stacking faults; three dimensional voids and inclusions. Among all these, due to low-dimensionality of graphene and its analogous materials, the types of possible defects also reduces. However, like any other bulk-materials, different defects play crucial

roles in electronic, magnetic, optical, transport and mechanical properties of these low-dimensional systems even in very low concentration [57]. Due to the scattering of carriers at defective region, the electron/hole conductivity in these materials modulate a lot [58]. Inclusion of dopant atoms modifies the local electronic properties as well as carrier concentration in wide range [59]. Appearance of defect-induced finite and stable magnetic moments in these system also studied extensively [60–62]. The thermal conductivity and mechanical strength of these materials also alter depending upon the concentration and types of defects [63, 64]. Looking at these interesting properties, recently, a huge amount of experimental efforts have been devoted to deliberately induce defects in various 2D-materials using different techniques, such as, electron beam irradiation, chemical treatments etc.[65].

1.2.1 Types of Defects

Broadly, defects can be intrinsic i.e. distortion in lattice without any extra foreign atom and extrinsic which appears due to incorporation of impurity atom(s) in otherwise perfect lattice. We briefly discuss about these defects here.

1.2.1.1 Point Defects

Stone-Wales (SW) defects

This is one of the most commonly found point defects in graphene and its analogous materials, where, removal or addition of atoms is not involved. For SW-defects, as shown in Fig. 1.6(a), one C–C bond rotate by 90° with respect to the centre of the bond, transforming four hexagonal rings into two pentagons and two heptagons [57]. Importantly, SW-defect containing sheets retain same number of atoms as it's in pristine form. All the atoms remain three-fold coordinated and there exist no dangling bonds. The formation energies of it in different 2D-sheets appear to be a few eV [57, 62].

Single vacancy (SV) and multiple vacancy defects

In SV defect, one lattice point remains empty in a otherwise perfect crystal. The SV defects have been demonstrated by a number of TEM and STM-based experimental investigations [66, 67]. Particularly, as shown in Fig. 1.6(b), in graphene, the SV defect gets reconstructed by forming stable C–C bonds by saturating two of the

three dangling bonds [66]. Thus, only one dangling bond remains in the SV site, resulting in formation of a five- and nine-membered ring. However, for boron nitride (see Fig. 1.6(c) for boron monovacancy) and silicene sheets, the SV sites remain stabilized with three dangling bonds and with sp^3-hybridized central Si atom (no dangling bonds), respectively [62, 67]. Unlike graphene, 5-9 reconstruction process is not favourable in these sheets. Like SW defects, formation energies of SV defect in these sheets remain in the range of eV also. For graphene the formation energy appears to be maximum of 7.5 eV, due to the presence of under-coordinated lattice sites [68]. Note that, SV defects can also migrate in the plane of these 2D-sheets and have been demonstrated for graphene at above the room temperature.

These mobile SV defects in 2D-materials diffuse and coalesce to form different multiple vacancies. Two SV defects can be fused to each other and generate double vacancies (DV) . Removal of a dimer of atoms by irradiation can also produce same defect in these 2D-lattices. Interestingly, unlike SV, DV in graphene gets reconstructed to two-pentagon and one octagon (5-8-5) without leaving any dangling bond in the structure (see Fig. 1.6(c)) [69]. Further, it has been found that rotating one or two bonds of octagon ring of 5-8-5 defect can form more stable defects with three pentagons and three heptagons (555-777) or four pentagon, one hexagon and four heptagon (5555-6-7777), respectively (see Fig. 1.6(e,f)) [69]. Different spectroscopic experiments have already demonstrated the existence of these defects in graphene. Vacancies with removal of more number of atoms are also observed in microscopy experiments where bending, warping of layer is quite evident [42, 57].

Adatoms

Apart from these vacancies, other kind of point defects are the presence of adatoms in the regular lattice. These adatoms can be homo-elemental (e.g. C on graphene, shown in Fig. 1.7(a)) or foreign atoms (e.g. B/N/transition metal atoms on graphene) [71, 72]. Generally, homo-elemental adatoms form stable covalent bonds with atoms of perfect lattice in suitable configurations, such as, in bridge position (C on graphene) or on-top position (Si on silicene) [62, 71]. The binding energies of these adatoms appear as high as a few eV. However, these adatoms also remain quite mobile on the surface of the 2D-sheet, as the diffusion barriers for their migration are generally appear to be quite small in magnitude [71, 73]. Unlike above, foreign atoms can physisorb or chemisorb on the 2D-sheets, depending

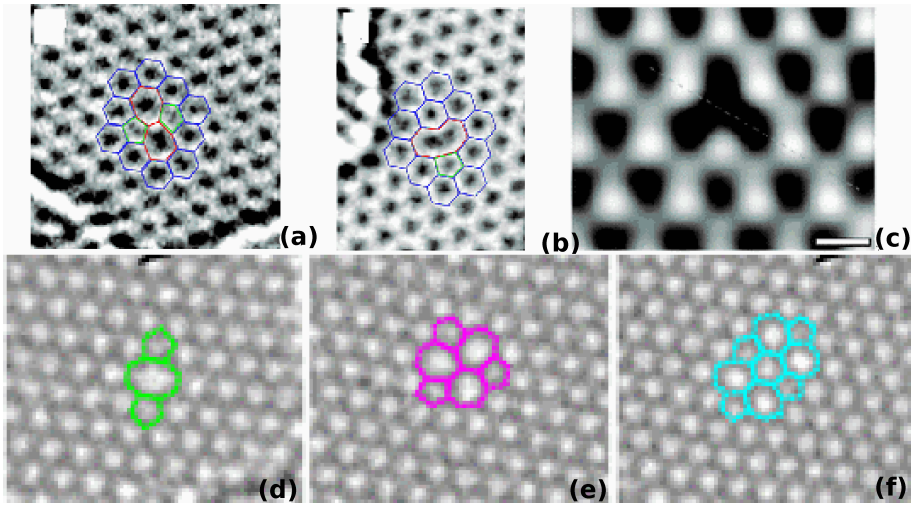

Figure 1.6: Experimental transmission electron microscopy images for (a) Stone-Wales defects and (b) single vacancy defects in graphene. (c) boron monovacancy in h-BN using typical HRTEM. TEM images for graphene with (d) double vacancy, and transformed defects due to bond rotations i.e. (e) 555-777 (f) 5555-6-7777. (a,b) are adopted from Ref. [69], (c) is from Ref. [67] and (e-f) are from Ref. [70].

upon their particular chemical nature [74]. Theoretically, it has been shown that transition metal atoms form weak bonding with pristine graphene sheet [75]. Interestingly, further experimental as well as theoretical studies have demonstrated a strong bonding interaction between transition metal and defect-sites of 2D-sheets [76, 77].

Substitutional Impurities

One or more atoms of the pristine 2D-sheets can be replaced by different foreign atom(s) (see Fig. 1.7(b) for N-substitution in graphene) [78–80]. For graphene, a number of studies have shown that boron or nitrogen substitution has negligible structural impact due to the similar atomic radius as that of carbon atoms [78]. However, these substitutions have considerable impact upon the electronic and magnetic properties of parental 2D-sheets [81]. Apart from non-metals, incorporation of transition metals in regular 2D-lattices have also been studied extensively by experimental as well as theoretical groups. Stable coordination bond formation between metal atoms and host 2D-sheets exhibit promising performance towards catalysis, spintronic applications. [77, 82]

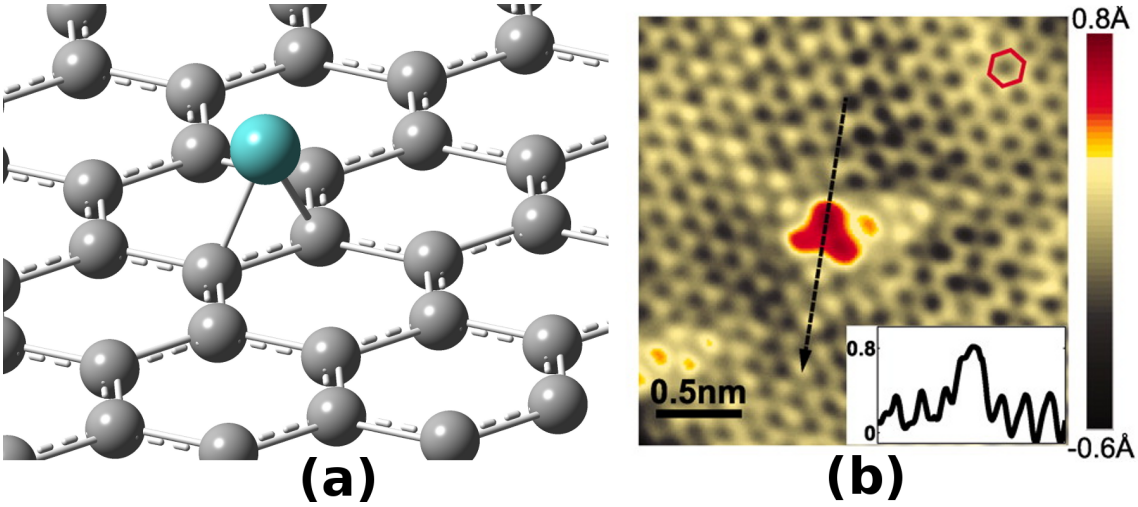

Figure 1.7: (a) Schematic for single carbon atom on bridge position of C-C bond of graphene. Carbon adatom is shown in different colour from clarity. (b) STM image of the N-doped graphene on copper foil, corresponding to a single graphitic N dopant. (Inset) Line profile across the dopant shows atomic corrugation and apparent height of the dopant; adopted from Ref. [83].

1.2.1.2 Topological Line Defects

Recent experimental and theoretical studies have demonstrated that individual defects used to align in the 2D-sheets to form thermodynamically favourable extended defects. Interestingly, several studies have identified the primary building block of common grain boundaries (GBs) appear in graphene is 5-7 topological defects (see Fig. 1.8(a)) [84–86]. In these cases, two initially separated domains of sheets grow with different lattice orientations and meet at grain boundaries, forming a tilt angle there. And to adjust to these structural mismatches, different nonhexagonal rings like five-, seven- and eight-membered rings get introduced. The particular structure of line defects depends on the misorientation angle between two adjacent grains. For small angle, the 5-7 pair of rings remain largely separated in the lattice. Whereas, for higher misorientation angles, the 5-7 pairs form continuous line defect in the sheet (see Fig. 1.8(a)) [86]. Apart from these, recently, Lahiri *et. al.* have experimentally observed another kind of grain boundaries in graphene; periodic alignment of two pentagons and one octagon (5-5-8) of carbon (see Fig. 1.8(b)) [87]. The line defect here appears due to the lattice mismatch in graphene patches, grown on the different crystallographic plane of Ni(111) surface. Further, using controlled

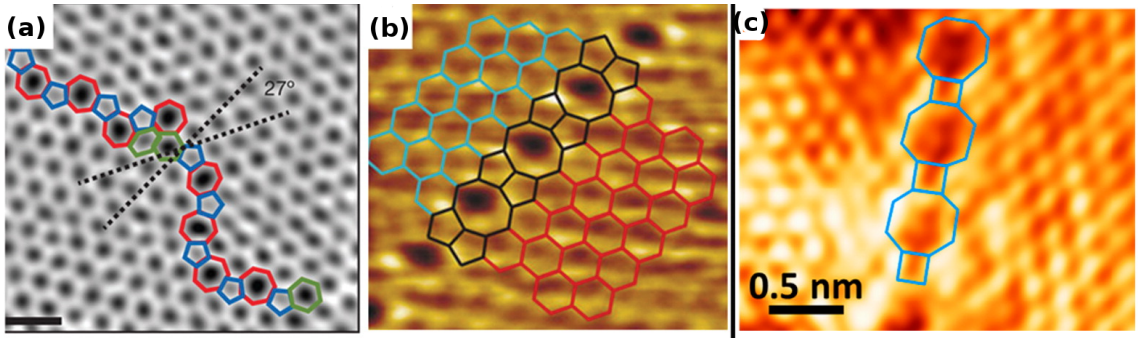

Figure 1.8: (a) Aberration-corrected annular dark-field scanning transmission electron microscopy (STEM) of a grain boundary with misorientation angle of $\theta = 27^o$. Scale bar is 0.5 nm, taken from Ref. [84], (b) scanning transmission microscopy (STM) image of a grain boundary, 0^o formed by 5 and 8 carbon atom rings, adopted from Ref. [87]. (c) High-resolution STM image of the 4-8 line defect in h-BN sheet, taken from Ref. [88].

growth and annealing process, stable line defect, consisting of one tetragon and one octagon (4-8), has also been demonstrated (see Fig. 1.8(c)) [88].

These reconstructed grain boundaries with topological line defects have shown technologically important electronic and magnetic properties [86, 89]. The scanning tunneling spectroscopy (STS) study shows the self-doping at grain boundaries, where electron affinity remains higher than other pristine part [87]. This results in strong localized n-doping at the defect region and can form efficient p-n-p junctions there [87, 90]. Yazyev *et. al.* have proposed precise transmission or reflection of charge carriers across the GB of graphene [86]. Fundamentally, these transport behaviours depend upon the matching (transmission of carrier) or mismatching (reflection of carriers) of conductance channels on both side of the GB. In this way, the on/off ratio of conductance across the GB becomes as high as 1000. Further, appearance of van Hove singularities in the local density of states of graphene near the Dirac point, indicate the possibility of realising various exciting properties, such as, charge density waves, localized magnetism, superconductivity etc. [86, 91]. Theoretical investigations reveal that 5-5-8 line defects can also induce localized spin-dependent metallic transport channel in otherwise semiconducting or semimetallic sheets [92, 93]. Importantly, magnetism in these sheets can also be modulated by different external perturbations such as strain, electron-doping etc.

1.2.2 In-plane Interfaces Between Graphene and Hexagonal Boron Nitride

Similar bonding pattern (i.e. hexagonal lattice) and small lattice mismatch of 2 % between h-BN and graphene sheet, have stimulated the experimental as well as theoretical groups to study the in-plane interfaces of these two materials (see Fig. 1.9(a,b)) [94–97]. Apart from structural similarities, very different electronic nature of these two sheets make this interface very interesting to study. In last few years, extensive theoretical studies on this interface have predicted various unusual electronic and magnetic properties, such as, tuning of bandgap, interfacial electronic redistribution, appearance of magnetic ordering, stable half-metallicity, unique thermal transport etc [97–99]. These exciting properties depend upon the precise atomic arrangements in the graphene–h-BN interfaces (graphene/h-BN). However, achieving atomically precise heterojunction remained quite challenging for a long time. Recently, with the advancement of sophisticated fabrication techniques, various groups have demonstrated interfaces without any intermixing [95, 96, 100]. Sutter *et. al.* have shown that a sequential chemical vapor deposition can grow boron nitride sheet at the edges of already deposited graphene domains on Ru(0001) plane [95]. The heterostructure, fabricated by this way, shows atomically sharp interfaces in their scanning tunneling microscopy-based study. More recently, Liu *et. al.* etched CVD-grown h-BN sheet with extreme precision with the help of photolithography and then have grown the graphene sheet at that etched regions on the surface of copper/nickel foils (see Fig. 1.9(a)) [96]. Following this way, complete control over the domain sizes as well as nature of interfaces in this heterostructures has been achieved. Moreover, this as-prepared graphene/h-BN heterostructure can easily be transferred to any other substrate without creating any mechanical fracture in the systems. This creates possibility for device fabrication with these heterostructures. Fabricated field-effect transistors with these graphene/h-BN has demonstrated versatile and high-performance electronic behaviour [96].

1.3 Quantum Transport in Molecular Nano-junctions

In general, the junctions which incorporate nanometer sized objects, such as, molecules, nanowires, nanodisks, quantum dots etc. are termed as nano-junctions

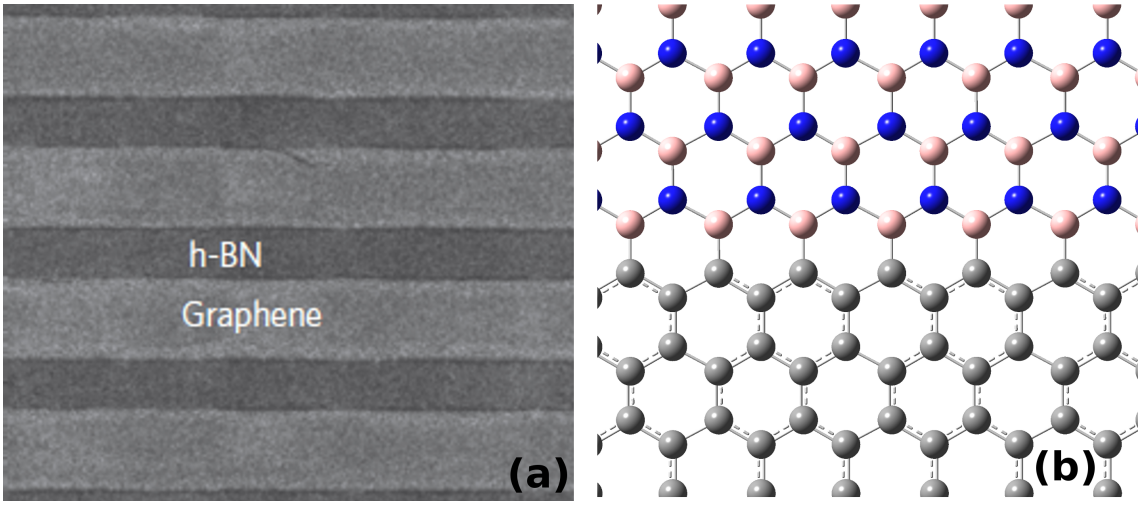

Figure 1.9: (a) Scanning electron microscope (SEM) image of graphene/h-BN stripes, adopted from Ref. [96], (b) Schematic of zigzag interface between graphene and h-BN.

[101–104]. Due to their various exciting properties and promising applications in technologically important fields, nano-junctions have attracted substantial research attention from both experimental as well as theoretical groups [105, 106]. And consequently, nanosized objects with controlled composition, size, and morphology are getting synthesized quite regularly in recent times [107]. Well-explored methodologies have also shown reliable functionalities, structures and reproducibilities for wide range of these nano-junctions [101, 108]. Apart from their device applications, these junctions are also exciting tools for understanding the rich physics, appearing at the nanometer scaled objects. The particular field of research which focuses on the nano-object based electronic nano-junctions for applications like switching, sensing, current rectifications etc. is named as "nano-electronics". A subset of that vast field where one specifically chooses molecules as the nano-object, is nomenclatured as "molecular electronics". For this present thesis, we consider the nano-objects, most of which are molecules, are in electrical contact with two bulk conductors. We have investigated electron and heat transport through these molecular nano-circuits and demonstrated applications, such as, switching, sensing, current rectification etc.

1.3.1 Experimental Investigations

The proposal by Aviram and Ratner in 1974 to use a single molecule as a rectifier, was most probably the first report on the molecular electronics [109]. However, due to lack of experimental set up, it remained just as a hypothesis for nearly 20 years. Very first experimental realization of molecular device appeared from Metzger, who studied Langmuir-Blodgett films of γ-(n-hexadecyl) quinolinium tricyanoquino-dimethanide, keeping between metal electrodes. With the advent of scanning probe microscopy and other techniques, a large number of reliable and reproducible experiments of junction-electronics have appeared now [110]. Now a days, addressing, imaging, manipulating, and performing measurements of nanoscale molecular systems connected to metal leads is quite routine work for researchers. [110] Interestingly, semiconductor manufacturing methods and materials synthesis techniques have been adapted in ways that now allow for the nearly conventional fabrication of a host of exotic devices, such as, single-molecule devices [111]. And these devices exhibit efficient performance towards probing charge transport through nanoscale-junctions.

Nanoscale electronics is a very large field and it is very difficult to review the field completely. Thus, to make the discussion compact and relevant to the present thesis, we only discuss about a few path-breaking experiments on molecular nanojunctions now. In a two-terminal molecular junction, Reed *et. al.* first measured the conductance of benzene-1,4-dithiol using controllable break junction technique in 1997 [112]. Following same procedure, Reichert *et. al.* demonstrated diode like properties by studying anthracene based molecular junctions [113]. Several similar studies on oligo(phenylene-ethynylene) (OPE) have measured the conductivity and interestingly observed rectification and negative differential resistance (NDR) behavior in transport measurements [114, 115]. In another study, Joachim *et. al.* sandwiched the C_{60} molecule between a substrate and a STM tip and measured the conductance through that molecular junction [116]. Interestingly, rotaxene, a special family of molecules, have been studied extensively for their potential for being used as an active component in switching and logic devices [117]. Catenane based molecular junctions are another kind of devices that also shows prominent bistable behavior in its I-V characteristics [118]. Photo-induced molecular switching have also been observed in some molecules where application of light efficiently switches

the device between on/off states. Controlling current in a bistable molecule with light irradiation gives rise to efficient opto-electronic molecular devices [119, 120]. As an example, photochromic dithienylethene molecule switches from the conducting to the insulating state after illuminating it with visible light [121]. Apart from these devices of coherent transport regime, molecules also exhibit exotic behaviors in Coulomb blockade regime [122]. In this regime, the charging energy is very high and temperature is very low. Park *et. al.* have demonstrated a molecule, containing Co ion which is bonded to different polypyridyl ligands, shows prominent Kondo signature and Coulomb blockade effects [123]. Further, carbon nanotube have also exhibited exciting Coulomb blockade and Kondo effects in controlled experiments [124]. In last few years, biomolecular electronics have also got a boost due to their promising performances [125]. Lots of transport measurement have been performed on various biomolecules.

However, very specifically, DNA remained in limelight due to the contradictory results about its transport character, ranging from superconducting, conducting, semiconducting and to even insulating nature [126]. Recently, protein also found to offer significant advantages over other biological polymers for constructing electronic devices. As an example, Maruccio *et. al.* have fabricated field-effect transistor based on blue copper protein, azurin [127].

1.3.2 Molecular Spintronics

Apart from initial motivation of ultimate miniaturization of electronic devices, researchers also explored inherent quantum mechanical aspects of molecular nano-junctions [128]. In this regard, the concept of new devices appear where the spin along with the charge of the electron was manipulated and named as molecular spintronics [129–131]. Potential applications in information storage and processing have made these nano-devices extremely interesting for research [131, 132]. In these devices, the spin-state of a molecule or the spin-polarization of the flowing electrons are attempted to control [128]. Generally, researchers have achieved the conduction of spin-dependent transport either by incorporating magnetic molecule between two non-magnetic electrodes or by using magnetic electrodes anchoring with a non-magnetic molecule. Devices with non-magnetic electrodes and magnetic molecule

have demonstrated various diverse phenomena, such as, Kondo effect, negative differential resistance, detection and control of magnetic anisotropy [123, 133–135]. In their recent experiment, van der Zant and co workers demonstrated electronic control of spin state of a single molecule also [136]. In another kind of experiment, Schmaus *et. al.* have found the conductance dependence of a non-magnetic molecule upon relative magnetic moment alignment of tip and substrate [137]. In the present thesis, we have extensively explored the spin dependent transport of magnetic molecules sandwiched between non-magnetic gold electrodes.

1.3.3 Theory of Transport Phenomena

Over 200 years ago, the phenomenological description of electricity by some of the pioneers of physics like A. M. Ampere, A. Volta, G. S. Ohm, C. A. De Coulomb, M. Faraday, was the historical starting point of understanding modern theory of electronics. After a century, in 1900, P. Drude put forward a model, famously called as Drude Model, which provided an intuitive explanation for the experimentally observed Ohmic resistance in metals. [138] With dawn of quantum mechanics, these originally classical models were soon modified by A. Sommerfeld.[139] In this improved model for free electrons, he considered the correct Fermi-Dirac statistics of particles and further used Pauli principle to distribute them in the available energy states. By this way, Sommerfeld was able to correct the quantitative deficiencies, arising from the classical nature of earlier theory. Note that, all these models are for bulk materials. With the advent of technology, reliable production and handling of structures at a nano-scale has become quite common. Interestingly, these structures themselves give rise to quantum effects due to their size. Theory to investigate electron transport in such systems was also being developed in parallel with the development of nano-technology. In 1958, R. Landauer formulated the coherent electron transport in quantum systems [140]. It is quite evident that quantum transport in low-dimension is governed by the competition of various characteristic length scales. These characteristic length scales have been defined to determine the border between two transport regimes (i.e. classical and quantum transport regimes). And these are the Fermi wavelength (λ_F), momentum relaxation length (L_m) and phase relaxation length L_ϕ.

Fermi wavelength:

The Fermi-Dirac statistics depict the equilibrium distribution of fermions in any macroscopic system. The electrons fill the energy states from the bottom of the electronic spectrum up to the Fermi energy, E_F. Most of these states in the spectrum remain either completely filled or empty at moderate temperatures. Apart from these, a narrow region of spectrum around E_F effectively contributes to the degrees of freedom of the system, determining its electronic properties. For crystalline solids, a specific wave-vector, K_F, represents the energy, E_F, in their band structure. The wave-vector remains associated with the wavelength, $\lambda_F = 2\pi/K_F$. Generally, this wavelength tells about the length scale at which quantum mechanical interferences are to be expected. When the size of a nano-system remains in the same order of magnitude as the Fermi wavelength or below, the spectrum becomes quantized and provides a discrete set of electronic energy states.

Phase coherence length:

In realistic materials, due to the scattering of electrons with various disturbances, such as, phonons, electrons, magnetic impurities, particular phase of incoming electrons gets randomized. The 'phase coherence length (l_ϕ)', is defined as the mean distance that electrons travel before they lose their quantum mechanical phase due to the scattering with various scatters, as mentioned above. The Fermi velocity directly connect the phase coherence length and phase coherence time, τ_ϕ, by following relation, $l_\phi = V_F\tau_\phi$. This coherence length, i.e. l_ϕ, decreases as temperature of the system or density of states at the E_F increase. The l_ϕ becomes shorter due to the increase in electron-electron collisions for both of these situations.

Momentum coherence length:

This particular length represents the average distance that an electron travels before colliding with some impurities and/or defects in the sample, losing its initial momentum. This mean free path can be formulated as, $l_p = V_F\tau_p$, where τ_P is the momentum relaxation time.

Localization length:

The localization length, l_l, is defined as the average spatial length over which quantum mechanical states are localized. Considering a perfectly periodic system,

the Bloch states appear to be spread out infinitely ($l = l\infty$). In 1958, P. W. Anderson, in his seminal paper, stated that presence of defects and disorder in a two-dimensional system may lead to a complete localization of all quantum mechanical states, resulting in a finite value of the localization length [141].

To study spin transport in the nanoscale devices, one has to consider some other length scale, called as spin diffusion length.

Spin diffusion length:

Concept of spintronics is based on the use of intrinsic spin degrees of freedom of carrieres that are neglected in conventional electronics [142]. In the spin based electronics, one needs to generate and manipulate spin-polarized population of electrons (i.e. unequal distribution of two spin types i.e. $S_z = \pm 1/2$) near to the E_F. The period of time up to which such a non-equilibrium population sustains is known as the spin lifetime, τ_S. For a diffusive conductor, the distance travelled by spin within spin lifetime, is called as spin diffusion length (λ_S). Spin-flip scattering and spin dephasing are dominating among several other processes for decay of a spin polarized populations.

1.3.3.1 Transport Regimes

Depending upon various competing length scales as discussed above, we can divide various regimes of quantum transport depending on the size of system, l. A discrete spectrum appears for the system with $l \sim \lambda_F$. Various effects, such as, Coulomb blockade or resonant tunneling can probe the individual states of the system. For $l >> \lambda_F$, the other length scales appear to be relevant. When $l >> l_p$, the system remains in the diffusive transport regime, where transport characteristics is dominated by multiple scatterings and resistance grows with system size. However, for $l << l_p$, the system exhibits ballistic transport characteristics. In this regime, the resistance of a system becomes independent of l and depends only on the contacts. When $l << l_\phi$, the system shows coherent transport where resistance grows exponentially with the length. For $l >> l_\phi >> l_p$, the system goes to classical transport regime and consequently, Ohm's law is recovered. Further, in the delocalized regime (i.e. $l << l_l$), the individual electronic states spread from one contact to the other and allow coherent transport of electrons. In this regime, decoherence is

destructive for the transport and resistance grows with increase in dephasing length. On the other hand, in the regime of strong localization (i.e. $l >> l_l$), coherent transport shows exponential suppression within a single state. As conductance can only originate from thermally activated hopping between the levels, the resistance would go down along with increment in dephasing.

1.3.3.2 Landauer Formalism

The Landauer formalism is the most common theoretical framework used to describe transport through mesoscopic devices. The detailed reviews about the Landauer approach can be found in a number of papers and books [140, 143]. According to this formalism, the conductance through nano-junction can be formulated in terms of transmission probabilities, T_n, i.e., the probability for an electron in channel, n, to be transmitted through the sample. The mathematical expression for Landauer formula is as follows,

$$G = \frac{2e^2}{h} \sum_n T_n(E_F) \tag{1.1}$$

In this chapter, we derive the Landauer formula in a simple way [143]. The population of the states in the leads is considered by the Fermi-Dirac distribution $f(E - \mu_\alpha)$, where μ_α is the chemical potential of the reservoir, $\alpha = 1, 2$ (i.e. left and right lead). The electrical current arising from electrons in lead, α, carried by channel, n, is expressed as,

$$I_{\alpha nE} = \frac{2e}{L} \sum_k T_n(E) v(k) f(E - \mu_\alpha), \qquad \alpha = 1, 2 \tag{1.2}$$

where, L depicts length of the device. The factor 2 is introduced to consider two spin-components, $v(k)$ is the group velocity of the electrons and $T_n(E)$ gives the transmission probability of channel, n, at energy $E(k)$. Considering the difference between the currents emerging from the two leads and summing them over all quantum channels, the net current can be obtained as,

$$I = \sum_n [I_{1nE} - I_{2nE}] = \frac{2e}{L} \sum_{n,k} T_n(E) v(k) [f(E - \mu_1) - f(E - \mu_2)]. \tag{1.3}$$

Conventionally, flowing of current from the lead to the device is considered as positive. Changing the sum over the momentum k into an integral according to the usual rule,

$$\sum_k \rightarrow \frac{L}{2\pi}\int dk \tag{1.4}$$

and using further the relation,

$$v(k) = \frac{1}{\hbar}\frac{dE}{dk}, \tag{1.5}$$

we can formulate,

$$I = \frac{2e}{h}\sum_n \int dE T_n(E)[f(E-\mu_1) - f(E-\mu_2)]. \tag{1.6}$$

At the regime of low temperature and low voltage, eV $= \mu_1 - \mu_2$, the Taylor expansion of $f(E-\mu_1) - f(E-\mu_2)$ around the Fermi energy can be made. And that leads us to $f(E-\mu_1) - f(E-\mu_2) \approx \delta(E-E_F)(\mu_1-\mu_2)$. Incorporating this in last equation, finally the conductance through the system arises as,

$$G = \frac{2e^2}{h}\sum_n T_n(E_F) \equiv \frac{2e^2}{h}.T(E_F) \tag{1.7}$$

where, $\frac{2e^2}{h}$ is the quantum of conductance.

1.3.3.3 Green's Function

Generally, the Green's function is a powerful concept in physics and has been applied widely in various fields, such as, electromagnetics, electrostatics and circuits theory. This concept has also been used as a strong mathematical tool to evaluate the transmission coefficients. In quantum mechanics, we are in general interested in solving the time-independent Schrödinger equation,

$$[E - H]\Psi = 0, \tag{1.8}$$

where H is the Hamiltonian, describing the system. The Green's function corresponding to H is defined as the solution of the differential equation,

$$[E - H]G(r, r', E) = \delta(r - r'). \tag{1.9}$$

Applying the Dirac's operator notation, the above differential equation can be represented as

$$[E - H]G(E) = 1, \tag{1.10}$$

where H is the Hamiltonian operator and $G(r, r', E) = < r|G(E)|r' >$. If, in case, E is not an eigenvalue of the Hamiltonian, H, a formal solution for the Green's function operator is given by

$$G = [E - H]^{-1}. \tag{1.11}$$

However, as we know, to define the inverse of a differential operator uniquely, we must specify the boundary conditions. If we consider for example, H is the Hamiltonian for a point-particle moving in a one-dimensional wire with constant potential, the corresponding Green's function, G(r, r′, E), can be pictured as the wavefunction at r, arising due to a unit excitation, applied at r′. This can be correlated with an outgoing wave from point, r′. However, as one can argue, G can also be viewed as the source of such an excitation, which would correspond to an incoming wave. Commonly, one defines these solutions as the retarded and advanced Green's functions associated with two different boundary conditions. One can incorporate these boundary conditions by adding or subtracting an infinitesimal imaginary part ($i\eta$) to the energy. And that leads us to the following equation,

$$[E \pm i\eta - H]G^{R/A}(E) = 1. \tag{1.12}$$

The retarded and advanced Green's function operator is defined as follows,

$$G^{R/A}(E) = lim_{\eta \to 0^+}[E \pm i\eta - H]^{-1}. \tag{1.13}$$

1.3.3.4 Relation Between the Green's Function and Transmission-coefficient

As discussed above, the Landauer formalism formulates the conductance of a device in terms of the transmission coefficients. Using the Fisher-Lee relation [144],

these transmission coefficients can be expressed in terms of the Green's function. We are not presenting the detailed derivation of this relation here. The transmission coefficient between lead p and q is represented as,

$$T_{pq} = Tr[\Gamma_p G_{pq} \Gamma_q G_{pq}^{\dagger}]. \tag{1.14}$$

Function Γ_p is the broadening function which signifies the coupling of the device to the leads. It can be expressed in terms of a self-energy, Σ_p as,

$$\Gamma_p = i[\Sigma_p - \Sigma_p^{\dagger}]. \tag{1.15}$$

Here, the real part of self-energy is related to the shift in energy-level of system and imaginary part takes care of the broadening of these levels as they are coupled to the continuum electrode. The self-energy in turn can be considered as an effective Hamiltonian, representing the interaction between device and leads.

1.4 Thermoelectric Effect

To meet sharply increasing world-wide requirement for energy production and storage, a intense research interest has been created to find efficient ways for power generation. Apart from conventional sources, majorly based on fossil fuels, various renewable energy sources, such as, solar, wind, rain, waves, biomass, geothermal heat are potential candidates to increase the energy supply. The use of thermoelectric devices is another promising alternative answer to the growing energy demand [145, 146]. These devices use the concept of well known thermoelectric effect to generate electricity. Fundamentally, heat energy gets converted to electricity directly in these devices and burning of fossil fuels, solar energy, nuclear decay, waste-heat can be used as the source of heat. Thus, thermoelectric devices can be used in both ways, power generation as well as energy conservation (by waste-heat managements). The thermoelectric generators, generally are solid-state devices with no moving parts [147]. Thus, these are silent, reliable and scalable which make the device ideal for small, distributed power generation. Interestingly, thermoelectric devices are successfully applied in new generation cars, space-craft, power generators on gas pipelines etc. and some products are already in the commercial market.

A thermoelectric converter is fundamentally a heat engine and consequently, alike all heat engines, the laws of thermodynamics is obeyed here. When two ends of a wire are held at different temperatures and forms a temperature gradient, a voltage develops across the wire. This effect is known as the Seebeck effect, discovered by T. J. Seebeck in 1822. The voltage between the two ends is directly proportional to the temperature difference across the wire. The proportionality constant is defined as the Seebeck coefficient or thermoelectric power and can be calculated from the ratio of the voltage generated and the applied temperature difference. It can be formulated as,

$$S = \frac{\Delta V}{\Delta T}. \tag{1.16}$$

The Peltier effect, the inverse of the Seebeck effect, was discovered in 1834 by J. C. A. Peltier. This effect appears when current passes through a wire. The current will carry thermal energy so that the temperature of one end of the wire decreases and the other increases. Thus, the heat is directly proportional to the current passing through the junction and can be described as,

$$dQ = \Pi dI \tag{1.17}$$

Note that, irreversible Joule heating which also originates from electronic current, submerge the Peltier effect most often. Another kind is the Thomson effect which was predicted in 1854 and experimentally verified in 1856 [148]. The Thomson effect appears when a current flows across two points of a homogeneous wire, where a temperature gradient is present along its length. Heat gets emitted or absorbed in addition to the Joule heating in this process. Conventionally, the Thomson coefficient, μ_T, is positive if heat is generated when positive current flows from a higher temperature to lower temperature. The heat current can be written as,

$$dQ = \mu_T \frac{\partial T}{\partial x} dx dI. \tag{1.18}$$

The performance of a thermoelectric device directly depends on the temperature gradient (ΔT) as well as an intrinsic parameter of the material, named as figure of merit (ZT). In 1912, Altenkirch introduced the concept of this figure of merit

for the first time [149, 150]. It was demonstrated that to be a good thermoelectric material, system should have large Seebeck coefficients, high electrical conductivity which minimize Joule heating and low thermal conductivity, which retains heat at the junctions that in turn will help to maintain a large temperature gradient. In 1957, Ioffe gave the mathematical expression of figure of merit (ZT) [151],

$$Z = \frac{S^2\sigma}{K} \tag{1.19}$$

where σ is the electrical conductivity and K is the total (electronic + phononic) thermal conductivity. Slightly modified, dimensionless figure of merit which is commonly used now-a-days is,

$$ZT = \frac{S^2\sigma T}{K} \tag{1.20}$$

1.4.1 Thermoelectric Materials

Initially studied thermoelectric materials were metallic in nature, where the Seebeck coefficients were a few tens of μV/K. However, the field of thermoelectrics got a real boost in 1950s, when Bi_2Te_3 and its alloys with Bi_2Se_3 and Bi_2Se_3, PbTe and its alloys with PbSe and SnTe and SiGe came into the picture [145, 146]. Bi_2Te_3 and PbTe have heavy elements which results in small phonon group velocity and low thermal conductivity [152]. Further, these heavy elements also show small band gaps and large mobility. Following the suggestion by Ioffe, the thermal conductivity were further reduced by alloying these materials with others. Quite wide range of operation temperatures is covered by these three materials. Beside the development of bulk materials with enhanced thermoelectric properties, superlattices have been proposed as structures that may improve ZT [153]. As proposed, figure of merit can also be enhanced by using quantum dot superlattices; many structures of which have also been proposed in recent time [154]. Still, finding an efficient and commercially viable thermoelectric compounds with better ZT remain quite an open challenge.

1.5 Model Hamiltonian

1.5.1 Hubbard Hamiltonian

The Hubbard Hamiltonian is one of the most simple but highly celebrated ways to get fundamental insight about the nature of the interactions between electrons that give rise to insulating, magnetic, and even novel superconducting effects in a solid. It was written down independently by Kanamori,[155] Gutzwiller [156] and Hubbard [157, 158, 158] in the early 1960's in an entirely different context. Initially it was applied to understanding the behavior of the transition metal monoxides (FeO, NiO, CoO), compounds which are antiferromagnetic insulators, yet had been predicted to be metallic by methods which treat strong interactions less carefully. However, over the years, the Hubbard model has been successfully applied to number of many systems, such as, conjugated polymer, magnetic system, heavy fermionic systems and even to high temperature superconductors [159–162].

To understand the Hubbard Hamiltonian, first, we need to consider the fact that there is a regular array of nuclear positions in a solid, which can be consider as fixed atoms (i.e. we assume the lattice vibrations are freeze) for simplicity . This suggests that, we effectively consider a lattice of atoms (sites) on which the electrons remain quite mobile. A single atom with many different energy levels, is already a very complex structure. The most simple 'atom' one can imagine would have a single atomic orbital. Then, the Pauli exclusion principle would tell us that, at most two electrons with opposite spin, can sit on this 'orbital'. Generally, in a solid, electrons move around in the system and interact via a screened Coulomb interaction. The biggest interaction by this way will be for two electrons on the same orbital. This interactions are modeled by a particular term which appears as zero for the atom with no or single electron on it, however has the non-zero value, U if the atom contains two electrons. Further, the kinetic energy is consist of an expression which allows electrons to move from one site to its neighbors. The energy scale, t, which governs this 'hopping' will be determined by the overlap of two wavefunctions on the pair of atomic-orbitals. Since wavefunctions reduce exponentially, we can initially consider the hopping only between the closest atoms in our lattice. With all these,

the mathematical form of Hubbard Hamiltonian can be considered as,

$$H = \sum_{i=1}^{N} (\epsilon_i) a_i^\dagger a_i + \sum_{i,j,\sigma} -t_{ij}(a_{i\sigma}^\dagger a_{j\sigma} + h.c.) + U \sum_{i=1}^{N} n_{i\uparrow} n_{i\downarrow} \tag{1.21}$$

where, $a_{i\sigma}$ and $a_{i\sigma}^\dagger$ are the creation and annihilation operators for electrons with spin, σ, at the ith site, respectively. t_{ij} is the hopping strength between the sites i and j with same spin (σ), ϵ_i represents the on-site energies and U is the Hubbard interaction between electrons at the same site. For $U >> t$, the strong Coulomb repulsions give rise to each site containing one electron at half-filling. This results in infinitely degenerate ground state and with t_{ij} as perturbation, the ground state degeneracy can be lifted through second order degenerate perturbation theory, resulting in Heisenberg Hamiltonian for localized spin systems with frozen charge degrees of freedom. The Hubbard model is exactly solvable for one-dimensional systems with arbitrary band-filling [163, 164]. At half-filling, the ground state for any nonzero U is an insulating spin singlet state.

1.6 Numerical Methods

It's quite challenging to study the model Hamiltonian with explicit electronic correlations. In this process, one needs to first solve the Hamiltonian equation to obtain the energy eigenvalue along with the eigenvectors and then these can be used to calculate the expectation values of several observables. For one electron theories, such as, tight binding or density functional theory (DFT), the numerical calculations are computationally less expensive. Particularly, DFT method is quite useful, as it gives quite accurate ground state properties of molecules and periodic systems. On the other hand, it becomes very difficult to handle huge dimension of many body space, arising from the two electron operators. There exists no well controlled reliable analytical technique, except in limiting cases, such as, in the weak coupling limit or very strong coupling limit. Moreover, the mean field approach can often lead to unphysical solution. Also, the excited states are very poorly described within these approaches. These difficulties encourage for developing reliable and efficient nonperturbative numerical methods. Here we discuss some of the numerical

methods, which have been used to solve low-dimensional materials, studied in this thesis.

1.6.1 Exact Diagonalization

In this method, we consider the Hamiltonian matrix in a given basis and diagonalize it to obtain the energy eigenvalues and eigenvectors. The dimensionality of the Fock space is finite when we deal with finite size systems. Therefore, it appears that, all the model Hamiltonians would be exactly solvable for finite systems. And consequently, with proper finite size scaling, we can draw conclusions about their behavior in thermodynamic limit. However, Fock space dimension increases as 4^N in case of fermions, where N is the number of sites. This sharply increasing dimension restricts the numerical computations on a large systems by exact diagonalization procedure. However, the dimension can be truncated using various symmetries of the model Hamiltonians, such as the z-component of total spin (S_z^{tot}), the total number of electrons (N) or various spatial symmetries, which commute with the Hamiltonian, depending on the system of interest. However, the finite size scaling with very small system sizes, as possible to treat within exact diagonalization method, the results are not reliable enough to be extrapolated to the thermodynamic limit. Thus, this exact diagonalization technique has been widely used for studying small correlated molecules. It has been applied for the low-dimensional spin systems and interacting fermionic systems. [165–169] The most important merit of exact diagonalization lies in the fact that, it allows the benchmarking of various approximate numerical many body methods for various model Hamiltonians.

1.6.2 Density Functional Theory (DFT)

DFT is one of the most widespread quantum mechanical approaches for calculating the ground state properties of wide range of systems; from molecules to bulk materials, from insulators to metals, from diamagnetic to ferromagnetic materials. DFT can predict various ground state properties, such as, optimized geometry, vibrational frequency, atomization energy, ionization energy, electronic properties, one-particle magnetic states, optical properties, reaction pathways etc. very reliably. With the advancement of this theory, it has also been modified successfully

for several kinds of studies including molecular dynamics, spin dependent study, investigation at non-zero temperature, time dependent phenomena etc.

From elementary quantum mechanics, we know that all the information about a system is stored in its wave function, ψ. From the Schrödinger equation, the non-relativistic wavefunction is calculated with the external potential, $v(r)$, due to the nuclei. The equation looks like,

$$\left[-\frac{\hbar^2\nabla^2}{2m} + v(r)\right]\Psi(r) = \epsilon\Psi(r) \tag{1.22}$$

To treat many electron systems, the equation can be modified as follows,

$$\left[\sum_i^n \left(-\frac{\hbar^2\nabla_i^2}{2m} + v(r_i)\right) + \sum_{i<j} U(r_i, r_j)\right]\Psi(r_1, r_2 \ldots, r_N) = E\Psi(r_1, r_2 \ldots, r_N) \tag{1.23}$$

where N is the number of electrons in the system and $U(r_i, r_j)$ is the electron-electron interaction. It is evident that only through U term, simple single-body quantum mechanics of Eq. (1.22) differs from the complex many-body problem of Eq. (1.23). There are several many-body methods available for solving Schrödinger's equation, however, the computational resources required even for modest system sizes is exceedingly large. This implies that most realistic systems are out of the reach of these many-body methods. It is exactly at that point where DFT comes into the picture and proves its utility. In brief, DFT achieves this by successfully mapping the many-body problem of interacting particles in a potential, onto one of non-interacting particles in an effective potential. And thus, it effectively reduces the many-body problem to a single-body one.

The Hohenberg-Kohn theorems are the foundations of this highly explored method [170]. This theorems rigorously state that a ground state particle density $n(r)$ can be produced by at most *one* external one-body potential. Since for a particular system, the wavefunctions are determined by the potential $v(r)$, this clearly implies that wavefunctions, and consequently, all ground state observables are functionals of the ground-state particle density. The ground-state energy is the most important among all these observables. Note that, conceptually DFT is exact, approximation arises due to inherent difficulty in efficiently evaluating many-body interactions.

1.6.2.1 Kohn-Sham Equations

The most extensively used implementation of DFT is the Kohn-Sham approach [171]. It is a method of mapping the problem of interacting electrons onto one of non-interacting electrons in an effective potential.

The exact energy functional in terms of density functionals can be expressed as follows,

$$E[n] = T[n] + U[n] + V[n], \tag{1.24}$$

where the density functionals, $T[n]$, depicts the kinetic energy of a system of interacting particles, $U[n]$ is the Coulomb interaction between particles and $V[n]$ is the external potential. The particles are with density, n, here. $T[n]$ can be split into two components, $T_s[n]$, which is the kinetic energy functional for a system of non-interacting particles, and $T_c[n]$, which is the remainder, contains all correlation effects. Thus, one can formulate,

$$T[n] = T_s[n] + T_c[n] \tag{1.25}$$

As T_s is not known exactly as a functional of n, wavefunctions play an essential role in the Kohn-Sham approach, where the T_s can be expressed in terms of single-particle orbitals as

$$T_s[n] = -\frac{\hbar^2}{2m}\sum_i^N \int d^3r \phi_i^*(r)\nabla^2\phi_i(r). \tag{1.26}$$

This demonstrate that single-particle kinetic energy is an implicit functional of density. Following similar approach, $U[n]$ can also be divided into two components, $U_H[n]$, which is the Hartree energy, and the remainder, $U_c[n]$, which are effectively the correlation effects. The Hartree energy functional, $U_H[n]$ has the following form,

$$U_H[n] = \frac{q^2}{2}\int d^3r \int d^3r' \frac{n(r)n(r')}{|r-r'|}. \tag{1.27}$$

So, one can write down the exact energy functional as,

$$E[n] = T_s\left[\{\phi_i[n]\}\right] + U_H[n] + E_{xc}[n] + V[n], \tag{1.28}$$

where, by definition, E_{xc} contains the correlation parts of $T[n]$ and $U[n]$. In the absence of Hartree and exchange terms, the minimization condition for the energy functional for a non-interacting system in a potential, $v_s(r)$, is

$$\frac{\delta T_s[n]}{\delta n(r)} + v_s(r) = 0. \tag{1.29}$$

The density that solves this equation is the same for the interacting system,

$$v_s(r) = v(r) + v_H(r) + v_{xc}(r), \tag{1.30}$$

where the Hartree potential is $v_H(r) = \delta U_H/\delta n$ and the exchange-correlation potential $v_{xc}(r) = \delta E_{xc}/\delta n$. Thus, the density of the interacting system in potential, $v(r)$, can be found by solving the equations of a non-interacting system in potential, $v_s(r)$. The Schrödinger equation that needs to be solved to obtain the density of the interacting system is,

$$\left[-\frac{\hbar^2\nabla^2}{2m} + v_s(r)\right]\phi_i(r) = \epsilon_i\phi_i(r). \tag{1.31}$$

The solution that reproduce the density, $n(r)$, of the original system is,

$$n(r) = n_s(r) = \sum_i^N f_i|\phi_i(r)|^2, \tag{1.32}$$

where f_i is the occupation of the i'th orbital. Eq. (1.30), Eq. (1.31) and Eq. (1.32) are the Kohn-Sham equations. Since v_H and v_{xc} are functionals of density, which in turn depends on ϕ_i which depends on v_s, they need to be solved iteratively in what is termed a "self-consistency cycle". The potential, v_{xc}, since not known exactly, has to be approximated.

- Local Density Approximation (LDA)[172]:

  The first and simplest approximation of exchange-correlation potential is LDA and can be defined as

$$v_{xc}^{LDA} = \int d^3r v_{xc}(n(r)).n(r) \tag{1.33}$$

where $v_xc(n(r))$ is the exchange and correlation energy per electron of the homogeneous electron gas with density n(r). It assumes that the electronic density is a smooth function in space. Any region of space can then be locally seen as a homogeneous electron gas of density, n(r). Now, to obtain the total exchange-correlation energy, one has to perform summation of local exchange-correlation energy for all the electrons in every region of space. These functional works nicely for bulk solids but have a poor performance for the systems where the electron density does not vary smoothly in space.

- Generalized Gradient Approximation (GGA): In this approximation, the standard LDA has been extended to inhomogeneous systems where electron density varies non-uniformly. This improved approximation not only considers the local charge densities but also more physical parameter i.e. their gradients. Fundamentally, there are three kinds of GGA:

  - Ab-initio based: These functionals are based on exact results. Here exchange and correlation parts are calculated individually. The typical examples of this are PBE (Perdew-Burke-Ernzerhof)[173] or PW91 (Perdew-Wang 1991) [174, 175].
  - Atom based : It has some basic similarities with the previous one such as, these are also based on some exact results and exchange and correlations are treated separately. But for this type, the functional parameters are fitted on close-shell atom properties. Examples include, Becke's GGA for exchange[176] and Lee Yang and Parr (LYP) functional for correlation [177].
  - Empirical: In this formalism, the exchange and correlations are considered as a whole. Functional parameters are determined by fitting on a set of atomic and molecular properties. Common example are the HCTH (Hamprecht-Cohen-Tozer-Handy) functionals[178, 179].

- Incorporation of U: Though these exchange-correlation functionals are quite successful for most of the materials, serious problem arises when one applies them to treat materials, containing ions with partially filled valance d- of f-shells [180]. For example, many insulating transition metal oxides appear to

be metallic in LDA or GGA based DFT calculations [181]. Fundamentally, the inadequate consideration of the strong Coulomb repulsion between localized d/f-electrons of metal atoms causes this failure of DFT-based calculations [180]. Thus, an on-site correction which is characterized by the Hubbard U, can be introduced to take care about this strong electronic correlations. It can be formulated as,

$$\begin{aligned} E_{DFT+U} &= E_{DFT}[\rho(r)] + E_U[(n^{I\sigma}_{mm'})] \\ &= E_{DFT}[\rho(r)] + E_{HUB}[(n^{I\sigma}_{mm'})] - E_{DC}[(n^{I\sigma})] \end{aligned} \tag{1.34}$$

where $\rho(r)$ is the electron density, $n^{I\sigma}_{mm'}$ are generalized occupations if atomic orbitals, having spin σ associated to the atom I. $n^{I\sigma}$ signifies the sum of the occupations corresponding to all eigenstates. $E_{DFT}[\rho(r)]$ is the energy functional from standard LDA or GGA and $E_{HUB}[(n^{I\sigma}_{mm'})]$ formulates the on-site correlation energy. Now, as $E_{DFT}[\rho(r)]$ already has an approximate contribution from correlation effect, one need to subtract that $E_{DC}[(n^{I\sigma})]$ to avoid double consideration.

In the past few decades, a number of packages have been developed where self-consistent calculations for electronic structure using various methods such as Hartree-Fock, post Hartree-Fock and DFT have been implemented. Among all these, some of the packages like Gaussian General Atomic and Molecular Electronic Structure System (GAMESS) [182], Amsterdam Density Functional (ADF) [183, 184] are used extensively for molecular systems. As these packages use localized orbital basis functions, it cant handle large systems. However, the concept of numerical orbitals and pseudopotential come into play to study large periodic systems. Spanish Initiative for Electronic Simulations with Thousands of Atoms (SIESTA) [185] is an example of such kind of packages, where combination of numerical orbitals and norm-conserving pseudopotentials have been implemented successfully. Another way is to use plane augmented wave basis sets for calculations. Examples of this approach are Quantum-Espresso (PWscf) [186], Vienna Ab-initio Simulations Packages (VASP) [187, 188] etc.

1.6.3 Ab initio Molecular Dynamics

Understanding the nature of existing materials and designing new one with superior properties are the basic targets in material science research. And to do so, one need to predict the material properties quite accurately. Though usage of relativistic time-dependent Schrödinger equation is very reliable in this context, the method has serious limitation towards treating large and complex materials. Till now, systems with very small number of atoms have been studied by this method, To treat large systems, one need to find other suitable methods. In this regard, molecular dynamics (MD) simulations are quite reliable and computationally affordable to gain detailed structural and conformational aspects on a realistic and atomic level [189]. Simulating systems by MD, one eventually obtains ensemble-averaged properties, such as binding energy, relative stability of molecular conformations etc. by averaging over representative statistical ensembles of structures.

Fundamentally, during MD simulation, one obtains the numerical solution of Newton's equation of motion for all the nuclei within a system. In classical MD, the force (F_i) on a atom i with mass M, applied by other atoms is formulated as follows,

$$\overrightarrow{F_i} = M_i \frac{\partial^2 \overrightarrow{r_i}}{\partial t^2} \tag{1.35}$$

The vector notations in forces F_i and positions r_i, i.e. in three dimensions the whole system is described by 3N coordinates. The forces on a atom i is calculated as the negative derivative of the potential U, describing the interactions between the particles. And it can be written down as,

$$\overrightarrow{F_i} = \frac{\partial U}{\partial \overrightarrow{x_i}} \tag{1.36}$$

where, U, the inter-atomic potential, is a function of many degrees of freedom corresponding to all nuclei.

As can be realized already, one of the major challenge in MD simulations is calculating interatomic forces accurately [190]. In classical MD, forces are calculated from "predefined potentials", which are either based on empirical data or on independent electronic structure calculations [189]. Although, these empirical potentials have been modified over time to make them reliable, the transferability still is the major

issue. Moreover, these are still highly inefficient to capture the chemical bonding processes that use to take place in many dynamic systems. To handle these limitations, first-principle based approach i.e. ab-initio molecular dynamics (AIMD) has been developed by various groups [191]. Here, the forces are calculated on-the-fly from accurate electronic structure calculations. However, the better accuracy and reliable predictive power of AIMD simulations demands significant increase in computational effort. Thus, till now, DFT is the most commonly applied method for electronic structure calculation during AIMD simulations.

As discussed, evaluation of interatomic forces in AIMD does not depend on any adjustable parameters but only on position of nuclei. Depending upon the way of solving the electronic structures in every AIMD steps, there are different approaches developed by the researchers. These are Ehrenfest molecular dynamics, Born-Oppenheimer molecular dynamics (BOMD), Car-Parrinello molecular dynamics (CPMD) etc. In the present thesis, we extensively used BOMD simulations to investigate structural evaluation of various low-dimensional systems at finite temperatures.

1.6.3.1 Born-Oppenheimer Molecular Dynamics

BOMD simulation relies on the direct solving the static electronic structure problem in each molecular dynamics step, given the set of fixed nuclear positions at any instance of time. Thus, effectively electronic structure part is reduced to solving the time-independent Schrödinger equation and then propagating the nuclei via classical molecular dynamics. Note that, unlike other AIMD methods, the time-dependence of the electronic structure is a consequence of nuclear motion for BOMD simulations. One can define the BOMD method as follows,

$$M_i \ddot{R}_i(t) = \nabla_i \min_{\psi_0} <\psi_0|H_e|\psi_0> \tag{1.37}$$

for the electronic ground state.

1.7 Outline of Thesis

As discussed till now, low-dimensional systems exhibit many exotic phenomena due to quantum confinement. Owing to their extraordinary properties, low-dimensional materials are potential candidates for future electronic, spintronic and caloritronic devices, selective gas trapping etc. In this thesis, we have discussed electronic and magnetic structures in a few mesoscopic nanostructures, such as, hybrid graphene and boron nitride nanoribbons, silicene, transition metal incorporated graphitic C_3N_4 systems. Moreover, we also studied quantum transport of electrons and heat through molecular junctions.

In the **second chapter**, using constant-temperature Born-Oppenheimer (BOMD) simulation, a way to insert extended line defects (ELDs) at the grain boundary in hybrid graphene and boron nitride nanoribbons (BNCNRs) have been demonstrated. Different kinds of extended line defects can be stabilized by depositing different adatoms such as carbon, boron, and nitrogen at the grain boundaries. It has been found that the electronic and magnetic structures of these nanoribbons can highly be modulated in presence of these ELDs.

In the **third chapter**, emergence of different kinds of stable line defects in silicene have been discussed by performing BOMD simulations. Our results show that, depending upon the presence of silicon adatoms, edge shape of grain boundaries (i.e. armchair or zigzag), stable line-defects can be introduced in a controlled manner. Importantly, 5-5-8 line defects modify the non-magnetic semimetallic pristine silicene sheet to spin-polarized metal. As ferromagnetically ordered magnetic moments remain strongly localized at the line-defect, an one-dimensional spin-channel gets created in silicene.

Electronic, magnetic and optical properties of 3d-transition metal embedded graphitic carbon nitride sheets with and without graphene support have been explored in the **fourth chapter**. Depending upon the 3d-metal atoms, different kinds of magnetic ground state can appear in these systems. Stacking with graphene layer, composite systems demonstrate increase in structural stability and magnetic interactions with respect to transition metal deposited carbon nitride sheets. Performing Heisenberg model based Monte Carlo simulations, the Curie temperatures are calculated for different ferromagnetically stable systems.

Nitrogen substituted point-defects containing graphene sheets have been explored

for their potential application towards trapping of pollutant gases in the **fifth chapter**. BOMD studies demonstrate that, electron-rich point-defect sites can selectively and efficiently trap different kinds of poisonous and greenhouse polar gas molecules. Moderately strong hydrogen-bond formation between the hydrogen atom of the gas molecules and nitrogen of defect-sites stabilized the adsorbed molecules.
In the **sixth chapter**, using ab-initio numerical methods, the spin-dependent transport and thermoelectric properties of a spin-crossover molecule based nano-junction have been explored. A large magnetoresistance, efficient conductance-switching, and spin-filter activity in this molecule-based two-terminal device has been demonstrated. The spin-crossover process also modulates the thermoelectric entities.
In the **seventh chapter**, reversible spin-state switching of NO-adsorbed manganese porphyrin (MnP) on top of gold (111) surface has been explored using on-site Coulomb interaction incorporated density functional theory. The spin-state switching can be achieved by inducing conformational change in the molecular geometry. Mechanical manipulation of conformation by a STM tip in this regard has been studied. Transport and thermoelectric characteristics in the two-terminal device architecture embedding these molecular systems, have been studied thoroughly.
In the **eighth chapter**, electronic transport in molecular nanojunction based on heteronuclear six-membered rings have been discussed. The master (rate) equation approach has been used to treat the system which stays within Coulomb blockade regime. The results show how the chemical nature of site, attached to electrodes, can influence the response of this nano-system to an external source-drain bias. Depending on attachment of electrodes at various atomic sites, we have been able to obtain a host of exotic current-voltage characteristics, from negative differential conductance to rectification to Coulomb blockade behaviors.
At last, in **ninth chapter**, we summarise and give a brief outlook of the present thesis.

Bibliography

[1] K. Barnham and D. Vvedensky, *Low-dimensional semiconductor structures: fundamentals and device applications* (Cambridge University Press, 2008).

[2] H. Kroto, Nature **329**, 529 (1987).

[3] M. J. Oconnell, *Carbon nanotubes: properties and applications* (CRC press, 2006).

[4] X. Wu and X. C. Zeng, Nano Lett. **9**, 250 (2008).

[5] A. K. Geim and K. S. Novoselov, Nat. Mater. **6**, 183 (2007).

[6] M. Scarselli, P. Castrucci, and M. De Crescenzi, Journal of Physics: Condensed Matter **24**, 313202 (2012).

[7] M. J. Allen, V. C. Tung, and R. B. Kaner, Chem. Rev. **110**, 132 (2009).

[8] P. R. Wallace, Phys. Rev. **71**, 622 (1947).

[9] L. Landau, Phys. Z. Sowjetunion **11**, 26 (1937).

[10] R. Peierls, in *Annales de l'institut Henri Poincaré*, Vol. 5 (1935) pp. 177–222.

[11] K. S. Novoselov, A. K. Geim, S. Morozov, D. Jiang, Y. Zhang, S. Dubonos, , I. Grigorieva, and A. Firsov, Science **306**, 666 (2004).

[12] A. Fasolino, J. Los, and M. I. Katsnelson, Nat. Mater. **6**, 858 (2007).

[13] K. Novoselov, A. K. Geim, S. Morozov, D. Jiang, M. Katsnelson, I. Grigorieva, S. Dubonos, and A. Firsov, Nature **438**, 197 (2005).

[14] M. H. Gass, U. Bangert, A. L. Bleloch, P. Wang, R. R. Nair, and A. Geim, Nat. Nanotechnol. **3**, 676 (2008).

[15] Y. Zhang, Y.-W. Tan, H. L. Stormer, and P. Kim, Nature **438**, 201 (2005).

[16] F. Schedin, A. Geim, S. Morozov, E. Hill, P. Blake, M. Katsnelson, and K. Novoselov, Nat. Mater. **6**, 652 (2007).

[17] O. V. Yazyev and L. Helm, Phys. Rev. B **75**, 125408 (2007).

[18] D. A. Areshkin, D. Gunlycke, and C. T. White, Nano Lett. **7**, 204 (2007).

[19] M. Katsnelson, K. Novoselov, and A. Geim, Nat. Phys. **2**, 620 (2006).

[20] Y.-M. Lin, K. A. Jenkins, A. Valdes-Garcia, J. P. Small, D. B. Farmer, and P. Avouris, Nano Lett. **9**, 422 (2008).

[21] M. Liu, X. Yin, E. Ulin-Avila, B. Geng, T. Zentgraf, L. Ju, F. Wang, and X. Zhang, Nature **474**, 64 (2011).

[22] V. C. Sanchez, A. Jachak, R. H. Hurt, and A. B. Kane, Chem. Res. Toxicol. **25**, 15 (2011).

[23] X. Wan, G. Long, L. Huang, and Y. Chen, Adv. Mater. **23**, 5342 (2011).

[24] A. C. Neto, F. Guinea, N. Peres, K. S. Novoselov, and A. K. Geim, Rev. Mod. Phys **81**, 109 (2009).

[25] M. Xu, T. Liang, M. Shi, and H. Chen, Chem. Rev. **113**, 3766 (2013).

[26] A. Ismach, H. Chou, D. A. Ferrer, Y. Wu, S. McDonnell, H. C. Floresca, A. Covacevich, C. Pope, R. Piner, M. J. Kim, *et al.*, ACS Nano **6**, 6378 (2012).

[27] D. Golberg, Y. Bando, Y. Huang, T. Terao, M. Mitome, C. Tang, and C. Zhi, ACS Nano **4**, 2979 (2010).

[28] S. Cahangirov, M. Topsakal, E. Aktürk, H. Şahin, and S. Ciraci, Phys. Rev. Lett. **102**, 236804 (2009).

[29] B. Feng, Z. Ding, S. Meng, Y. Yao, X. He, P. Cheng, L. Chen, and K. Wu, Nano Lett. **12**, 3507 (2012).

[30] P. Vogt, P. De Padova, C. Quaresima, J. Avila, E. Frantzeskakis, M. C. Asensio, A. Resta, B. Ealet, and G. Le Lay, Phys. Rev. Lett. **108**, 155501 (2012).

[31] L. Meng, Y. Wang, L. Zhang, S. Du, R. Wu, L. Li, Y. Zhang, G. Li, H. Zhou, W. A. Hofer, *et al.*, Nano Lett. **13**, 685 (2013).

[32] X. Wang, K. Maeda, A. Thomas, K. Takanabe, G. Xin, J. M. Carlsson, K. Domen, and M. Antonietti, Nat. Mater. **8**, 76 (2009).

[33] G. Dong, Y. Zhang, Q. Pan, and J. Qiu, J. Photochem. Photobiol. C: Photochem. Rev. **20**, 33 (2014).

[34] J. Cai, P. Ruffieux, R. Jaafar, M. Bieri, T. Braun, S. Blankenburg, M. Muoth, A. P. Seitsonen, M. Saleh, X. Feng, *et al.*, Nature **466**, 470 (2010).

[35] H. Zeng, C. Zhi, Z. Zhang, X. Wei, X. Wang, W. Guo, Y. Bando, and D. Golberg, Nano Lett. **10**, 5049 (2010).

[36] P. De Padova, C. Quaresima, C. Ottaviani, P. M. Sheverdyaeva, P. Moras, C. Carbone, D. Topwal, B. Olivieri, A. Kara, H. Oughaddou, *et al.*, Appl. Phys. Lett. **96**, 261905 (2010).

[37] S. Dutta and S. K. Pati, J. Mater. Chem. **20**, 8207 (2010).

[38] C.-H. Park and S. G. Louie, Nano Lett. **8**, 2200 (2008).

[39] Y. Ding and J. Ni, Appl. Phys. Lett. **95**, 083115 (2009).

[40] X. Jia, M. Hofmann, V. Meunier, B. G. Sumpter, J. Campos-Delgado, J. M. Romo-Herrera, H. Son, Y.-P. Hsieh, A. Reina, J. Kong, *et al.*, Science **323**, 1701 (2009).

[41] P. Koskinen, S. Malola, and H. Häkkinen, Phys. Rev. Lett. **101**, 115502 (2008).

[42] Ç. Ö. Girit, J. C. Meyer, R. Erni, M. D. Rossell, C. Kisielowski, L. Yang, C.-H. Park, M. Crommie, M. L. Cohen, S. G. Louie, *et al.*, Science **323**, 1705 (2009).

[43] B. Xu, J. Yin, Y. Xia, X. Wan, K. Jiang, and Z. Liu, Appl. Phys. Lett. **96**, 163102 (2010).

[44] Y. Ding, Y. Wang, and J. Ni, Appl. Phys. Lett. **94**, 233107 (2009).

[45] Y. Ding and Y. Wang, Appl. Phys. Lett. **102**, 143115 (2013).

[46] Y.-W. Son, M. L. Cohen, and S. G. Louie, Phys. Rev. Lett. **97**, 216803 (2006).

[47] F. Zheng, G. Zhou, Z. Liu, J. Wu, W. Duan, B.-L. Gu, and S. Zhang, Phys. Rev. B **78**, 205415 (2008).

[48] X. Jia, J. Campos-Delgado, M. Terrones, V. Meunier, and M. S. Dresselhaus, Nanoscale **3**, 86 (2011).

[49] L. Tapasztó, G. Dobrik, P. Lambin, and L. P. Biró, Nat. Nanotechnol. **3**, 397 (2008).

[50] C. Berger, Z. Song, X. Li, X. Wu, N. Brown, C. Naud, D. Mayou, T. Li, J. Hass, A. N. Marchenkov, *et al.*, Science **312**, 1191 (2006).

[51] S. S. Datta, D. R. Strachan, S. M. Khamis, and A. C. Johnson, Nano Lett. **8**, 1912 (2008).

[52] X. Li, X. Wang, L. Zhang, S. Lee, and H. Dai, Science **319**, 1229 (2008).

[53] X. Yang, X. Dou, A. Rouhanipour, L. Zhi, H. J. Räder, and K. Müllen, J. Am. Chem. Soc **130**, 4216 (2008).

[54] J. Wu, W. Pisula, and K. Müllen, Chem. Rev. **107**, 718 (2007).

[55] D. V. Kosynkin, A. L. Higginbotham, A. Sinitskii, J. R. Lomeda, A. Dimiev, B. K. Price, and J. M. Tour, Nature **458**, 872 (2009).

[56] L. Jiao, L. Zhang, X. Wang, G. Diankov, and H. Dai, Nature **458**, 877 (2009).

[57] F. Banhart, J. Kotakoski, and A. V. Krasheninnikov, ACS Nano **5**, 26 (2010).

[58] I. Deretzis, G. Fiori, G. Iannaccone, and A. La Magna, Phys. Rev. B **81**, 085427 (2010).

[59] B. Biel, X. Blase, F. Triozon, and S. Roche, Phys. Rev. Lett. **102**, 096803 (2009).

[60] O. V. Yazyev, Rep. Prog. Phys. **73**, 056501 (2010).

[61] A. Du, Y. Chen, Z. Zhu, R. Amal, G. Q. Lu, and S. C. Smith, J. Am. Chem. Soc **131**, 17354 (2009).

[62] J. Gao, J. Zhang, H. Liu, Q. Zhang, and J. Zhao, Nanoscale **5**, 9785 (2013).

[63] F. Hao, D. Fang, and Z. Xu, Appl. Phys. Lett. **99**, 041901 (2011).

[64] A. A. Balandin, Nat. Mater. **10**, 569 (2011).

[65] A. Krasheninnikov and F. Banhart, Nat. Mater. **6**, 723 (2007).

[66] M. M. Ugeda, I. Brihuega, F. Guinea, and J. M. Gómez-Rodr´iguez, Phys. Rev. Lett. **104**, 096804 (2010).

[67] C. Jin, F. Lin, K. Suenaga, and S. Iijima, Phys. Rev. Lett. **102**, 195505 (2009).

[68] A. El-Barbary, R. Telling, C. Ewels, M. Heggie, and P. Briddon, Phys. Rev. B **68**, 144107 (2003).

[69] J. C. Meyer, C. Kisielowski, R. Erni, M. D. Rossell, M. Crommie, and A. Zettl, Nano Lett. **8**, 3582 (2008).

[70] J. Kotakoski, A. Krasheninnikov, U. Kaiser, and J. Meyer, Physical Review Letters **106**, 105505 (2011).

[71] P. Lehtinen, A. S. Foster, A. Ayuela, A. Krasheninnikov, K. Nordlund, and R. M. Nieminen, Phys. Rev. Lett. **91**, 017202 (2003).

[72] J. Li, G. Zhou, Y. Chen, B.-L. Gu, and W. Duan, J. Am. Chem. Soc **131**, 1796 (2009).

[73] L. Tsetseris and S. T. Pantelides, Carbon **47**, 901 (2009).

[74] F. Banhart, Nanoscale **1**, 201 (2009).

[75] K. T. Chan, J. Neaton, and M. L. Cohen, Phys. Rev. B **77**, 235430 (2008).

[76] O. Cretu, A. V. Krasheninnikov, J. A. Rodr´iguez-Manzo, L. Sun, R. M. Nieminen, and F. Banhart, Phys. Rev. Lett. **105**, 196102 (2010).

[77] A. Krasheninnikov, P. Lehtinen, A. S. Foster, P. Pyykkö, and R. M. Nieminen, Phys. Rev. Lett. **102**, 126807 (2009).

[78] H. Liu, Y. Liu, and D. Zhu, J. Mater. Chem. **21**, 3335 (2011).

[79] J. Sivek, H. Sahin, B. Partoens, and F. M. Peeters, Phys. Rev. B **87**, 085444 (2013).

[80] X. Wei, M.-S. Wang, Y. Bando, and D. Golberg, ACS Nano **5**, 2916 (2011).

[81] D. Boukhvalov and M. Katsnelson, Nano Lett. **8**, 4373 (2008).

[82] J. Hu and R. Wu, Nano Lett. **14**, 1853 (2014).

[83] L. Zhao, R. He, K. T. Rim, T. Schiros, K. S. Kim, H. Zhou, C. Gutiérrez, S. Chockalingam, C. J. Arguello, L. Pálová, *et al.*, Science **333**, 999 (2011).

[84] P. Y. Huang, C. S. Ruiz-Vargas, A. M. van der Zande, W. S. Whitney, M. P. Levendorf, J. W. Kevek, S. Garg, J. S. Alden, C. J. Hustedt, Y. Zhu, *et al.*, Nature **469**, 389 (2011).

[85] O. V. Yazyev and S. G. Louie, Nat. Mater. **9**, 806 (2010).

[86] O. V. Yazyev and S. G. Louie, Phys. Rev. B **81**, 195420 (2010).

[87] J. Lahiri, Y. Lin, P. Bozkurt, I. I. Oleynik, and M. Batzill, Nat. Nanotechnol. **5**, 326 (2010).

[88] Q. Li, X. Zou, M. Liu, J. Sun, Y. Gao, Y. Qi, X. Zhou, B. I. Yakobson, Y. Zhang, and Z. Liu, Nano Lett. **15**, 5804 (2015).

[89] D. Gunlycke and C. T. White, Phys. Rev. Lett. **106**, 136806 (2011).

[90] L. Tapasztó, P. Nemes-Incze, G. Dobrik, K. J. Yoo, C. Hwang, and L. P. Biró, Appl. Phys. Lett. **100**, 053114 (2012).

[91] G. Li, A. Luican, J. L. Dos Santos, A. C. Neto, A. Reina, J. Kong, and E. Andrei, Nat. Phys. **6**, 109 (2010).

[92] L. Kou, C. Tang, W. Guo, and C. Chen, ACS Nano **5**, 1012 (2011).

[93] S. S. Alexandre, A. Lúcio, A. C. Neto, and R. Nunes, Nano Lett. **12**, 5097 (2012).

[94] L. Ci, L. Song, C. Jin, D. Jariwala, D. Wu, Y. Li, A. Srivastava, Z. Wang, K. Storr, L. Balicas, *et al.*, Nat. Mater. **9**, 430 (2010).

[95] P. Sutter, R. Cortes, J. Lahiri, and E. Sutter, Nano Lett. **12**, 4869 (2012).

[96] Z. Liu, L. Ma, G. Shi, W. Zhou, Y. Gong, S. Lei, X. Yang, J. Zhang, J. Yu, K. P. Hackenberg, *et al.*, Nat. Nanotechnol. **8**, 119 (2013).

[97] S. Dutta, A. K. Manna, and S. K. Pati, Phys. Rev. Lett. **102**, 096601 (2009).

[98] Y. Liu, X. Wu, Y. Zhao, X. C. Zeng, and J. Yang, J. Phys. Chem. C **115**, 9442 (2011).

[99] J. Jung, Z. Qiao, Q. Niu, and A. H. MacDonald, Nano Lett. **12**, 2936 (2012).

[100] L. Liu, J. Park, D. A. Siegel, K. F. McCarty, K. W. Clark, W. Deng, L. Basile, J. C. Idrobo, A.-P. Li, and G. Gu, Science **343**, 163 (2014).

[101] S. Guo, Nanoscale **2**, 2521 (2010).

[102] L. P. Kouwenhoven, D. Austing, and S. Tarucha, Rep. Prog. Phys. **64**, 701 (2001).

[103] S. Ciraci, A. Buldum, and I. P. Batra, J. Phys.: Condens. Matter **13**, R537 (2001).

[104] A. Nitzan and M. A. Ratner, Science **300**, 1384 (2003).

[105] Y. Cui and C. M. Lieber, Science **291**, 851 (2001).

[106] C. Joachim and M. A. Ratner, Proc. Natl. Acad. Sci. U.S.A. **102**, 8801 (2005).

[107] N. Tao, Nat. Nanotechnol. **1**, 173 (2006).

[108] J. M. Tour, Acc. Chem. Res. **33**, 791 (2000).

[109] A. Aviram and M. A. Ratner, Chem. Phys. Lett. **29**, 277 (1974).

[110] R. M. Metzger, Chem. Rev. **115**, 5056 (2015).

[111] K. Moth-Poulsen, *Handbook of single-molecule electronics* (Pan Stanford, 2015).

[112] M. A. Reed, C. Zhou, C. Muller, T. Burgin, and J. Tour, Science **278**, 252 (1997).

[113] J. Reichert, R. Ochs, D. Beckmann, H. Weber, M. Mayor, and H. v. Löhneysen, Phys. Rev. Lett. **88**, 176804 (2002).

[114] J. Kushmerick, D. Holt, J. Yang, J. Naciri, M. Moore, and R. Shashidhar, Phys. Rev. Lett. **89**, 086802 (2002).

[115] J. Chen, W. Wang, M. Reed, A. Rawlett, D. Price, and J. Tour, *Room-temperature negative differential resistance in nanoscale molecular junctions*, Tech. Rep. (DTIC Document, 2000).

[116] C. Joachim, J. K. Gimzewski, R. R. Schlittler, and C. Chavy, Phys. Rev. Lett. **74**, 2102 (1995).

[117] M. Xue, Y. Yang, X. Chi, X. Yan, and F. Huang, Chem. Rev. **115**, 7398 (2015).

[118] G. Gil-Ram´irez, D. A. Leigh, and A. J. Stephens, Angew. Chem. Int. Ed. **54**, 6110 (2015).

[119] D. Gust, T. A. Moore, and A. L. Moore, Chem. Commun. , 1169 (2006).

[120] D. Gust, J. Andréasson, U. Pischel, T. A. Moore, and A. L. Moore, Chem. Commun. **48**, 1947 (2012).

[121] H. Tian and S. Yang, Chem. Soc. Rev. **33**, 85 (2004).

[122] B. Song, D. A. Ryndyk, and G. Cuniberti, Phys. Rev. B **76**, 045408 (2007).

[123] J. Park, A. N. Pasupathy, J. I. Goldsmith, C. Chang, Y. Yaish, J. R. Petta, M. Rinkoski, J. P. Sethna, H. D. Abruña, P. L. McEuen, *et al.*, Nature **417**, 722 (2002).

[124] N. Yoneya, E. Watanabe, K. Tsukagoshi, and Y. Aoyagi, Appl. Phys. Lett. **79**, 1465 (2001).

[125] N. Vsevolodov, *Biomolecular electronics: an introduction via photosensitive proteins* (Springer Science & Business Media, 2012).

[126] R. G. Endres, D. L. Cox, and R. R. Singh, Rev. Mod. Phys **76**, 195 (2004).

[127] G. Maruccio, A. Biasco, P. Visconti, A. Bramanti, P. P. Pompa, F. Calabi, R. Cingolani, R. Rinaldi, S. Corni, R. Di Felice, *et al.*, Adv. Mater. **17**, 816 (2005).

[128] S. V. Aradhya and L. Venkataraman, Nat. Nanotechnol. **8**, 399 (2013).

[129] L. Bogani and W. Wernsdorfer, Nat. Mater. **7**, 179 (2008).

[130] S. Sanvito, Chem. Soc. Rev. **40**, 3336 (2011).

[131] C. Chappert, A. Fert, and F. N. Van Dau, Nat. Mater. **6**, 813 (2007).

[132] M. Mannini, F. Pineider, P. Sainctavit, C. Danieli, E. Otero, C. Sciancalepore, A. M. Talarico, M.-A. Arrio, A. Cornia, D. Gatteschi, *et al.*, Nat. Mater. **8**, 194 (2009).

[133] H. Heersche, Z. De Groot, J. Folk, H. Van Der Zant, C. Romeike, M. Wegewijs, L. Zobbi, D. Barreca, E. Tondello, and A. Cornia, Phys. Rev. Lett. **96**, 206801 (2006).

[134] M.-H. Jo, J. E. Grose, K. Baheti, M. M. Deshmukh, J. J. Sokol, E. M. Rumberger, D. N. Hendrickson, J. R. Long, H. Park, and D. Ralph, Nano Lett. **6**, 2014 (2006).

[135] A. S. Zyazin, J. W. van den Berg, E. A. Osorio, H. S. van der Zant, N. P. Konstantinidis, M. Leijnse, M. R. Wegewijs, F. May, W. Hofstetter, C. Danieli, *et al.*, Nano Lett. **10**, 3307 (2010).

[136] E. A. Osorio, K. Moth-Poulsen, H. S. van der Zant, J. Paaske, P. Hedegård, K. Flensberg, J. Bendix, and T. Bjørnholm, Nano Lett. **10**, 105 (2009).

[137] S. Schmaus, A. Bagrets, Y. Nahas, T. K. Yamada, A. Bork, M. Bowen, E. Beaurepaire, F. Evers, and W. Wulfhekel, Nat. Nanotechnol. **6**, 185 (2011).

[138] D. Paul, Physikalische Zeitschrift **1**, 161 (1900).

[139] A. Sommerfeld and H. Bethe, in *Aufbau Der Zusammenhängenden Materie* (Springer, 1933) pp. 333–622.

[140] R. Landauer, Physica Scripta **1992**, 110 (1992).

[141] P. W. Anderson, Phys. Rev. **109**, 1492 (1958).

[142] S. Wolf, D. Awschalom, R. Buhrman, J. Daughton, S. Von Molnar, M. Roukes, A. Y. Chtchelkanova, and D. Treger, Science **294**, 1488 (2001).

[143] S. Datta, *Electronic transport in mesoscopic systems* (Cambridge university press, 1997).

[144] D. S. Fisher and P. A. Lee, Phys. Rev. B **23**, 6851 (1981).

[145] G. J. Snyder and E. S. Toberer, Nat. Mater. **7**, 105 (2008).

[146] M. S. Dresselhaus, G. Chen, M. Y. Tang, R. Yang, H. Lee, D. Wang, Z. Ren, J.-P. Fleurial, and P. Gogna, Adv. Mater. **19**, 1043 (2007).

[147] D. M. Rowe, *CRC handbook of thermoelectrics* (CRC press, 1995).

[148] W. Thomson, Proc. Roy. Soc. Edinburgh , 91 (1851).

[149] A. E., Phys. Zeitschrift **10**, 560 (1909).

[150] A. E., Phys. Zeitschrift **12**, 920 (1911).

[151] M. Vedernikov and E. Iordanishvili, in *Thermoelectrics, 1998. Proceedings ICT 98. XVII International Conference on* (IEEE, 1998) pp. 37–42.

[152] C. Wood, Rep. Prog. Phys. **51**, 459 (1988).

[153] D. Vashaee and A. Shakouri, Phys. Rev. Lett. **92**, 106103 (2004).

[154] T. Harman, P. Taylor, M. Walsh, and B. LaForge, Science **297**, 2229 (2002).

[155] J. Kanamori, Progr. Theoret. Phys. **30**, 275 (1963).

[156] M. C. Gutzwiller, Phys. Rev. Lett. **10**, 159 (1963).

[157] J. Hubbard, in *Proceedings of the Royal Society of London A: Mathematical, Physical and Engineering Sciences*, Vol. 276 (The Royal Society, 1963) pp. 238–257.

[158] J. Hubbard, in *Proceedings of the Royal Society of London A: Mathematical, Physical and Engineering Sciences*, Vol. 277 (The Royal Society, 1964) pp. 237–259.

[159] W. Nolting and W. Borgiel, Phys. Rev. B **39**, 6962 (1989).

[160] C. Honerkamp and M. Salmhofer, Phys. Rev. Lett. **87**, 187004 (2001).

[161] S. Trugman, Phys. Rev. B **37**, 1597 (1988).

[162] P. W. Anderson, Science **235**, 1196 (1987).

[163] E. H. Lieb and F. Y. Wu, Phys. Rev. Lett. **20**, 1445 (1968).

[164] A. Ovchinnikov, The Hubbard Model: A Reprint Volume **30**, 58 (1992).

[165] J. Bonča, P. Prelovšek, and I. Sega, Phys. Rev. B **39**, 7074 (1989).

[166] Y. Hasegawa and D. Poilblanc, Phys. Rev. B **40**, 9035 (1989).

[167] N. Elstner and A. Young, Phys. Rev. B **50**, 6871 (1994).

[168] E. Dagotto and A. Moreo, Phys. Rev. B **39**, 4744 (1989).

[169] H. Lin, Phys. Rev. B **42**, 6561 (1990).

[170] P. Hohenberg and W. Kohn, Phys. Rev. **136**, B864 (1964).

[171] W. Kohn and L. J. Sham, Phys. Rev. **140**, A1133 (1965).

[172] D. M. Ceperley and B. Alder, Phys. Rev. Lett. **45**, 566 (1980).

[173] J. P. Perdew, K. Burke, and M. Ernzerhof, Phys. Rev. Lett. **77**, 3865 (1996).

[174] J. P. Perdew and Y. Wang, Phys. Rev. B **46**, 12947 (1992).

[175] J. P. Perdew, J. Chevary, S. Vosko, K. A. Jackson, M. R. Pederson, D. Singh, and C. Fiolhais, Phys. Rev. B **46**, 6671 (1992).

[176] A. D. Becke, J. Chem. Phys **98**, 5648 (1993).

[177] C. Lee, W. Yang, and R. G. Parr, Phys. Rev. B **37**, 785 (1988).

[178] F. A. Hamprecht, A. J. Cohen, D. J. Tozer, and N. C. Handy, J. Chem. Phys **109**, 6264 (1998).

[179] A. D. Boese, N. L. Doltsinis, N. C. Handy, and M. Sprik, J. Chem. Phys **112**, 1670 (2000).

[180] S. Dudarev, G. Botton, S. Savrasov, C. Humphreys, and A. Sutton, Phys. Rev. B **57**, 1505 (1998).

[181] K. Terakura, A. Williams, T. Oguchi, and J. Kübler, Phys. Rev. Lett. **52**, 1830 (1984).

[182] M. W. Schmidt, K. K. Baldridge, J. A. Boatz, S. T. Elbert, M. S. Gordon, J. H. Jensen, S. Koseki, N. Matsunaga, K. A. Nguyen, S. Su, *et al.*, J. Comput. Chem. **14**, 1347 (1993).

[183] F. M. Bickelhaupt and E. J. Baerends, Rev. Comput. Chem. , 1 (2007).

[184] G. Te Velde, F. M. Bickelhaupt, E. J. Baerends, C. Fonseca Guerra, S. J. van Gisbergen, J. G. Snijders, and T. Ziegler, J. Comput. Chem. **22**, 931 (2001).

[185] J. M. Soler, E. Artacho, J. D. Gale, A. Garc´ia, J. Junquera, P. Ordejón, and D. Sánchez-Portal, J. Phys.: Condens. Matter **14**, 2745 (2002).

[186] P. Giannozzi, S. Baroni, N. Bonini, M. Calandra, R. Car, C. Cavazzoni, D. Ceresoli, G. L. Chiarotti, M. Cococcioni, I. Dabo, *et al.*, J. Phys.: Condens. Matter **21**, 395502 (2009).

[187] G. Kresse and D. Joubert, Phys. Rev. B **59**, 1758 (1999).

[188] G. Kresse and J. Furthmüller, Phys. Rev. B **54**, 11169 (1996).

[189] D. Frenkel and B. Smit, *Understanding molecular simulation: from algorithms to applications*, Vol. 1 (Academic press, 2001).

[190] M. P. Allen and D. J. Tildesley, *Computer simulation of liquids* (Oxford university press, 1989).

[191] D. Marx and J. Hutter, Modern methods and algorithms of quantum chemistry **1**, 141 (2000).

Chapter 2

Line Defects at the Heterojunction of Hybrid Boron Nitride/Graphene Nanoribbons*

2.1 Introduction

As discussed in Chapter 1, in the last decade, research on one-atom-thick two-dimensional (2D) carbon allotrope i.e. graphene, gained tremendous interest because of their fascinating and extraordinary physical, chemical, and mechanical properties [1]. Apart from graphene, monolayer hexagonal boron nitride (h-BN) and its in-plane hybrid with graphene (h-BNC) have also been demonstrated as potential candidates for different types of technological applications [2–4]. In particular, quasi-one dimensional (1D) zigzag nanoribbons (ZNRs) of these 2D materials already have exhibited promising performance toward nanoscale electronics and spintronics application [5, 6]. The appearance of the peculiar edge states makes the difference in various properties of ZNRs with respect to their corresponding 2D sheets.

Most of the experimental procedures to form these 1D and 2D materials unavoidably include different kinds of defects in them [7]. Theoretical investigations have

*Works reported in this chapter are published in: (a) D. Ghosh, P. Parida and S. K. Pati, J. Mater. Chem. C, **2**, 392-398 (2014). Reprinted (adapted) with permission from The Royal Society of Chemistry (RSC),(b) D. Ghosh, P. Parida and S. K. Pati, J. Phys. Chem. C, **118**, 14670 - 14676 (2014). Reprinted (adapted) with permission from American Chemical Society

demonstrated that the presence of point as well as line defects can largely modify the electronic, magnetic, and mechanical properties of these low-dimensional materials [7]. However, insertion of defects (particularly line defects) in these covalently bonded hexagonal lattices in a controlled way is a challenge for experimentalists. Very recently, Lahiri *et. al.* have experimentally synthesized an extended line defect (ELD), containing two pentagons and one octagon (5-5-8) periodically, in a graphene sheet [8]. Nevertheless, this particular approach is highly sensitive to the experimental conditions, purity of the substrate, etc. There are a few theoretical studies such as deposition of dimer [9], reconstruction of vacancies or special type of ELDs [10], adsorption of C/N atoms, etc. [11], which all demonstrate possible ways to form different ELDs in the graphene/h-BN as well as in nanoribbons of them. However, the controlled insertion and effects of various types of line defects at the heterojunctions of hybrid zigzag BN-C nanoribbons (ZBNCNRs) have not been explored theoretically for quite sometime. As line defects significantly modify the properties in zigzag graphene nanoribbons (ZGNRs) and zigzag boron nitride nanoribbons (ZBNNRs) individually, it would be interesting to investigate the formation and effects of various line defects at the heterojunctions of h-ZBNCNRs.

In this chapter, performing Born-Oppenheimer molecular dynamics (BOMD) simulations, we demonstrate a much easier and controlled way to insert an ELD at the in-plane heterojunction of ZBNCNRs, made of zigzag graphene nanoribbons (ZGNRs) and zigzag boron nitride nanoribbons (ZBNNRs). By depositing C/B/N atoms at the grain boundaries, we predicted different kinds of line defects during the reconstruction process. Here, we considered two types commonly observed arrangements of neighbouring grains (1) face-to-face arrangement (see Fig. 2.1) and (2) half-lattice translated arrangement (see Fig. 2.9). Density functional theory (DFT) based study of these reconstructed ELD structures shows a wide range of electronic and magnetic properties ranging from semiconducting to spin-polarized metallic behaviour.

2.2 Computational Details

We perform BOMD simulations using the QUICKSTEP module in the CP2K package with a reasonable energy cut off of 280 Ry [12]. It uses a mixed basis set

where the Kohn-Sham orbitals are expanded in an atom-centered Gaussian basis set while the electronic charge density is described using an auxiliary plane wave basis set [13]. The valence electrons are treated with a double-ζ valence basis set with one set of polarization functions, i.e., DZVP basis set [14], whereas the core electrons and nuclei are represented using an analytical dual-space pseudopotential recommended by Goedecker, Teter, and Hutter (GTH) [15]. We apply extensively used exchange-correlation, Perdew-Burke-Ernzerhof (PBE) functional within the generalized gradient approximation(GGA) for all calculations [16]. We carried out most of the simulations at a constant temperature of 300 K using a Nose-Hoover thermostat [17, 18]. For some of the NRs, to check the stability of ELD at higher temperature, we also performed BOMD at 1000 K. The time step of 1 fs is used to integrate the equations of motion. The 5 or 10 ps trajectory is generated and used for analysis.

For electronic and magnetic structure calculations for all NRs, we used spin-unrestricted density functional theory (DFT) as implemented in the SIESTA package [19]. We used a double-ζ polarized (DZP) basis set for all atoms and a mesh cutoff of 400 Ry. Moreover, the same exchange-correlation functional as mentioned earlier, i.e., GGA (PBE), is used. To avoid spurious interaction in non-periodic directions, we use a cell of 30 $\times$ 40 $\times$ 2c Å, where c is the length of the unit cell in the periodic direction. We used Monkhorst-Pack [20] 1 $\times$ 1 $\times$ 250 (total number of k points is 126) to sample the 1D Brillouin zone for all electronic and magnetic structure calculations.

The formation energy of these NRs has been calculated using the following formula,

$$E_{form} = E_{tot} - [n_C \times E_C + n_B \times E_B + n_N \times E_N + n_H \times E_H] \tag{2.1}$$

where E_{tot} is the total energy of the system and E_C, E_B, C_N and C_H are the total energies per atom of graphene, α-boron, N_2 and H_2 molecule, respectively. n_C, n_B, n_N and n_H represent the number of carbon, boron, nitrogen and hydrogen atoms present in the system, respectively.

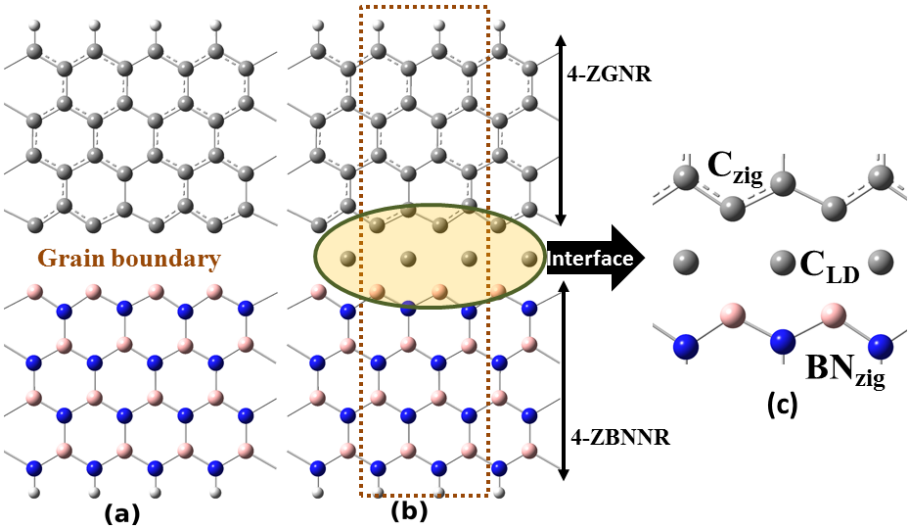

Figure 2.1: (a and b) Proposed model for stepwise formation of initial heterojunction of ZBNCNR where the grains are arranged in face-to-face manner. Here, we represent C-ZBNCNR-CN as an example. (a) Two separate ZGNR and ZBNNR segments are formed; (b) C atoms are deposited at the grain boundary of ZGNR and ZBNNR. Highlighted portion is the interface. (c) Zoomed view of interface. White, light pink, gray, and blue balls represent H, B, C, and N, respectively.

2.3 Results and Discussion

In this section, first we explore the formation and effects of ELDs where the adjacent grains of ZGNRs and ZBNNRs meet face-to-face at the boundary. In later part, the insertion of different ELDs at the grain boundaries where the grains are shifted by half-lattice have been investigated. The influence of these ELDs upon electronic and magnetic properties also explored thoroughly. Further, we consider all ZBNCNRs as having both edges passivated with hydrogen atoms for all the studies in this chapter.

2.3.1 ELDs at Face-to-Face Grain Boundaries

2.3.1.1 Reconstruction at Heterojunctions

In Fig. 2.1, we present an example of grain boundary (GB) at the heterojunction of ZGNR and ZBNNR. The width of two NRs on both sides of the grain boundary is

considered to be the same in this chapter. As a proposed bottom-up approach, initially NR of each side of GB can be grown separately on top of the same metal (e.g., Cu [21], Ru(0001) [22] or Ni(111) [8]) surface. Note that, the initial geometry for the MD simulation does not include any lattice translation between the two adjacent grains of NRs. As the zigzag edges of these two NRs come reasonably close to each other, one can deposit the adatoms (i.e. C/B/N) at that narrow GB. With this procedure, initial structures of the study can be prepared. Interestingly, a similar kind of approach has been considered to fabricate a planar h-BNC sheet with atomically separate domains of graphene and h-BN recently [21]. We define the NRs with a line defect as X-ZBNCNR-AB where X indicates the type of adatom and AB denotes the nature of atoms at two edges of the NR (atoms of kind A at one of the edges and atoms of kind B at the other edge of the NR). Atoms deposited at the GB are referred to as X_{LD}, whereas atoms nearest to these X_{LD} are denoted as M_{zig} (i.e., C_{LD} and B_{zig}/C_{zig} at Fig. 2.1 (c)). As an example, the structure shown in Fig. 2.1 (b) can be denoted as C-ZBNCNR-CN. To explore the reconstruction processes in these systems, we perform finite temperature (300 K/1000 K) BOMD simulations. The equilibrated geometries of these NRs are considered further to investigate the magnetic and electronic properties using first-principle methods. Unless it is mentioned, we considered 4 zigzag chains (n = 4) of C/BN on both sides of the grain boundary.

We begin our study by investigating the reconstruction processes of ZBNCNRs where C atoms are deposited at GB (C-ZBNCNR-CB and C-ZBNCNR-CN). By investigating the MD trajectories, we gain a clear idea about the atomic processes happening at the GB during reconstruction of these NRs. In Fig. 2.2, we show the snapshots of the reconstruction process of C-ZBNCNR-CB at about 300 K. As the simulation begins, C5 and C6 atoms move closer to C1 and N2, respectively, and form the very short bonds shown in Fig. 2.2 (b). However, these bonds are not stable, and C_{LD} (C5 and C6) atoms remain mobile at the GB before they could form a dimer between them as can be seen from Fig. 2.2 (c). This dimer formation stabilizes the equilibrated structure of ZBNCNR (see Fig. 2.2 (d, e). Along with dimer formation, C5 forms covalent bonds with C1 and N1 and C6 forms covalent bonds with C3 and N2. Thus, C_{LD} atoms become sp^2 hybridized, forming three covalent bonds. Reconstruction finally leads to creation of 5-5-8 ELD at the GB. Within 4.0

ps, the reconstructed ZBNCNR attains the equilibrium state, where the fluctuation in the total energy becomes negligible as shown in Fig. 2.3 (a). Therefore, without any further structural reconstruction the 5-5-8 ELD at the GB in the ZBNCNR appears to be very stable. Similarly, the other structure, C-ZBNCNR-CN, also gets reconstructed to form 5-5-8 ELD at the GB.

Next, we study N-deposited ZBNCNR i.e. N-ZBNCNR-CN. Interestingly, N-ZBNCNR-CN, in particular, gets reconstructed into two different geometries at two different temperatures. It forms a new kind of 8-8-8 ELD (see Fig. 2.4) at room temperature, while a 5-5-8 ELD is formed at higher temperature (1000 K). Initially, for both temperatures, deposited N atoms remain quite mobile at the GB without forming a stable covalent bond (see Fig. 2.4 (b,c)). Later, as shown in Fig. 2.4 (d,e) at 300 K, N_{LD} forms stable linear covalent bonds with C_{zig} and B_{zig}, giving rise to almost planar 8-8-8 ELD at the GB. In this particular low-temperature structure each N_{LD} remains undercoordinated and electron rich as it has only two C-N covalent bonds. Plotting total energy vs simulation time in Fig. 2.3 (b), it is evident that within 2.5 ps this reconstructed ZBNCNR achieves the equilibrium geometry. To check the stability of this 8-8-8 ELD at larger simulation time, we extended the simulation up to 10 ps and find that this structure is well equilibrated within that time period (see Fig. 2.4 (e)). On the other hand, at higher temperature, i.e., at 1000K, N_{LD} form dimers among them and give rise to 5-5-8 ELD at the heterojunction as equilibrated structure.

This temperature-dependent reconstruction processes can be understood from the electron density at the ELD. Formation of dimer among electron-rich N_{LD} atoms at the GB faces an energy barrier due to strong electron lone-pair repulsion. Thus, at low temperature, the GB cannot get reformed to 5-5-8 ELD as formation of NLD dimer is the primary step for it. As a result, at 300 K, it forms 8-8-8 ELD, where N_{LD} atoms remain relatively far from each other ($\sim$ 2.5 Å), reducing the electron lone-pair repulsion between them. However, at higher temperature, N_{LD} are much more mobile and can overcome the energy barrier quite easily, giving rise to 5-5-8 ELD.

Alike C-ZBNCNRs, B-ZBNCNR-CB also gets reconstructed to form 5-5-8 ELD, where B_{LD} atoms form B-B dimer at the GB. We note that when deposited adatoms at the GB are C or B, structures always form thermodynamically preferred 5-5-8

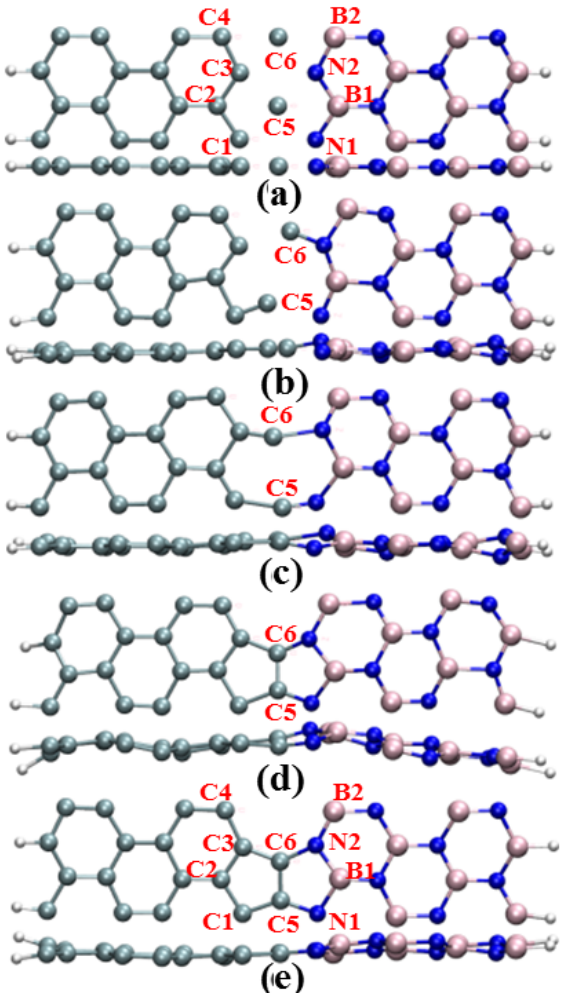

Figure 2.2: Snapshots of top and side view of C-ZBNCNR-CB during BOMD simulations at constant temperature (300 K) and pressure (1 atm) after (a) 0.0, (b) 0.008, (c) 0.01, (d) 0.05, and (e) 5 ps.

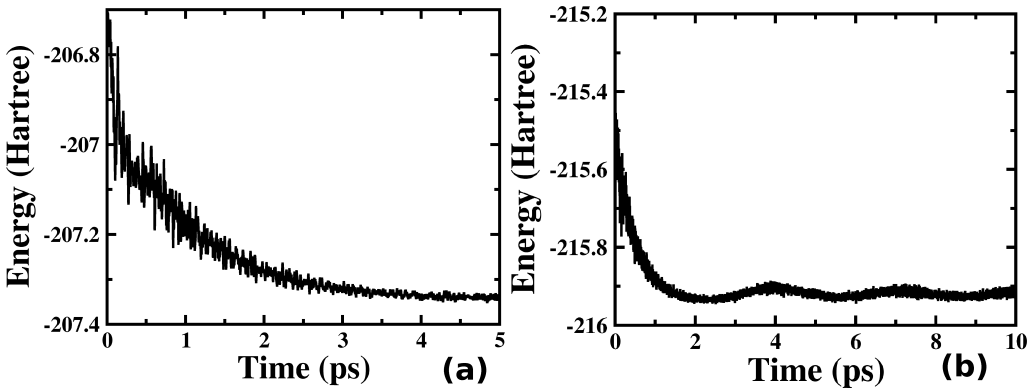

Figure 2.3: Total energy during BOMD simulation of reconstruction of (a) C-ZBNCNR-CB and (b) N-ZBNCNR-CN at 300 K and 1 atm pressure.

Table 2.1: Relative energies (with respect to the ground state) of different spin configurations of the studied nanoribbons. The relative energies among different spin configurations are given in meV/cell and formation energy is given in meV/atom. Formation energies of their ground state are given. Values in parentheses correspond to wider NRs. The spin configuration of the ground state remains the same for both widths.

Structures	UUUU	UUDD	UDUD	UDUU	UUUD	Formation Energy
C-ZBNCNR-CB	0(0)	-	84(110)	-	-	-720(-710)
C-ZBNCNR-CN	0(0)	-	82(99)	-	-	-750(-730)
N-ZBNCNR-CB (8-8-8)	0(0)	-	90(106)	-	-	-780(-750)
N-ZBNCNR-CB (5-5-8)	24(13)	0(0)	100(147)	76(51)	76(51)	-820(-780)
B-ZBNCNR-CB	38(15)	0(0)	137(170)	71(53)	71(53)	-710(-710)

ELD, irrespective of temperature. In fact, as strong lone pair-lone pair repulsion during dimerization of B_{LD} or C_{LD} is absent for these NRs, the energy barrier to form 5-5-8 ELD is negligibly small.

The negative formation energies for all these structures as tabulated in Table 2.1 proves their thermodynamic stability. Doubling the width of NRs (i.e., 8 zigzag chains on either side of the GB) we performed BOMD simulations of reconstruction processes. We found that the nature of each reconstruction does not depend upon the width of NRs. Furthermore, the formation energies tabulated in Table 2.1 show that the width of NRs has little influence over the thermodynamic stability of them.

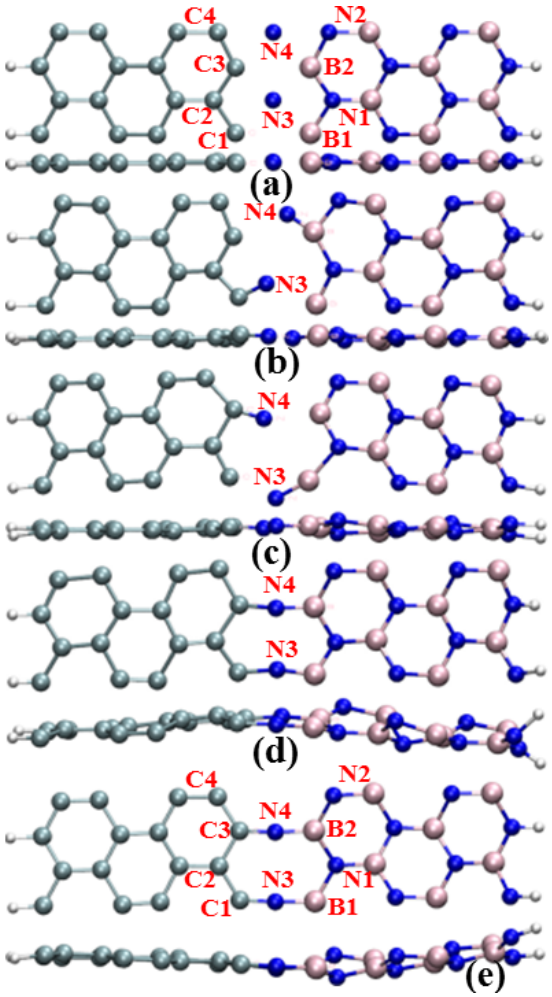

Figure 2.4: Snapshots of the top and side view of N-ZBNCNR-CN during BOMD simulations at constant temperature (300 K) and pressure (1 atm) after (a) 0.0, (b) 0.0035, (c) 0.0085, (d) 1, and (e) 10 ps.

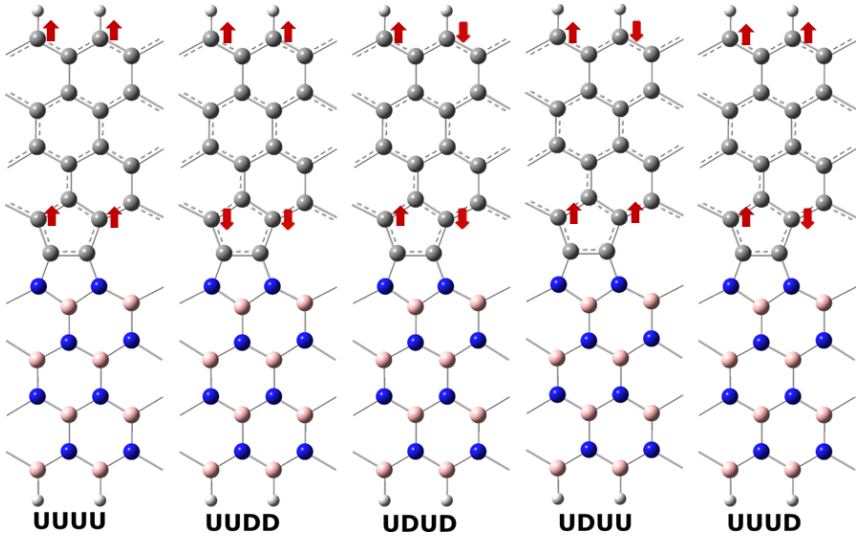

Figure 2.5: Various Spin configurations and their corresponding name for C-ZBNCNR-CB. Up- and down-spins are denoted are U and D, respectively.

2.3.1.2 Electronic and Magnetic Properties

To investigate the magnetic ground state of ZBNCNRs, we considered several magnetic configurations of edge C (i.e., C_{ed}) atoms and C_{zig} atoms as shown in Fig. 2.5. Note that B/N atoms with hydrogen passivation at the edge contribute negligibly to the total spin polarization. The band structure for C-ZBNCNR-CB and C-ZBNCNR-CN, as shown in Fig. 2.6 (a,b), evidently exhibit these NRs as spin-polarized metal. Each C_{ed} atom of C-ZBNCNR-CB (C-ZBNCNR-CN) contributes a magnetic moment of 0.27 μB/C atoms (0.26 μB/C atoms). On the other hand, the magnetic ordering of C_{zig} gets destroyed because of the presence of 5-5-8 ELD. Thus, these C_{zig} atoms in C-ZBNCNR-CB (C-ZBNCNR-CN) contribute much less moment of -0.07 μB/C atom (-0.01 μB/C atom) to the total magnetic moment i.e. 0.82 μB/supercell (0.74 μB/supercell). The relative energies among different magnetic states for both C-ZBNCNR-CB and C-ZBNCNR-CN are summarized in Table 2.1. As shown in Fig. 2.6, both the systems are spin-polarized metal as band 2 (majority spin band) and band 3 (minority spin band) cross the Fermi level. Wave function analyses of these electronic bands demonstrate that the band 1 and band 3 are localized at the defect region, whereas the other two bands arise from carbon edges (see Fig. 2.6 (d, e)). We note that the low-energy electronic bands are mainly derived from the ZGNR part of C-ZBNCNR-CN as bands from ZBNNR stay far

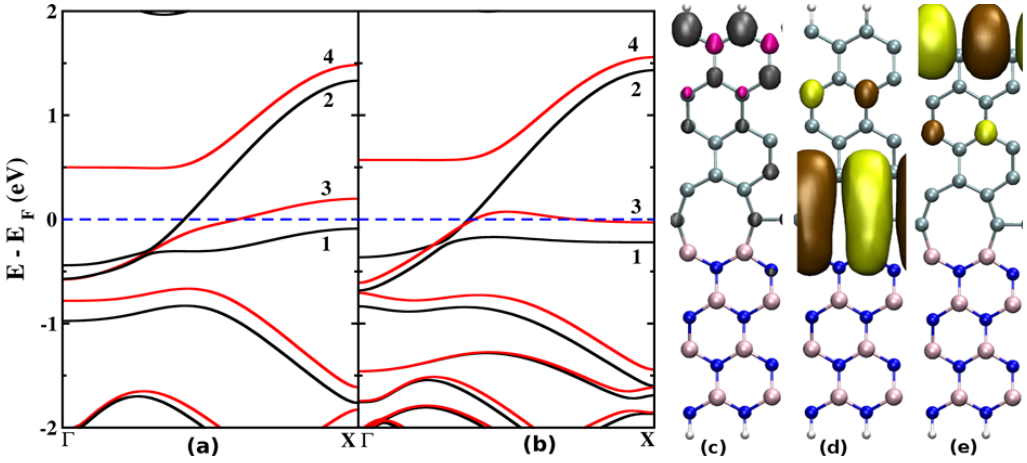

Figure 2.6: (a) Spin-polarized band structure of (a) C-ZBNCNR-CB and (b) C-ZBNCNR-CN. Black and red solid lines correspond to the majority and minority spin bands, respectively. (c) Spin density plot and wave function plot of C-ZBNCNR-CN for (d) band 1 and (e) band 2 at the Γ point. Gray and magenta-colored isosurface represent the positive and negative values of the moment, respectively. The isosurface for spin density plot is 0.025 au. This isosurface remains the same for all cases in this chapter.

from the Fermi level. Due to the Lewis acidic nature of boron, the C_{LD}-C_{LD} dimer in C-ZBNCNR-CN (where it is covalently attached to B atoms) becomes electron deficient after donating electrons to adjacent BN chain. Throughout the ribbon, a potential gradient is generated due to this charge transfer. Mulliken population analysis reveals that each C_{LD} atom donates 0.22 e^-. On the other hand, for C-ZBNCNR-CB, where C_{LD}-C_{LD} dimer is attached to an electron-rich N atom, such kind of charge transfer is absent at the GB.

Interestingly, both B-ZBNCNR-CB and the high-temperature (1000 K) structure of N-ZBNCNR-CN (i.e., 5-5-8 ELD) show the UUDD spin configuration as their ground state (see Fig. 2.5 for the definition of UUDD configuration). C_{ed} atoms at the edge couple ferromagnetically among themselves, while they couple antiferromagnetically to C_{zig} atoms, giving rise to net zero magnetic moment. Formation of covalent bonds among C_{zig} and dimer of B/N at the heterojunction allows C_{zig} to retain their spin ordering. From Table 2.1, it can be clearly seen that the UUDD spin configuration is energetically more stable than that of UUUU by 38 and 24 meV for B-ZBNCNR-CB and N-ZBNCNR-CN, respectively. These two NRs exhibit semiconducting behaviors with different band gaps for two different spin

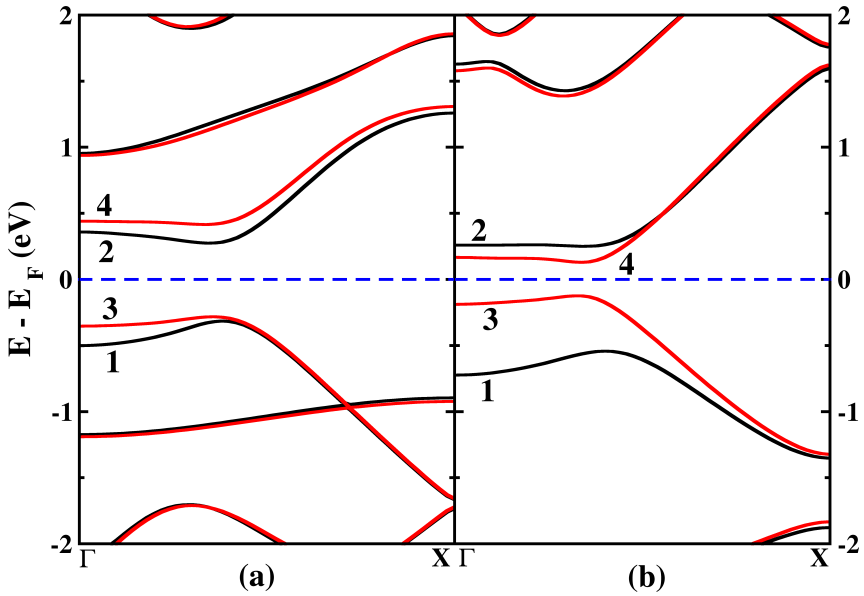

Figure 2.7: Spin-polarized band structures for (a) B-ZBNCNR-CB and (b) N-ZBNCNR-CN which contain 5-5-8 ELD.

channels (see Fig. 2.7 (a,b)).

In Fig. 2.8 (a), we plot the band structure for the low temperature structure of N-ZBNCNR-CN (i.e., 8-8-8 ELD). This NR is predicted to be a spin-polarized metal with a magnetic moment of 0.7 μB/unit cell. As shown in Fig. 2.8 (b), the spin density distribution confirms that the spin moment is mostly localized on C atoms at the ZGNR edge. Wave function analysis exhibit that both majority band 1 and minority band 3 originate mainly from the edge states (see Fig. 2.8 (c,d)). Further, as shown in Fig. 2.8 (e), other two highly dispersive and degenerate bands, band 2 and band 4, which cross the Fermi level, remain delocalize over the line defect regions at the GB. The edge states are mainly contributed from $2p_z$ orbitals of C_{ed} atoms, whereas the states at the defect region mainly appear from $2p_x/2p_y$ orbitals of B, N, and C atoms.

2.3.2 ELDs at Half-lattice Shifted Grain Boundaries

2.3.2.1 Reconstruction at Heterojunctions

For these heterojunctions, as mentioned earlier, two adjacently growing grains remain mutually shifted by a half lattice. After depositing the adatoms at the GB,

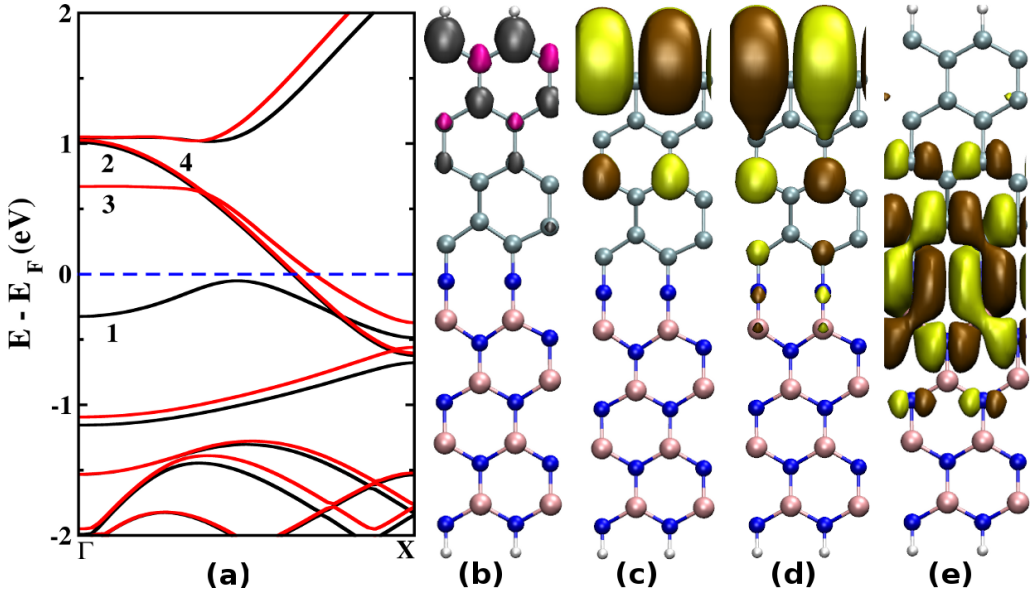

Figure 2.8: (a) Spin-polarized band structure of (a) N-ZBNCNR-CN containing 8-8-8 ELD. (b) Spin density plot and wave function plot of N-ZBNCNR-CN for (c) band 1, (d) band 3, and (e) band 2 at the Γ point.

initially, an extended line defect (ELD) of four membered rings (4-ELD) generates. In various studies, similar kind of ELDs are already considered as the initial geometries to stabilize other different types of ELD at graphene and h-BN sheets. [23, 24]. To make the discussion easily understandable, we represent these ZBNCNRs with a 4-ELD at the heterojunction as LD-ZBNCNR. Stepwise formation of this 4-ELD can be seen in the Fig. 2.9 (a-c). In this example, as shown in Fig. 2.9 (b,c), N adatoms are deposited at the heterojunction. Throughout this part of the discussion, we consider a LD-ZBNCNR, which is constructed by joining 5-ZBNNR and 5-ZGNR through a 4-ELD at the heterojunction, as the initial geometry for structural reconstruction. A 4-ELD consists of a zigzag chain of BN or C atoms and a linear chain of C/B/N atoms (see Fig. 2.9 (e)). In this section, we name the nanoribbons in different way compared to previous one. Here, we represent the systems by the symbol (P-Q)4-ELD-R, where P and Q signify the nature of the zigzag line and the linear chain in the 4-ELD, respectively and R represents the type of edge atoms at the BNNR. As an example, the geometry in Fig. 2.9(c) can be represented as (C_{zig}-N_{line})4-ELD-N_{edge} according to our nomenclature. The 4-coordinated atoms that are at the core of the 4-ELD are named as X_{LD} (e.g. C_{LD} in Fig. 2.9(d), and

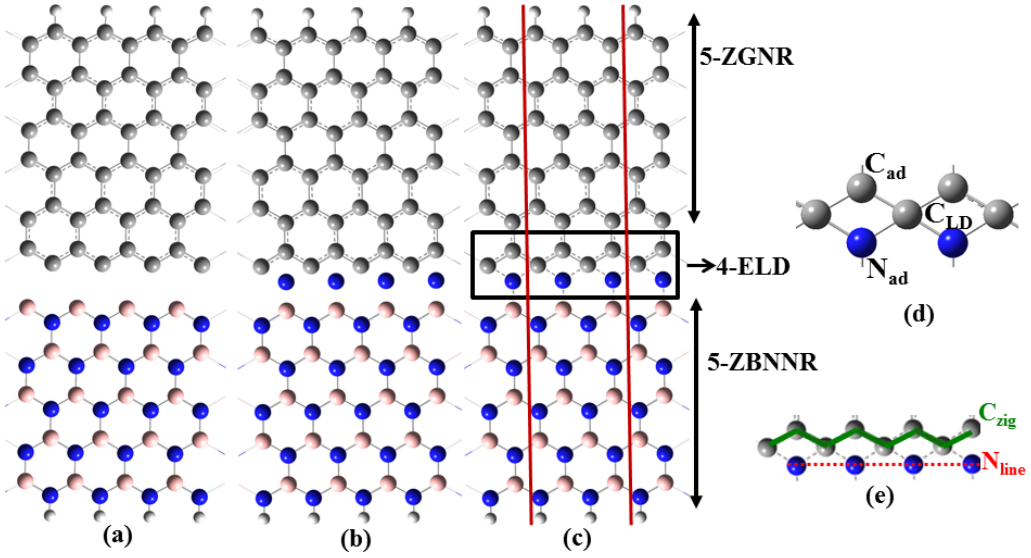

Figure 2.9: (a-c) A proposed model for the stepwise formation of a 4-ELD at the heterojunction of a half-lattice shifted ZBNCNR. Here we show the model for (C_{zig}-N_{line})4-ELD-N_{edge} as an example. (a) Two separate ZGNR and BNNR segments are formed, (b) nitrogen atoms are deposited at the grain boundary of ZGNR and ZBNNR and (c) a 4-ELD is formed. (d) A zoomed in view of the 4-ELD. (e) The constituents of a 4-ELD; a zigzag and a linear chain.

the four atoms that are directly bonded to X_{LD} are named as Y_{ad} (e.g. C_{ad} and N_{ad} in Fig. 2.9(d)).

Following the above nomenclatures, one can consider eight LD-ZBNCNRs as the initial geometries for the BOMD simulations. As shown in Fig. 2.10, these 8 NRs are clustered into two types: (1) 4-ELDs composed of mixed atoms of C and B/N/B-N atoms i.e. Fig. 2.10 (a-d) and (2) 4-ELDs composed of only C or only B-N atoms i.e. Fig. 2.10 (e-h). Let's first consider the geometries in type-1.

To begin with, we study (BN_{zig}-C_{line})4-ELD-N_{edge} and (BN_{zig}-C_{line})4-ELD-B_{edge} where C atoms are additionally deposited at the grain boundary (Fig. 2.10 (a,b)). Remarkably, we find that these two LD-ZBNCNRs get reconstructed in entirely different ways. (BN_{zig}-C_{line})4-ELD-N_{edge} reconstructs to a planar 5-5-8 ELD (see Fig. 2.11 (a,b)), while (BN_{zig}-C_{line})4-ELD-B_{edge} forms a non-planar 7-4-7 ELD at the heterojunction (see Fig. 2.11 (c-e)). Initially, the atoms at and near the 4-ELD are in highly strained conditions because of the unfavourable four-coordinated B_{LD} and N_{LD} atoms in these two structures. In the case of (BN_{zig}-C_{line})4-ELD-N_{edge}, the B_{LD} atoms preferably become sp^2 hybridized and relax the strain by

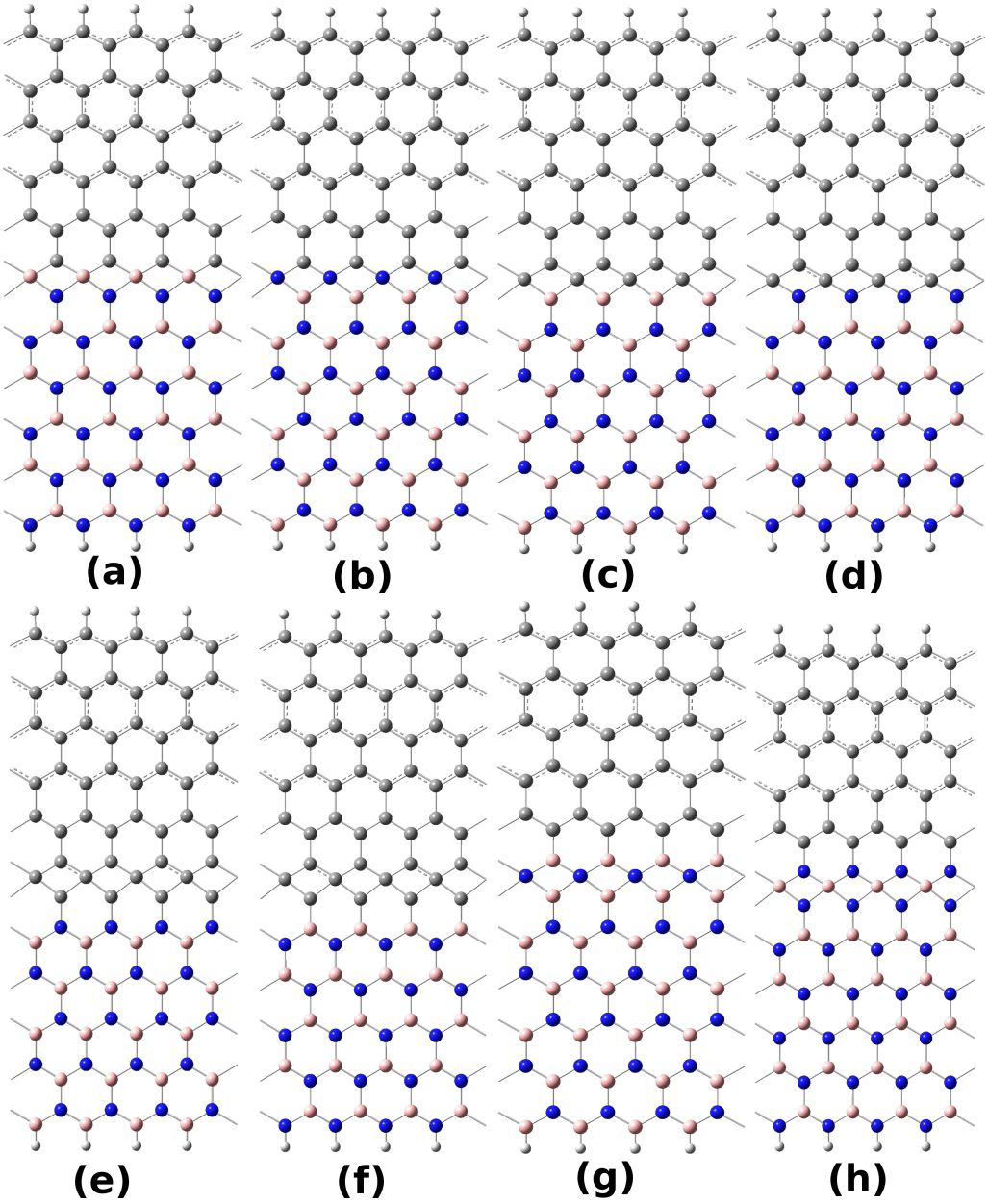

Figure 2.10: Initial structures of (a) (BN_{zig}-C_{line})4-ELD-N_{edge}, (b) (BN_{zig}-C_{line})4-ELD-B_{edge}, (c) (C_{zig}-B_{line})4-ELD-B_{edge}, (d) (C_{zig}-N_{line})4-ELD-N_{edge}, (e) (C_{zig}-C_{line})4-ELD-B_{edge}, (f) (C_{zig}-C_{line})4-ELD-N_{edge}, (g) (BN_{zig}-B_{line})4-ELD-B_{edge} and (h) (BN_{zig}-N_{line})4-ELD-N_{edge}.

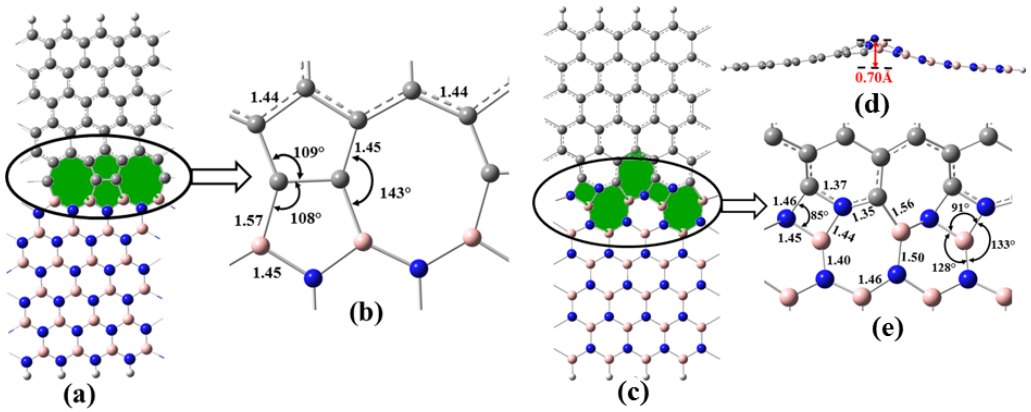

Figure 2.11: (a) The top view of the equilibrated structure of (BN_{zig}-C_{line})4-ELD-N_{edge}; (b) A zoomed in view of the defect region in (BN_{zig}-C_{line})4-ELD-N_{edge}, along with important bond lengths and bond angles. (c) The top view and (d) the side view of the equilibrated structure of (BN_{zig}-C_{line})4-ELD-B_{edge}. The amount of out-of-plane movement of the heterojunction is given. (e) A zoomed in view of the defect region (7-4-7) in (BN_{zig}-C_{line})4-ELD-B_{edge} with important bond lengths and bond angles. The green shaded areas represent the line defects.

forming a 5-5-8 ELD at the heterojunction (see Fig. 2.11(a,b)). Moreover, the reconstruction is facilitated by the favourable charge transfer from C_{ad} to B_{LD} atoms. As discussed earlier, here also electron deficient B_{LD} atom acts as a Lewis acid and accepts electrons from the C_{ad} atom. Mulliken charge population analysis shows that the C_{ad} atom favourably transfers 0.225 e^- to two B_{LD} atoms, making the heteronuclear B_{LD}-C_{ad} bonds stable. The stable dimer formation of C_{ad} atoms also supports this reconstruction. On the other hand, for (BN_{zig}-C_{line})4-ELD-B_{edge}, the four-coordinated square planar N_{LD} is also not energetically stable in the initial geometry. As the higher on-site Coulomb repulsion of N (∼14.46 eV) hampers the charge transfer from C to N, the initial geometry cannot easily reconstruct into any planar geometry. To stabilize the structure, N_{LD} therefore moves out of the plane of the NR to have a less strained sp^3 environment, while forming a 7-4-7 ELD (see Fig. 2.11(c,d)).

For (C_{zig}-B_{line})4-ELD-B_{edge} and (C_{zig}-N_{line})4-ELD-N_{edge} (see Fig. 2.10 (c,d) for initial structures), the GBs get reconstructed by forming distorted tetrahedral 4-ELD (see Fig. 2.12(a-c)) and 7-4-7 ELD, respectively. For (C_{zig}-B_{line})4-ELD-B_{edge}, the reconstruction is also gets influenced by favourable charge transfer from C_{LD}

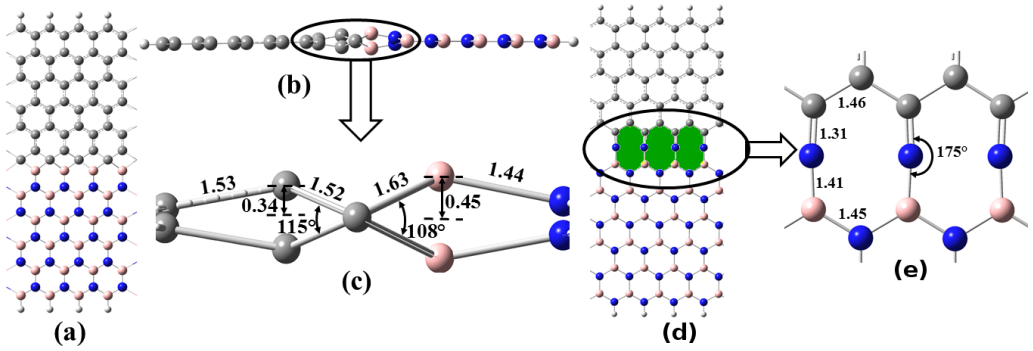

Figure 2.12: (a) The top view and (b) the side view of the equilibrated (C_{zig}-B_{line})4-ELD-B_{edge} structure, and (c) a zoomed in view of the defect region of this structure. (d) The top view of the equilibrated (BN_{zig}-N_{line})4-ELD-N_{edge} structure and (b) a zoomed in view of the defect region of that.

to B_{ad}. Mulliken charge population analysis shows that the C_{LD} atom transfers 0.33 e^- to two B_{ad} atoms. Moreover, the carbon (C_{ad}) and boron (B_{ad}) atoms that are bonded to these C_{LD} atoms move out of the plane, similar to what happens in pure graphene systems [23]. On the other hand, for (C_{zig}-N_{line})4-ELD-N_{edge}, due to the electron rich heterojunction and unfavourable charge transfer between C and N atoms, distorted 7-4-7 ELD forms.

Next, we investigate the structural reconstruction processes in type-2 4-ELDs (i.e. Fig. 2.10 (e-h)), where the 4-ELD is composed of only C/B-N atoms. When the 4-ELD is made up of only C atoms, a 5-5-8 and 7-4-7 ELDs form for (C_{zig}-C_{line})4-ELD-B_{edge} and (C_{zig}-C_{line})4-ELD-N_{edge}. When 4-ELD consists of only B-N atoms i.e. (BN_{zig}-B_{line})4-ELD-B_{edge} and (BN_{zig}-N_{line})4-ELD-N_{edge} GBs get reconstruct into a 7-4-7 ELD and a 8-8-8 ELD (see Fig. 2.12 (d,e)), respectively. These reconstructions also can be understood from the distribution of charges at the heterojunctions as we discussed for other structures. Particularly, for (BN_{zig}-N_{line})4-ELD-N_{edge}, as we found in earlier section, the lone pair-lore pair repulsion restrict the formation of N-N bond formation at the GB, resulting in 8-8-8 ELD.

Note that, calculated formation energies for all these ribbons prove that all of these are energetically stable.

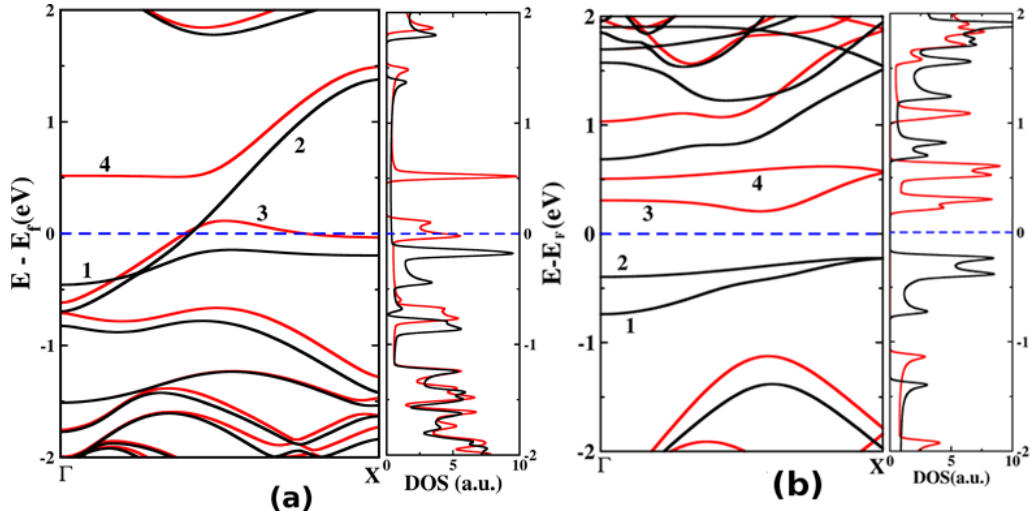

Figure 2.13: The spin polarized band structures and density of states (DOS) plots of (a) (BN_{zig}-C_{line})4-ELD-N_{edge} and (b) (C_{zig}-B_{line})4-ELD-B_{edge}. The black and red solid lines correspond to the majority and minority spin bands/DOS, respectively.

2.3.2.2 Electronic and Magnetic Properties

Here, we discuss the electronic and magnetic properties of the reconstructed LD-ZBNCNRs very briefly. Both (BN_{zig}-C_{line})4-ELD-N_{edge} and (BN_{zig}-C_{line})4-ELD-B_{edge} appear to be spin-polarized metal (see Fig. 2.13 (a) for band structure and density of state of (BN_{zig}-C_{line})4-ELD-N_{edge}). The spin density distribution for these NRs depict that spin moment remains majorly localized at the edge C atoms and couple ferromagnetically. Further, we find that low-energy dispersive bands which remain majorly localized at the carbon edge and defect lines at Γ-point of band structure, induce the metallic nature in these NRs.

Interestingly, as shown in Fig. 2.13 (b), band structure and DOS plot of (C_{zig}-B_{line})4-ELD-B_{edge} demonstrate its spin polarized semiconducting nature. An indirect band gap of 0.88 eV and a direct gap of 1.33 eV open up for the majority and minority spin channels, respectively. Further, the spin density distribution shows that the net magnetic moment of 2 μB is localized at the edge C atoms as well as at the defect region. We also find (C_{zig}-N_{line})4-ELD-N_{edge} as a spin polarized narrow-gap semiconductor.

Among the type-2 NRs, (C_{zig}-C_{line})4-ELD-B_{edge} is a spin-polarized metal whereas

(C_{zig}-C_{line})4-ELD-N_{edge} is a spin-polarized semiconductor. For (BN_{zig}-B_{line})4-ELD-B_{edge}, NR does not have any net magnetic moment in its ground state and appear to be a narrow-gap semiconductor. The moment at the edge cancels with the moment localized at the defect region. Interestingly, (BN_{zig}-N_{line})4-ELD-N_{edge} which consists of a 8-8-8 ELD shows a spin-polarized metallic ground state with a magnetic moment of 0.7 μB.

2.4 Conclusions

In conclusion, we demonstrate the reconstruction processes of ZBNCNRs at the heterojunction. Performing BOMD, we demonstrate the formation of several kinds of ELDs such as 5-5-8, 8-8-8, 7-4-7, 4-ELD etc. upon deposition of adatoms atoms at the grain boundaries. It appears that several factors like (1) mutual orientation of adjacent grains, (2) chemical nature of deposited adatoms, (3) simulation temperature etc. have huge influence on the reconstruction processes. Further, these reconstructed nanoribbons show a wide range of electronic and magnetic characters. We believe that these kinds of line defects may be realized during the growth process of the studied nanoribbons in near future.

Bibliography

[1] A. K. Geim and K. S. Novoselov, Nat. Mater. **6**, 183 (2007).

[2] M. Xu, T. Liang, M. Shi, and H. Chen, Chem. Rev. **113**, 3766 (2013).

[3] S. Dutta, A. K. Manna, and S. K. Pati, Phys. Rev. Lett. **102**, 096601 (2009).

[4] J. Jung, Z. Qiao, Q. Niu, and A. H. MacDonald, Nano Lett. **12**, 2936 (2012).

[5] S. Dutta and S. K. Pati, J. Mater. Chem. **20**, 8207 (2010).

[6] X. Wang, Y. Ouyang, L. Jiao, H. Wang, L. Xie, J. Wu, J. Guo, and H. Dai, Nat. Nanotechnol. **6**, 563 (2011).

[7] F. Banhart, J. Kotakoski, and A. V. Krasheninnikov, ACS Nano **5**, 26 (2010).

[8] J. Lahiri, Y. Lin, P. Bozkurt, I. I. Oleynik, and M. Batzill, Nat. Nanotechnol. **5**, 326 (2010).

[9] A. R. Botello-Méndez, X. Declerck, M. Terrones, H. Terrones, and J.-C. Charlier, Nanoscale **3**, 2868 (2011).

[10] D. Ghosh, P. Parida, and S. K. Pati, J. Mater. Chem. C **2**, 392 (2014).

[11] Y. Li, R.-Q. Zhang, Z. Lin, and M. A. Van Hove, Appl. Phys. Lett. **101**, 253105 (2012).

[12] J. Hutter, M. Iannuzzi, F. Schiffmann, and J. VandeVondele, Wiley Interdisciplinary Reviews: Computational Molecular Science **4**, 15 (2014).

[13] J. VandeVondele, M. Krack, F. Mohamed, M. Parrinello, T. Chassaing, and J. Hutter, Comput. Phys. Commun. **167**, 103 (2005).

[14] J. VandeVondele and J. Hutter, J. Chem. Phys **127**, 114105 (2007).

[15] S. Goedecker, M. Teter, and J. Hutter, Phys. Rev. B **54**, 1703 (1996).

[16] J. P. Perdew, K. Burke, and M. Ernzerhof, Phys. Rev. Lett. **77**, 3865 (1996).

[17] S. Nosé, J. Chem. Phys **81**, 511 (1984).

[18] W. G. Hoover, Phys. Rev. A **31**, 1695 (1985).

[19] J. M. Soler, E. Artacho, J. D. Gale, A. Garc´ia, J. Junquera, P. Ordejón, and D. Sánchez-Portal, J. Phys.: Condens. Matter **14**, 2745 (2002).

[20] H. J. Monkhorst and J. D. Pack, Phys. Rev. B **13**, 5188 (1976).

[21] Z. Liu, L. Ma, G. Shi, W. Zhou, Y. Gong, S. Lei, X. Yang, J. Zhang, J. Yu, K. P. Hackenberg, *et al.*, Nat. Nanotechnol. **8**, 119 (2013).

[22] P. Sutter, R. Cortes, J. Lahiri, and E. Sutter, Nano Lett. **12**, 4869 (2012).

[23] Y. Li, R.-Q. Zhang, Z. Lin, and M. A. Van Hove, Nanoscale **4**, 2580 (2012).

[24] X. Li, X. Wu, X. C. Zeng, and J. Yang, ACS Nano **6**, 4104 (2012).

Chapter 3

Stable Line Defects in Silicene*

3.1 Introduction

Silicene, slightly buckled, hexagonal monolayer sheet of silicon is a newly emerged two-dimensional material. It has already shown its huge possibility to be used in future nanoelectronic devices due to its compatibility with existing silicon-based devices [1, 2]. Confirming the earlier theoretical predictions about the existence of silicene,[3–5] it has been synthesized successfully on the surface of various substrates such as Ag(111), Ir(111), $ZrB_2(0001)$ etc.[6–9]. Further investigations show that, alike graphene, free-standing sheet of it is a massless Dirac fermion containing zero-gap semimetal as well as possesses high Fermi-velocity [4–7, 10]. Moreover, due to the buckling nature, silicene appears to be superior than graphene in many aspects such as enhanced quantum Hall-effect, possibility of band-gap tuning by perpendicular electric field, better surface reactivity etc. [1, 5, 11–13]. Most importantly, recent experiment by Tao *et. al.* successfully fabricated silicene field-effect transistor and found quite appreciable room-temperature mobility of ≈ 100 $cm^2V^{-1}s^{-1}$ [14]. This evidently proves silicene as a potential 2D-material for next-generation electronic devices.

During the synthesis of any 2D-sheet, different kinds of imperfections, such as

*Works reported in this chapter is published in: D. Ghosh, P. Parida and S. K. Pati, Phys. Rev. B, **92**, 195136. Reprinted (adapted) with permission from American Physical Society.

point-defects, vacancies, adatom-adsorption appear inevitably [15, 16]. As demonstrated by several groups, these defects hugely alter the mechanical, electronic, magnetic, transport properties of pure sheets [17–19]. Interestingly, in case of silicene, as Si atoms nucleate at a much faster rate due to their low diffusion barrier on substrates, these defects form more frequently [20–23]. Moreover, these defects modulate some of the above mentioned properties of pristine silicene sheet more drastically than that of well-studied graphene [23]. However, these defective 2D-sheets suffer from poor stability as local structural rearrangements by annealing or chemical passivation can remove the defects easily [24, 25]. Importantly, another kind of structurally robust defects are topological line-defects which remain quite stable against local geometrical rearrangements [26–29]. Different types of line-defects are already found at the grain boundaries (GBs) of graphene, hexagonal boron nitride, molybdenum disulphide etc. where they induce significant modification of several properties of these sheets [30–37]. Nonetheless, creation of topological line-defects in a controlled manner is still a challenging task. Several experimental as well as theoretical reports show that controlled engineering of the GBs during or after the synthesis in these 2D materials eventually leads to insertion of different kinds of line-defects [26–28, 34–36, 38]. Interestingly, during the growth of silicene on Ag(111) using molecular beam epitaxy technique, Chiappe *et.al.* observed several kinds of GBs [20]. This opens up a huge possibility to modify these GBs in a controlled manner to insert different kinds of line-defects.

In the present chapter, we propose easily achievable ways to insert several kinds of line-defects in the free-standing silicene 2D-sheet as well as in its nanoribbons by performing constant temperature Born-Oppenheimer molecular dynamics (BOMD) simulations. We also explore the stability of these defective sheets on the surface of Ag(111). Unreactive Ag(111) is the most widely used substrate to synthesize silicene due to its 6-fold symmetry and low tendency to form Si-Ag alloy [6]. Further, to explore the effects of these line-defects on electronic and magnetic properties of free-standing silicene and its nanoribbons, we perform density functional theory (DFT) based calculations. Note that, as various groups propose different ways such as insertion of buffer layers,[1, 39] utilization of quantum well states of ultrathin metallic substrates [40], to suppress silicene-substrate interactions, we exclude the surface-effects during the electronic structure calculations for our present investigation. It

appears that, depending upon the nature of GBs and adatoms, different kinds of line-defects such as one-dimensional chain of tetragons (4-4-4) or two pentagons and one octagon (5-5-8) or one tetragon and one octagon (4-8) can be embedded in this material. Interestingly, these line-defects largely tune the electronic and magnetic behaviors of the silicene sheet and nanoribbons. In Fig.3.1 , we present three kinds of initial GBs which can arise during the growth of silicene on the substrate. Importantly, to make our present study more specific and compact, we consider that, two crystalline grains meet at GB face-to-face, i.e., without forming any misoriented angle there. These structures have already been considered as the initial geometry in other 2D-sheet materials to perform BOMD simulations for investigating the formation of line defects.[34–36, 38] In the present study, these structures are divided into two types: (1) In Fig. 3.1 (a) and (c), two grains of silicene grow adjacently and their zigzag edges meet at the GB. (2) In Fig. 3.1 (b), armchair edges of grains face each other at GB. To nomenclature the defects in detail, in Fig. 3.1 (a), two pure zigzag edges construct the GB without any mutual translation followed by the deposition of silicon adatoms at the GB. This system is named as ZSi-ZSi. In Fig. 3.1 (c), one zigzag and another Klein edge form the GB without having any additional adatoms and we denote it as ZSi-KSi. Fig. 3.1(b) exhibits the GB where two pure armchair edges come closer without any adatoms at the GB and named as ASi-ASi. During reconstruction, we keep two nearest ELDs separated by 8 zigzag/armchair chains of Si atoms. Systems with larger ELD separation, are also considered to check the impact of defect-defect interaction upon the reconstruction. Moreover, to inhibit the coupling between two extended line defects (ELDs) during the calculation of electronic and magnetic properties, we increase the inter-defect separation to 18 zigzag/armchair chains. To make the discussion well understandable, the Si atoms deposited at the GB (for ZSi-ZSi) and Si atoms nearest to GB are named as Si_{ad} and Si_{near}, respectively (See Fig. 3.1 (a)). The nanoribbons of these sheets are represented as N-M-XNR where N and M denote the number of zigzag/dimer lines on the two sides of ELD and X is the corresponding sheet. The edge atoms of these nanoribbons are named as Si_{edge}.

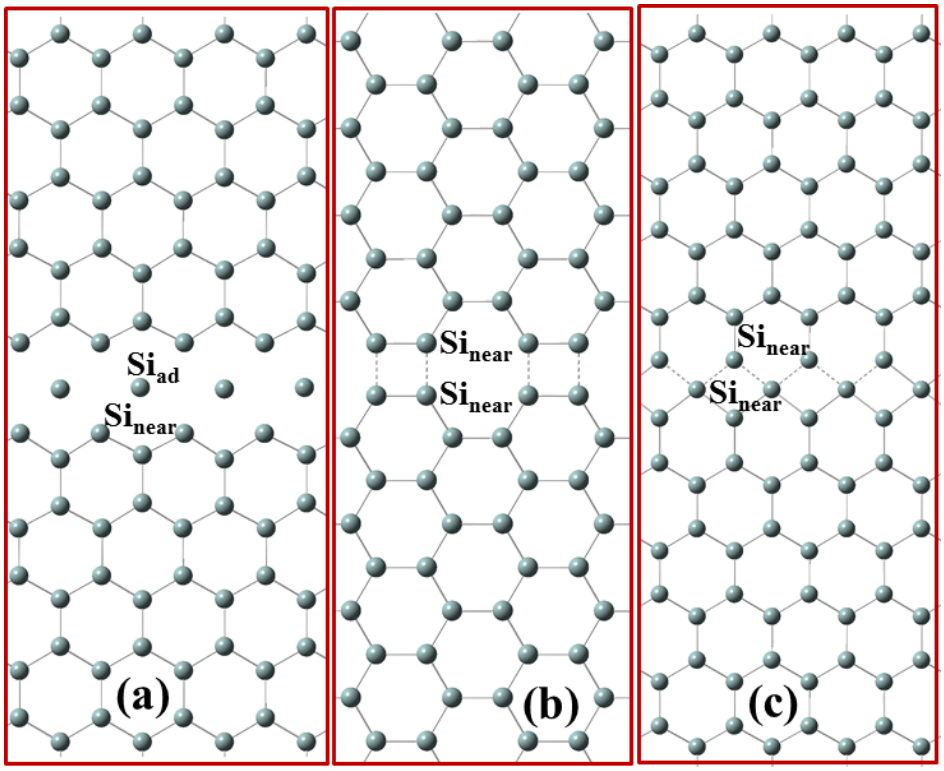

Figure 3.1: Initial structures (i.e. before reconstruction) of grain boundaries of (a) ZSi-ZSi (b) ASi-ASi and (c) ZSi-KSi

3.2 Computational Details

We perform constant temperature BOMD simulations considering canonical ensemble (NVT) as implemented in Vienna ab initio simulation package (VASP) [41]. Perdew-Burke-Ernzerhof (PBE) functional within the generalized gradient approximation (GGA) is used as exchange-correlation functional [42]. The projected augmented-wave (PAW) potential with a plane-wave basis set having a cutoff 400 eV, is used for all BOMD calculations [43, 44]. We use Nose-Hoover thermostat to adjust the temperature during the simulations and a time step of 1 fs is considered to integrate the equation of motion [45, 46]. To avoid the spurious interaction in non-periodic direction, we consider a cell of a×b×15 Å where a and b are lattice constant in periodic directions. For 5-5-XNRs and 10-10-XNRs, cells are considered as a×60×15 Å and a×120×15 Å, respectively. To investigate the stability of these reconstructed sheets on Ag substrate, we consider a rectangular slab of

Ag(111) ((3×7) cell of a rectangular unit cell of 6 Ag atoms), containing 3 atomic-layers. The periodic images are separated from the slab by a vacuum region of 40 Å. Geometry of the Ag slab is relaxed until the acting forces on the atoms become smaller than 0.02 eV/Å. During BOMD computation, to reduce computational cost, we freeze the positions of all Ag atoms, keeping only Si atoms free to move. van der Waals dispersion forces acting between surface and silicene are incorporated by Grimme's method [47]. To investigate electronic and magnetic properties of these equilibrated, reconstructed free-standing systems, we carry out DFT-based calculations using VASP. For these calculations, the plane wave cutoff is considered as 500 eV and k-point mesh for 2D-sheets as 9×7×1 (23 irreducible k-points). Test-calculations with higher plane wave cutoff and denser k-mesh show well convergence of total energy of systems within the considered values of these parameters. The energy threshold is chosen as 10^{-8} eV for all static calculations. For nanoribbons, one-dimensional Brillouin zone is sampled by 31×1×1 automatic-mesh k-points. As pristine and other modified silicene sheets possess considerably strong spin-orbit coupling (SOC) effect, we calculate the electronic property of the present systems by incorporating SOC effect as implemented in VASP package. In VASP, spin-orbit interactions are implemented in the PAW method and evaluated taking into account only the spherical part of the potential inside muffin tins surrounding the nuclei. For valance electrons inside the atomic spheres, it considers scalar relativistic approximation and includes SO interaction by second variational method.

3.3 Results and Discussion

3.3.1 Reconstruction in 2D-sheets

At first, performing BOMD simulation at 300 K and analyzing the resulting trajectory, we explore the reconstruction process of the GB for ZSi-ZSi sheet. As shown in Fig. 3.2, initially, quite mobile Si_{ad} atoms form bonds with Si_{near} and create distorted unstable 8-8-8 ELD at the GB (Fig. 3.2 (b)). However, in process of equilibration, this unstable ELD gets transformed to 5-5-8 ELD where Si_{ad} forms dimer among themselves along with stable covalent bonds with Si_{near} atoms (Fig. 3.2 (c,d)). The variation of potential energy of the system with simulation-time,

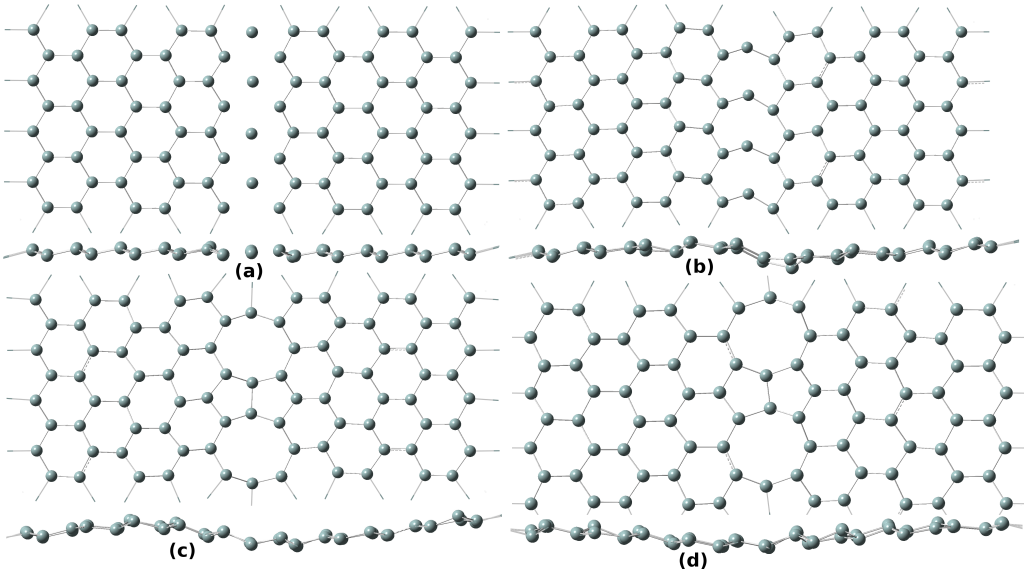

Figure 3.2: Snapshot of top and side view of ZSi-ZSi during BOMD simulations at constant temperature (300K) and constant pressure (1 atm) after (a) 0, (b) 0.25 (c) 0.8 and (d) 5 ps.

shown in Fig. 3.3, evidently indicates that formation of 5-5-8 ELD stabilizes the reconstructed sheet. Fundamentally, strong covalent bond formation among the initially non-bonded Si_{ad} atoms results in this structural stabilization. Though the potential energy of the sheet exhibits little oscillating behaviour, we do not observe any kind of further reconstruction or out-of-plane movement in the system after the formation of 5-5-8 ELD. Further, equilibrium bond lengths and bond angles related to the ELD region predict that alike rest of the system, Si_{ad} and Si_{near} atoms also remain in sp^2-sp^3 hybridized state. Importantly, silicene sheet shows rippling which is well known for 2D structures under finite temperatures [48, 49]. Furthermore, as substrate-temperature for deposition of silicene is generally much higher than 300K, we also perform BOMD simulation at 500 K and 1000 K [6, 7, 20]. It appears that simulation-temperature has a little effect on the step wise formation and the nature of GB in the reconstruction process.

Now, performing a 10 picoseconds long BOMD simulation for ASi-ASi structure at 300 K, GB shows the formation of stable ELD which contains alternative tetragons and octagons (see Fig. 3.4 (a)). This kind of ELD has already been observed in h-BN sheets after exposing it to e-beam irradiation at high temperature [28]. Note that,

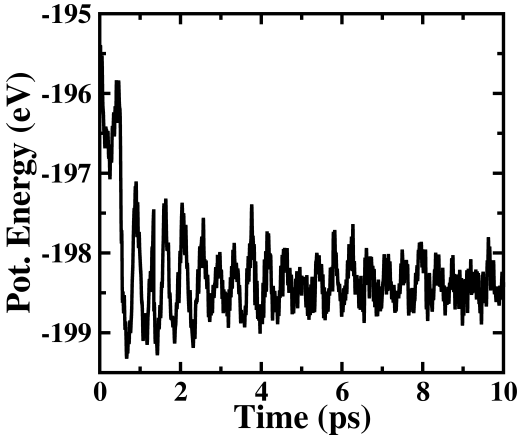

Figure 3.3: Total potential energy during BOMD simulations of reconstruction of ZSi-ZSi GB.

Si_{near} atoms involved in tetragonal rings have equilibrium bond angles of $\approx 90°, 135°$ and 135°, which deviate largely from the $\angle Si-Si-Si$ angle in pristine sheet i.e. $\approx 116°$. As these Si_{near} atoms remain in unfavourable structural situation, 4-8 ELD remain in strained condition. However, interestingly this local strain does not lead to any further structural modifications such as out-of-plane movement of GB at this temperature. Performing BOMD at 500 K and 1000 K, we further confirm that planar 4-8 ELD is very stable and remains unaltered even at these higher temperatures. Note that, Fujimoto *et. al.* also predicted stable 4-8 ring formation in the crystalline silicon under tensile stress [50].

For ZSi-KSi sheet, initial bonds at GB remain unaltered during BOMD simulation at 300 K (Fig. 3.4 (b)). However, during equilibration, the GB and its adjacent rings move out-of-plane significantly ($\approx$ 1 Å). Thus, equilibrated geometry of this sheet shows huge ripple in the structure (Fig. 3.4 (b)). Note that here GB has four-membered ring containing ELD (i.e. 4-4-4 ELD) where Si_{near} of zigzag-edged silicene grain forms four covalent bonds and remain in purely sp^3 hybridized state. Thus, these Si_{near} try to form bond angles $\angle Si-Si-Si \approx 109°$ whereas planarity of silicene sheet oppose that by keeping the angles 120° and 60°. As a result, the GB along with other adjacent rings move out of the plane of the sheet to adjust these two competing factors. Here one should note that, as initially Si_{ad} atoms don't have bonds with Si_{near} in ZSi-ZSi, they can move quite freely in the in-plane and eventually form 5-5-8 ELD. Whereas for ZSi-KSi, all Si_{near} atoms at the GB

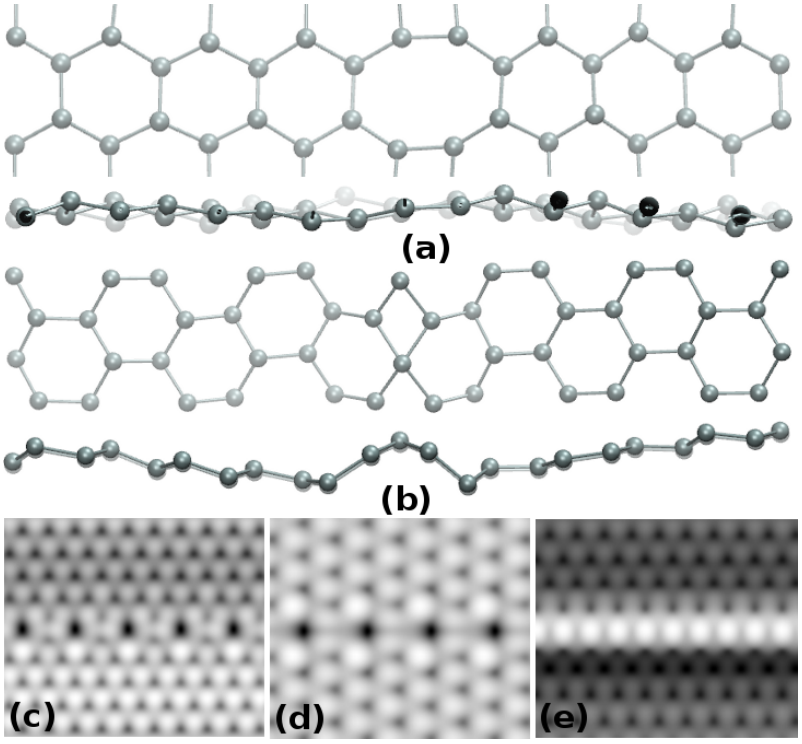

Figure 3.4: The top and side view of equilibrated structure (i.e. after 10 ps) of (a) ASi-ASi and (b)ZSi-KSi. Simulated STM images of (c) 5-5-8 ELD, (d) 4-8 ELD and (e) 4-4-4 ELD are shown. The isosurface is taken at 3.25 Åfrom topmost Si atom in all these sheets.

are covalently bonded during the initial growth process and any in-plane movement must face high energy demanding breakage of covalent bonds. Thus, GB of ZSi-KSi preferentially move out-of-plane and form high rippling in this 2D-sheet. Further, BOMD simulations for all these systems with different ELD-ELD separations show that defect-defect interaction does not have any major impact over the structural reconstructions.

We also theoretically simulate the scanning tunneling microscopy (STM) images of these ELD containing silicene sheets using Tersoff-Hamann approximation[51]. STM images are considered to be an efficient tool to identify these defects in various 2D-sheets. [20, 28, 52, 53] In Fig. 3.4 (c-e), one can find the STM images of these sheets where the ELD can be identified quite clearly. Note that, as the defect states of these systems stay near to the Fermi level (discussed in later part), ELDs become very prominent in the STM images.

Further, BOMD study at 300K shows that reconstructed ZSi-ZSi sheet on Ag(111) surface becomes structurally distorted after equilibration (see Fig. 3.5 (a,b)). However, most importantly, geometry of 5-5-8 ELD remain almost unaffected in presence of Ag substrate. The average substrate-silicene distance remain $\approx$ 2.3 to 2.8 Åwhich is slightly higher than earlier DFT-based calculation due to finite-temperature effect [6]. Geometries of other ELDs also remain quite unaltered on the Ag(111) surface. As these ELD containing sheets are quite stable on top of Ag(111), we speculate that FET of these materials can be fabricated applying growth-transfer-fabrication technique as demonstrated by Tao *et. al.* [14].

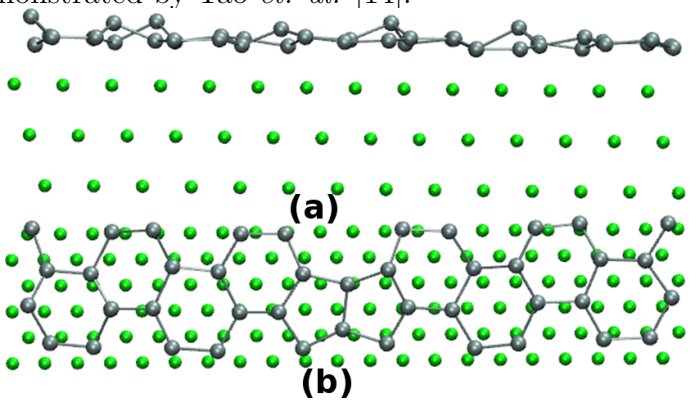

Figure 3.5: The (a) side and (b) top view of equilibrated structure (i.e. after 5 ps) of ZSi-ZSi on the surface of Ag(111). Green spheres represent Ag atoms.

We also investigate the reconstruction process of all these GBs when they appear at the middle of silicene nanoribbons. The GBs of these ribbons transform in the identical ways as these get evolved in corresponding 2D-sheet structures. Moreover, varying the width of two parts of these nanoribbons symmetrically as well as asymmetrically, it is evident that the reconstruction processes are completely independent of the absolute and relative width of this nanoribbons.

3.3.2 Electronic and Magnetic Properties in 2D-sheets

Insertion of line defects in graphene and its analogous systems form localized defect-states which result in many exciting phenomena such as spin-polarized electron transport, gate-tunable valley filtration, strain modulated magnetism, formation of 1D-channel of free carriers etc. [31, 35, 36, 54–56]. Thus it would be interesting to explore the electronic and magnetic properties of different ELD embedded silicene and its nanoribbons in search of some emerging technologically important

phenomena. To investigate the band structure of these 2D-sheets (ZSi-ZSi for example in Fig. 3.6 (a)), we consider a rectangular Brillouin zone (BZ) with four high-symmetry k-points as shown in Fig. 3.6 (b). The GB is considered to be periodic along x-axis, i.e. zigzag (armchair) direction for ZSi-ZSi and ZSi-KSi (ASi-ASi) sheets.

We explore the electronic and magnetic nature of 2D-sheets of silicene with 5-5-8 ELD. Note that, due to the rectangular shape of the BZ, the K point of the hexagonal BZ gets folded at $2\pi/3a$ distance away from the Γ point along Γ-X line where spin-degenerate Dirac point in pristine silicene appears. We denote this point as K$''$. From the band structure and density of states (DOS) in Fig. 3.6 (c,d), it becomes evident that, even though all Si atoms are three-fold coordinated in the defective sheet, electronic and magnetic behaviour of it largely deviates from the pristine silicene. Near the Fermi level (FL) (i.e. -0.69 eV to +0.1 eV), the spin-degeneracy of energy-bands (labelled as band 1- band 6) get lifted. The unequal distribution of electrons in these spin-polarized bands result in finite magnetic moment which will be discussed later on. The bands from both the spin-channels i.e. band 2, band 3 and band 5 cross the FL (Fig. 3.6 (c)), demonstrating the prominent spin-polarized metallic nature of the sheet. Moreover, the bands near to the FL are dispersive in nature only along Γ-X and L-Y lines (which are parallel to the direction of GB). Along the line X-L and Y-Γ (which are perpendicular to the GB), these bands remain almost nondispersive. In the presence of 5-5-8 ELD, the hexagonal symmetry of the BZ gets disrupted and consequently the exact Dirac point at K$''$ also disappears. However, similar kind of band dispersion appears at K$''$ but -0.05 eV below the FL (see Fig. 3.6 (c)). Thus, we although find the Dirac-like point at K$''$, the overall dispersion of these bands get hugely modified due to the insertion of ELD.

To find real-space origin of these bands, we analyze the site projected wave function characters and band decomposed charge densities of them at different high-symmetry k-points of the band-structure. First of all, as shown in Fig. 3.7, all the bands near to FL are π bands i.e. contributed by $3p_z$ orbitals of Si atoms. This is quite natural as unlike point defects, the formation of 5-5-8 ELD does not introduce any kind of dangling σ bonds in the structure. At Γ point, all six bands near FL localize over Si_{ad} and Si_{near} atoms (see Fig. 3.7 (a-c)). Thus, as all these bands localize at and near line-defect region, they are considered as defect-states at Γ

point. However, at Γ-X direction i.e. parallel to ELD, these initially localized states start interacting with other $3p_z$ orbitals of neighboring Si atoms and eventually become delocalized over the whole sheet. This delocalization of charges results in large dispersion of these bands along that direction of the BZ. Further, as evident from Fig. 3.7 (a-c), along the X-L direction, band 2/band 5 remain localized at and near the line-defect whereas other four bands remain mostly delocalized over the whole structure.

The density of states (DOS) plot near to the FL shows spin-splitted peaks, indicating breakage of spin-degeneracy in the system (see Fig. 3.6 (d)). Major peak of majority and minority spin channels appear below and above the FL, respectively, demonstrating the net spin-polarization in the ground state of this sheet. Summing up the contributions of Si_{ad} and Si_{near} atoms to the total DOS, we further find that these peaks are mostly localized around the ELD region and have weak coupling with rest of the sheet. Thus, the insertion of 5-5-8 ELD in silicene results in a strongly localized spin-polarized one-dimensional defect channel near to the FL of silicene sheet.

Concentrating on magnetic properties of the sheet, we find a magnetically ordered ground state with a magnetic moment of 0.2 μ_B per unit cell. This magnetic state is lower in energy than the non-magnetic state by 13 meV/unit cell which is much larger compared to the case of graphene [54, 57]. However, the spin-spin interaction in this system is still too weak to maintain magnetic ordering at room-temperature where spin-fluctuation randomizes the direction of spin-moments. This interaction can be increased by various ways, such as, n-type doping through gate-electrode, applying tensile strain *etc*, a subject of our future studies. The spin-density (i.e. $\Delta\rho = \rho_{major}$ - ρ_{minor}) of this sheet as shown in Fig. 3.6 (e), demonstrates a predominant localization of majority spin at the $3p_z$ orbitals of Si_{near} atoms which ferromagnetically couple along each as well as across the sides of Si_{ad} dimer line. One can experimentally detect this local out-of-plane spin-ordering by performing magnetic force microscopy (MFM) measurements which has already been used widely for defective graphene [17]. Now, to obtain a quantitative description, we calculate the magnetic moment distribution around the defect-line. We compute the local magnetic moment (μ_{local}) by defining it as the sum over magnetic moment of equidistant atoms from the core of ELD (i.e. Si_{ad} dimer line) divided by the

number of equidistant Si atoms. In Fig. 3.6 (f), the μ_{local} shows a sharp peak of 0.018 μ_B at $\pm$ 2.12 Å (i.e. nearest-neighbour distance from the defect-core) and then gets reduced sharply in almost symmetric way at both sides of ELD with increase in distance from the defect-core.

Note that, earlier investigations on graphene containing 5-5-8 ELD also manifested prominent ferromagnetic ground state due to spin-localization near ELD line but only under external perturbations like electron doping, tensile strain etc. [54, 57]. Now the question arises, why 5-5-8 ELD at silicene contains intrinsic spin-localization? Here one should consider the difference between graphene and silicene in terms of π-bands which involve p_z orbitals of C or Si atoms. As the extent of delocalization of the π-bonds in silicene are much lesser than that of graphene,[13] electrons in $3p_z$ orbitals of Si_{near} remain more strongly localized than the same in $2p_z$ orbitals of corresponding C atoms. Consequently, this localization of electrons in silicene results in strong electron-electron interaction and spin-split the π-bands near to FL, exhibiting intrinsic magnetic ordering along 5-5-8 ELD in silicene. Fundamentally, the formation of 5-5-8 ELD can be visualized as stitching of zigzag edges of two Si grains by Si_{ad} dimers where either side of ELD shows pseudo-edge-state like behaviour and Si_{near} atoms act as pseudo-edge atoms. And magnetic moments of individual pseudo-edges interact ferromagnetically, giving rise to a spin-polarized metallic ground state. Thus, even though this system does not contain any real edge, electronic and magnetic properties mostly influenced by these pseudo-edge states. Importantly, magnetic properties of these pseudo-edge states are more robust than real-edge states as the bulk silicene protects the pseudo-edge localized magnetic moments from structural reconstruction or contamination. Therefore, without incorporation of any magnetic adatoms or electron/hole doping, we successfully embed stable ferromagnetically ordered one dimensional array of spins just by inserting 5-5-8 ELD at silicene sheet. Silicene sheet, containing this type of spin channel, is very important for future silicon-based spintronics devices.

Concentrating on the 4-8 ELD, the band structure and the DOS plot in Fig. 3.8 (a,b) evidently demonstrate its metallic nature. Though alike 5-5-8 ELD, the line-defect here does not leave any kinds of dangling bonds in the structure, the ground state appears to be a nonmagnetic one. In fact, as mentioned earlier, the formation of 4-8 ELD is face-to-face (i.e. without any mutual angle) attachment

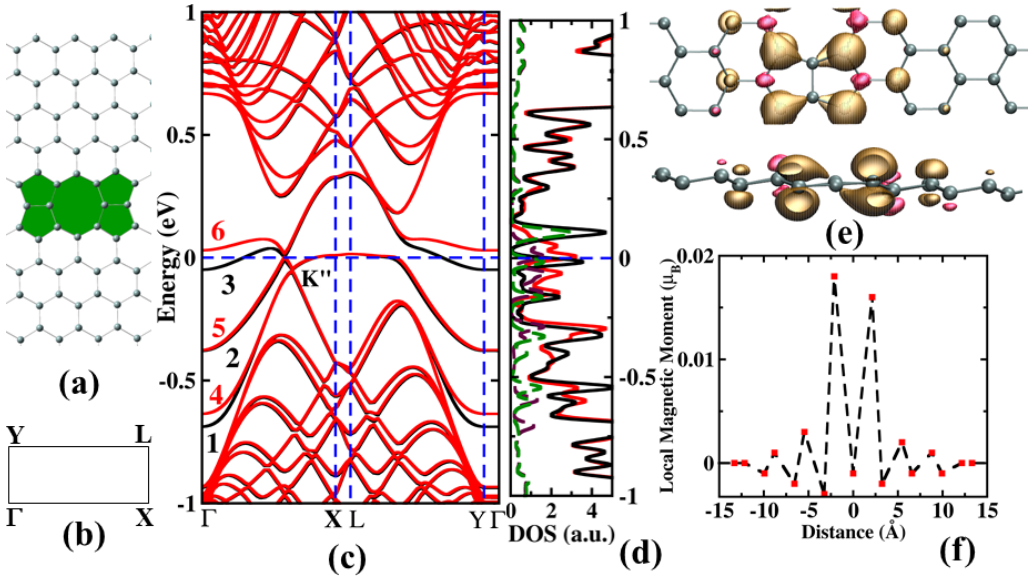

Figure 3.6: (a) ZSi-ZSi structure with 5-5-8 ELD (filled with green colour) and (b) the rectangular BZ with high-symmetry k-points, used here. Spin-polarized (c) band structure and (d) density of state plot for 5-5-8 ELD containing silicene sheet. Black (red) solid lines in (c) and (d) correspond to majority (minority) spin bands and majority (minority) total DOS, respectively. In (d), green (maroon) dashed lines represent the majority (minority) site-projected DOS where contribution up to the second nearest neighbour of Si_{ad} atoms are summed up; (e) Top and side view of spin-densities for ZSi-ZSi where ochre (red) coloured isosurfaces signify majority (minority) spin. Isosurface value is considered as 0.001 e $Å^{-3}$; (f) Local magnetic moment with respect to distance from Si_{ad} dimer atoms. Dimer line of Si_{ad} is considered as origin.

of two armchair edges of silicene sheets. Contrary to the zigzag kind, as armchair edges do not possess any kind of spin-localization, the pseudo-edge induced magnetic ordering remains absent in this 4-8 ELD. [58] Note that, in Fig. 3.8 (a), partially occupied band 1 and band 2 which cross the FL, incorporate metallic behaviour in the sheet. Site-projected wave function character as well as band decomposed charge densities in Fig. 3.8 (c) identify these bands as π-bands which have major contributions from $3p_z$ orbitals. Fig. 3.8 (c) also reveals that both the bands remain delocalized over whole sheet at Γ and Y-point and exhibit high dispersive nature along Γ-X and L-Y directions. However, at X-point, these become localized over the ELD and remain nondispersive along X-L. Alike 5-5-8 ELD, dispersive (localized) nature of these bands appear along Γ-X and L-Y (X-L) as 4-8 ELD is parallel

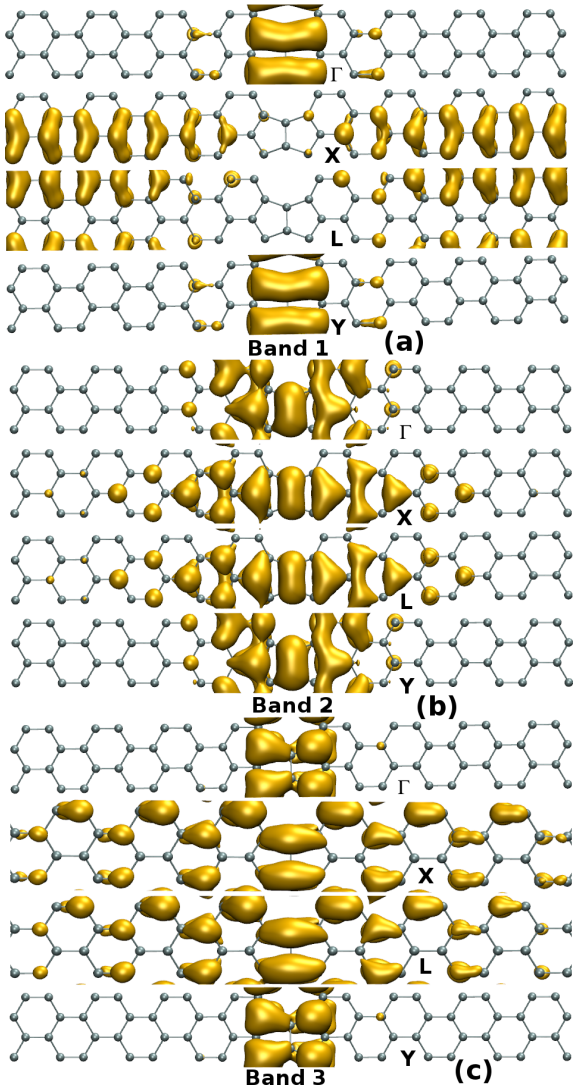

Figure 3.7: Band decomposed charge densities of ZSi-ZSi structure with 5-5-8 ELD at high symmetry k-points for (a) band 1 (b) band 2 and (c) band 3. The isosurface value is considered as 0.001 e $Å^{-3}$ for all charge densities.

(perpendicular) to these directions. In Fig. 3.8 (b), we also plot total DOS (black solid line) and projected DOS at 4-8 ELD sites (red dashed line; i.e. summation of contributions from all Si atoms near to ELD). From Fig. 3.8 (a,b), it is evident that although projected DOS of ELD sites has a little contribution to total DOS near the FL, two peaks at -0.5 and +0.4 eV (denoted by '*' in Fig. 3.8 (b)) appear due to the localization of charge densities at the defect region along X-L direction.

Fig. 3.8 (d,e) shows that formation of 4-4-4 ELD in silicene results in a nonmagnetic metallic state. In band structure plot, band 1 and band 2 cross each other (i.e. K″ and Z points) at the FL along Γ-X and L-Y directions, causing metallic character of the sheet. Analyzing the site projected wave function character and band decomposed charge densities of these bands at Γ and Y point, it is evident that two types of orbitals contribute to band 1, (1) $3p_z$ orbitals of Si atoms which are covalently attached with core of 4-4-4 ELD and (2) sp^3 hybridized orbitals of Si atoms in the defect core (see Fig. 3.8 (f)). Band 2 at Γ and Y remains strongly localized at the defect core where 3s and $3p_z$ orbitals of Si atoms hybridize. Importantly, band 1 and band 2 which remain delocalized and localized in nature, respectively, near to K″ and Z points, exhibit band-crossing at FL. In Fig. 3.8 (e), the DOS and the site-projected DOS over defect region also demonstrates that, states near to the FL of this metallic sheet are majorly localized at the atoms of 4-4-4 ELD.

3.3.3 Electronic and Magnetic Properties in Nanoribbons

As nanoribbons are more relevant than infinite sheets in the field of device applications, we briefly investigate the effects of these line-defects in the electronic and magnetic properties of silicene nanoribbons. Due to the sensitivity of these properties towards the width of nanoribbons, we also vary the size of the system here. Starting with 5-5-8 ELD, note that apart from the pseudo-edges at the ELD region, now nanoribbons have real edges too. And depending upon the magnetic coupling between two real edges as well as among real and pseudo-edges, we can consider different magnetic states such as ferromagnetic coupling among all the edges (FM-1), ferromagnetic between real edges but antiferromagnetic coupling between real and pseudo-edges (FM-2), antiferromagnetic coupling between two real edges (AFM). For 5-5-ZSi-ZSi-NR (Fig. 3.9), first we calculate the relative stability of nonmagnetic (NM), FM-1, FM-2 and AFM states. The magnetically ordered states i.e. FM-1, FM-2 and AFM states are more stable than NM state by 88, 91 and 88 meV/unit cell, respectively. Importantly, FM-2 state gets stabilized over FM-1 and AFM state only by 3 meV/unit cell. With suitable perturbations such as magnetic field, uniaxial pressure etc. one can stabilize any of these magnetic states. Thus, we discuss the properties of all the states in details.

For FM-1 and FM-2 states, majority-spin band in valence band (i.e. band 4) at

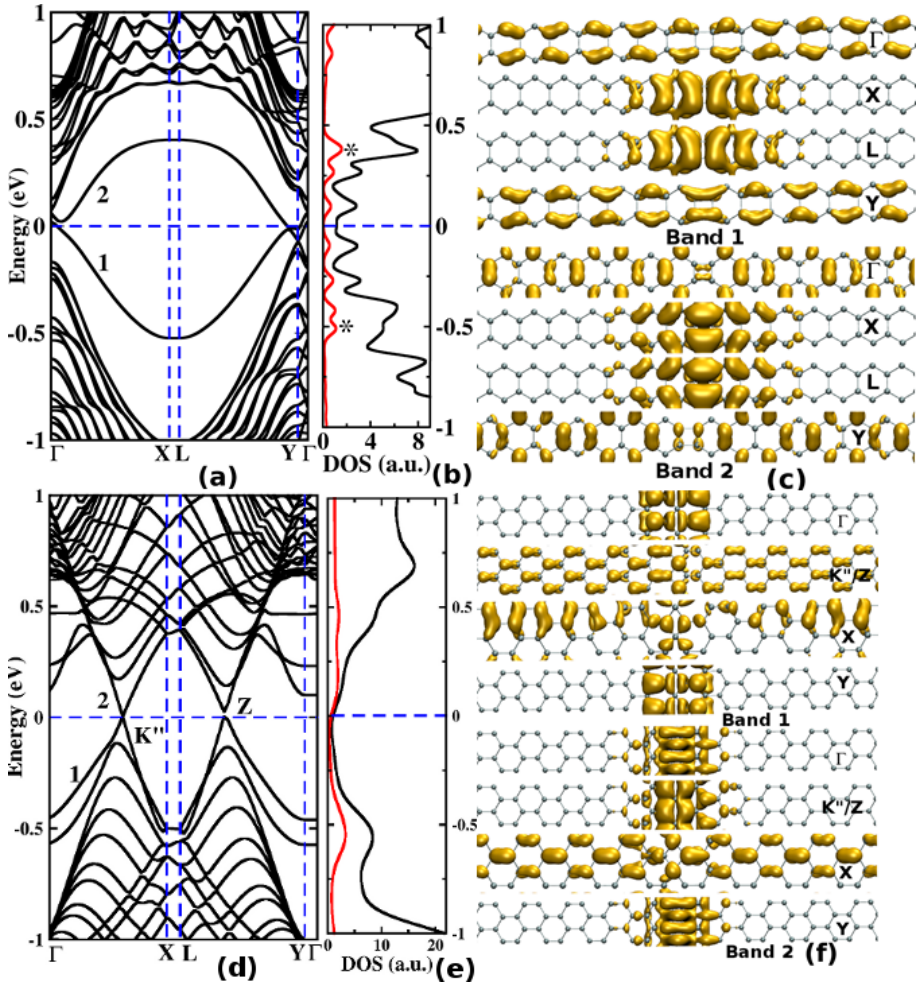

Figure 3.8: (a,d) Band structure and (b,e) total and site projected DOS plot for 4-8 ELD and 4-4-4 ELD containing silicene sheet, respectively. In DOS plot, red dashed lines represent the site-projected DOS where contribution up to the second nearest neighbour of Si_{ad} atoms are summed up. Band decomposed charge densities at high symmetry k-points of band 1 and band 2 for (c) ASi-ASi and (f) ZSi-KSi.

Γ-point has major contributions from $3p_z$ orbitals of Si_{near} atoms, while degenerate band 2 and band 3 originate from zigzag-edges (i.e. Si_{edge}) (see Fig. 3.10). As all these bands are localized, they show quite nondispersive, flat-band character near Γ-point (Fig. 3.9 (a,c)). However, in Γ-X direction, alike 2D sheet, these localized bands interact with $3p_z$ orbitals of neighbouring Si atoms of same plane and become quite delocalized and dispersive (see Fig. 3.9 (a,c) and Fig. 3.10). On the other hand, among minority spin bands, band 5 and band 6 (localized on Si_{ad} and Si_{near} atoms, respectively (see Fig. 3.10) at Γ-point), only band 6 becomes delocalized afterwards as it interacts with other Si atoms in the same plane. Further, band 2 and band 3 (band 7 and 8) which are majority-spin (minority-spin) edge-states of NR, remain almost flat for $0 \leq ka \leq 0.39\pi$. The degeneracy of edge-states near the Γ-point appears due to their equivalent geometrical as well as spin environment. However, this degeneracy gets lifted at $ka > 0.39\pi$, as they interact with other orbitals in different ways. Thus, as evident from Fig. 3.10, at X-point band 2 and band 8 become delocalized over the whole nanoribbon, while other two get localized at the defect region. Now, these spin-polarized bands result in magnetic moment of 1.89 and 0.78 μ_B/unit cell for FM-1 and FM-2 states, respectively. The spin-densities of this nanoribbon also show that majority spin gets localized on the $3p_z$ orbitals of Si_{edge} for both the FM states (Fig.3.9 (b,d)). However, magnetic coupling between Si_{near} and Si_{edge} atoms show a ferromagnetic and antiferromagnetic nature for FM-1 and FM-2 states, respectively.

For AFM state, as shown in Fig. 3.9 (e), bands near the FL disperse quite differently than the FM states. Unlike FM states, at Γ-point, edge states of both spin-channels become nondegenerate as two edges remain populated with opposite spins facing nonequivalent spin environment. As a result, one of the majority-spin edge states becomes the valence band i.e. band 2 whereas other one i.e. band 4 remains well above the FL. Importantly, as none of the majority-spin bands cross the FL, an indirect semiconducting gap of 0.11 eV opens up for this spin-channel. Whereas, for minority-spin, band 6 and band 7, which originate from both defect and edge orbitals, show high dispersive nature and cross the FL. As only minority-spin bands populate the FL, this NR shows intrinsic half-metallic character. Note that the half-metallic gap i.e. the gap between FL and valence band maxima (VBM) of majority-spin channel is 20 meV. Thus, the half-metallic phase needed to be

stabilized further by applying some kinds of perturbations such as magnetic field or strain. Importantly, as the spin-moments of real-edges orient oppositely (see Fig. 3.9 (f), the net magnetic moment becomes ≈ 0 μ_B/unit cell. Note that, alike 2D silicene sheet with 5-5-8 ELD, as all these states show an out-of-plane alignment of magnetic moments, the magnetic configuration of 5-5-ZSi-ZSi-NR can easily be found by performing MFM measurement.[17]

Next, we briefly discuss the electronic and magnetic properties for 10-10-ZSi-ZSi-NR. Firstly, as the spatial separations between two real edges (66.4 Å) and between real and pseudo edges (31 Å) are quite large, spin-spin interactions between these edges become negligible. That consequently results in all the magnetic configurations i.e. FM-1, FM-2 and AFM states, almost degenerate in energy. Electronically, all these ribbons exhibit prominent spin-polarized metallic nature. Importantly, spin density distributions in these configurations remain localized to ELD and edges, similar to narrower ribbons. Note that, half-metallic 5-5-ZSi-ZSi-NR in its AFM state becomes spin-polarized metal as the ribbon width increases. Similar kind of half-metal to metal transition with increment in nanoribbon width has also been found in BN-fused polyacene zigzag nanoribbons [59]. Thus, to use this defective SiNR as intrinsic half-metallic 1D-material, nanoribbons must be of smaller width.

SiNRs with 4-8 ELD and 4-4-4 ELD appear to be nonmagnetic in their different widths. Note that, alike pristine systems,[58] 4-8 ELD containing SiNRs appear to be metallic or semiconducting depending upon the number of Si chains present in two sides of ELD. However, 4-4-4 ELD embedded SiNRs are always metallic irrespective of its width.

3.3.4 Spin-orbit Coupling Effect

To investigate the SOC effect on the electronic properties, we first calculate the band-structure of pristine silicene. For the rectangular unit cell of pristine silicene, the orbital degeneracy gets lifted at K point in presence of SOC, breaking down the linear dispersion of π-bands (formed mainly by $3p_z$ orbitals of Si atoms) near the Fermi level. Consequently, a band-gap of 1.6 meV appears at the K point. Fundamentally, as π and σ ($3p_x$ and $3p_y$) orbitals of silicene directly overlap due to its buckled geometry, σ-π mixing results in a considerable band-gap at K point. This SOC-induced band-structure shows a good agreement with other recent studies

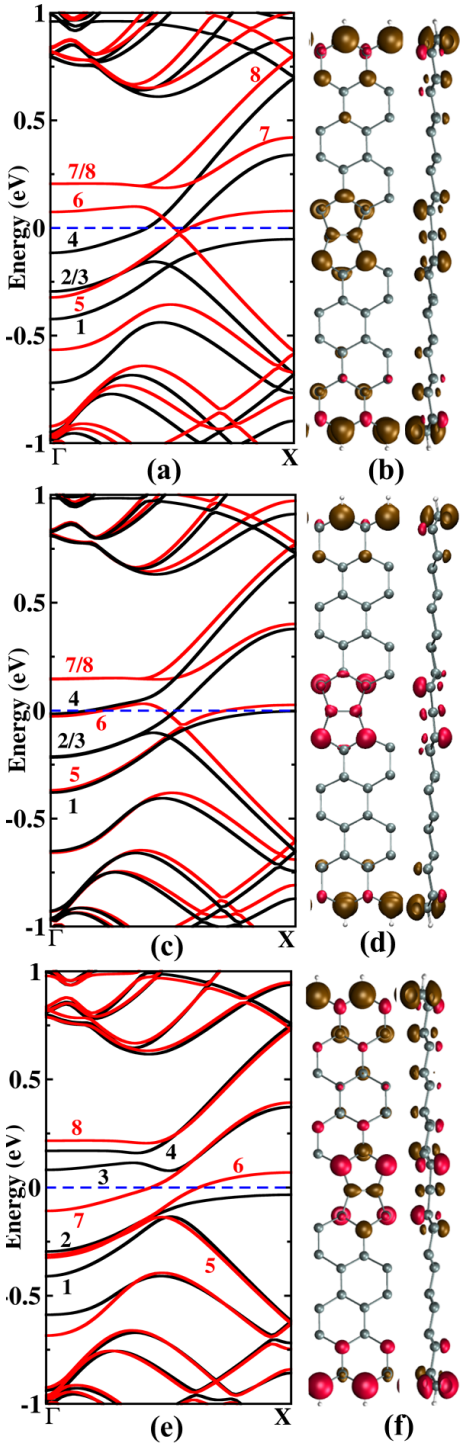

Figure 3.9: Band structures of 5-5-ZSi-ZSi-NR in (a) FM-1 (c) FM-2 and (e) AFM states. Top and side view of spin density plot for these states are shown in (b), (d) and (f), respectively. Ochre and red coloured isosurfaces signify majority and minority spin. Isosurface value is 0.01 e $Å^{-3}$

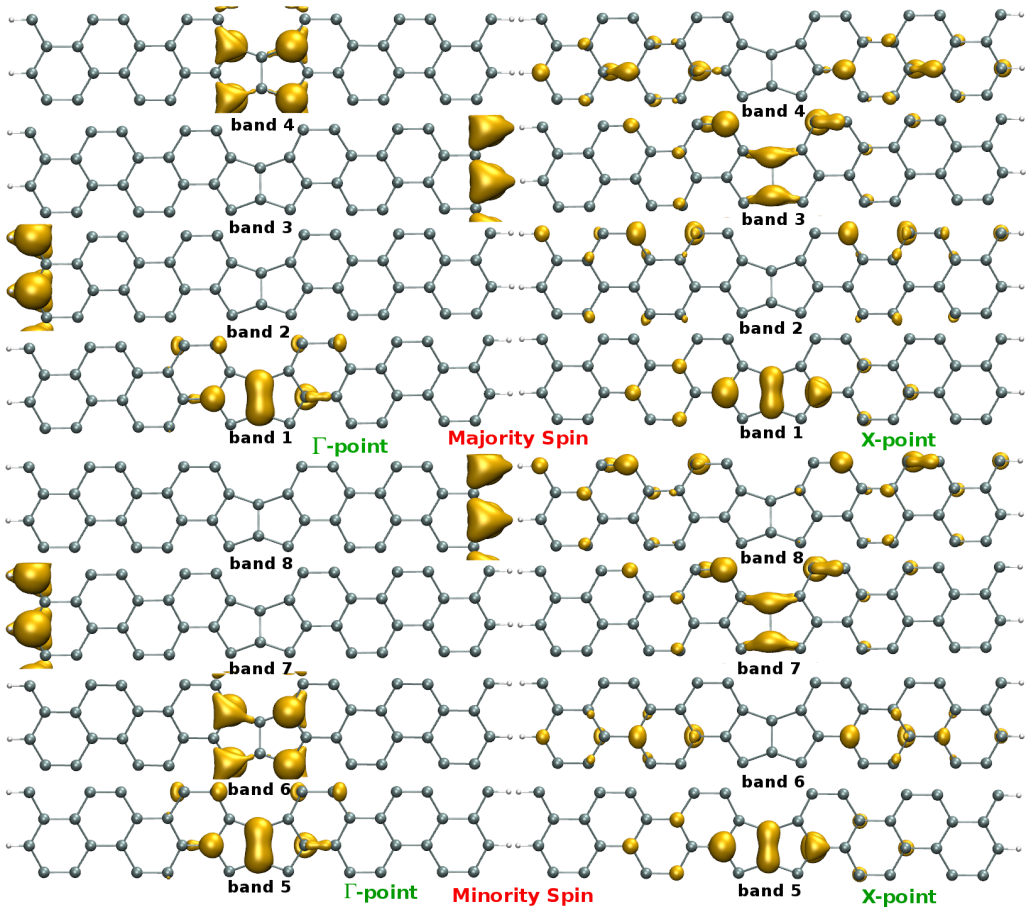

Figure 3.10: Band decomposed charge densities at high-symmetry k-points i.e. Γ and X points of 5-5-ZSi-ZSi-NR in FM-1 and FM-2 states. Isosurface value is 0.0075 e $Å^{-3}$

[5, 60].

Now, we concentrate on line-defect embedded silicene systems where structural symmetry gets destroyed and consequently electronic properties deviates a lot from the pristine case due to the appearance of defect-bands near the Fermi level. In the following part, we discuss the effect of SOC on the defect bands for all the systems. Note that, due to computational limitations, we keep two ELDs 8 zigzag/armchair chains apart in 2D-sheets during these calculations. For ZSi-ZSi, i.e. 5-5-8 ELD containing silicene sheet, SOC modifies the band dispersion near the K″ point (see Fig. 3.11 (a)). As shown in Fig. 3.11, near M and K″ points, two bands (with opposite symmetry when SOC was absent, as seen in the Fig. 3.6(c)) show "avoided crossing" effect, resulting in a energy gap of the order 2-8 meV, when SOC is introduced. Analysing the band decomposed charge densities as shown in Fig. 3.11 (b), quantum tunneling among these SOC-splitted bands become evident. We find Rashba-type SOC and p_π-p_π exchange field as the microscopic reasons behind the observed band lifting. Rashba SOC appears due to the broken structural symmetry of defect embedded sheet. Whereas, effective overlap between spin-polarized defect-π-states and bulk π-states produces the exchange field. Similar kind of situations arise for transition metal(TM)-doped 2D-sheets where both Rashba SOC and exchange field appear due to the spin-polarized metal atoms [61–63]. Note that, unlike these TM-doped sheets, as the Fermi level stays in the valence band, SOC does not induce band-gap for the present system.

For ASi-ASi, defect π-bands show opening of energy gap near to the high-symmetry Y-point due to SOC effect. However, metallic nature as well as band dispersion through other high-symmetry points remain almost unchanged under SOC effect for this sheet. In case of ZSi-KSi, both at K″ and Z points, where defect π-bands cross each other, energy gaps appear due to SOC. As in this sheet, Si atoms at defect-core remain sp^3 hybridized and system shows prominent structural distortion, the σ-π mixing become apparently quite strong in nature. Consequently, the band-crossings get removed by the incorporation of SOC.

Including SOC for zigzag nanoribbons of silicene with these three different kind of line-defects, we find that metallic nature of these systems remain unaltered.

So, for the systems under study, SOC introduces "avoided crossing" of bands at certain symmetry points and removes the band-crossing and band-degeneracy of the

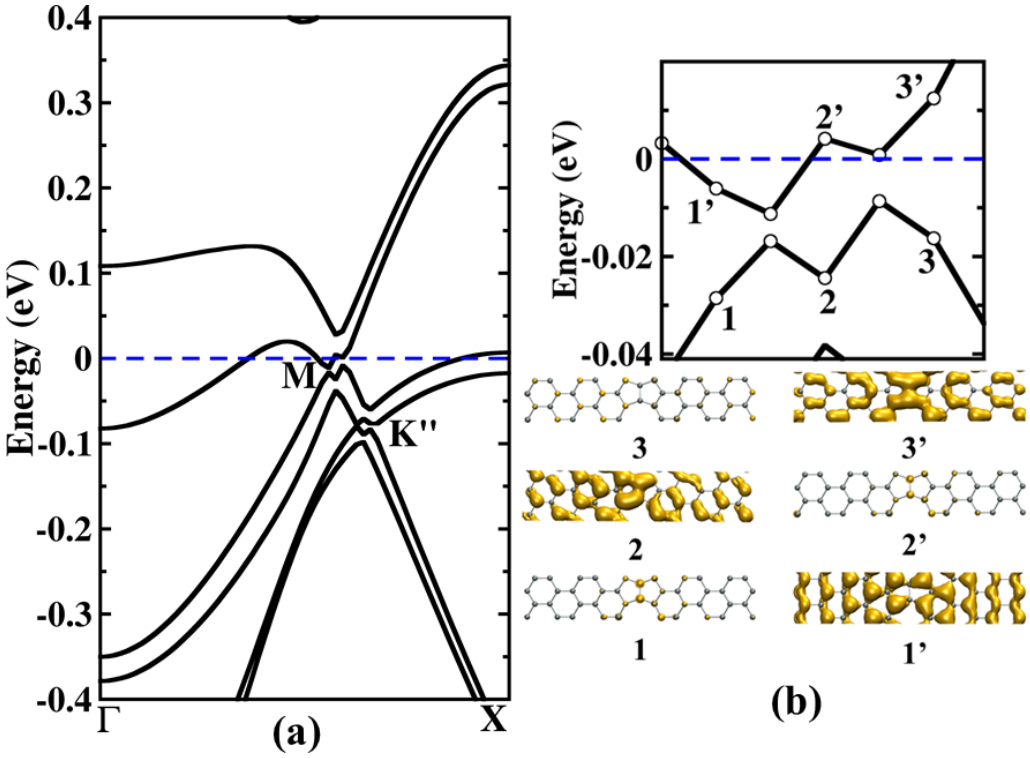

Figure 3.11: (a)Band structure of ZSi-ZSi considering spin-orbit coupling effect. Band dispersion near Fermi level only through Γ-X direction is shown here. Band splitting at M and K″ points are shown;(b)zoomed view of band near M point and band decomposed charge densities of SOC-splitted bands at particular k-points are shown

energy-bands, keeping the overall metallic nature unchanged.

3.4 Conclusions

In conclusion, our room-temperature BOMD studies show that depending upon the nature of GBs in silicene, one can insert different kinds of ELDs such as 5-5-8, 4-8, 4-4-4, in a controlled way. These ELDs are found to be quite stable at much higher temperatures as well as on Ag (111) surface. Most importantly, these ELDs can hugely modify the electronic and magnetic properties of free-standing silicene sheet. Especially, 5-5-8 ELD shows ferromagnetic ordering of spin-moments which are strongly localized at the defect-line. Irrespective of type of ELDs, the Dirac-cone nature of the silicene disappears and these modified 2D-sheets become metallic. Alike 2D-sheets, SiNRs with different kinds of ELDs are also quite stable at room-temperature. Importantly, SiNRs with 5-5-8 ELD exhibit that differently coupled real edges are almost degenerate in energy. Moreover, stabilizing the antiferromagnetic state for nanoribbons of smaller width, one can achieve 100 % spin-polarized ground-state, which is very important for its spintronic applications. Lastly, unlike pristine silicene, the electronic property of all the studied defect-embedded sheets remain unaltered even after considering spin-orbit coupling.

Bibliography

[1] Z. Ni, Q. Liu, K. Tang, J. Zheng, J. Zhou, R. Qin, Z. Gao, D. Yu, and J. Lu, Nano Lett. **12**, 113 (2011).

[2] W.-F. Tsai, C.-Y. Huang, T.-R. Chang, H. Lin, H.-T. Jeng, and A. Bansil, Nature Commun. **4**, 1500 (2013).

[3] G. G. Guzmán-Verri and L. C. Lew Yan Voon, Phys. Rev. B **76**, 075131 (2007).

[4] S. Cahangirov, M. Topsakal, E. Aktürk, H. Şahin, and S. Ciraci, Phys. Rev. Lett. **102**, 236804 (2009).

[5] C.-C. Liu, W. Feng, and Y. Yao, Phys. Rev. Lett. **107**, 076802 (2011).

[6] P. Vogt, P. De Padova, C. Quaresima, J. Avila, E. Frantzeskakis, M. C. Asensio, A. Resta, B. Ealet, and G. Le Lay, Phys. Rev. Lett. **108**, 155501 (2012).

[7] L. Chen, C.-C. Liu, B. Feng, X. He, P. Cheng, Z. Ding, S. Meng, Y. Yao, and K. Wu, Phys. Rev. Lett. **109**, 056804 (2012).

[8] L. Meng, Y. Wang, L. Zhang, S. Du, R. Wu, L. Li, Y. Zhang, G. Li, H. Zhou, W. A. Hofer, and H.-J. Gao, Nano Lett. **13**, 685 (2013).

[9] A. Fleurence, R. Friedlein, T. Ozaki, H. Kawai, Y. Wang, and Y. Yamada-Takamura, Phys. Rev. Lett. **108**, 245501 (2012).

[10] B. Feng, H. Li, C.-C. Liu, T.-N. Shao, P. Cheng, Y. Yao, S. Meng, L. Chen, and K. Wu, ACS Nano **7**, 9049 (2013).

[11] H. Sahin and F. M. Peeters, Phys. Rev. B **87**, 085423 (2013).

[12] X. Lin and J. Ni, Phys. Rev. B **86**, 075440 (2012).

[13] D. Jose and A. Datta, Acc. Chem. Res. **47**, 593 (2013).

[14] L. Tao, E. Cinquanta, D. Chiappe, C. Grazianetti, M. Fanciulli, M. Dubey, A. Molle, and D. Akinwande, Nature Nanotechnol. **10**, 227 (2015).

[15] F. Banhart, J. Kotakoski, and A. V. Krasheninnikov, ACS Nano **5**, 26 (2010).

[16] K. T. Chan, J. B. Neaton, and M. L. Cohen, Phys. Rev. B **77**, 235430 (2008).

[17] J. Červenka, M. Katsnelson, and C. Flipse, Nature Phys. **5**, 840 (2009).

[18] R. Nair, M. Sepioni, I.-L. Tsai, O. Lehtinen, J. Keinonen, A. Krasheninnikov, T. Thomson, A. Geim, and I. Grigorieva, Nature Phys. **8**, 199 (2012).

[19] F. Hao, D. Fang, and Z. Xu, Appl. Phys. Lett. **99**, 041901 (2011).

[20] D. Chiappe, C. Grazianetti, G. Tallarida, M. Fanciulli, and A. Molle, Adv. Mater. **24**, 5088 (2012).

[21] H. Shu, D. Cao, P. Liang, X. Wang, X. Chen, and W. Lu, Phys. Chem. Chem. Phys. **16**, 304 (2014).

[22] H. Sahin, J. Sivek, S. Li, B. Partoens, and F. M. Peeters, Phys. Rev. B **88**, 045434 (2013).

[23] J. Gao, J. Zhang, H. Liu, Q. Zhang, and J. Zhao, Nanoscale **5**, 9785 (2013).

[24] X. Miao, S. Tongay, and A. F. Hebard, Carbon **50**, 1614 (2012).

[25] L. Wang, X. Zhang, H. L. Chan, F. Yan, and F. Ding, J. Am. Chem. Soc **135**, 4476 (2013).

[26] P. Y. Huang, C. S. Ruiz-Vargas, A. M. van der Zande, W. S. Whitney, and e. a. Levendorf, Nature **469**, 389 (2011).

[27] J. Lahiri, Y. Lin, P. Bozkurt, I. I. Oleynik, and M. Batzill, Nature Nanotechnol. **5**, 326 (2010).

[28] O. Cretu, Y.-C. Lin, and K. Suenaga, Nano Lett. **14**, 1064 (2014).

[29] S. Najmaei, Z. Liu, W. Zhou, X. Zou, G. Shi, S. Lei, B. I. Yakobson, J.-C. Idrobo, P. M. Ajayan, and J. Lou, Nat. Mater. **12**, 754 (2013).

[30] O. V. Yazyev and S. G. Louie, Phys. Rev. B **81**, 195420 (2010).

[31] O. V. Yazyev and S. G. Louie, Nat. Mater. **9**, 806 (2010).

[32] Z. Song, V. Artyukhov, J. Wu, B. I. Yakobson, and Z. Xu, ACS Nano **9**, 401 (2015).

[33] Y. Liu, X. Zou, and B. I. Yakobson, ACS Nano **6**, 7053 (2012).

[34] X. Li, X. Wu, X. C. Zeng, and J. Yang, ACS Nano **6**, 4104 (2012).

[35] D. Ghosh, P. Parida, and S. K. Pati, J. Phys. Chem. C **118**, 14670 (2014).

[36] D. Ghosh, P. Parida, and S. K. Pati, J. Mater. Chem. C **2**, 392 (2014).

[37] A. N. Enyashin, M. Bar-Sadan, L. Houben, and G. Seifert, J. Phys. Chem. C **117**, 10842 (2013).

[38] Y. Li, R.-Q. Zhang, Z. Lin, and M. A. Van Hove, Nanoscale **4**, 2580 (2012).

[39] H. Liu, J. Gao, and J. Zhao, J. Phys. Chem. C **117**, 10353 (2013).

[40] A. Podsiadły-Paszkowska and M. Krawiec, Phys. Rev. B **92**, 165411 (2015).

[41] G. Kresse and J. Hafner, Phys. Rev. B **47**, 558 (1993).

[42] J. P. Perdew, K. Burke, and M. Ernzerhof, Phys. Rev. Lett. **77**, 3865 (1996).

[43] P. E. Blöchl, Phys. Rev. B **50**, 17953 (1994).

[44] G. Kresse and D. Joubert, Phys. Rev. B **59**, 1758 (1999).

[45] S. Nosé, J. Chem. Phys. **81**, 511 (1984).

[46] W. G. Hoover, Phys. Rev. A **31**, 1695 (1985).

[47] S. Grimme, J. Comput. Chem **27**, 1787 (2006).

[48] A. Fasolino, J. Los, and M. I. Katsnelson, Nat. Mater. **6**, 858 (2007).

[49] J. Brivio, D. T. Alexander, and A. Kis, Nano Lett. **11**, 5148 (2011).

[50] Y. Fujimoto, T. Koretsune, S. Saito, T. Miyake, and A. Oshiyama, New J. Phys. **10**, 083001 (2008).

[51] J. Tersoff and D. Hamann, Phys. Rev. Lett. **50**, 1998 (1983).

[52] D. E. P. Vanpoucke and G. Brocks, Phys. Rev. B **77**, 241308 (2008).

[53] Y. Fujimoto and S. Saito, Phys. Rev. B **84**, 245446 (2011).

[54] L. Kou, C. Tang, W. Guo, and C. Chen, ACS Nano **5**, 1012 (2011).

[55] M. Gibertini and N. Marzari, Nano Lett. **15**, 6229 (2015).

[56] J.-H. Chen, G. Autès, N. Alem, F. Gargiulo, A. Gautam, M. Linck, C. Kisielowski, O. Yazyev, S. Louie, and A. Zettl, Phys. Rev. B **89**, 121407 (2014).

[57] S. S. Alexandre, A. Lúcio, A. C. Neto, and R. Nunes, Nano Lett. **12**, 5097 (2012).

[58] Y. Ding and J. Ni, Appl. Phys. Lett. **95**, 083115 (2009).

[59] A. K. Manna and S. K. Pati, Journal of Materials Chemistry C **1**, 3439 (2013).

[60] C.-C. Liu, H. Jiang, and Y. Yao, Phys. Rev. B **84**, 195430 (2011).

[61] Z. Qiao, S. A. Yang, W. Feng, W.-K. Tse, J. Ding, Y. Yao, J. Wang, and Q. Niu, Phys. Rev. B **82**, 161414 (2010).

[62] H. Zhang, C. Lazo, S. Blügel, S. Heinze, and Y. Mokrousov, Phys. Rev. Lett. **108**, 056802 (2012).

[63] X.-L. Zhang, L.-F. Liu, and W.-M. Liu, Sci. Rep. **3**, 1 (2013).

Chapter 4

Transition Metal Embedded Two-Dimensional Graphitic C_3N_4-sheets : A Multifunctional Material*

4.1 Introduction

Nowadays, miniaturization of the size of the devices is the prime focus for most of the electronics related research [1]. Different kinds of magnetic materials are extensively used for these devices. And as has already been realized, a potential option to shrink the device-size is to successfully mimic the characteristics of bulk magnetic materials in nanoscale entities like zero dimensional (0D) molecules and nanoclusters [2, 3], one-dimensional (1D) organic polymers [4], organometallic sandwich complexes and nanowires [5], two dimensional (2D) sheets [6, 7] etc. Fundamentally, uniform spin ordering in these magnetic materials is the prime requirement for their possible usage in memory and spintronics applications [8]. Although experimentalists as well as theoreticians have investigated a large number of nanomaterials with the hope to find a suitable candidate for this purpose, success till date is quite limited [9]. Weak magnetic interactions among the spin-centres in low dimensional materials

*Works reported in this chapter are published in: (a) D. Ghosh, G. Periyasamy, B. Pandey and S. K. Pati, J. Mater. Chem. C, **2**, 7943 - 7951 (2014). Reprinted (adapted) with permission from The Royal Society of Chemistry (RSC), (b) D. Ghosh, G. Periyasamy and S. K. Pati, J. Phys. Chem. C, **118**, 15487 - 15494 (2014). Reprinted (adapted) with permission from American Chemical Society

is the basic drawback to stabilize the magnetic ground-state in these systems.

In recent time, various 2D-sheets have attracted significant attention from the scientific community because of their easy synthesis processes and various surprising properties [10]. The successful isolation of graphene in 2004 can be considered as the beginning of this field [11]. Apart from graphene, other analogous 2D-layered materials, like, hexagonal boron nitride (h-BN), molybdenum disulfide (MoS_2), silicene, and tungsten disulfide (WS_2) also exhibit several extraordinary chemical, electrical, optical, thermal and mechanical properties [10, 12]. Based on these properties, several research groups have already demonstrated practical applications of these 2D-materials in electronic integrated circuits, field effect transistors, supercapacitors, optics, catalysis, bioimaging, toxic gas-trapping etc. [13, 14]. Further, because of the low-dimensionality, these 2D-sheets could also be used as the potential materials for high-performance spintronics devices [15]. Importantly, the ability of controlled modulation of charge carrier density, which is very crucial for electronic as well as photonic applications, has been achieved in these materials [16, 17]. However, the absence of an intrinsic spin center, which is the foremost requirement for spintronics, restricts the application of these materials in this field. Incorporation of 3d transition metals (TMs) on top of these single layered 2D-sheets, are considered as a probable solution of this problem. Here, the monodispersed single TM atoms are used as a source of spin moment. [18, 19]. However, these TM-embedded sheets have a serious limitation regarding their structural stability. It has been found that TMs on top of the layer are quite mobile in ambient condition and form clusters due to strong d-d interactions [20]. To freeze these TMs and achieve their monodispersion, several kinds of point defect (i.e., single, double or multiple vacancies) have been introduced in these 2D sheets [18, 21]. The real-time dynamics of metal trapping on the defect sites of pristine as well as doped graphene have been probed by aberration-corrected transmission electron microscopy [21, 22]. Though incorporation of point defects are one the most reliable ways to obtain a metal-embedded material with well-defined geometry, creating regular vacancies in graphene or h-BN sheets in a controlled way is always experimentally quite challenging. In such condition, it is necessary to find some structurally stable 2D-host materials which can trap TM atoms strongly as well as regularly. In the present chapter, we demonstrate two of such materials, monolayered graphitic carbon nitrides (g-C_3N_4) and its composite with graphene

(C_3N_4@graphene) as the highly desired host 2D-sheets which embed the TMs.

As mentioned in the introduction of this thesis, the polymer of heptazine units forms monolayer of g-C_3N_4, which is most stable structure among all the graphitic carbon nitrides (see Fig. 4.1) [23]. Further, the synthesis and characterization of transition metal-doped (V, Fe, Cu, Zn etc.) g-C_3N_4 in the stacked-layered form have already been reported by several groups [24–26]. These TM embedded g-C_3N_4 systems have shown much improved catalytic activities for various reactions. For example, Chen *et. al.* have shown that Fe containing g-C_3N_4 can catalyse the oxidation of benzene to phenol [26]. In another report, Fe and Zn containing g-C_3N_4, synthesized by Wang *et. al.*, demonstrated more-efficient photocatalytic activity than that of bare g-C_3N_4 [24]. Apart from stacked layers, recent report on formation of ultrathin layer of g-C_3N_4 using a liquid phase exfoliation process and the trapping of various TM atoms in mesoporous g-C_3N_4 strongly encourage one to explore the properties of monolayer of the g-C_3N_4 sheet with TM atoms (TM-g-C_3N_4) embedded in it [27, 28].

Another recently explored and highly reliable way to increase the activity of g-C_3N_4 towards various applications is to form its nanocomposite with graphene (C_3N_4@graphene) [29–31]. Getting stacked with graphene in third dimension via relatively weak van der Waals forces, it forms a stable nanocomposite. This nanocomposite is a narrow-gap semiconductor and already has been explored for several applications, such as optoelectronics, electrocatalysts, photocatalysts, etc [30]. Interestingly, Liu *et. al.* have synthesized Co-embedded C_3N_4@graphene, which demonstrate better electrocatalytic performance in an oxygen reduction reaction [31]. From their study, it is quite clear that Co atoms remain embedded in the g-C_3N_4 cavity uniformly without forming any cluster or oxide. We strongly believe that, following the same procedure, one can easily deposit other TMs uniformly in the g-C_3N_4, stacked over graphene layer (TM-C_3N_4@graphene).

As these monolayers and their nanocomposites with graphene possess regular spin ordering, the most essential requirement for memory and spintronics applications, one should investigate their electronic and magnetic properties thoroughly. With this, in the present chapter, using density functional theoretical calculations and Monte Carlo simulations, we have systematically demonstrated structural, electronic, and magnetic properties of TM-g-C_3N_4 and TM-C_3N_4@graphene where TMs

are 3d TMs, except Sc and Ti (i.e., V, Cr, Mn, Fe, Co, Ni, Cu, and Zn). Depending upon the system, these sheets exhibit a wide range of magnetic ground state from nonmagnetic to strongly ferromagnetic. Apart from exciting magnetic properties, the graphene layer of TM-C_3N_4@graphene composites shows considerable ($\sim$10 times) enhancement in charge carrier density due to its n-doping. Further, exploring optical absorption spectra, we find several low-energy peaks which clearly demonstrate improved visible light response of these layered materials.

4.2 Computational Details

We perform spin-polarized density functional theory (DFT) based simulation as implemented in the Vienna Ab initio Simulation Package (VASP) for the present study [32]. For exchange-correlation, we use the Perdew-Burke-Ernzerhof (PBE) functional within the Generalized Gradient Approximation (GGA) [33]. As it is well-known that only the GGA functional cannot accurately describe partially filled d-orbital containing systems, we use the well implemented GGA+U method [34, 35]. In this method, localized d-orbitals are taken care with Coulomb and exchange corrections, whereas s- and p-orbitals are described by only the GGA functional. We consider correlation energy (U) as 4 eV and exchange energy (J) as 1 eV, which are well testified by several other studies focused on 3d transition metal-based organometallic complexes [19, 36]. We use the projected augmented wave (PAW) method with a plane wave basis set with a cutoff energy of 400 eV for all systems [37, 38]. To interpolate the correlation energy, we performed a Vosko-Wilk-Nusir modification for the spin polarized calculations [39]. As all the systems are 2D-sheets, we avoid the spurious interaction in nonperiodic directions (i.e., z direction here) by creating a vacuum of 20 Å in the z direction. To find the magnetic ground state of these systems, we consider a (2 $\times$ 2) supercell. For periodic calculations, Monkhorst-Pack[40] 7 $\times$ 7 $\times$ 1 and 5 $\times$ 5 $\times$ 1 k-point grids (total number of k-points are 25 and 13, respectively) are used to sample the 2D Brillouin zone of the unit cell and the (2 $\times$ 2) supercell of these sheets (i.e. TM-g-C_3N_4 as well as TM-C_3N_4@graphene), respectively. We carry out geometry optimizations without imposing any kind of symmetry constraints, and interatomic forces are relaxed up to

0.01 eV/Å. For TM-C_3N_4@graphene composite, we include the van der Waals interaction between TM-C_3N_4 and graphene by applying DFT-D2 method as suggested by Grimme and well implemented in VASP [41]. We further perform Heisenberg model based Monte Carlo (MC) simulation by taking a supercell of 80 × 80 (100 × 100) sites of TM-g-C_3N_4 (TM-C_3N_4@graphene) and involving 4×10^6 MC steps to study magnetic ordering at finite temperature. For optical property calculation, we calculate the frequency-dependent dielectric matrix using the GGA functional and a k-mesh of 13 × 13 × 1 to sample the Brillouin zone finely [42]. Previous study has proved that the GGA functional can reproduce the experimental spectra of these kinds of materials efficiently [23]. The imaginary part of the dielectric matrix is used further to calculate absorption spectra. To determine the structural stability of TM-g-C_3N_4, the binding energies were calculated using the following formula,

$$E_{bind} = E_{sheet-TM} - (E_{sheet} + E_{TM}) \tag{4.1}$$

and for TM-C_3N_4@graphene,

$$E_{bind} = E_{TM-C_3N_4@grap} - (E_{g-C_3N_4} + E_{graphene} + E_{TM}) \tag{4.2}$$

where $E_{sheet-TM}$, E_{sheet} and E_{TM} are the energies of TM-g-C_3N_4, bare g-C_3N_4 and chemical potential of the TM atom in its bulk phase, respectively. In the same way, $E_{TM-C_3N_4@grap}$, $E_{g-C_3N_4}$ and $E_{graphene}$ represent the energies of TM-C_3N_4@graphene, bare g-C_3N_4 and graphene, respectively.

Further, for TM-C_3N_4@graphene, we calculate the adhesion energy as follows,

$$E_{adhesion} = E_{TM-C_3N_4@grap} - (E_{TM-g-C_3N_4} + E_{graphene}) \tag{4.3}$$

4.3 Results and Discussion

In this section, first we discuss about the properties of TM-C_3N_4@graphene in details and then about TM-g-C_3N_4 in brief.

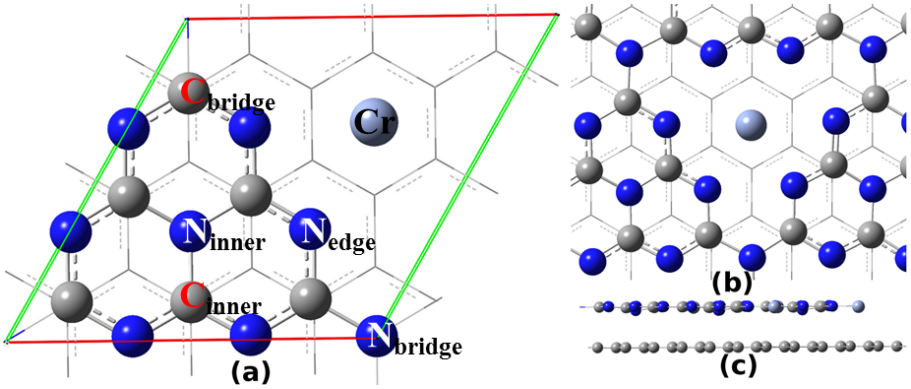

Figure 4.1: Atomic configurations of Cr-C_3N_4@graphene: (a) unit cell, (b) zoomed top view of electron-rich cavity where TM atoms get trapped, and (c) side view of Cr-C_3N_4@graphene sheet. Blue, gray, and light blue balls are nitrogen, carbon, and Cr atoms, respectively. Graphene sheet has been shown in wireframe mode for clarity.

4.3.1 Electronic, Magnetic and Optical Properties of TM-C_3N_4@graphene

4.3.1.1 Structures

To compute the geometric and electronic properties of metal free C_3N_4@graphene nanocomposites, we keep the 1 × 1 g-C_3N_4 unit on top of the 3 × 3 supercell of graphene, where the lattice mismatch between two layers is very small (i.e., 1.5%). Importantly, as shown in Fig. 4.1, the adhesion of g-C_3N_4 on top of graphene removes its intrinsic structural buckling and makes it planar to have better π-π stacking between two layers. The interlayer distance between these two planar sheets is ∼3.04 Å, which compares well with previous reports [43]. Further, the presence of g-C_3N_4 sheet over graphene breaks the potential periodicity of graphene, leading to its band-gap opening at the Γ-point (graphene fold K-point).

As can be seen from Fig. 4.1, the deposition of TM atoms at the cavity formed by N_{edge} atoms of C_3N_4@graphene generates a consistent distribution of these TMs (Cr atoms for example) over this nanocomposite sheet. Interestingly, we evidently find that the structural reformation of the nanocomposite due to the incorporation of TM in the N_{edge} cavity is quite negligible. The stacked graphene sheet remains almost unaltered, whereas the N_{inner} atoms (see Fig. 4.1 (a)) of g-C_3N_4 stay out

of plane slightly (by ∼0.2-0.5 Å depending upon the TM) for all sheets. Furthermore, thorough investigation exhibit that V, Mn, Cu, and Zn atoms stay in exactly the middle of the cavity, whereas others remain in a slightly distorted hexagonal field. Under a hexagonal crystal field environment, 2p-orbitals of N_{edge} atoms of g-C_3N_4 act as interacting ligand orbitals, which breaks the degeneracy of 3d-orbitals of the TM atom and splits them into four energy states, as can be seen from Fig. 4.2 (a). Quite obviously, as can also be found from pDOS of 3d-orbitals of Cr of Cr-C_3N_4@graphene in Fig. 4.2 (b), three d-bands, which are out of the xy plane (considering xy plane as composite's plane), become much stabilized (∼1 eV) than the other two d-bands, i.e.,$d_{x^2-y^2}$ and d_{xy}, which are in the xy plane and face the $2p_x/2p_y$-orbitals of N_{edge} directly. Now, for V^{2+}, three 3d-electrons singly occupy these lowest three d-bands, leaving $d_{x^2-y^2}$ and d_{xy} empty. However, for Mn^{2+} and Cu^{1+}/Zn^{2+}, all the d-orbitals are filled up with single and a pair of electrons, respectively. Thus, both directly interacting d-orbitals (i.e., $d_{x^2-y^2}$ and d_{xy}) of these TM atoms face the hexagonal crystal field with symmetrical occupancy of zero electrons (for V), one electron (for Mn), or two electrons (for Cu, Zn). That in turn results in incorporation of these TMs at the almost exact center of the cavity. Other TMs, i.e., Cr, Fe, Co, and Ni, have unsymmetrical fillings of the d-orbitals which cause the breakage of the perfect hexagonal symmetry around them. Further, optimized TM-N_{edge} distances show that these metal atoms stay nearer to two N_{edge} atoms and relatively far from the other four N_{edge}. Like the situation, usually appears in Jahn-Teller distortion, the doubly occupied d-orbitals always circumvent direct interaction with p-orbitals of N_{edge} and gain stabilization energy by destroying the above-mentioned symmetry. However, we should note that the overall structures of TM-C_3N_4@graphene remain almost planar with nearly the same interlayer distance as it is for g-C_3N_4@graphene. The negative binding energies as tabulated as in Table 4.1 proves the structural stability of these nanocomposites. Moreover, calculated interface adhesion energies as given in Table 4.1, show that the TM-C_3N_4 layer gets stacked on top of graphene quite strongly.

Table 4.1: Binding energies (E_{bind}) and adhesion energies ($E_{adhesion}$) per unit cell of TM-C_3N_4@graphene, magnetic moment per TM (Mag. Mom.), exchange energies for 2 × 2 supercell ($\triangle E_{ex}$) are tabulated. Considering a unit cell of TM-C_3N_4@graphene, electric field strength inside the nanocomposite(E_{int}), carrier concentration in graphene (ρ), transferred electrons to graphene (e_{trans}) and Fermi level shift ($\triangle E_{fermi}$)due to that are also given.

Metals	V	Cr	Mn	Fe	Co	Ni	Cu	Zn
E_{bind} (eV)	-3.66	-1.99	-2.65	-2.20	-1.92	-1.40	-1.49	-1.20
$E_{adhesion}$ (eV)	-0.22	-0.24	-0.29	-0.23	-0.31	-0.28	-0.29	-0.25
Mag. Mom. (μB)	3	4	5	4	3	1	0	0
$\triangle E_{ex}$(meV)	2	-179	4	-201	-11	-14	0	0
E_{int}(V/nm)	0.57	0.50	0.64	0.63	0.44	0.42	0.43	0.58
ρ ($\times$ 10^{13} cm^{-2})	3.9	3.2	5.0	3.5	3.3	2.6	2.1	3.0
e_{trans} (e^-)	0.18	0.15	0.23	0.16	0.15	0.12	0.10	0.14
$\triangle E_{Fermi}$ (eV)	0.41	0.38	0.51	0.43	0.37	0.33	0.27	0.36

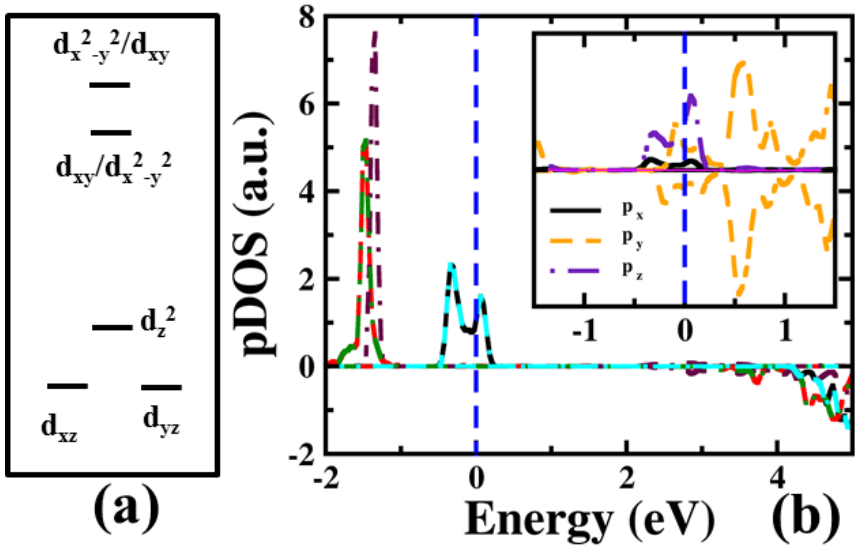

Figure 4.2: (a) The crystal field splitting of TMs in a hexagonal environment (energy is not scaled) and (b) pDOS of d-orbitals on the Cr atom of Cr-C_3N_4@graphene (symbols: solid black, dashed red, dashed dotted maroon, dashed double dotted deep green, and double dashed dotted cyan represent d_{xy}, d_{yz}, d_{z^2}, d_{xz}, and $d_{x^2-y^2}$ orbitals, respectively). In the inset of (b), pDOS of p-orbitals on the N_{edge} of the same structure has been plotted. Note that positive and negative pDOS values correspond to majority and minority spins, respectively.

4.3.1.2 Electronic and Magnetic Properties

Plotting the spin density distribution for all TM embedded nanocomposite sheets (except Cu and Zn), we clearly find that most of the magnetic moments are localized at the metal atom and N_{edge} atoms. Just as an example, we have shown the spin density plot for Fe-C_3N_4@graphene in Fig. 4.3 (a,b). Importantly, adhesion of TM-C_3N_4 on a graphene sheet does not break the spin symmetry of the latter sheet. Here, we can safely exclude Cu- and Zn-C_3N_4@graphene for further discussions about magnetism as these sheets are d^{10} systems and possess a nonmagnetic ground state. Now, we determine the nature of magnetic coupling between two neighboring TM atoms through d-p exchange where electrons of d-orbitals of TM and p-orbitals of N_{edge} from the g-C_3N_4 layer get engaged in magnetic interaction. As mentioned earlier, a 2 $\times$ 2 supercell has been considered for all 2D sheets to determine the properties. The energies of the systems, where TM atoms get coupled ferromagnetically (FM) and antiferromagnetically (AFM), are computed separately to calculate the exchange energy ($\triangle E_{ex} = E_{FM}$ - E_{AFM}). Negative and positive values of $\triangle E_{ex}$ indicate ferromagnetic and antiferromagnetic ground states, respectively. The $\triangle E_{ex}$ and magnetic moment per unit cell for these nanocomposites are tabulated in Table 4.1. Evaluated $\triangle E_{ex}$ energies show that, among all of these TMs, Cr, Fe, Co, and Ni interact magnetically with each other when these atoms get embedded in a C_3N_4@graphene sheet. It can be understood by looking at the pDOS of d-orbitals on the TM atoms of the nanocomposite, as shown in Fig. 4.4. It is well-known that electrons that fill up the spin-polarized bands near the Fermi level only can get involved in magnetic coupling with other ligand bands of the same energy. Thus, the magnetic coupling appears to be quite weak for V- and Mn-based composite sheets as their singly occupied d-orbitals remain well below the Fermi level (see pDOS of these TM in Fig. 4.4). Consequently, these sheets exhibit paramagnetism in their ground state. However, the Fermi levels of other nanocomposites, i.e., Cr, Fe, Co, and Ni embedded C_3N_4@graphene, remain populated by spin-polarized d-orbitals, resulting in an effective magnetic interaction among TMs. Calculated exchange energies evidently show a ferromagnetically coupled ground state for all of them. This ferromagnetic interaction between TMs can be understood with the help of Goodenough-Kanamori-Anderson rules [44]. For systems under study, TM-ligand-TM forms a 180^o angle, and depending upon the interacting 3d-orbitals of TM and

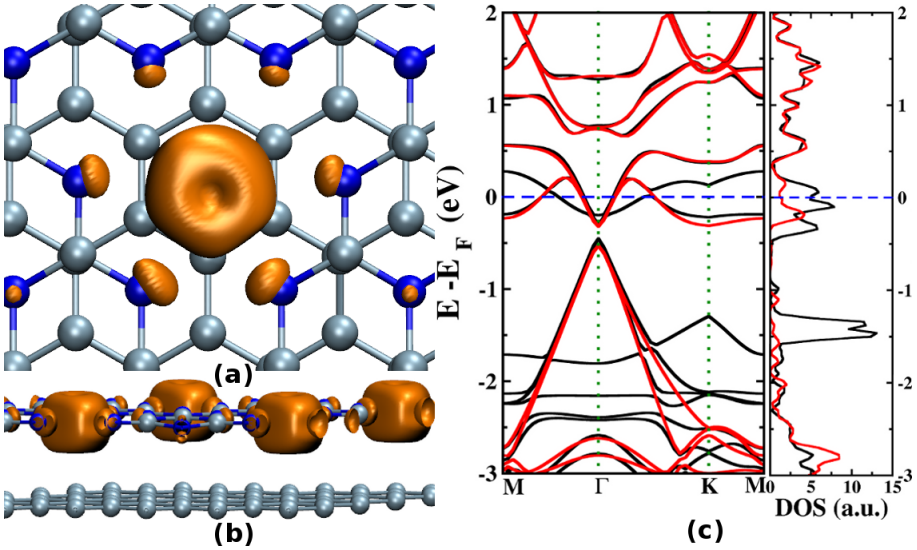

Figure 4.3: (a) Top and (b) side views of spin density of Fe-C_3N_4@graphene with an isosurface of 0.025 e $\AA^{-3}$ where up and down spin densities are represented as orange and yellow (not visible here) colored surfaces, respectively. (c) Calculated spin-resolved band structure and corresponding DOS of Fe-C_3N_4@graphene (Γ(0,0,0), M(1/2,1/2,0), K(2/3,1/3,0) are high-symmetry K-points. (Symbols: black and red solid lines denote majority and minority spin bands, and blue dotted line shows Fermi level).

2p-orbitals of N_{edge}, the magnetic coupling nature can be either ferromagnetic or antiferromagnetic. By analyzing the pDOS of the d-orbitals of Cr and p-orbitals on N_{edge} in Fig. 4.2(b), it is apparent that interacting d-orbitals are a hybrid consisting of majority spin bands of $d_{x^2-y^2}$ and d_{xy}, which overlap with p_z/p_y of the same spin of the ligand, but this results in a total zero effective overlap due to symmetry of orbitals. As a result, Cr-C_3N_4@graphene gives rise to a ferromagnetic ground state as also described in Heitler-London theory [45]. For Fe, the interacting d-orbitals (i.e., near to E_F) are different i.e. d_{xz}/d_{yz} which also results in ferromagnetic d-p exchanges after interacting with ligand p_y orbitals. Here also the effective overlap among these interacting 3d and 2p orbitals is zero due to their spatial arrangement. Further, ferromagnetism in Co and Ni embedded sheets can also be explained considering the same approach. Note that, as the interacting d-orbitals, i.e., minority spin-band of d_{yz}/d_{xz}, just touches the Fermi level, the d-p exchange coupling appears to be quite weak for these two systems (i.e., Co and Ni), This weak interaction in turn results in a smaller exchange energy, as can be seen in Table 4.1.

Quite excitingly, our study predicts that sheets embedded with Cr and Fe atoms have quite high ferromagnetic exchange energies, i.e., -179 and -201 meV per supercell, respectively. These values are well comparable with other already explored 2D magnetic sheets [19, 46]. The large ferromagnetic exchange energy makes these materials highly promising candidates for realizing a high-temperature 2D ferromagnetic system. We come back to this point in later part of our discussions.

Importantly, as these TM deposited g-C_3N_4 sheets get physisorbed on top of graphene, the characteristic Dirac cone of the latter still remains at the Γ-point (i.e., graphene fold K point) but with a finite gap. This kind of phenomenon is quite common for other physisorption-based graphene nanocomposites [47, 48]. Exploring the band structures of TM-C_3N_4@graphene (see Fig. 4.3 (c) for Fe-C_3N_4@graphene as an example) we find the upward shift of the Fermi level in these sheets. This clearly indicates a net electron transfer from TM-g-C_3N_4 to graphene, which is also further evident from Bader charge analysis as well as the electron density difference plot (Fig. 4.5), as discussed in next paragraph. Depending upon the charge transfer, as shown in Table 4.1, the shift of the Fermi level varies in a range of 0.27-0.51 eV for these systems. These transferred electrons partly populate the composite's conduction band, which has a major contribution from p_z-orbitals of carbon atoms of graphene. Partially occupied graphene-based bands as well as bands arising from spin-polarized 3d-orbitals show a dispersive nature and pass through the Fermi level, giving rise to the metallic nature of this organometallic nanocomposite (see Fig. 4.3 (c) for example). Furthermore, pDOSs of d-orbitals of TM atoms also demonstrate the proper origin of local magnetic moments of these sheets. For V and Mn, as shown in Fig. 4.4 (a,b), the majority spin bands arising from d-electrons remain as highly localized with non-dispersive singly occupied states, staying far below the Fermi level. This results in a total magnetic moment of 3 and 5 μB/unit cell for V- and Mn-embedded sheets, respectively. For other TM included sheets (i.e., Cr, Fe, Co, and Ni), although the metal atoms remain in a slightly distorted hexagonal crystal field environment, d-bands of these TM atoms split in the same manner as for V/Mn, i.e., 2 (d_{xz}, d_{yz}) + 1 (d_{z^2}) + 1 ($d_{xy}/d_{x^2-y^2}$) + 1 ($d_{x^2-y^2}/d_{xy}$) in the increasing energy order. For Cr atoms, as can be seen in Fig. 4.2 (b), majority spin bands from higher energetic d_{xy} and $d_{x^2-y^2}$ orbitals also get populated and give rise to a magnetic moment of 4 μB/unit cell. Because of the increase of d-electrons in

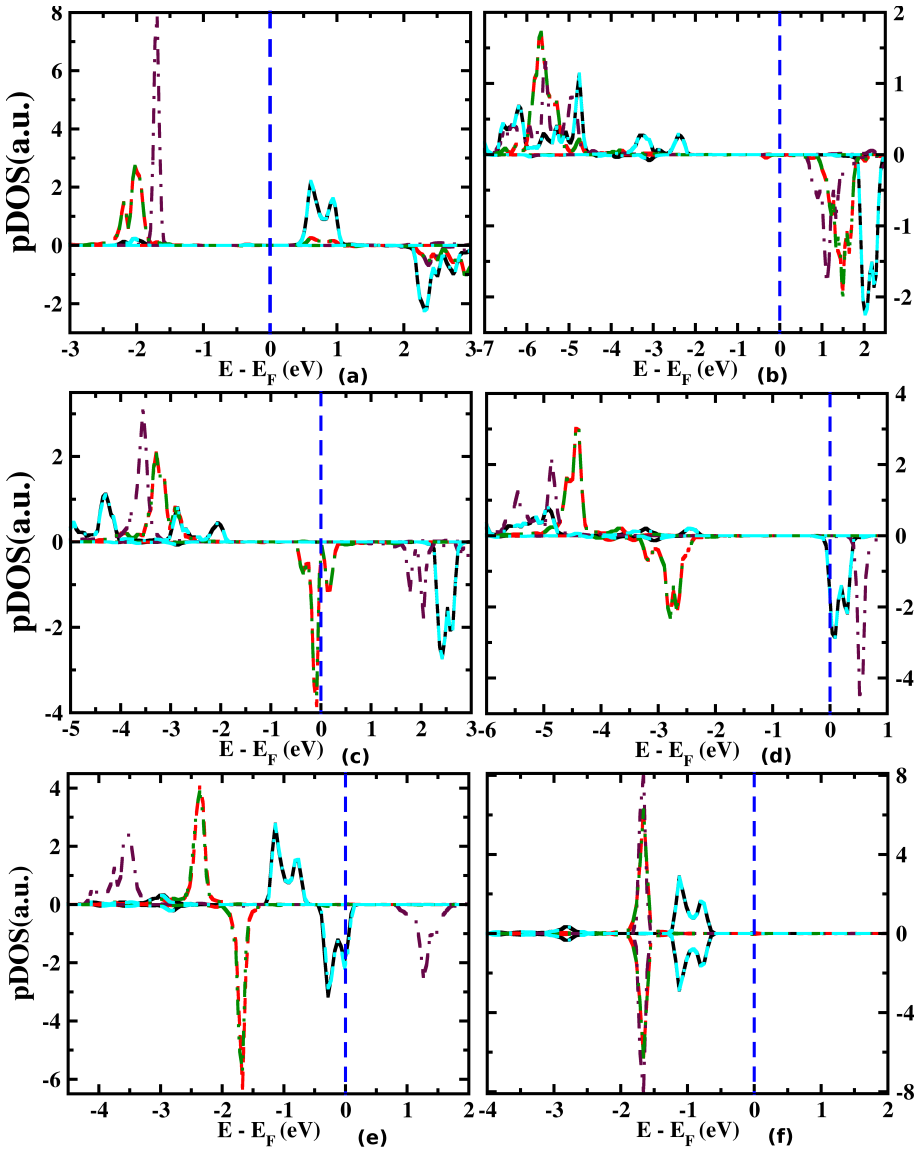

Figure 4.4: Projected DOS of d-orbitals on the TM atoms of TM-C_3N_4@graphene where TM is (a) V, (b) Mn, (c) Fe, (d) Co, (e) Ni, and (f) Cu.

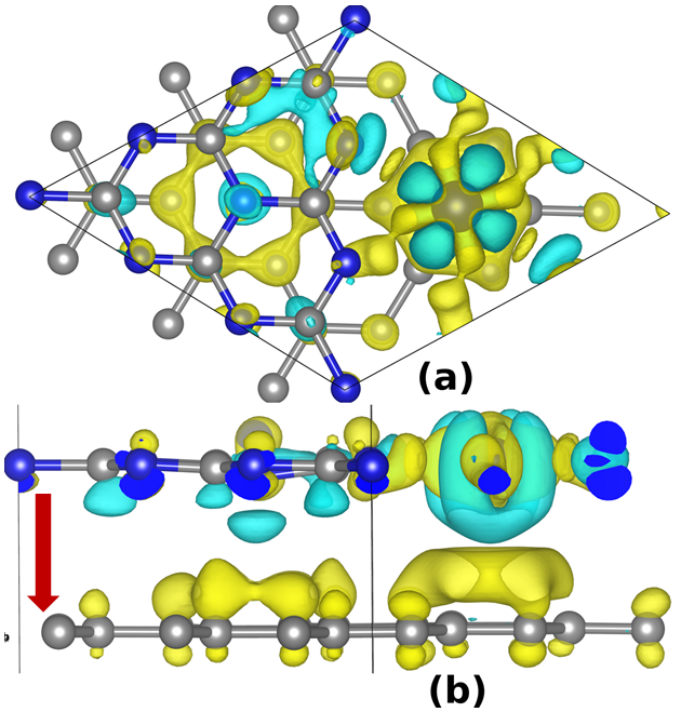

Figure 4.5: (a) Top and (b) side views of three-dimensional transferred charge density plot at the interface between graphene and Cr-C_3N_4. Yellow and light blue isosurfaces show charge accumulation and depletion with respect to isolated graphene and Cr-C_3N_4 layer. The red arrow shows the direction of built-in electric field. The isovalue used here is 0.002 e $\AA^{-3}$.

Fe, Co, and Ni atoms (i.e., 6, 7, and 8 electrons), all majority spin bands as well as minority spin bands start getting fill-up, which eventually reduce the magnetic moment of corresponding units cells (Fig. 4.4 (c-e)). The local magnetic moments of these three metal atoms in unit cells appear as 4, ∼3, and 1 μB, respectively. At this point, one should note that all TM atoms remain in their corresponding high-spin states; i.e., the spin pairing at low-lying d-bands results in higher energy than the single occupancy at higher energy d-orbitals. As mentioned, Cu- and Zn-C_3N_4@graphene show nonmagnetic behavior in their electronic ground state. Unlike other TM atoms, Cu remains in a +1 oxidation state in Cu-C_3N_4 due to back-donation of electrons from ligand to metal. Complete filling of d-orbitals, i.e., d^{10}, also gives extra stabilization to the +1 oxidation state of Cu.

Performing Bader charge analysis [49], as tabulated in Table 4.1, we find that graphene accepts electrons from the TM-g-C_3N_4 layer and becomes n-doped. We

have plotted three-dimensional charge density difference of Cr-C_3N_4@graphene in Fig. 4.5 which clearly demonstrates the charge depletion from Cr-C_3N_4 and accumulation of that in graphene. Because of the difference in electrostatic potentials of these two layers, charge transfer occurs. These induced charges couple strongly in between two layers and remain localized to the inner layer (i.e., closer to Cr-C_3N_4) of graphene. Interestingly, it is in contrast to the C_3N_4@graphene nanocomposite, where electron transfer occurs in the opposite direction [43]. Thus, the incorporation of TM in the g-C_3N_4 cavity changes the doping nature of graphene from p-type to n-type. This charge separation between two layers eventually creates a built-in electric field inside the nanocomposite. Knowing the energy gap at the Γ-point (△E) and the distance between two layers (d) and considering the tight-binding model, we can approximately formulate the internal electric field (E_{int}) as [47], $E_{int} \approx$ △E/d. Calculated E_{int} values, tabulated in Table 4.1, are well comparable with other similar charge separated systems [47]. The electron doping also results in an enhancement in the carrier concentration in the graphene layer. As given in Table 4.1, considering a unit cell of the nanocomposites, we find the carrier concentration of graphene in the range of 2.1 $\times$ 10^{13} to 5.0 $\times$ 10^{13} cm^{-2}, which is quite comparable with other n-doped graphene systems [17, 47]. As Samuels *et. al.* demonstrated for bilayer graphene, the creation of such high carrier density by applying conventional gate voltage is quite difficult [47]. However, for TM-C_3N_4@graphene, it can be achieved very easily, and these materials can be ideal for ultrafast electronics.

High exchange energies for Cr- and Fe-C_3N_4@graphene due to d-p interactions have encouraged us to find their magnetic behavior under finite temperature. In this regard, several groups have performed Monte Carlo (MC) simulations using the Ising model to estimate the Curie temperature (T_C) [19, 46]. For our study, we implement MC simulations considering the complete Heisenberg Hamiltonian. The Hamiltonian can be formulated as [50],

$$H = \sum_{<ij>} J_{ij}(S_{ix}S_{jx} + S_{iy}S_{jy} + S_{iz}S_{jz}) \tag{4.4}$$

where i, j, and J_{ij} are the nearest neighbour magnetic sites and the exchange coupling constant between them, respectively. S_{ix}, S_{iy}, and S_{iz} are the x, y, and z components of the spin vector at the i^{th} magnetic center of the 2D sheets. To apply

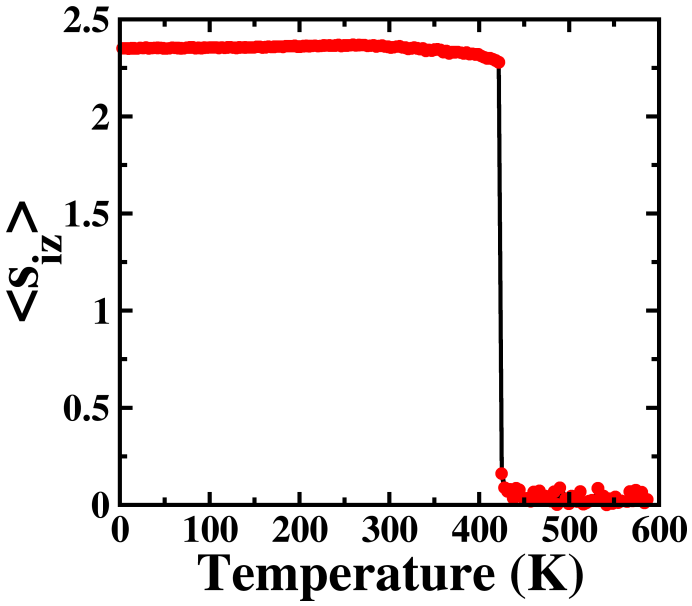

Figure 4.6: Values of the average of S_{iz} per unit cell of Fe-C_3N_4@graphene with respect to the temperature. The transition from ferromagnetic to paramagnetic state occurs (i.e., Curie temperature) at 428 K.

this Hamiltonian for the MC simulations, we evaluate the J values (both its magnitude and sign) from the previously mentioned DFT-calculations following standard procedure. From our calculations, the estimated J values for Cr and Fe embedded sheets appear as -4.97 and -5.58 meV, respectively. By plotting the average of S_{iz} per unit cell vs temperature in Fig. 4.6 , it is evident that these sheets retain their ferromagnetic spin ordering perfectly even at room temperature. We find the T_C values of Cr- and Fe-C_3N_4@graphene as 381.4 and 428.2 K, respectively (see Fig. 4.6 for Fe-C_3N_4@graphene). The values of these T_C are much higher than the reported T_C of dilute magnetic semiconductors as well as of several other 2D sheets [19, 46, 51]. Importantly, strong ferromagnetic ordering in these sheets is completely intrinsic and it does not need any application of external stimuli like strain [52]. Because of the considerably high Curie temperatures, we strongly believe that these sheets will attract huge attention for advanced magnetic device industries.

4.3.1.3 Optical Properties

As discussed previously, pristine g-C_3N_4, which is a wide-band semiconductor, has poor photoabsorption efficiency, due to its inability to capture visible light.

However, studies have shown that, when it stacks with graphene, a new optical transition occurs due to strong coupling between these two layers and, eventually, the visible photoresponse increases a lot. For present systems, the inclusion of transition metals closes the band gap of C_3N_4@graphene completely and induces more levels near the Fermi energy, indicating a much greater enhancement of performance in terms of visible light response. To have a quantitative picture, we calculate the absorption spectra of these nanocomposite sheets by evaluating the imaginary part of the dielectric function as shown in Fig. 4.7. For Cr, Fe, Co, and Ni embedded g-C_3N_4@graphene, at the visible light range (i.e., $<$ 3.3 eV), there are four major types of transitions, (1) p_z of C (graphene) $\rightarrow$ d-orbitals of TM, which gives the lowest energy absorption peaks (i.e., <0.5 eV; denoted as "*" in Fig. 4.7), (2) p_z of C (graphene) $\rightarrow$ $p_{\pi/z}$ of C/N of g-C_3N_4, which is responsible for peaks at 0.7-2 eV ("$\bigtriangledown$" in Fig. 4.7), (3) d-orbitals of TM $\rightarrow$ $p_{\pi/z}$ of C/N of g-C_3N_4, which gives absorption peaks at the energy range of 2-3 eV (" $\bigtriangleup$ " in Fig. 4.7), and (4) higher energy transition corresponding to p_z of C (graphene) $\rightarrow$ $p_{\pi/z}$ of C/N of g-C_3N_4, which appears in the 2.5-3.5 eV (shown as "#" in Fig. 4.7) energy range. Note that, for some broad peaks (for Fe-C_3N_4@graphene) at the range of 2.5-3 eV, both (3) and (4) types of transitions occur around the same energy. For other sheets, as the unoccupied d-orbitals stay well above the Fermi level, 2p $\rightarrow$ 3d transition at low energy is not possible. Thus, although other peaks at high energy are the same as previous systems, we do not find any prominent peak <0.5 eV range for these systems.

4.3.2 Electronic, Magnetic and Optical Properties of TM-g-C_3N_4

In this section, we have considered here the free-standing monolayers of TM-g-C_3N_4.

4.3.2.1 Structures

Metal-embedded g-C_3N_4 sheets are optimized by considering a supercell with four nitride cavities (i.e., a 2 $\times$ 2 supercell). Generally, TM atoms have a strong tendency to segregate on the surface of low-dimensional materials, where TM binding

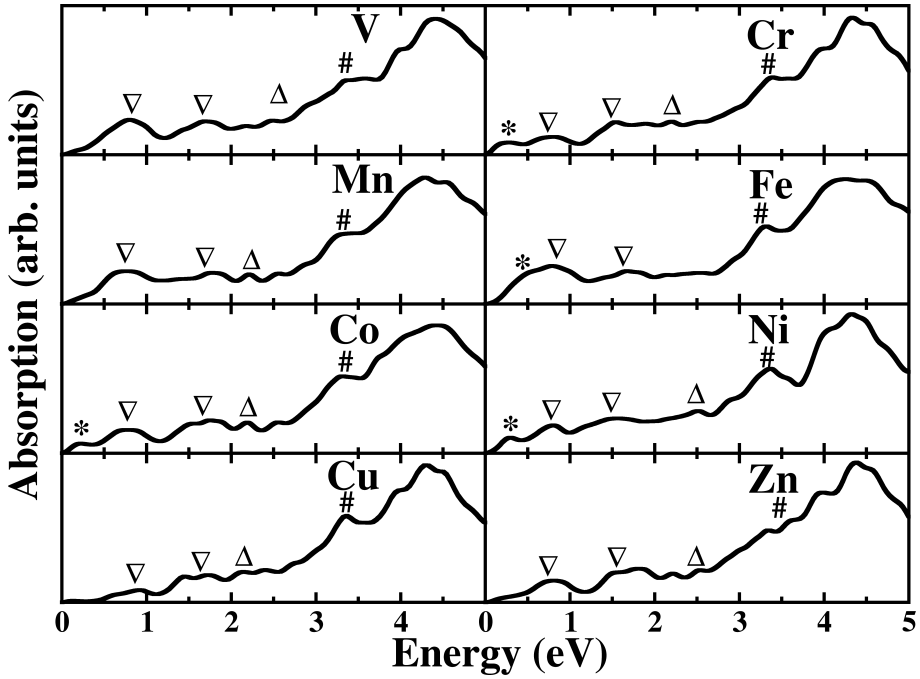

Figure 4.7: Computed absorption spectra of TM-C_3N_4@graphene where TMs are written at the upper right corner of each plot. *, ▽, △, and # denote the high intensity peaks at energy ranges of 0-0.5, 0.7-2.0, 2.0-3.0, and 2.5-3.5 eV, respectively. We have used a Gaussian broadening of 0.05 eV.

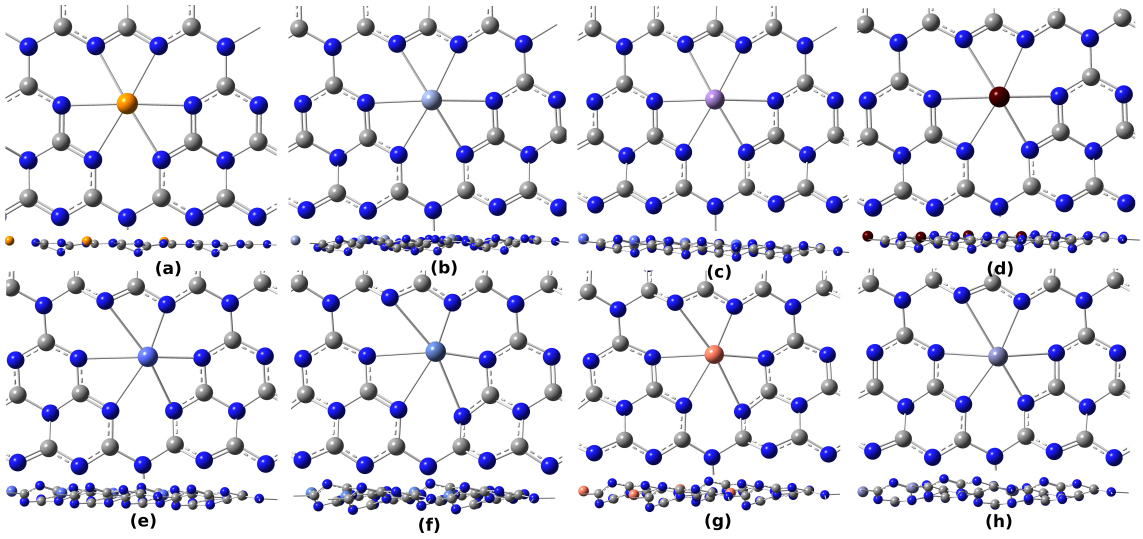

Figure 4.8: Top view and side view of TM-embedded g-C_3N_4, where TM is (a) V, (b) Cr, (c) Mn, (d) Fe, (e) Co, (f) Ni, (g) Cu, and (h) Zn.

Table 4.2: Binding (E_{bind}) and clustering energies ($E_{cluster}$) per unit cell of TM-g-C_3N_4, magnetic moment per TM (Mag. Mom.) and exchange energies ($\triangle E_{ex}$) for each 2 × 2 supercell ($\triangle E_{ex}$) are tabulated.

Metals	V	Cr	Mn	Fe	Co	Ni	Cu	Zn
E_{bind}(eV)	-1.87	-3.65	-4.48	-0.68	1.40	1.97	2.1	1.4
$E_{cluster}$ (eV)	1.98	1.03	1.1	1.15	0.73	0.60	0.67	0.78
Mag. Mom. (μB)	3	4	5	4	2	1	0	0
$\triangle E_{ex}$ (meV)	-90	-80	20	-53	-	-	0	0

with the surface is much weaker than in the bulk phase [53]. From Table 4.2, it can be seen that for V, Cr, Mn, and Fe embedded sheets, the binding energy is negative, i.e., the TM atoms are more stable in the cavity of the g-C_3N_4 system than that of their bulk phase. However, positive binding energies for Co, Ni, Cu, and Zn imply that these TM atoms have a tendency to segregate and form metal clusters in the cavity

However, as pointed out by several groups [54, 55], the possibility of dimer formation or aggregation should be confirmed by comparing the single atom and dimer binding energies with the surface. Note that, cluster formation can be circumvented if the TM dimer binding on the surface becomes less stable compared to single atom binding. Thus, we calculated the clustering energy ($E_{cluster}$), which is defined as the difference between the binding energy of the dimer ($E_{b,di}$) and of the single ($E_{b,mono}$) TM in the g-C_3N_4 cavity,

$$E_{cluster} = E_{b,di} - E_{b,mono} \tag{4.5}$$

where both $E_{b,di}$ and $E_{b,mono}$ are in eV per TM. A negative (positive) value of $E_{cluster}$ signifies that the TM atoms are prone toward cluster formation (dispersion). From Table 4.2, it is evident that all the TM atoms have positive clustering energy on this sheet. Thus, we can conclude that single TM atoms embedded on the g-C_3N_4 sheets under study are reasonably stable and prevent the segregation of TMs on the cavity. This is in full agreement with the experimental observations [26, 56].

The optimized structures of these sheets can be seen in Fig. 4.8. We find that the TM inclusion does not change the sheet structures drastically, which is consistent with the X-ray diffraction study of TM-g-C_3N_4[24]. Interestingly, the planarity of

optimized TM-embedded g-C_3N_4 sheets increases with the decrease in the TM's atomic number i.e. early TMs which are V, Cr, Mn, and Fe, get embedded almost symmetrically in the g-C_3N_4 cavity. Whereas, late TMs i.e. Co, Ni, Cu, and Zn form an asymmetric coordination in the cavity. There are several factors such as size of the cationic TM atoms, crystal field stabilization energy etc. which strongly influence the planarity of the TM-g-C_3N_4 sheets.

4.3.2.2 Electronic and Magnetic Properties

Alike, their graphene composites, the early transition metal (V-Fe) embedded sheets exhibit localized magnetic moments at the metal atom and on the N_{edge} atoms. Further, we focus on the nature of the magnetic interaction between the two neighbouring TM metal atoms, as well as among the d-orbitals of TM and the p-orbitals of N_{edge} of g-C_3N_4. Following similar procedure as adopted for earlier investigation, we find that V, Cr, and Fe atoms couple ferromagnetically with each other, whereas Mn atoms exhibit an antiferromagnetic Mn-Mn coupling. And sheets with Cu and Zn have nonmagnetic ground states, as the TMs are $3d^{10}$ systems here, containing all paired d-electrons. Further, as shown in Table 4.2, our study demonstrate ferromagnetic exchange energies, i.e., -90, -80, and -53 meV for g-C_3N_4 sheets embedded with V, Cr, and Fe atoms, respectively. The origin of different kinds of magnetic couplings in these planar sheets can be understood by considering the spatial arrangement of the interacting magnetic orbitals as discussed in detail for TM-C_3N_4@graphene systems. Fundamentally, the orthogonal arrangement of the interacting d-orbitals of TMs (i.e. V, Cr, and Fe) and 2p-orbitals N_{edge} atoms results in ferromagnetic ground state. Whereas for Mn-g-C_3N_4, the interacting d-orbital is empty d_{z^2}, which is parallel to the interacting p_z orbital of N_{edge}. It results in dominating AFM coupling between metal and ligands. Further, we tabulate the local magnetic moment of the TMs in Table 4.2. The trend of the magnetic moments can be understood from the hexagonal crystal field splitting of d-orbitals as discussed in previous part of the chapter (see Fig. 4.2 (a)).

As explored for earlier composite systems, we investigate the magnetic behavior of these sheets under finite temperature by performing MC simulations considering complete Heisenberg Hamiltonian. Here, we considered V, Cr, and Fe embedded sheets under consideration, as these three sheets show higher $\triangle E_{ex}$ values. The

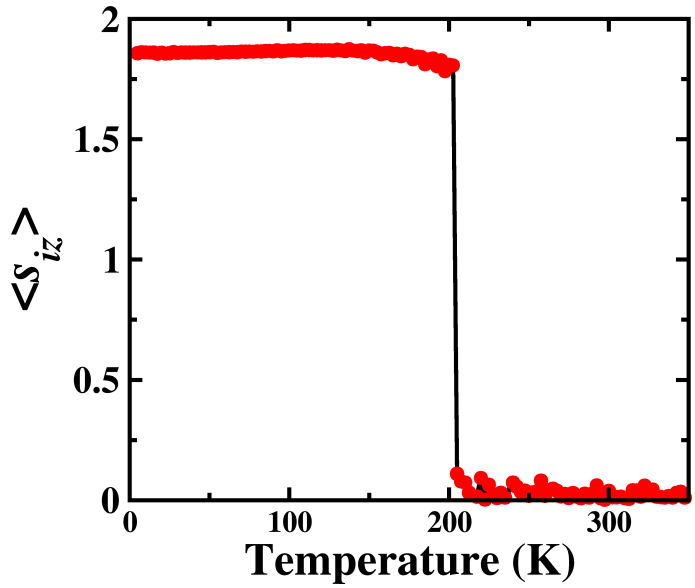

Figure 4.9: Values of the average of S_z per unit cell of V-g-C_3N_4 with respect to the temperature. The transition from ferromagnetic to paramagnetic state occurs (i.e., the Curie temperature) at 205 K.

estimated J values from our calculations turn out to be, -4.3 meV, -2.22 meV, and -1.5 meV for V-, Cr-, and Fe-g-C_3N_4, respectively. By plotting the average of S_{iz} per unit cell versus temperature, it is evident that all three sheets retain their ferromagnetic spin ordering at low temperatures. The T_C values appear as 205 K, 170.54 K, and 115 K for V-, Cr-, and Fe-g-C_3N_4, respectively (see Fig. 4.9 for V-g-C_3N_4 as an example).

4.3.2.3 Optical Properties

To find out the improved photoabsorption efficiency of g-C_3N_4 upon inclusion of 3d-transition metals, we calculate the absorption spectra of these sheet materials in the visible light energy range. Efficient absorption of low-energy light (i.e., <3.3 eV) is quite evident for these sheets. Exploring these spectra, we find that there are different types of transitions such as, p_π of C/N $\rightarrow$ $d_{xy}/d_{x^2-y^2}$ of early TMs (V-Fe), $d_{xz}/d_{yz}/d_{z^2}$ of TM $\rightarrow$ $d_{xy}/d_{x^2-y^2}$ of early TM (i.e., d-d transition), different d-orbitals of late TMs (Co, Ni) $\rightarrow$ p_z orbitals of C and N of g-C_3N_4 occur in these systems.

Here, we should note that only absorption at visible range is not enough to

comment about the possibility of applications of these sheets in different fields (like, photocatalytic activity). However, it certainly gives an idea about how and why these sheets respond to visible light. These informations will be in turn very helpful to design various efficient optical devices.

4.4 Conclusions

In conclusion, performing DFT-based computations, we have discussed the structural, electronic, magnetic, and optical properties of recently experimentally synthesized TM embedded g-C_3N_4 and their graphene composite sheets. We find that inclusion of TM atoms in the pristine sheets of g-C_3N_4 and C_3N_4@graphene significantly modify their magnetic properties. From MC calculations, some of these sheets are found to show ferromagnetic ordering at room temperature. Moreover, as the band-gap of these pristine sheets get closed by TM inclusion, the visible photoresponse also gets modified to a large extent. The prominent absorption peaks at the low energy range for these sheets confirms their ability to absorb visible light. Therefore, our study strongly exhibits the possible multifunctional behavior of these 2D-sheets. With the progress of experimental techniques, we hope that these sheets will become promising materials for advanced device applications.

Bibliography

[1] M. Warner, S. Din, I. S. Tupitsyn, G. W. Morley, A. M. Stoneham, J. A. Gardener, Z. Wu, A. J. Fisher, S. Heutz, C. W. Kay, *et al.*, Nature **503**, 504 (2013).

[2] M. Ratner, Nat. Nanotechnol. **8**, 378 (2013).

[3] J. P. Liu, E. Fullerton, O. Gutfleisch, and D. J. Sellmyer, *Nanoscale magnetic materials and applications* (Springer, 2009).

[4] S. Möller, C. Perlov, W. Jackson, C. Taussig, and S. R. Forrest, Nature **426**, 166 (2003).

[5] D. Ghosh, P. Parida, and S. K. Pati, J. Phys. Chem. C **116**, 18487 (2012).

[6] Z. Zhang, X. Zou, V. H. Crespi, and B. I. Yakobson, ACS Nano **7**, 10475 (2013).

[7] K. M. McCreary, A. G. Swartz, W. Han, J. Fabian, and R. K. Kawakami, Phys. Rev. Lett. **109**, 186604 (2012).

[8] S. Wolf, D. Awschalom, R. Buhrman, J. Daughton, S. Von Molnar, M. Roukes, A. Y. Chtchelkanova, and D. Treger, Science **294**, 1488 (2001).

[9] D. D. Awschalom and M. E. Flatté, Nat. Phys. **3**, 153 (2007).

[10] S. Z. Butler, S. M. Hollen, L. Cao, Y. Cui, J. A. Gupta, H. R. Gutiérrez, T. F. Heinz, S. S. Hong, J. Huang, A. F. Ismach, *et al.*, ACS Nano **7**, 2898 (2013).

[11] K. S. Novoselov, A. K. Geim, S. Morozov, D. Jiang, Y. Zhang, S. Dubonos, , I. Grigorieva, and A. Firsov, Science **306**, 666 (2004).

[12] A. K. Geim and K. S. Novoselov, Nat. Mater. **6**, 183 (2007).

[13] S.-J. Han, A. V. Garcia, S. Oida, K. A. Jenkins, and W. Haensch, Nat. Commun. **5** (2014).

[14] M. Xu, T. Liang, M. Shi, and H. Chen, Chem. Rev. **113**, 3766 (2013).

[15] O. V. Yazyev, Rep. Prog. Phys. **73**, 056501 (2010).

[16] P. Avouris, Z. Chen, and V. Perebeinos, Nat. Nanotechnol. **2**, 605 (2007).

[17] H. Medina, Y.-C. Lin, D. Obergfell, and P.-W. Chiu, Adv. Funct. Mater. **21**, 2687 (2011).

[18] A. Krasheninnikov, P. Lehtinen, A. S. Foster, P. Pyykkö, and R. M. Nieminen, Phys. Rev. Lett. **102**, 126807 (2009).

[19] J. Zhou and Q. Sun, J. Am. Chem. Soc. **133**, 15113 (2011).

[20] T. Hardcastle, C. Seabourne, R. Zan, R. Brydson, U. Bangert, Q. Ramasse, K. Novoselov, and A. Scott, Phys. Rev. B **87**, 195430 (2013).

[21] A. W. Robertson, B. Montanari, K. He, J. Kim, C. S. Allen, Y. A. Wu, J. Olivier, J. Neethling, N. Harrison, A. I. Kirkland, *et al.*, Nano Lett. **13**, 1468 (2013).

[22] Y.-C. Lin, P.-Y. Teng, C.-H. Yeh, M. Koshino, P.-W. Chiu, and K. Suenaga, Nano Lett. **15**, 7408 (2015).

[23] X. Ma, Y. Lv, J. Xu, Y. Liu, R. Zhang, and Y. Zhu, J. Phys. Chem. C **116**, 23485 (2012).

[24] X. Wang, X. Chen, A. Thomas, X. Fu, and M. Antonietti, Adv. Mater. **21**, 1609 (2009).

[25] G. Ding, W. Wang, T. Jiang, B. Han, H. Fan, and G. Yang, ChemCatChem **5**, 192 (2013).

[26] X. Chen, J. Zhang, X. Fu, M. Antonietti, and X. Wang, J. Am. Chem. Soc. **131**, 11658 (2009).

[27] P. Niu, L. Zhang, G. Liu, and H.-M. Cheng, Adv. Funct. Mater. **22**, 4763 (2012).

[28] X. Zhang, X. Xie, H. Wang, J. Zhang, B. Pan, and Y. Xie, J. Am. Chem. Soc. **135**, 18 (2012).

[29] X.-H. Li, J.-S. Chen, X. Wang, J. Sun, and M. Antonietti, J. Am. Chem. Soc. **133**, 8074 (2011).

[30] Y. Zhang, T. Mori, L. Niu, and J. Ye, Energy Environ. Sci. **4**, 4517 (2011).

[31] Q. Liu and J. Zhang, Langmuir **29**, 3821 (2013).

[32] G. Kresse and J. Hafner, Phys. Rev. B **47**, 558 (1993).

[33] J. P. Perdew, K. Burke, and M. Ernzerhof, Phys. Rev. Lett. **77**, 3865 (1996).

[34] V. I. Anisimov, F. Aryasetiawan, and A. Lichtenstein, J. Phys. Condens. Matter. **9**, 767 (1997).

[35] S. Dudarev, G. Botton, S. Savrasov, C. Humphreys, and A. Sutton, Phys. Rev. B **57**, 1505 (1998).

[36] K. Sato, L. Bergqvist, J. Kudrnovskỳ, P. H. Dederichs, O. Eriksson, I. Turek, B. Sanyal, G. Bouzerar, H. Katayama-Yoshida, V. Dinh, *et al.*, Rev. Mod. Phys. **82**, 1633 (2010).

[37] P. E. Blöchl, Phys. Rev. B **50**, 17953 (1994).

[38] G. Kresse and D. Joubert, Phys. Rev. B **59**, 1758 (1999).

[39] S. Vosko, L. Wilk, and M. Nusair, Can. J. Phys. **58**, 1200 (1980).

[40] H. J. Monkhorst and J. D. Pack, Phys. Rev. B **13**, 5188 (1976).

[41] S. Grimme, J. Comput. Chem. **27**, 1787 (2006).

[42] M. Gajdoš, K. Hummer, G. Kresse, J. Furthmüller, and F. Bechstedt, Phys. Rev. B **73**, 045112 (2006).

[43] A. Du, S. Sanvito, Z. Li, D. Wang, Y. Jiao, T. Liao, Q. Sun, Y. H. Ng, Z. Zhu, R. Amal, *et al.*, J. Am. Chem. Soc. **134**, 4393 (2012).

[44] P. Anderson, Phys. Rev. **79**, 350 (1950).

[45] W. Heitler and F. London, Zeitschrift für Physik **44**, 455 (1927).

[46] M. Kan, J. Zhou, Q. Sun, Y. Kawazoe, and P. Jena, J. Phys. Chem. Lett. **4**, 3382 (2013).

[47] A. J. Samuels and J. D. Carey, ACS Nano **7**, 2790 (2013).

[48] S. M. Kozlov, F. Viñes, and A. Görling, Adv. Mater. **23**, 2638 (2011).

[49] G. Henkelman, A. Arnaldsson, and H. Jónsson, Comput. Mater. Sci **36**, 354 (2006).

[50] D. P. Landau and K. Binder, *A guide to Monte Carlo simulations in statistical physics* (Cambridge university press, 2014).

[51] T. Dietl, Nat. Mater. **9**, 965 (2010).

[52] X. Li, J. Zhou, Q. Wang, Y. Kawazoe, and P. Jena, J. Phys. Chem. Lett. **4**, 259 (2012).

[53] R. Zan, U. Bangert, Q. Ramasse, and K. S. Novoselov, Nano Lett. **11**, 1087 (2011).

[54] M. Chen, Y.-J. Zhao, J.-H. Liao, and X.-B. Yang, Phys. Rev. B **86**, 045459 (2012).

[55] M. Chen, X.-B. Yang, J. Cui, J.-J. Tang, L.-Y. Gan, M. Zhu, and Y.-J. Zhao, Int. J. Hydrogen Energy **37**, 309 (2012).

[56] E. Z. Lee, Y.-S. Jun, W. H. Hong, A. Thomas, and M. M. Jin, Angew. Chem. Int. Ed. **49**, 9706 (2010).

Chapter 5

Gas Trapping on Defective N-doped Graphene*

5.1 Introduction

Graphene, a two dimensional honeycomb lattice of sp^2-hybridized carbon has revolutionized the field of nanoscopic material science due to its number of extraordinary properties [1–3]. Apart from its several outstanding applications in the field of electronics,[4–6] electrocatalysis,[7, 8] DNA sensing,[9, 10] optics,[11, 12] graphene has been demonstrated as highly efficient adsorbent for gas-storage, separation, capturing and sensing [13–17]. Importantly, theoretically measured surface area of graphene is $2630 m^2/g$, which is quite high and useful to store large amount of gases [18]. However, low binding energy between pristine graphene and adsorbate molecules severely affect the adsorption processes of gas molecules in these sheets at room temperature. Leenaerts *et. al.* have demonstarted a small amount of charge transfer between different gas molecules and pristine graphene [19]. And consequently, the adsorbate-adsorbent interactions also appeared to be very weak for these systems. To increase the binding strength between various adsorbates and graphene sheet, different chemical and physical modification of graphene have been proposed [20, 21]. Recently, experimental as well as theoretical studies point out

*Works reported in this chapter are published in: (a) D. Ghosh, G. Periyasamy and S. K. Pati, J. Phys. Chem. C, **117**, 21700 - 21705 (2013). Reprinted (adapted) with permission from American Chemical Society (b) D. Ghosh and S. K. Pati (2016, under preparation)

that substitutional doping in graphene can be a promising way in this regard. Inclusion of different kinds of p-type dopants, such as, boron (B), aluminium (Al) and n-type dopants, like, oxygen (O), nitrogen (N), sulphur (S) etc. enhances the adsorption capacity, binding strength of gases on the graphene surface by several orders of magnitude [20, 22]. Parambhath *et. al.* showed that pyrrolic-N dominant graphene increases H_2 storage capacity by 66% compared to pristine graphene [23]. Chandra *et. al.* demonstrated increased CO_2 storage ability for N-doped graphene systems [24]. Performing first-principle calculations, Dai *et. al.* demonstrated high binding affinities of B-, Al-. N-doped graphene towards various pollutants such as NO, NO_2, SO_2 etc.[22]. Apart from these chemical doping, incorporation of structural defects, such as, point defects in pristine graphene can also results in better performance towards gas adsorption due to charge accumulation at the defect sites.[20] Combining these two potential factors, one can predict efficient adsorption of various gas molecules on different types of N-doped vacancies in graphene sheet. Interestingly, these nitrogen-doped defective sheets are already in limelight of research for their better activity than pristine graphene in the fields of electrocatalysis, field-effect transistor, lithium ion battery, supercapacitor, biosensing etc. [25]. Moreover, recent experimental as well as theoretical studies demonstrated strong trapping of single metal atom in these defects sites [26, 27]. However, potential application of these monolayers towards adsorptive removal of toxic and greenhouse gases remain quite unexplored. Interestingly, Zuo *et. al.* have shown enhanced adsorption of different organic contaminants on the N-doped multiwalled carbon nanotubes in their recent study [28]. Combined experimental and theoretical study of this group showed 2 - 10 folds of increment for adsorption of 2-naphthol and 1-naphthalmine in N-doped nanotubes.

Emission of toxic and greenhouse gases due to various industrial and domestic usages is a major concern nowadays. [29, 30] These hazardous gases affect acutely to the human health as well as environment in various direct and/or indirect ways. A number of porous materials, such as, zeolite, metal-organic framework etc. have been explored for their possible promising usage as gas-sensor, adsorbent, catalytically active pollutant-degrading agent etc. [31, 32] However, to achieve these fascinating properties, one needs to have precise control over the pore-size/shape, chemical nature of surface in these adsorbent systems. And it appears that controlling these

factors experimentally in these materials is quite challenging indeed.

In this regard, in present chapter, we have investigated nitrogen-doped graphene systems i.e. pyridinic graphene for their probable usage as adsorbent for adsorption of various poisonous gases, such as, hydrogen fluoride (HF) and hydrogen cyanide (HCN) and greenhouse gases, like, chlorodifluoromethane ($CHClF_2$) and trifluoromethane (CHF_3), which have high potential to adsorb heat. Using Born Oppenheimer molecular dynamics (BOMD), we demonstrate that these gas molecules get adsorbed specifically on the defect-sites at room-temperature. Electrostatic interactions between nitrogen atoms of defect-sites and hydrogen of adsorbent molecules results in stability of adsorbate-adsorbent interaction. Detail analyses show that there is no chemical bond formation/breakage in these adsorbate-absorbent systems, suggesting the strong physisorption of gases on defects. Density functional theory (DFT) based calculations further helped us to gain an atomistic understanding about the absorbate-adsobent interaction in these systems. Geometric signature, considerable high binding energies and absence of effective charge transfer strongly indicate the formation of moderately strong hydrogen-bonds in these nano-systems.

5.2 Computational Details

For present simulations, we perform BOMD calculations using the QUICKSTEP module as provided by the CP2K code[33]. The CP2K code has implemented a mixed basis set where the Kohn-Sham orbitals are expanded in an atom-centered Gaussian basis set and the electronic charge density is described using an auxiliary plane wave basis set [34]. In our BOMD calculations, we use an energy cut-off of 280 Ry to describe the plane wave charge density. Further, analytical duel-space pseudopotential, as implemented by Goedecker, Teter, and Hutter (GTH), are used to represent the electron-ion interactions for all the elements [35]. The valence electrons are modeled by double-ζ basis set with one set of polarization functions i.e. DZVP basis set [36]. Generalized gradient approximation (GGA) with the form of Perdew-Burke-Ernzerhof (PBE) is used to capture exchange and correlation effects of electrons [37]. Additionally, as the noncovalent interactions play an important role in our present study, we apply empirical van der Waals interactions, as prescribed by Grimme (DFT-D2) for all the BOMD calculations [38].

To study the interactions between adsorbate and adsorbents in ambient condition, we perform BOMD simulation considering canonical (NVT) ensemble. We apply a Nose-Hoover thermostat to perform the constant temperature simulation [39, 40]. To integrate the equations of motion, we use the time step of 0.5 femtosecond (fs). To avoid the spurious interaction of nonperiodic direction, we consider the simulation box, containing 30 Å vacuum space in that direction. We generate 15 picosecond (ps) trajectories for all adsorbate-adsorbent systems and further used them all for analysis.

For electronic structure calculations, we use the accurate frozen-core full-potential projector augmented-wave (PAW) based method, as incorporated in the Vienna ab initio simulation package (VASP) [41]. Like BOMD simulations, here also we used GGA-PBE functionals for density functional theory based calculations. A plane-wave kinetic energy cutoff of 400 eV is used for all the DFT calculations. To obtain the ground state geometry at 0 K temperature, we relax the adsorbate-adsorbent systems using conjugate-gradient method. We sample the full Brillouin zone by using Γ-centred Monkhorst-Pack scheme [42]. For geometry optimization and accurate binding energy calculations, we use $5 \times 5 \times 1$ and $9 \times 9 \times 1$ k-points grids, respectively. The structural minimization of these systems are performed until the interatomic forces acting there become less than 0.02 eV/Å. To incorporate van der Waals corrections, we use Grimme's DFT-D2 method here also. We further calculate the charge transfer between adsorbates and adsorbents using the method described by Bader [43].

The binding energy of the gas molecules on the adsorbate is calculated using following formula,

$$E_{bind} = E_{sheet-molecule} - E_{sheet} - E_{molecule} \tag{5.1}$$

where E_{bind} in the binding energy of the adsorbate on adsorbent. $E_{sheet-molecule}$, E_{sheet} and $E_{molecule}$ are the energies of the optimized structure of adsorbate-adsorbent composite, isolated adsorbent sheet and adsorbate molecules, respectively. Note that, as per formulation, negative binding energy signifies favourable adsorption of molecules on defective graphene.

5.3 Structural Models

To simulate the adsorbent, we consider a 7×7 supercell of two-atom rhombic unit cell of graphene. In pristine form, this supercell contains 98 atoms of carbon. To introduce N-doped point defects in this sheet, we modify the pristine graphene accordingly. The defective graphene-based adsorbents which we have explored in our study, are shown in Fig. 5.1 (a,b). The defective sheet, shown in Fig. 5.1 (a), can be considered as a graphene sheet where single carbon is missing (i.e. SV) and nearest three carbon atoms of the vacant site have been substituted by nitrogen atoms. This sheet is named as SV-3N for further discussions. In the same way, in the other sheet, as shown in Fig. 5.1 (b), a carbon dimer is removed (i.e. double vacancy, DV) and four carbon atoms which were covalently bonded with the dimer, are substituted by nitrogen atoms. This particular sheet is nomenclatured as DV-4N in this chapter. Apart from these defective regions, other part of graphene remains in its pristine form. The concentrations of N-doping in the SV-3N and DV-4N appear as 3.09 % and 4.17 %, respectively. We also increase the doping concentration of N, as stated in later part of the chapter.

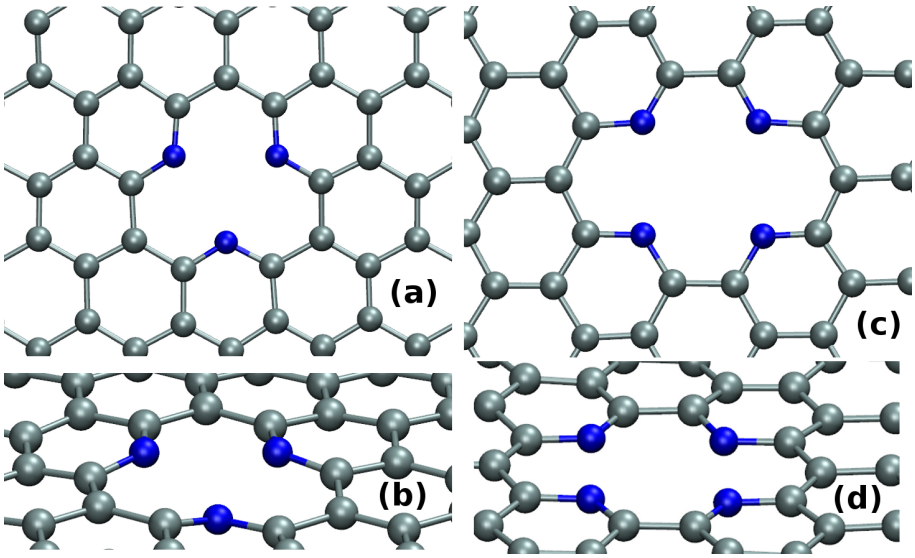

Figure 5.1: Snapshots of (a,c) top and (b,d) side view of equilibrated structures of SV-3N and DV-4N sheets after BOMD simulations at constant temperature (300K).

5.4 Results and Discussion

We first discuss about the stability of the single and double vacancies (SV and DV, respectively) at finite temperatures. Performing constant temperature (i.e. at 300 K) BOMD studies, defect-sites at both SV-3N and DV-4N sheets appear to be stable without any major structural reconstruction at equilibrium. As shown in Fig. 5.1 (a, b), the equilibrated sheets are almost planar, without any considerable out-of-plane distortion of defect-sites. Our finding about the planarity of these sheets is completely in agreement with the previous experimental observation by Wang *et. al.* [44] The equilibrium distances between any two nitrogen atoms at these SV (DV) sites are $\sim$ 2.6 Å-2.75Å ($\sim$ 2.7 Å-2.8 Å), quite larger than N-N single bond length ($\sim$ 1.47 Å. Thus, in these sheets, nitrogen atoms do not undergo reconstruction, forming homonuclear N - N covalent bonds. This is once again consistent with several experimental investigations, where X-ray photoelectron spectroscopy (XPS) spectra as well as scanning tunneling microscope (STM) imaging proves the absence of N-N bonds in the systems [25]. Interestingly, the SV and DV defects are quite unstable in pristine graphene. Here, two dangling bonds, appearing from half-filled sp^2 orbitals of under-coordinated carbon atoms at defect site, form stable C-C covalent bond. Consequently, as shown in different experimental as well as theoretical studies, these SV and DV defects get reconstructed to 5-9 and 5-8-5 defects, respectively [45]. However, SV-3N and DV-4N defects remain stable at ambient condition due to two major factors: (1) the stability of the lone pairs of electrons in the doped-N atoms and (2) unfavourable formation of weak homonuclear N-N bond(s) in possible reconstructed geometries (i.e. 5-9 or 5-8-5). In these sheets, N atoms of each pyridinic rings keep the lone pair of electrons in an sp^2 orbital, which remains in-plane with the system. As sp^2 orbitals of lone pairs are completely occupied, the defect sites become quite stable and less active towards reconstruction compared to the SV and DV in graphene. Moreover, due to the presence of these lone pairs, two N atoms repel each other electrostatically and avoid formation of the N-N bonds at defect-sites. Lower bond energy of N-N bond [46] also reflects this fact and consequently justify the stability of these defects. We discuss about the electron density distribution of these defects in later part of the chapter.

Before exploring the pollitant gas adsorption on the defective graphene sheets, we study the dynamics of these pollutant gas molecules on the pristine graphene

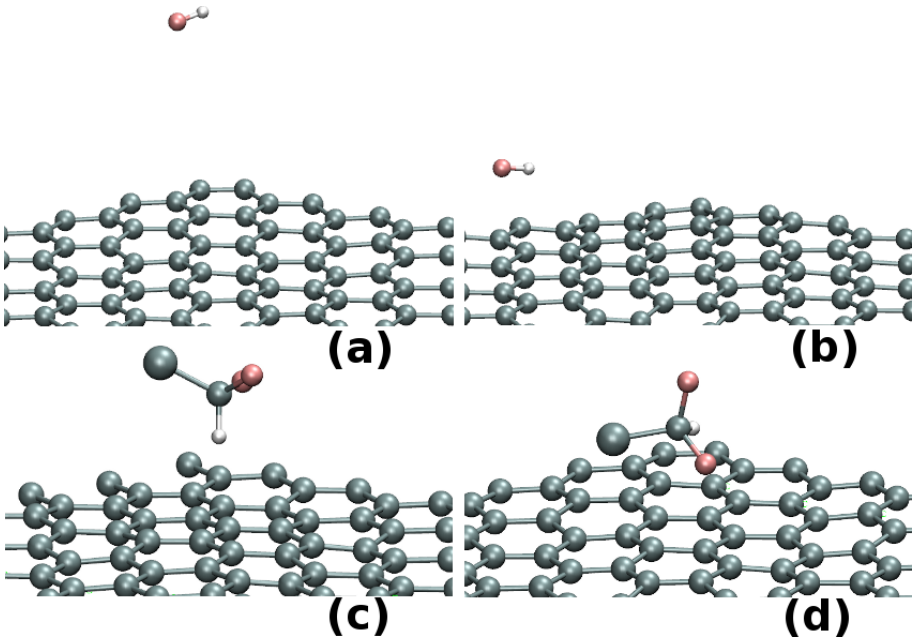

Figure 5.2: Snapshots of (a,b) HF and (c,d) $CHClF_2$ on top of pristine graphene. BOMD simulations are performed in 300 K; snapshots are captured at (a,c) 0.5 ps and (b,d) 6 ps.

sheet at 300 K. As can be seen from the snapshots of the BOMD simulations in Fig. 5.2 (a-d), HF and $CHClF_2$ molecules remain quite mobile inside the simulation box, without exhibiting any kind of binding interactions with graphene π-surface. Similar kind of dynamics are found for other two gas molecules on top of pristine graphene sheet also. Fundamentally, highly stable π-electron surface of pristine graphene prevents binding with these polar adsorbates. Thus, other weak interactive forces (such as, van der Waals interaction) play the major role in the present adsorption processes. It appears that these forces are too weak to bind the adsorbates on graphene surface at room temperature, resulting in negligible adsorption. Interestingly, very recent experimental study by Kulkarni *et. al.* demonstrated the fast desorption rate of various polar molecules from pristine graphene at room temperature [47]. These findings strongly support the repellent nature of pristine graphene towards adsorption of different small polar molecules at room temperature, explored in the present BOMD simulations.

Next, we investigate the pollutant gas adsorption on the defective graphene sheets, performing BOMD simulations of adsorbate-adsorbent systems at 300 K.

Initial adsorbate-absorbent conformation is considered as the geometry, where gas molecules stay on top of the the N-doped point-defects. BOMD simulations of 15 ps for each adsorbate-adsorbent system evidently demonstrate the molecular adsorption on defective graphene-sheets. As shown in Fig. 5.3 (a-d) and 5.4 (a-d), both the adsorbents i.e. SV-3N and DV-4N prominently trap small polar gas molecules on their defect-sites. Importantly, within the investigated time-scale and temperature, we do not observe any event of desorption of gas molecule from these defect-sites. Further, we focus on the distance between adsorbate and adsorbent systems in equilibrium. To compute this, we calculate the distance between the centre of mass of gas molecule and the defect-sites (considering the doped N atoms only). As shown in Table 5.1, the adsorbed molecules remain in the range of 2.24 Å to 3.6 Å apart, from the adsorbents. These distances are quite similar to the other non-covalently bonded graphene - molecule composites as found in different studies [21]. Thus, we confirm the adsorption of pollutant molecules on the defect-sites in our study. Further, in all the equilibrated systems, H-atom of the adsorbate molecules remains close to the defect-sites. More specifically, as shown in Fig. 5.3 (a-d) and 5.4 (a-d), these H-atoms are quite directional towards the N atoms of the sheets. Thus, at ambient condition, these N-doped defect-sites trap both kinds of gases i.e. linear as well as tetrahedral adsorbates.

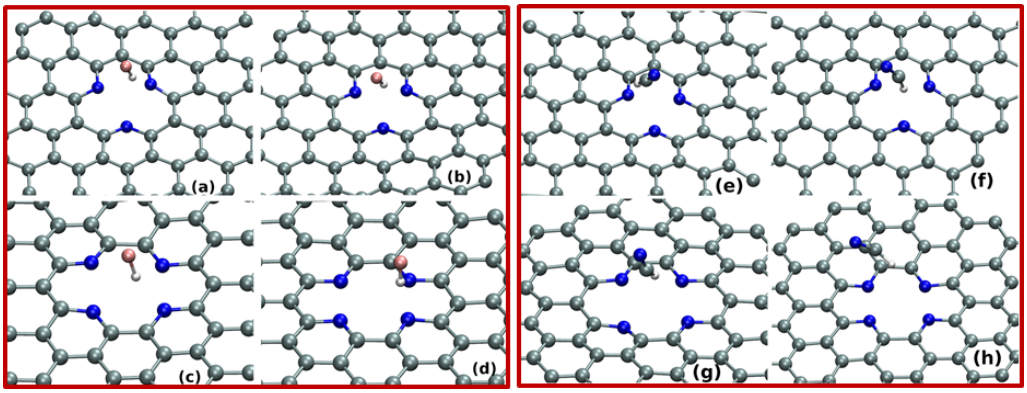

Figure 5.3: Various snapshots of configurations of HF trapped on defect-site of SV-3N and DV-4N after (a,c) 10 ps and (b,d) 15ps BOMD simulation. Snapshots of trapping of HCN on SV-3N and DV-4N after (e,g) 10 ps and (f,h) 15ps are given.

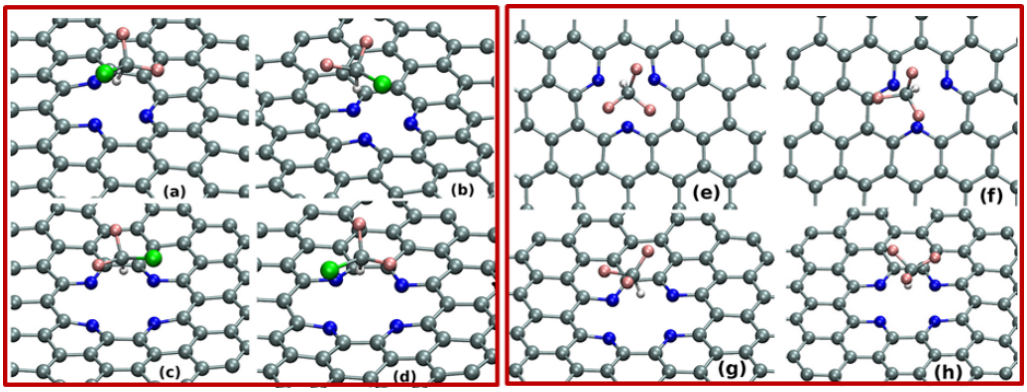

Figure 5.4: Various snapshots of configurations of $CHClF_2$ trapped on defect-site of SV-3N and DV-4N after (a,c) 10 ps and (b,d) 15ps BOMD simulation. Snapshots of trapping of CHF_3 on SV-3N and DV-4N after (e,g) 10 ps and (f,h) 15ps are given.

To quantify the adsorbate-adsorbent interaction strength, we focus on the binding energies of the gas molecules on the defect-sites of SV-3N and DV-4N, considering the corresponding optimized geometries at 0 K. Calculated binding energies indicate strong adsorption of polar molecules on N-doped defective site of graphene. Further, to acquire an atomistic understanding of adsorbate-adsorbent interactions, we majorly concentrate on the static properties of investigated systems by exploring the DFT-based optimized geometries.

Exploring the optimized adsorbate-graphene structures, it is evident that planarity of the SV-3N defect-site is lost in presence of HF and HCN gas molecules. As shown in Fig. 5.5 (a,b), one N atom among three in these defect sites comes out from the graphene plane by 0.3 Å and 0.15 Å, respectively. We named this particular out-of-plane shifted N atom as N_{out}. Further, on SV-3N defect site, H atom of HF and HCN remain directed towards N_{out}. As given in Table 5.1, for HF (HCN), H atom stays much closer to N_{out} i.e. 1.66 Å (2.06 Å) away than the other two N atoms of the defect sites where the N-H distances are 2.29 Å and 2.30 Å (2.23 Å and 2.26 Å). However, for $CHClF_2$ and CHF_3, as shown in Fig.5.5 (c,d), the H atom of molecules interacts with all the three N atoms almost identically. The defect site remains almost planar for these adsorbates where H of the molecule stays almost equidistance apart from all the three N of SV-3N. For DV, as shown in Fig. 5.6 (a-d), we do not find any prominent out-of-plane shift of N atoms. Apart from HF,

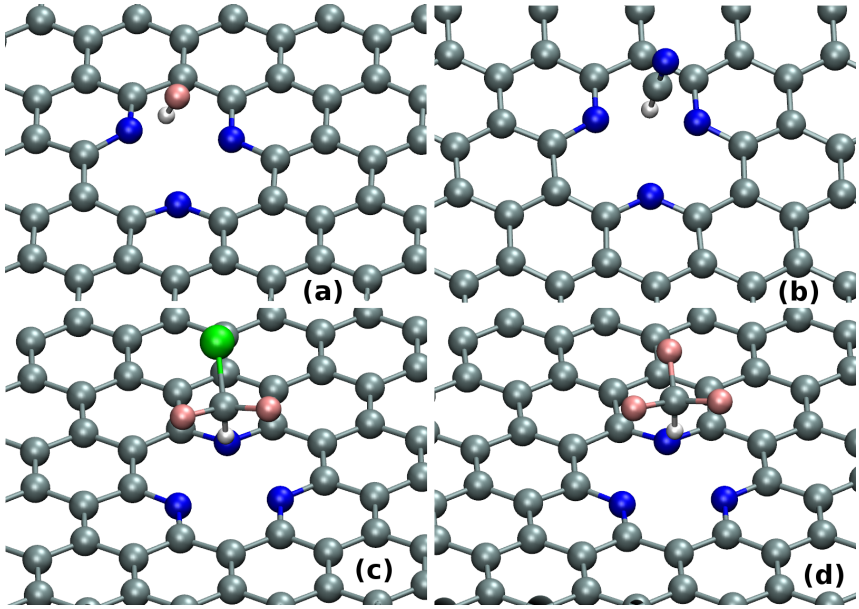

Figure 5.5: DFT-based optimized structures of (a) HF (b) HCN (c) $CHClF_2$ and (d) CHF_3 on top of the defect-site of SV-3N.

H atom of other three molecules stay almost at the middle of the cavity. However, H of HF remains closer to two N atoms (2.00 Å and 2.06 Å) and far from other two (2.53 Å and 2.57 Å) (see Fig. 5.6 (a)).

Focusing on binding energies as given in Table 5.1, among all gases, HF binds most strongly with both SV-3N and DV-4N defect sites with binding energies of -0.58 eV and -0.74 eV, respectively. Further, binding energies for other gases also demonstrate strong trapping of them on SV-3N and DV-4N sites. These strong adsorbate-adsorbent binding affinities evidently support the trapping of these gas molecules on SV/DV defect-sites at 300 K. Note that, calculated binding energies are quite high and fall in the range between weak chemisorption and strong physisorption phenomena. Thus, we look back into the dynamics of BOMD equilibrated adsorbate-adsorbent systems carefully to confirm the sorption process. The equilibrium bond lengths (i.e. for 10 - 15 ps simulations) of F-H for HF and C-H for other gases, as shown in Fig. 5.7 (a-d), demonstrate little fluctuating behaviour when these molecules are trapped on the SV-3N defect-sites. Similar kind of fluctuations also appear for molecules adsorbed on DV-4N sites. These fluctuations in bond lengths are quite common due to the presence of vibration of molecules at

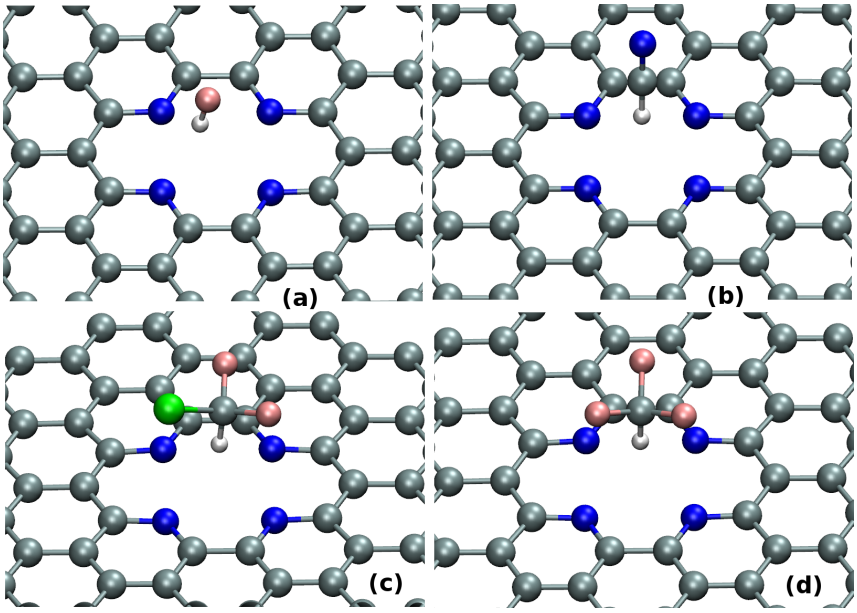

Figure 5.6: DFT-based optimized structures of (a) HF (b) HCN (c) $CHClF_2$ and (d) CHF_3 on top of the defect-site of DV-4N.

finite temperatures. Note that, fluctuation amplitudes of the bond-length in all the systems are in the range of 0.12 to 0.34 Å which is much smaller than their corresponding F-H or C-H bond lengths. Further, as given in Table 5.1, time-average of F-H or C-H bond lengths in each equilibrated system do not show any major deviation from the corresponding gas-phase molecular bond length values (given in the Table 5.1). All these phenomena strongly indicate that in the present cases, gas molecules remain in their molecular form without undergoing any kinds of bond breaking/making in presence of the N-doped defect-sites.

To find the microscopic origin of strong adsorbate-adsorbent interaction in these systems, we first look into the charge distribution in the adsorbates and adsorbents, considering their corresponding isolated structures. Here, all these isolated gas molecules contain partially positively charged H atom. Consequently, these molecules are strongly polar in nature and contain considerable permanent electric dipole moments of 1.82 D, 2.97 D, 1.61 D, 1.39 D for HF, HCN, $CHClF_2$ and CHF_3, respectively. Quite obviously, dipole moment of all these molecules remains directed along the H-F/C-H bond, which is most polar in nature. Presence of strong electronegative atoms, such as, N, F, Cl in the molecules is responsible for the polar

Table 5.1: Average adsorbate-adsorbent ($d_{mol-grap(avg)}$), F-H/C-H distances in BOMD simulations ($d_{F-H/N-H(avg)}$). Binding energies of adsorbates (E_{bind}), charge transfer (e_{tran}) from adsorbent to adsorbate, smallest distance between N of cavity and H of adsorbate ($d_{N-H(smallest)}$) and bond length of C-H/F-H ($d_{F-H/N-H,opt}$) in adsorbate after optimization, evaluated from DFT-based calculations. In the bracket of second column, gas phase value of C-H/F-H bond length for isolated adsorbates are given. All distances are in Å, binding energies are in kJ/mol and charge transfer in electron unit.

Systems	$d_{mol-grap(avg)}$	$d_{F-H/N-H(avg)}$	E_{bind}	e_{tran}	$d_{N-H(smallest)}$	$d_{F-H/N-H,opt}$
HF@SV-3N	2.4	0.97 (0.92)	-55.96	0.07	1.66	0.99
HCN@SV-3N	3.48	1.10 (1.06)	-49.21	0.05	2.20	1.11
$CHClF_2$@SV-3N	3.6	1.10 (1.08)	-34.74	0.04	2.16	1.10
CHF_3@SV-3N	3.06	1.10 (1.08)	-49.21	0.04	2.06	1.10
HF@DV-4N	2.24	1.00	-71.40	0.05	2.00	0.97
HCN@DV-4N	3.15	1.13	-60.786	0.04	2.31	1.10
$CHClF_2$@DV-4N	3.1	1.13	-66.58	0.04	2.38	1.10
CHF_3@DV-4N	3.19	1.14	-60.786	0.04	2.34	1.09

nature of these adsorbates.

Further, as shown in Fig. 5.8 (a, b), the charge distributions in the adsorbents demonstrate accumulation of negative charges at the defect-sites. As discussed earlier, the pyridinic nitrogen atoms are sp^2-hybridized in nature where two of these orbitals get involved into to form C-N σ-bonds, leaving other one as an in-plane dangling sp^2-orbital. These orbitals which are in-plane of the sheet and directed towards the centre of the SV/DV, remain doubly occupied. Importantly, as each N atom has one singly occupied $2p_z$ orbitals to enable its participation in π-space aromatic structures, no charge transfer occurs from the lone pair of sp^2-orbital to π-space. This is quite evident from the electron distribution plots also that charge accumulation in these sheets is strongly localized only at the SV/DV sites. Thus, these lone-pairs of electrons make the defect-sites electron-rich in nature and consequently provide suitable pockets for trapping of polar gases.

Now, focusing on the adsorbent-adsorbate systems, as shown in Table 5.1, calculated charge transfer between the gas molecules and graphene sheets appear to be quite small for all the systems. It directly indicates that positive charge at H-atoms and negative charge at N-atoms of SV/DV remain strongly localized at their corresponding atomic sites. Moreover, as shown in Table 5.1, the optimized distance between these polarized atoms i.e. H and N, remain quite larger than their single bond length, indicating no direct overlaps of electron densities between adsorbate

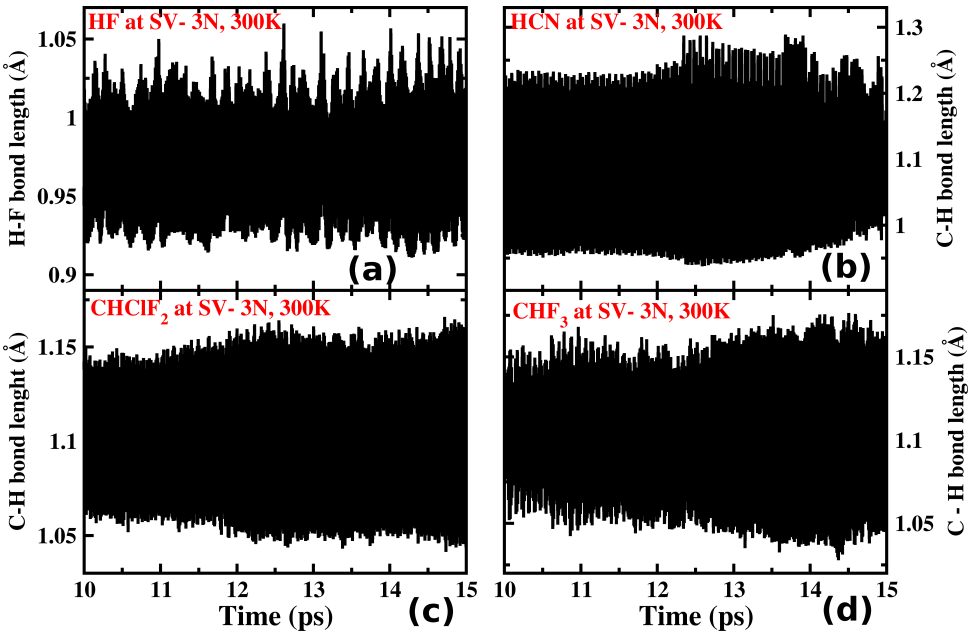

Figure 5.7: The bond length of F-H/C-H in the adsorbate molecules, adsorbed on top of SV-3N, during the BOMD simulation for 10-15 ps time-scale. The adsorbate molecule is given in the plot.

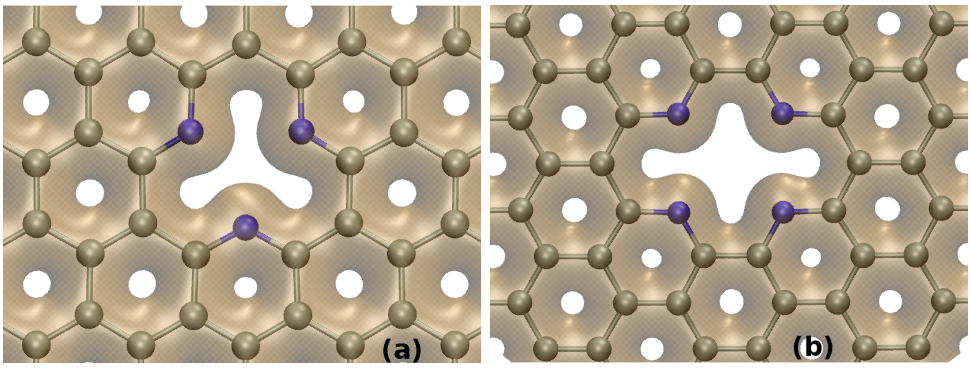

Figure 5.8: The charge density distribution at the defect-site of (a) SV-3N and (b) DV-4N sheets. The isosurface is 0.25 e $\AA^{-3}$

and adsorbent systems. Therefore, non-covalent electrostatic interactions between the gas molecules and defect-sites governs the adsorption process. Most importantly, large partial positive charge in H atom of gas molecules and accumulated negative charge at defects illustrates the formation of moderately strong H-bond at the adsorption-site [48]. Here, C-H/F-H bonds of adsorbate and N atoms of defect-sites act as proton donor and acceptor, respectively.

To be sure about the H-bond formation, we focus on various parameters, which reliably provide the signatures of that. First, we consider the sum of van der Waals radii of H and N which amounts to 2.75 Å. As the distances between H and nearest N are smaller than 2.75 Å in all adsorbate-adsorbent systems, presence of non-covalent bonding interaction in these systems is quite clear. Further, it is quite well known that a major structural feature for H-bonded systems is the linearity between donor and acceptor moieties [48]. As shown in optimized (Fig. 5.5) as well as equilibrated (by BOMD simulation; Fig. 5.4) geometries of adsorbate-adsorbent systems, the $\angle \mathrm{N_{out}}...H-F/\angle \mathrm{N...H-C}$ (for other molecules apart from HF) angles remain very close to 180°. Thus, almost linear angles between donors and acceptors strongly support the existence of H-bonding in the presently studied systems. Further, as Table 5.1 depicts, the smallest distance between N and H atoms are in the range of 1.66 to 2.38 Å which are quite larger than donor i.e. F-H/C-H bond lengths. Thus, considering all these parameters, according to the well accepted guidelines prescribed by Steiner [48], we conclude that presently studied adsorbate-adsorbent interactions majorly originate from the moderately strong H-bond formation.

Interestingly, performing BOMD simulations of these systems at 300 K temperature, we find that gas molecules remain quite mobile on the SV and DV sites without staying to any one particular N atom. The H atom of molecules stay nearer to any one of the three or four equivalent N atoms at a particular instant of simulation time. And during the simulations, H atom as well as corresponding gas molecule changes its position by changing the interacting N atom-site over time. Thus, due to thermal fluctuations at finite temperatures, the molecules remain trapped on top of the N-doped defect-sites but with local motions. Further this motion indicates that the gas molecules are not chemically bonded to the N atoms of the defect-sites.

Selective adsorption of the pollutant gases in open atmosphere is one of the major criteria for the adsorbents to be used in efficient practical applications. Thus,

we investigate the adsorption of most abundant gases of atmosphere i.e. N_2 and O_2 on the SV-3N and DV-4N sites of N-doped graphene at ambient condition. As shown in Fig. 5.9 (a-d), BOMD simulations at 300 K demonstrate strong repulsion between defect-sites and N_2 and O_2 molecules. And consequently, these non-polar gas molecules do not get adsorbed on the SV/DV sites. High electron densities of the adsorbates and adsorbents results in the strong repulsion among them. Thus, the present adsorbent systems are quite selective towards polar gas molecules. Importantly, the presence of water vapour in atmosphere can create serious limitations towards the efficient removal of various pollutant adsorbents. BOMD simulations depict the adsorption of polar water molecules on the SV-3N and DV-4N at 300 K (see Fig. 5.9 (e, f)). Thus, the polluted air must be water-free before it flows through the N-doped graphene sheets.

We further increase the defect concentration in the adsorbent to find a reliable way to increase the pollutant molecule trapping capacity. We incorporate four SV-3N defects in a 8×8 graphene sheets, where the N-doping concentration gets increased to 9.6 %. Performing BOMD simulation at 300 K, we find that this sheet remains intact at this high concentration of defect also. To check the dynamics of gas molecules on these highly defective sheets, we introduced HF atoms on top of the defect-sites. As shown in Fig. 5.10 (a,b), the equilibrated structures evidently demonstrate the trapping of HF molecule on each defect-site. Interestingly, trapping does not get affected due to the presence of other defect-sites with adsorbed molecules even if they remain quite closer to each other ($\sim$9.8 Å for present case). Further, we also perform simulation, taking more bulky tetrahedral molecule i.e. $CHClF_2$ as the adsorbate. As shown in Fig. 5.10 (c,d), similar kind of dynamics i.e. strong trapping of gases on each defect site is found here also. Thus, our simulation clearly demonstrate the possibility to increase the gas-adsorption capacity of these defective sheets by increasing the N-doped defect-concentration on the graphene sheets.

5.5 Conclusions

To conclude, in this chapter, we demonstrate the efficient trapping of different poisonous and greenhouse gases on the different pyridinic N containing graphene

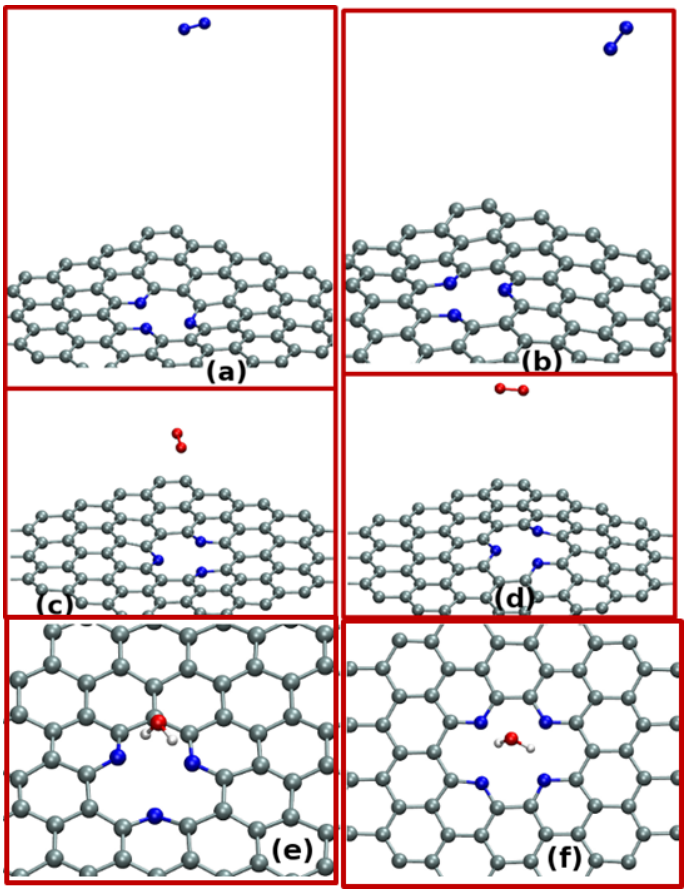

Figure 5.9: Snapshots of configurations of N_2 and O_2 on SV-3N after (a,c) 0.5 ps and (b,d) 10 ps BOMD simulation. Snapshots of trapping of H_2O molecule on defect-site of (e) SV-3N and (f) DV-4N after 10 ps.

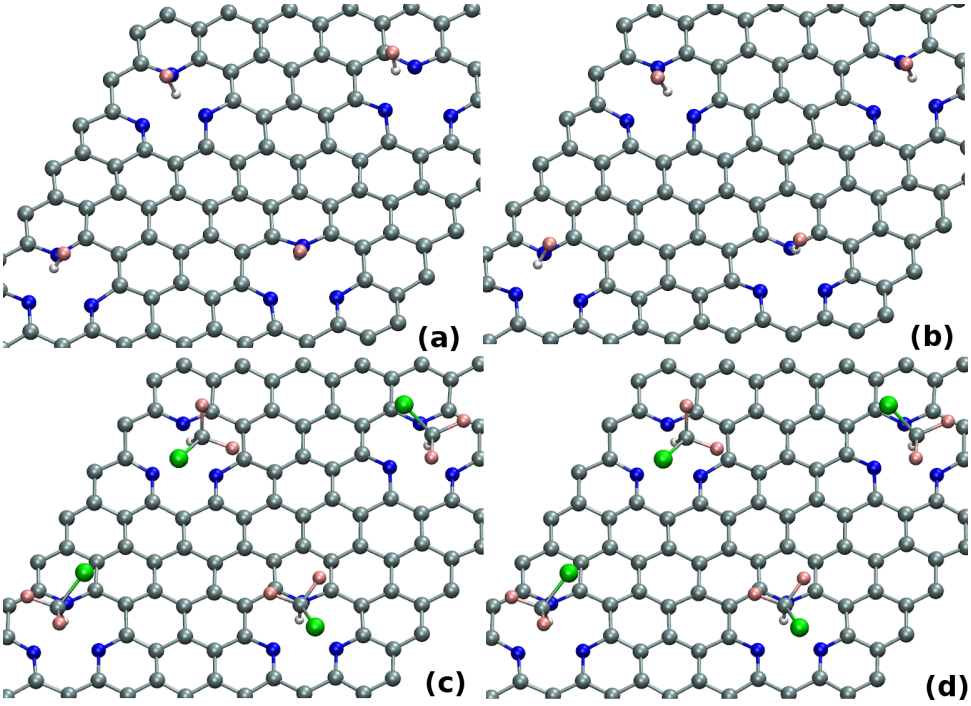

Figure 5.10: Snapshots of configurations of HF and $CHClF_2$ on concentrated defective sheets with SV-3N after (a,c) 5 ps and (b,d) 10 ps BOMD simulation.

sheets. BOMD simulations exhibit that polar gases, such as, HF, HCN, $CHClF_2$ and CHF_3, get trapped on the defect-site at 300 K temperature. Moderately strong H-bond formation between the N-atoms of the defect-sites and H atoms of the adsorbate molecules results in this stable adsorption phenomena. Importantly, these defect-sites, which strongly repel the non-polar N_2 and O_2 gases, appear to be very much selective towards the polar gas molecules. Further, increasing the defect concentration of N-doped defects in the graphene, we find the increase of gas adsorption capacity of these adsorbents.

Bibliography

[1] K. Novoselov, A. K. Geim, S. Morozov, D. Jiang, M. Katsnelson, I. Grigorieva, S. Dubonos, and A. Firsov, Nature **438**, 197 (2005).

[2] A. K. Geim and K. S. Novoselov, Nat. Mater. **6**, 183 (2007).

[3] M. J. Allen, V. C. Tung, and R. B. Kaner, Chem. Rev. **110**, 132 (2009).

[4] F. Schwierz, Nat. Nanotechnol. **5**, 487 (2010).

[5] K. S. Kim, Y. Zhao, H. Jang, S. Y. Lee, J. M. Kim, K. S. Kim, J.-H. Ahn, P. Kim, J.-Y. Choi, and B. H. Hong, Nature **457**, 706 (2009).

[6] X. Du, I. Skachko, A. Barker, and E. Y. Andrei, Nat. Nanotechnol. **3**, 491 (2008).

[7] L. Qu, Y. Liu, J.-B. Baek, and L. Dai, ACS Nano **4**, 1321 (2010).

[8] Y. Li, W. Zhou, H. Wang, L. Xie, Y. Liang, F. Wei, J.-C. Idrobo, S. J. Pennycook, and H. Dai, Nat. Nanotechnol. **7**, 394 (2012).

[9] C.-H. Lu, H.-H. Yang, C.-L. Zhu, X. Chen, and G.-N. Chen, Angew. Chem. Int. Ed. **121**, 4879 (2009).

[10] S. He, B. Song, D. Li, C. Zhu, W. Qi, Y. Wen, L. Wang, S. Song, H. Fang, and C. Fan, Adv. Funct. Mater **20**, 453 (2010).

[11] A. Vakil and N. Engheta, Science **332**, 1291 (2011).

[12] A. Grigorenko, M. Polini, and K. Novoselov, Nat. Photonics **6**, 749 (2012).

[13] F. Schedin, A. Geim, S. Morozov, E. Hill, P. Blake, M. Katsnelson, and K. Novoselov, Nat. Mater. **6**, 652 (2007).

[14] D.-e. Jiang, V. R. Cooper, and S. Dai, Nano Lett. **9**, 4019 (2009).

[15] H. W. Kim, H. W. Yoon, S.-M. Yoon, B. M. Yoo, B. K. Ahn, Y. H. Cho, H. J. Shin, H. Yang, U. Paik, S. Kwon, *et al.*, Science **342**, 91 (2013).

[16] S. Blankenburg, M. Bieri, R. Fasel, K. Müllen, C. A. Pignedoli, and D. Passerone, Small **6**, 2266 (2010).

[17] K. C. Kemp, H. Seema, M. Saleh, N. H. Le, K. Mahesh, V. Chandra, and K. S. Kim, Nanoscale **5**, 3149 (2013).

[18] M. D. Stoller, S. Park, Y. Zhu, J. An, and R. S. Ruoff, Nano Lett. **8**, 3498 (2008).

[19] O. Leenaerts, B. Partoens, and F. Peeters, Phys. Rev. B **77**, 125416 (2008).

[20] Y.-H. Zhang, Y.-B. Chen, K.-G. Zhou, C.-H. Liu, J. Zeng, H.-L. Zhang, and Y. Peng, Nanotechnology **20**, 185504 (2009).

[21] V. Georgakilas, M. Otyepka, A. B. Bourlinos, V. Chandra, N. Kim, K. C. Kemp, P. Hobza, R. Zboril, and K. S. Kim, Chem. Rev. **112**, 6156 (2012).

[22] J. Dai, J. Yuan, and P. Giannozzi, Appl. Phys. Lett. **95**, 232105 (2009).

[23] V. B. Parambhath, R. Nagar, and S. Ramaprabhu, Langmuir **28**, 7826 (2012).

[24] S. UkáYu, S. HoáKim, Y. SeobáYoon, D. YoungáKim, A. HyunáKwon, *et al.*, Chem. Commun. **48**, 735 (2012).

[25] H. Wang, T. Maiyalagan, and X. Wang, ACS Catal. **2**, 781 (2012).

[26] A. W. Robertson, B. Montanari, K. He, J. Kim, C. S. Allen, Y. A. Wu, J. Olivier, J. Neethling, N. Harrison, A. I. Kirkland, *et al.*, Nano Lett. **13**, 1468 (2013).

[27] A. Krasheninnikov, P. Lehtinen, A. S. Foster, P. Pyykkö, and R. M. Nieminen, Phys. Rev. Lett. **102**, 126807 (2009).

[28] L. Zuo, Y. Guo, X. Li, H. Fu, X. Qu, S. Zheng, C. Gu, D. Zhu, and P. J. Alvarez, Environ. Sci. Technol. (2015).

[29] D. A. Lashof and D. R. Ahuja, Nature **344**, 529 (1990).

[30] C. Snyder, T. Bruulsema, T. Jensen, and P. Fixen, Agric. Ecosyst. Environ. **133**, 247 (2009).

[31] J.-R. Li, Y. Tao, Q. Yu, X.-H. Bu, H. Sakamoto, and S. Kitagawa, Chem. Eur. J. **14**, 2771 (2008).

[32] E. Barea, C. Montoro, and J. A. Navarro, Chem. Soc. Rev. **43**, 5419 (2014).

[33] J. Hutter, M. Iannuzzi, F. Schiffmann, and J. VandeVondele, Wiley Interdisciplinary Reviews: Computational Molecular Science **4**, 15 (2014).

[34] J. VandeVondele, M. Krack, F. Mohamed, M. Parrinello, T. Chassaing, and J. Hutter, Comput. Phys. Commun. **167**, 103 (2005).

[35] S. Goedecker, M. Teter, and J. Hutter, Phys. Rev. B **54**, 1703 (1996).

[36] J. VandeVondele and J. Hutter, J. Chem. Phys **127**, 114105 (2007).

[37] J. P. Perdew, K. Burke, and M. Ernzerhof, Phys. Rev. Lett. **77**, 3865 (1996).

[38] S. Grimme, J. Comput. Chem **27**, 1787 (2006).

[39] S. Nosé, J. Chem. Phys **81**, 511 (1984).

[40] W. G. Hoover, Phys. Rev. A **31**, 1695 (1985).

[41] G. Kresse and J. Hafner, Phys. Rev. B **47**, 558 (1993).

[42] H. J. Monkhorst and J. D. Pack, Phys. Rev. B **13**, 5188 (1976).

[43] G. Henkelman, A. Arnaldsson, and H. Jónsson, Comp. Mater. Sci **36**, 354 (2006).

[44] Y. Wang, Y. Shao, D. W. Matson, J. Li, and Y. Lin, ACS Nano **4**, 1790 (2010).

[45] F. Banhart, J. Kotakoski, and A. V. Krasheninnikov, ACS Nano **5**, 26 (2010).

[46] D. Stevenson, J. Am. Chem. Soc. **77**, 2350 (1955).

[47] G. S. Kulkarni, K. Reddy, W. Zang, K. Lee, X. Fan, and Z. Zhong, Nano Lett. (2015).

[48] T. Steiner, Angew. Chem. Int. Ed. **41**, 48 (2002).

Chapter 6

Spin-crossover Molecule Based Thermoelectric Junction*

6.1 Introduction

Molecular spintronics, an interdisciplinary field including spintronics and molecular electronics is a potential approach to make the electronic devices much smarter [1–3]. Recent discovery of several fascinating properties, like, giant magnetoresistance [4], spin-injection [5], spin-filtration [6, 7], negative differential resistance[8], have attracted huge research interest in this field. Contemporarily, these molecular devices are explored for their promising thermoelectric effects i.e. ability of converting heat to electrical power [9, 10]. Recently, simultaneous measurement of conductance and thermopower in the same molecular junction brought a break-through to realize multifunctionality of these devices [11]. Furthermore, successful coupling of spintronics and thermoelectricity, has introduced another promising research-field, spin-caloritronics [12]. The precise measurement of spin-Seebeck coefficient in FeNi alloy, already demonstrated that not only voltage but temperature-gradient also can generate typical spintronic effects in nano-devices [13].

One ultimate goal of these spintronic devices is to use single magnetic molecules as active channels for carrier-transport [3]. By controlling the molecular spin-states,

*Works reported in this chapter is published in: D. Ghosh, P. Parida and S. K. Pati, Appl. Phys. Lett, **106**, 193105 (2015). Reprinted (adapted) with permission from American Institute of Physics

these devices can have potential applications in generation of spin-dependent current, information storage and processing. However, the manipulation of molecular spin-states in a precise way is always a challenging task. Although, single molecular magnets could be a good choice, several disadvantages like ultra-low critical temperature, poor structural stability limit their usage in this regard [14, 15]. However, the usage of magnetically bistable spin-crossover (SCO) molecules would be another promising way to tune the spin-states [16–18]. Recent studies demonstrating the SCO phenomenon in single molecular level also support the possibility to realize single molecular switching devices in recent future [19, 20]. Apart from the ground state, these molecules have one or more metastable magnetic states which can be accessible by applying different external stimuli such as temperature, light, pressure, electric field etc.[21]. Generally, these molecules contain first-row transition-metal (TM) atom(s) with electronic configuration, $3d^4$-$3d^7$ as the spin center(s) [21]. Among these, mononuclear, hexacoordinated Fe^{+2} complexes which shows temperature-induced spin-crossover, are one of the mostly explored molecules [22]. However, low transition temperature of temperature-induced SCO molecules, which are mostly explored in literature, restrict their usage as room-temperature switching devices. Recently, Prins *et. al.* have synthesized nanoparticles of [Fe$(trz)_3BF_4$] and have shown efficient switching of conductance above room temperature [23]. Here, Fe^{+2}, which remains at the low-spin (LS, S=0) state below room-temperature with an electronic configuration of t_{2g}^6, switches to the high-spin (HS, S=2) state, which has the electronic configuration $t_{2g}^4 e_g^2$ at $\sim$ 340-380 K. This is a substantial step ahead to realize SCO molecule-based spintronics devices which can operate in the ambient temperature. Interestingly, Schafer *et. al.* have recently synthesized a neutral iron complex, using 2-(1H-pyrazol-1-yl)-6-(1H-tetrazole-5-yl)pyridine (LH) ligand, which shows a sharp transition from the low-spin (LS, S = 0) state to high-spin (HS, S = 2) state at room temperature [22]. To explore the conductance-switching and spin-crossover magnetoresistance (SCMR) properties of this SCO molecule i.e. $[Fe(L)_2]$, in the present chapter, we have performed the state-of-art density functional theory (DFT) combining with non-equilibrium Greens function (NEGF) based electron transport calculations. This molecular device shows high spin-filter properties with a high spin-crossover magnetoresistance (SCMR). Furthermore, we have also explored the extraordinary thermoelectric efficiency and spin-crossover magnetothermopower

(SCMTP) of this molecular junction. Controlling the molecular spin-state, charge and spin-thermopower can also be tuned to a great extent. Importantly, thermocurrent can be switched between on and off with an extreme efficiency. Because of these exciting electronic and thermoelectric properties, this SCO molecule can possibly be a potential component in modern molecular-spin based multifunctional thermoelectric devices.

6.2 Computational Details

To calculate the energies of gas-phase $[Fe(L)_2]$ in two different spin-states (i.e. LS and HS), we use Los Alamos double ζ with effective core-potential basis set for Fe and 6-31++G(d,p) for other atoms, as implemented in Gaussina09 [24]. As the relative stability between LS and HS states of SCO-molecule highly depends on the choice of different exchange-correlation functionals, we optimize the molecule in gas phase using various exchange-correlation functionals to find the appropriate geometry [25]. Exchange-correlation functionals which we use for our calculations are GGA and three hybrid functionals with different amount/types of Hartree-Fock (HF) exchange-interactions i.e. Becke three-parameter Lee-Yang-Parr hybrid (i.e. B3LYP; 20 %) [26, 27], PBE0 (25% HF exchange)[28], HSE06 (25% short-range HF exchange) [29]. Without imposing any symmetry constraints during optimization, we find the stable molecular conformations in the LS and HS states, separately.

For electronic transport property calculations, we use NEGF methodology extended for spin-polarized systems, as implemented in the TranSIESTA package.[30] The transmission function is formulated as follows,

$$T(E) \quad = Tr[\Gamma_L(E)G(E)\Gamma_R(E)G^{\dagger}(E)] \tag{6.1}$$

where the G(E) is Green's function and it is evaluated from the Hamiltonian of the central region and self-energies. $\Gamma_{\mathrm{L/R}}$(E) is (- 2 times) the imaginary part of the self-energies of the left and right electrode. Further, we use Landauer-Buttiker formula to calculate current [31],

$$I \quad = (\tfrac{G_0}{e}) \int_{\mu_L}^{\mu_R} [f(E,\mu_L) - f(E,\mu_R)]T(E)dE \tag{6.2}$$

where μ_{L} and μ_{R} are the chemical potential of left and right electrode, respectively and G_0 is the quantum of conductance. Here, $\mathrm{f}(\mathrm{E}, \mu_{\mathrm{L/R}})$ represents the Fermi Dirac distributions at the left/right electrodes.

6.3 Results and Discussion

As shown in Fig. 6.1(a), after gas phase optimization, Fe atom stays at the centre of a slightly distorted octahedron, where it gets surrounded by two identical tridentate ligands, 2-(pyrazol-1-yl)-6-(tetrazol-1-yl)pyridine. Similar to the previous studies [25], spin-crossover from LS to HS prominently elongates the Fe - N bonds by 0.10 Å - 0.28 Å due to the electron rearrangement in e_g orbitals (i.e. $3d_{x^2-y^2}/3d_{z^2}$) of Fe. Notably, none of the hybrid functionals (i.e. B3LYP, PBE0, HSE06) are able to determine the ground state spin-configurations accurately for the present molecule. As these hybrid functionals overestimate the exchange energy, they incorrectly stabilize the HS state of the SCO molecule. Only GGA functionals predict LS as the ground state, where the energy gap between LS-HS states is 1.51 eV. Furthermore, within GGA functionals, the optimized molecule in its LS state shows excellent agreement with available experimental crystal data [22] . Thus, we choose this functionals for further investigations. Note that, close structural match between isolated molecule and its crystallographic data [22] also depicts that these molecules remain weakly packed due to intermolecular π-π stacking in their crystalline form.

We plot the total energy as a function of reaction coordinate, X in Fig. 6.1(b). Here, X is varied from X = 0 (LS state) to X = 1 (HS state). Importantly, the LS state at X = 0 appears much more stable than that of HS state at X = 1, demonstrating the LS state as the ground state at 0 K. However, at X = 0.66, where the LS and HS states become almost degenerate in energy, molecular spin-crossover occurs from LS to HS.

Now, we explore the spin-dependent electron transmission of the $[Fe(L)_2]$ based nano-device. And to compute the transmission, the SCO molecule gets coupled with gold (Au) electrodes on either side (i.e. Electrode-Molecule-Electrode, E-M-E arrangement). The electrodes are 6 × 6 × 3 bulk gold (Au (111) plane) each of which contains 108 gold atoms. To have a strong coupling between molecular fragment and Au electrodes, we have used thiol (-SH) as an anchoring group. To

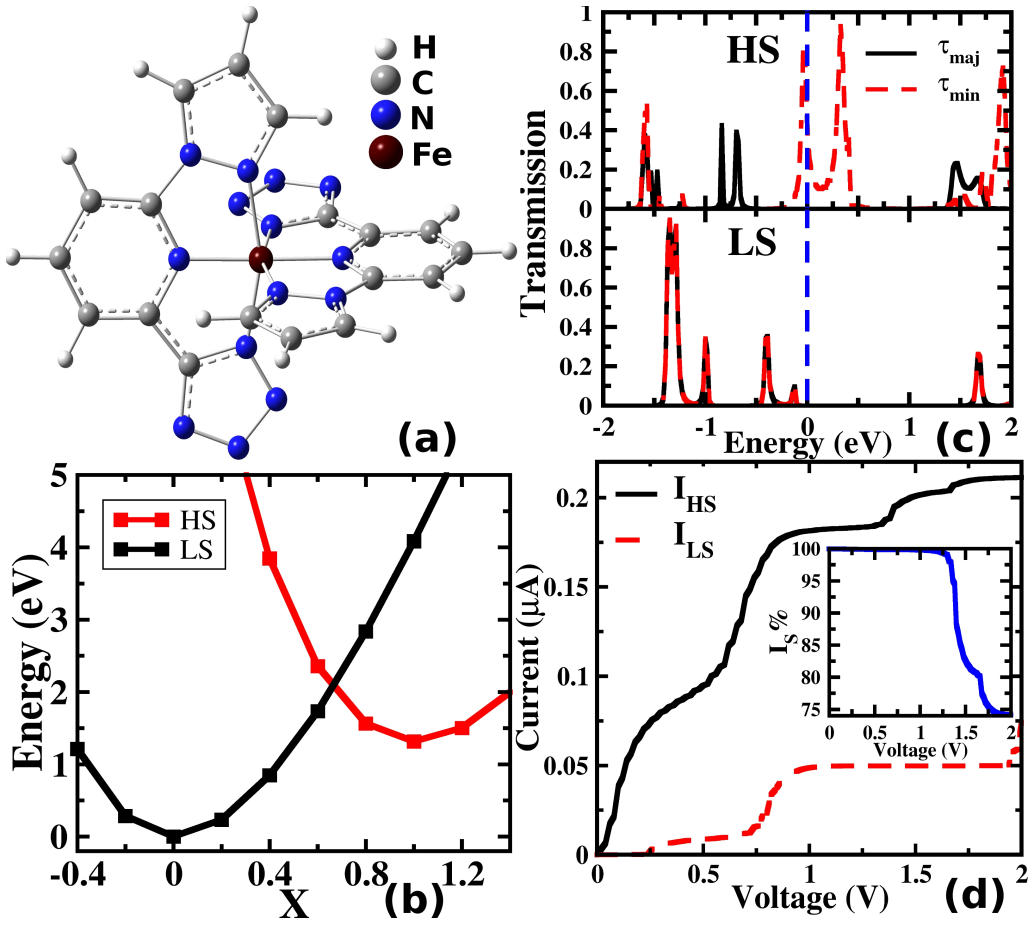

Figure 6.1: (a) The molecular structure of Fe(2-(1H-pyrazol-1-yl)-6-(1H-tetrazole-5-yl)pyridine)2 ($[Fe(L)_2]$). (b) Energy E for HS and LS states along X. Energies are scaled to E at X=0. (c) Zero-bias spin-polarized transmission spectra for HS (upper panel) and LS (lower panel) states as a function of energy. (d) I-V characteristics for HS and LS states. I_S-V plot is shown in the inset.

form molecule-Au electrode contact, thiol group is the most suitable and widely used anchoring group [32, 33]. First, we optimize the geometry of molecular fragment (with thiol groups), $[Fe(L)_2](SH)_2$ and gold electrodes individually. Then, following the experimental approaches [32, 33], we remove hydrogen atoms of -SH groups and placed the molecule between the two gold electrodes. We optimize the whole system, freezing the coordinates of the bulk gold electrodes using SIESTA package [34]. The geometry of this E-M-E system is optimized until inter-atomic forces become less than 0.04eV/Å. For all the atoms, we use a double-ζ polarized (DZP) basis set and Perdew-Burke-Ernzerhof (PBE) functional within the Generalized Gradient Approximation (GGA). A mesh cutoff of 300 Ry has been used. We impose periodic boundary condition orthogonal to the transport direction and used Monkhorst-Pack $2 \times 2 \times 1$ k-point grid to sample the Brillouin zone. The electronic temperature as 300K for all the calculations.

Note that, as previous studies [17, 18] suggested that transmission function of SCO-based molecular-junctions have insignificant effects over electrode-molecule contact geometries, we have excluded other energetically less stable contact-structures.

Although previous studies have demonstrated the instability of similar molecules upon deposition to metallic electrode-surfaces,[14] $[Fe(L)_2]$ almost retains its molecular structure even after chemisorption on to the gold electrodes. Most importantly, after deposition LS-HS energy separation of this molecule becomes 1.22 eV, which is slightly less than its gas-phase value. As this large energy-gap can't be closed by environmental influences, we conclude that $[Fe(L)_2]$ can exhibit sharp spin-state switching in the modeled molecular device. Most importantly, experimental study using X-ray absorption spectroscopy has already demonstrated temperature induced sharp LS-HS transition for single SCO molecules on Au(111) surface. [19]

In Fig. 6.1(c), we demonstrate the spin polarized zero-bias transmission coefficient, τ(E), for both the spin states within the energy window of -2 eV to 2 eV. Applying Landauer-Buttiker formalism [31], the total conductance (G) at Fermi energy (E_F) can be formulated as,

$$G = \frac{2e^2}{h} \sum_{\sigma} T_{\sigma}(E_F) \tag{6.3}$$

where $T_{\sigma}(E_F)$ is represented as the transmission coefficient for the spin channel σ

at E_F. As resonant transmission peaks near to E_F changes quite distinctly with the molecular phase-transition from LS to HS, we consequently find a substantial increment in G. We can quantify the change in G by calculating the magnetoresistance ratio, defined as, $[G_{HS} - G_{LS}]/[G_{HS} + G_{LS}]$. Notably, the calculated zero-bias magnetoresistance turns out to be $\sim$ 100 % at E_F, which shows a sharp conductance switching of this device upon spin-crossover. Thus, the electrical conductance through $[Fe(L)_2]$ can be switched on/off simply by tuning the molecular spin states in the spin-crossover process.

As can be found from Fig. 6.1(c), for HS state at and near the E_F, minority-spins show prominent transmission peaks, whereas majority-spins open up a transport gap of 2.1 eV. Thus, under a finite bias, the device can exhibits highly efficient spin-filter activity. We formulate the spin polarization of transmission ($\tau_{S(HS/LS}$) for a particular spin state as, [35]

$$\tau_{S,HS/LS} = \frac{|\tau_{min}(E_F) - \tau_{maj}(E_F)|}{\tau_{min}(E_F) + \tau_{maj}(E_F} \tag{6.4}$$

where τ_{min} (τ_{maj}) is the transmission coefficient for the minority-spin (majority-spin) channel. As transmission spectra are completely spin-unpolarized and $\sim$ 100 % spin-polarized for LS and HS states, respectively, τ_S changes sharply from 0% to $\sim$ 100% upon spin-crossover. The rearrangement of electrons in 3d orbitals of Fe during LS to HS transition abruptly changes the position of transport-active channels near E_F, resulting in a sharp modification of zero-bias transmission coefficient. Importantly, for HS state, only minority-spin MOs strongly couple with the electrode-states at and near E_F, resulting in $\sim$ 100 % spin-polarization of transmission at that energy.

As the real-world-devices work at a finite bias, we plot the current (I) - source-drain voltage (V_{SD}) characteristics in Fig. 6.1(d). For $V_{SD} \leq 0.2$ V, the I_{HS}/I_{LS} ratio reaches up to $\sim$ 700 which is quite high. Such a huge modification of current at low bias during the spin-crossover, exhibits the SCO-assisted switching behavior. To demonstrate the spin-filter property of HS state, we compute the spin resolved I - V_{SD} where the minority-spin current reaches $\sim$ 0.2 μA while the majority-spin component remains almost zero. To quantitatively represent this, we calculate spin-resolved current (I_S) at a particular voltage, V as [35],

$$I_S = \frac{|I_{min}(V) - I_{maj}(V)|}{I_{min}(V) + I_{maj}(V)} \tag{6.5}$$

where $I_{min/maj}(V)$ denotes minority/majority current. It can be evidently seen that I_S remains ~ 100 % up to 1.2 V and then reduces as the bias increases further (inset of Fig. 6.1(d)).

Very recent simultaneous measurements of conductance and thermoelectric properties in E-M-E systems stimulate us to discuss spin-dependent thermoelectric effects of the present nanojunction [11, 36]. The thermocurrent induced by temperature-difference in two electrodes is calculated by using Landauer formula [37]. The temperature difference is denoted as $T_{SD} = |T_S - T_D|$ where T_S and T_D are the temperatures of source and drain electrodes, respectively. The thermocurrent is formulated as,

$$I_{thermo,\sigma} = (\tfrac{e}{h}) \int \tau_\sigma [f_S(T_S, E) - f_D(T_D, E)] dE \tag{6.6}$$

where f_S and f_D are the Fermi distribution function for source and drain, respectively. Further, charge and spin current of the device is evaluated as $\mathrm{I_{charge}} = \mathrm{I_{maj}} + \mathrm{I_{min}}$ and $\mathrm{I_{spin}} = \mathrm{I_{maj}}$ - $\mathrm{I_{min}}$, respectively. In the linear response regime, we formulate spin-resolved Seebeck coefficient,

$$S_\sigma = -\tfrac{1}{eT} \tfrac{L_{1,\sigma}(T,\mu)}{L_{0,\sigma}(T,\mu)} \tag{6.7}$$

where $\mathrm{L_{n,\sigma}(T,\mu)} = \frac{1}{h} \int \tau_\sigma(E)(E-\mu)^n [\delta_E f(E,\mu,T)] dE$, T is temperature of the whole system and μ is chemical potential of electrodes [38]. To evaluate the charge-Seebeck coefficient $\mathrm{S_C}$, we consider the total transmission $\tau_{\mathrm{tot}} = \sum_\sigma \tau_\sigma$ whereas the spin-polarized Seebeck $\mathrm{S_S}$ is calculated by using the equation, $\mathrm{S_S} = \mathrm{S_{maj}}$ - $\mathrm{S_{min}}$ where $\mathrm{S_{maj}}$ ($\mathrm{S_{min}}$) is majority(minority)-spin Seebeck-coefficient [39]. Further, we define the figure of merit as,

$$ZT = \frac{S_C^2 GT}{\kappa_e + \kappa_{ph}} \tag{6.8}$$

where G is the charge conductance (i.e. $G = |L_{0,maj} + L_{0,min}|$ and κ_e and κ_{ph} are the electronic and phonon thermal conductance, respectively. The κ_e can be calculated as, $\kappa_e = 1/\mathrm{T}(L_2 - L_1^2/L_0)$ [40]. Importantly, as several studies have proposed different ways to suppress the κ_{ph} to the thermopower in molecular junctions [41–44], first we calculate $Z^{el}T$ neglecting this term. However, later on, we also calculate

thermoelectric figure of merit i.e. ZT including phonon contribution. Note that as molecular spin-crossover temperature $\approx$ 295 K [22], we consider the molecule with LS (HS) state when the average molecular temperature (i.e. $T_{mol} = (T_S + T_D)/2$) remain $\leq$ 295 K ($>$ 295 K).

We now calculate the thermally induced current ($I_{thermo,HS/LS}$) for both spin-states as a function of T_S at different T_{SD}. Note that as maximum T_{SD} = 100K, molecule can retain LS state up to $T_S \leq$ 345K, above which it transforms to HS state. Fig. 6.2(a,b) shows that $I_{thermo,HS}$ is several times higher than $I_{thermo,LS}$. Below a certain threshold T_S (T_{th}) i.e. $\sim$ 160-280K (depending on T_{SD}), $I_{thermo,LS}$ $\approx$ 0. Consequently, as shown in Fig. 6.2(c), at $T_S \approx$ 345 K and T_{SD} = 100K, (i.e. at T_C) thermocurrent can increase by $\sim$ 4 orders of magnitude upon spin-crossover. Moreover, the I_{on}/I_{off} ratio of I_{thermo} also reaches maximum of 10^{13} (see Fig. 6.2(c)). These results demonstrate that the molecular junction act as a high-performance-switching device. In fact, when $T_{SD} > 0$, it makes $[f_S(T_S, E) - f_D(T_D, E)] \neq 0$ and thermocurrent flows only if $\tau_{maj/min}(E)$ is finite at the applied temperature-difference window. Moreover, I_{thermo} is proportional to the area under the active transmission spectra. Now, as only HS state has finite transmission probability at and around E_F, $I_{thermo,HS}$ is much larger than $I_{thermo,LS}$ at spin-crossover temperature and moderate T_{SD}. Additionally, for LS state, T_S needs to cross T_{th} to switch-on thermo-transport by activating the closest transmission peak (i.e. at -0.12 eV).

Focusing on spin-polarized thermocurrent at HS state, we find from Fig. 6.1(c) that only τ_{min} is finite at and around E_F. Thus, applying a very small temperature-difference, we can obtain 100% spin-polarized carrier transport through the molecular junction (see Fig. 6.2(d) and the inset of it). Thus, the junction acts as a pure spin-polarized current generator. On the other hand, as the transmission function is spin-independent for LS state, thermocurrent becomes spin unpolarized here. Thus, controlling the temperature of the system, we can efficiently switch on/off the spin polarization of the thermocurrent.

From Fig. 6.2(a,b), we note that, (1) for both the spin-states, the I_{thermo} increases with T_{SD}. Essentially, as T_{SD} increases, more carriers become transport active , resulting in an rise in the total current. (2) $I_{thermo,HS}$ reaches its maxima at $T_S \approx$ 650K-700K and then decreases at higher T_S. In fact, at smaller T_S, minority-spin

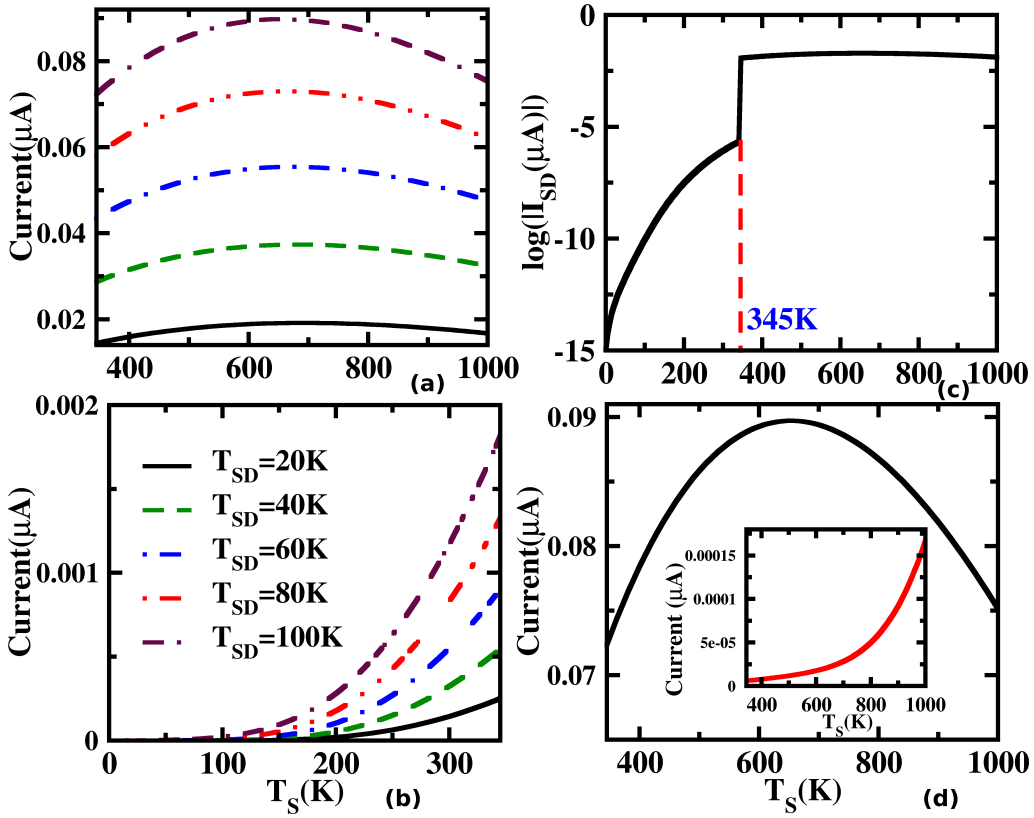

Figure 6.2: I_{thermo} versus T_S with various T_{SD} for (a) HS (b) LS state; (c) $\log(I_{SD})$ versus T_S plot with T_{SD} = 100K; (d) Minority-spin current for HS state versus T_S with T_{SD} = 100K. The corresponding majority-spin current is shown in the inset.

holes mostly carry the current, whereas electron-mediated current becomes significant at higher T_S and as stated later, it counteracts with the hole-current. Thus, the total $I_{thermo,HS}$ gets reduced for $T_S >$ 650K-700K. For LS state, as only hole-current gets generated within the temperature range of $0 \leq T_S \leq 345K$, $I_{thermo,LS}$ keeps on increasing with T_S (see Fig. 6.2(b)).

Next, we investigate the relation between S_σ and chemical potential (μ) of the electrodes. As $V_{SD} = 0$, the chemical potential of electrodes (i.e. μ_L, μ_R) are equal to the equilibrium E_F. Within linear response regime, we assume $T_S \approx T_D$ = 350K (250K) for HS (LS) state and vary μ as -1 $\leq \mu \leq$ 1. As the spin-dependent transmission spectra strongly influences the thermopower generation, this device exhibits an abrupt change in S_C and S_S during spin-crossover of the molecule (see Fig. 6.3(a)). Note that, as electrons and holes (i.e. active carriers for heat-conduction) move in

opposite directions to each other, one must break electron-hole symmetry to achieve non-zero thermopower at a particular μ. In other words, G(E) around μ must be asymmetric in nature. By tuning μ i.e. shifting the position of E_F, we eventually modify the carrier-types (i.e. electrons or holes). Note that, if electrons (holes) are the dominant carriers at E_F, thermopower becomes negative (positive). From Fig. 6.3(a-c) we find that (1) wherever G(E) is negligible or shows peak, thermopower is almost zero due to the presence of electron-hole symmetry; (2) S shows a finite value when finite conductance and electron-hole asymmetry appears simultaneously. Moreover, we also find a sign-change of thermopower wherever conductance peaks appear. This occurrence is due to the fact that, the carrier-type changes sign as μ crosses the peak position. As an example, at μ = 0, S_C of HS state ($S_{C(HS)}$) is -38 μV/K as electrons are the dominant thermopower-carrier (see Fig. 6.3(a)). However, at μ = -0.027eV, E_F reaches the peak of $G_{C(HS)}(E)$ where the electron-hole symmetry appears, resulting in $S_{C(HS)} \approx 0$ (Fig. 6.3(a,b)). As we move to higher negative μ value, electron-hole symmetry breaks down and holes become the dominant thermopower-carrier, making the $S_{C(HS)} > 0$. Notably, $S_{C(HS)}$ reaches the maximum value of 222 μV/K at = -0.21 eV where only holes are the active carriers. At more negative μ, electrons start contributing again, resulting in the reduction of $S_{C(HS)}$. (3) For the LS state, as τ_{maj} andτ_{min} are identical, the G and thermopower (S_{LS}) are completely spin-independent. Interestingly, the charge Seebeck coefficient for low-spin state, $S_{C(LS)}$ reaches a high value of -484 μV/K at μ = -0.84 eV due to sharp peak in the conductance (see Fig. 6.3(a,b)).

Furthermore, Fig. 6.3(a,c) evidently shows that one can control the magnitude and direction of charge and spin-thermopower to a great extent. In Fig. 6.3(a,c), we find three distinct regions for HS state (shown by blue arrows in Fig. 6.3(a)), (1) -0.02 eV $< \mu <$ 1 eV where $S_C - S_S$ and minority-spin electrons carry the thermopower; (2) -0.59 eV $< \mu < -0.02$ eV where $S_C < S_S$ and both spin channels are active; (3) -1 eV $< \mu < -0.59$ eV where $S_C \approx S_S$ and only majority-spin carry thermopower. Among all these, second region is the most important as S_S greatly exceeds S_C. In this region, thermopower carried by majority-spin electrons and minority-spin holes, move in opposite direction and get collected in different electrodes. It results in S_C to be small in magnitude while S_S becomes quite large. Particularly, at $\mu \approx -0.41$ eV where $S_C = 0$ but S_S = -289 μV/K (see the blue circles

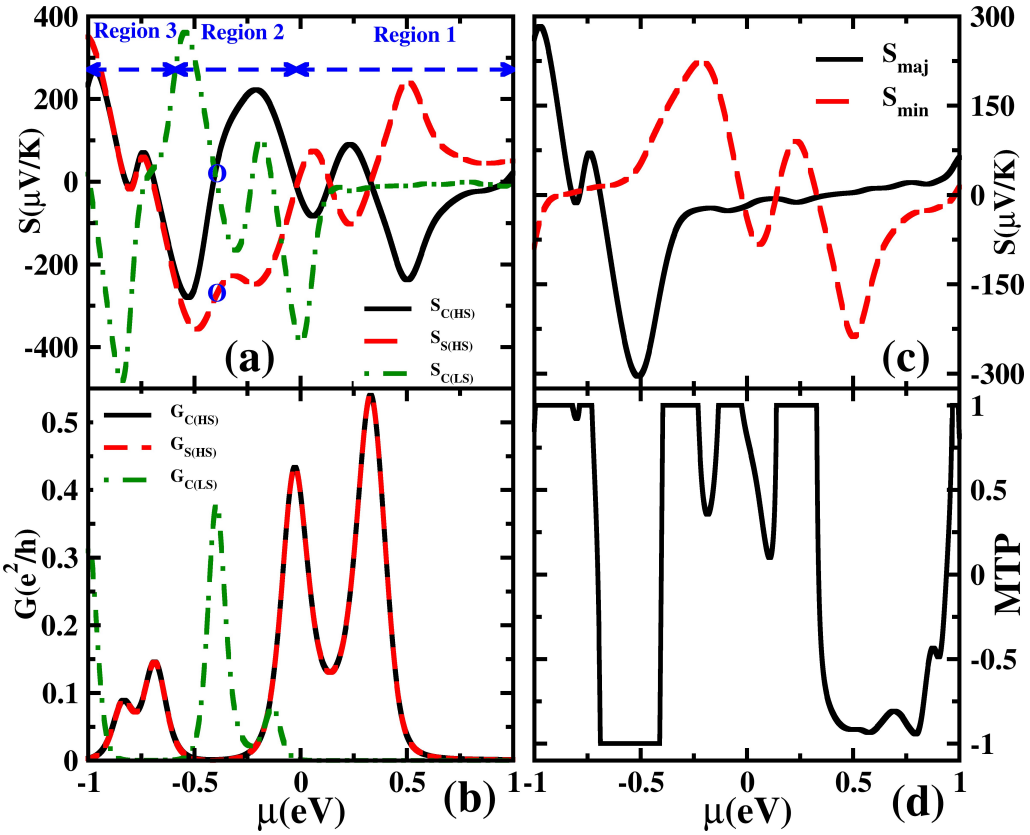

Figure 6.3: (a)$S_{C(HS)}$, $S_{S(HS)}$ and $S_{C(LS)}$ and (b) $G_{C(HS)}$, $G_{S(HS)}$ and $G_{C(LS)}$ as a function of μ. Three distinct regions in (a) are separated by blue arrows. At $\mu \approx$ -0.41 eV, values of S_C and S_S are pointed by blue circles. We consider $T_S \approx T_D = 350$K (250K) for HS (LS) state. (c) S_{maj}, S_{min} and (d) magnetothermopower (MPT) for HS state as a function of μ.

in Fig. 6.3(a)), we could achieve pure spin-thermopower without any charge component. For the LS state, as S_{LS} is spin-independent, we find $S_C = S_{LS}$ and $S_S = 0$. As the thermopower gets modified remarkably with the spin-crossover, we quantify this change by defining magnetothermopower as [45], $(S_{C(HS)} - S_{C(LS)}/S_{C(HS)} + S_{C(LS)})$ which is plotted in Fig. 6.3(d)). We find that magnetothermopower $\approx \pm 1$ which explicitly demonstrates the ability to tune the thermopower generation by controlling the spin-state of the molecule.

Finally, we investigate the efficiency of this molecular junction towards thermoelectric conversion. Here, figure of merit shows an oscillating behavior as conductance and thermopower are inversely correlated [46]. Considering $\kappa_{ph} = 0$, tuning the μ to -0.91 eV at HS state, results in the highest value of 4.65 for $Z^{el}T$ (see Fig. 6.4(a)). However as shown in Fig. 6.4(b), at LS state, we find highest $Z^{el}T$ as 20 which is quite higher than HS state.

Now, to include the phonon contribution to the thermal conductance, we use the equation $\kappa_{ph} = 3\kappa_0$ where $\kappa_0 = \pi^2 k_B^2 T/3h$ i.e. the quantum of thermal conductance [40, 47]. As can be seen in Fig 6.4(c,d), the position of peaks of ZT do not change even after inclusion of κ_{ph}. However, the relative magnitude of them get modified largely for both the spin states. Importantly, the absolute magnitude of ZT gets reduced due to phonon mediated thermal conductance.

Following the work by Chapuis *et. al.* [48], we find the heat transfer due to near-field radiation is $\approx 10^{3.5} W m^{-2} K^{-1}$ for our system. This quantity is quite negligible compared to the electronic heat transfer through molecular junction ($\approx 10^6(10^4) W m^{-2} K^{-1}$ for HS (LS) states). Thus, we can neglect the contribution of near-field radiative heat transfer for the present study.

6.4 Conclusions

In conclusion, we have discussed configurational changes and stability of different spin states during spin-crossover process. Upon spin-crossover, we surmise a huge modulation in electronic and thermoelectric entities. A large spin-crossover magnetoresistance in this SCO molecule based two-terminal device has been demonstrated. Moreover, for the HS state, the device shows efficient spin-filter property at low bias regime. The spin-crossover process also do a lot more to the thermoelectric entities:

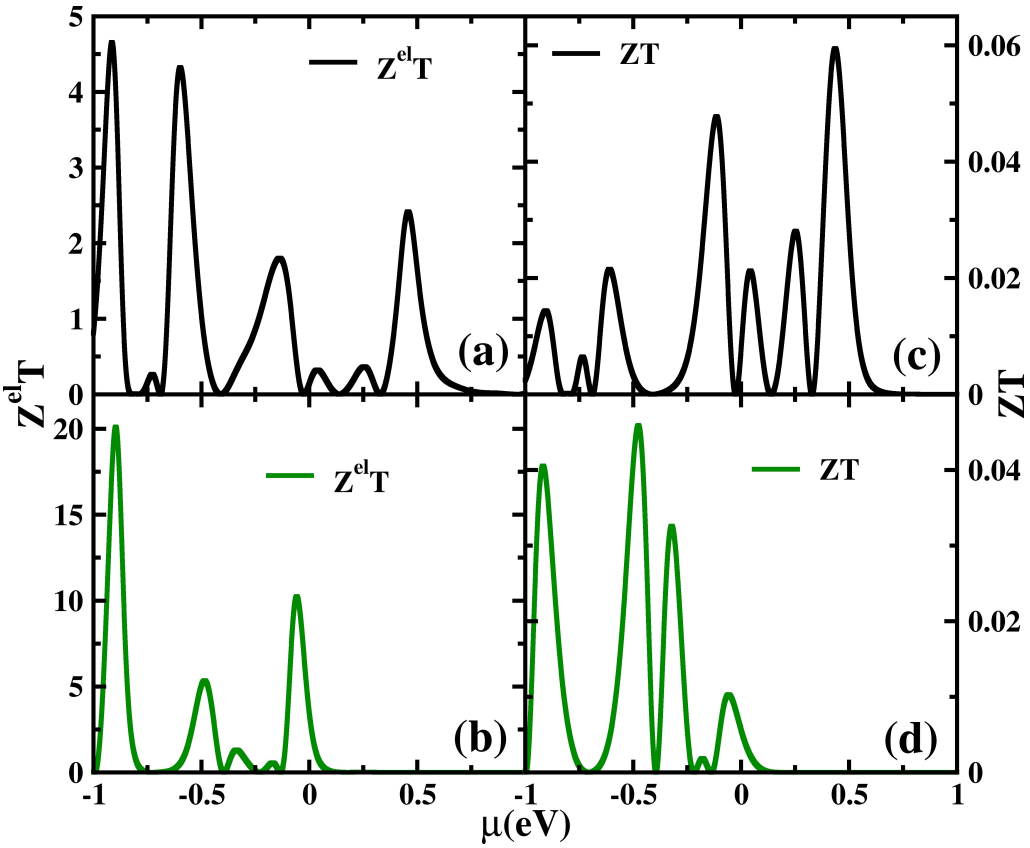

Figure 6.4: $Z^{el}T$ for (a) HS and (b) LS state; ZT for (c) HS and (d) LS state. We consider $T_S \approx T_D = 350K(250K)$ for HS (LS) state. Note that the position of peaks do not change with inclusion of phonon contribution. But relative peak-values do change.

(1) It can efficiently switch the magnitude as well as spin-polarization of the thermocurrent. We report that, thermocurrent is changed by ~ 4 orders of magnitude upon spin-crossover. (2) It also substantially affects the thermopower and consequently, the device shows extremely efficient SCMTP generation. Furthermore, in the certain range of μ, a pure spin-thermopower can be achieved for the HS state. (3) Interestingly, the large values of the figure of merit demonstrate a huge heat-to-voltage conversion efficiency of the device. The theoretical prediction of all these extraordinary properties in presently investigated SCO molecule based junction, will certainly make this study more impact in the field of spin caloritronics.

Bibliography

[1] L. Bogani and W. Wernsdorfer, Nat. Mater. **7**, 179 (2008).

[2] A. R. Rocha, V. M. Garcia-Suarez, S. W. Bailey, C. J. Lambert, J. Ferrer, and S. Sanvito, Nat. Mater. **4**, 335 (2005).

[3] S. Sanvito, Chem. Soc. Rev. **40**, 3336 (2011).

[4] Z. Xiong, D. Wu, Z. V. Vardeny, and J. Shi, Nature **427**, 821 (2004).

[5] A. J. Drew, J. Hoppler, L. Schulz, F. Pratt, P. Desai, P. Shakya, T. Kreouzis, W. Gillin, A. Suter, N. Morley, *et al.*, Nat. Mater. **8**, 109 (2009).

[6] P. Parida, A. Kundu, and S. K. Pati, Phys. Chem. Chem. Phys. **12**, 6924 (2010).

[7] D. Ghosh, P. Parida, and S. K. Pati, J. Phys. Chem. C **116**, 18487 (2012).

[8] P. Parida, S. K. Pati, and A. Painelli, Phys. Rev. B **83**, 165404 (2011).

[9] P. Reddy, S.-Y. Jang, R. A. Segalman, and A. Majumdar, Science **315**, 1568 (2007).

[10] Y. Dubi and M. Di Ventra, Rev. Mod. Phys. **83**, 131 (2011).

[11] J. R. Widawsky, P. Darancet, J. B. Neaton, and L. Venkataraman, Nano Lett. **12**, 354 (2011).

[12] G. E. Bauer, E. Saitoh, and B. J. van Wees, Nat. Mater. **11**, 391 (2012).

[13] K. Uchida, S. Takahashi, K. Harii, J. Ieda, W. Koshibae, K. Ando, S. Maekawa, and E. Saitoh, Nature **455**, 778 (2008).

[14] M. Mannini, P. Sainctavit, R. Sessoli, C. Cartier dit Moulin, F. Pineider, M.-A. Arrio, A. Cornia, and D. Gatteschi, Chem. Eur. J. **14**, 7530 (2008).

[15] M. Urdampilleta, S. Klyatskaya, J.-P. Cleuziou, M. Ruben, and W. Wernsdorfer, Nat. Mater. **10**, 502 (2011).

[16] T. Miyamachi, M. Gruber, V. Davesne, M. Bowen, S. Boukari, L. Joly, F. Scheurer, G. Rogez, T. K. Yamada, P. Ohresser, *et al.*, Nat. Commun. **3**, 938 (2012).

[17] N. Baadji and S. Sanvito, Phys. Rev. Lett. **108**, 217201 (2012).

[18] D. Aravena and E. Ruiz, J. Am. Chem. Soc. **134**, 777 (2011).

[19] B. Warner, J. C. Oberg, T. G. Gill, F. El Hallak, C. F. Hirjibehedin, M. Serri, S. Heutz, M.-A. Arrio, P. Sainctavit, M. Mannini, *et al.*, J. Phys. Chem. Lett. **4**, 1546 (2013).

[20] M. Bernien, D. Wiedemann, C. F. Hermanns, A. Kruger, D. Rolf, W. Kroener, P. Muller, A. Grohmann, and W. Kuch, J. Phys. Chem. Lett. **3**, 3431 (2012).

[21] P. Gütlich and H. A. Goodwin, *Spin crossover in transition metal compounds I* (Springer Science & Business Media, 2004).

[22] B. Schäfer, C. Rajnák, I. Šalitroš, O. Fuhr, D. Klar, C. Schmitz-Antoniak, E. Weschke, H. Wende, and M. Ruben, Chem. Commun. **49**, 10986 (2013).

[23] F. Prins, M. Monrabal-Capilla, E. A. Osorio, E. Coronado, and H. S. van der Zant, Adv. Mater. **23**, 1545 (2011).

[24] M. Frisch, G. Trucks, H. B. Schlegel, G. Scuseria, M. Robb, J. Cheeseman, G. Scalmani, V. Barone, . B. Mennucci, G. e. Petersson, *et al.*, "Gaussian 09," (2009).

[25] A. Droghetti, D. Alfè, and S. Sanvito, J. Chem. Phys **137**, 124303 (2012).

[26] A. D. Becke, J. Chem. Phys **98**, 5648 (1993).

[27] C. Lee, W. Yang, and R. G. Parr, Phys. Rev. B **37**, 785 (1988).

[28] C. Adamo and V. Barone, J. Chem. Phys **110**, 6158 (1999).

[29] J. Heyd, G. E. Scuseria, and M. Ernzerhof, J. Chem. Phys **118**, 8207 (2003).

[30] M. Brandbyge, J.-L. Mozos, P. Ordejón, J. Taylor, and K. Stokbro, Phys. Rev. B **65**, 165401 (2002).

[31] S. Datta, *Electronic Transport in Mesoscopic Systems* (Cambridge university press, 1997).

[32] M. A. Reed, C. Zhou, C. Muller, T. Burgin, and J. Tour, Science **278**, 252 (1997).

[33] H. Häkkinen, Nat. Chem. **4**, 443 (2012).

[34] J. M. Soler, E. Artacho, J. D. Gale, A. Garc´ia, J. Junquera, P. Ordejón, and D. Sánchez-Portal, J. Phys. Condens. Matter. **14**, 2745 (2002).

[35] P. Parida, E. A. Basheer, and S. K. Pati, J. Mater. Chem. **22**, 14916 (2012).

[36] S. Guo, G. Zhou, and N. Tao, Nano Lett. **13**, 4326 (2013).

[37] M. Zeng, Y. Feng, and G. Liang, Nano Lett. **11**, 1369 (2011).

[38] Y. Liu, X. Yang, F. Chi, M. Si, and Y. Guo, Appl. Phys. Lett. **101**, 213109 (2012).

[39] M. Czerner, M. Bachmann, and C. Heiliger, Phys. Rev. B **83**, 132405 (2011).

[40] Y. Dubi and M. Di Ventra, Phys. Rev. B **79**, 081302 (2009).

[41] H. Nakamura, T. Ohto, T. Ishida, and Y. Asai, J. Am. Chem. Soc. **135**, 16545 (2013).

[42] C. Finch, V. Garcia-Suarez, and C. Lambert, Phys. Rev. B **79**, 033405 (2009).

[43] J. P. Bergfield, M. A. Solis, and C. A. Stafford, ACS Nano **4**, 5314 (2010).

[44] Y.-S. Liu, Y.-R. Chen, and Y.-C. Chen, ACS Nano **3**, 3497 (2009).

[45] K. Zberecki, M. Wierzbicki, J. Barnaś, and R. Swirkowicz, Phys. Rev. B **88**, 115404 (2013).

[46] M. Zeng, W. Huang, and G. Liang, Nanoscale **5**, 200 (2013).

[47] D. Segal, A. Nitzan, and P. Hänggi, J. Chem. Phys **119**, 6840 (2003).

[48] P.-O. Chapuis, S. Volz, C. Henkel, K. Joulain, and J.-J. Greffet, Phys. Rev. B **77**, 035431 (2008).

Chapter 7

Spin-state Switching of Manganese Porphyrin by Conformational Modification*

7.1 Introduction

As we discussed earlier, small isolated molecules with stable paramagnetic ordering is the perfect ingredient for the molecular spintronics as well as spin-caloritronic applications [1, 2]. And in this regard, spin bearing transition metal (TM) atom containing organometallic molecules can be considered as the appropriate choice [3–5]. Among several kinds of organometallic systems, first-row transition metal (TM) centred metalloporphyrins (TMP), having localized 3d-states, are one of the hugely explored systems [6–11]. These metalloporphyrin molecules are commonly found in various biologically important macromolecules such as chlorophyll, cytochrome, heme etc. [12]. Apart from biological sources, all 3d-TM incorporated porphyrin molecules have been synthesized and are well characterized experimentally [13]. Recent experimental as well as theoretical studies have already revealed a number of fascinating electronic and spintronics properties like controlled magnetic ordering [6, 8, 9], tuned magnetic anisotropy [14], rectification of current [15], gas-sensing

*Works reported in this chapter is published in: D. Ghosh, P. Parida and S. K. Pati, J. Phys. Chem. C, (just accepted)(2016). Reprinted (adapted) with permission from American Chemical Society

[16], current switching [17], spin-filtering [18], long-range electron tunnelling [19] etc. in different porphyrin-based systems both in presence as well as in absence of suitable substrate.

Further, in spintronics, one of the major targets is to control the spin-states of the magnetic material by various external influences such as light-irradiation [20], temperature-control [4], molecular adsorption[7, 9], substrate interaction [8] etc. Recently, a number of studies demonstrate an efficient way to manipulate the spin-state of metalloporphyrins (TMP) by reversibly attaching small gaseous molecules at the metal centre [7, 9, 10, 21]. Wackerlin *et. al.* demonstrate that nature and strength of magnetic interaction between modified TMP and ferromagnetic surfaces (e.g. Ni(001)) can be reversibly tuned by adsorbing and thermally desorbing nitric oxide (NO) molecule [7, 9]. Further, Kim *et. al.* applied the same idea to reversibly switch off and on the Kondo effect in NO-ligated substituted cobalt porphyrin (CoP) on Au(111) surface [10]. Apart from surface-molecule interaction, the molecular adsorption/desorption also substantially modifies the spin-polarized electron transport through metalloprophyrins in a two-terminal spintronic devices. Kondo *et. al.* theoretically predicted that upon adsorption of carbon monoxide (CO) on FeP, the spin polarized carrier transport in this nano-junction gets suppressed [16]. However, in all these cases, small gaseous molecules have to be adsorbed and thermally desorbed repeatedly to tune the spin state of the metalloporphyrins [7]. This process is quite energy consuming and not suitable for practical purpose as desorption step generally requires very high temperature [7, 9].

In this chapter, first we thoroughly investigate the effects of NO binding on TM of TMP (TMs are V to Co). Further, we focus on exploring the conformation-induced spin-state manipulation of NO-ligated manganese porphyrin (MnP-NO), adsorbed on the (111) surface of gold. Initially NO molecule binds to Mn atom in the ground-state linear conformation. However, this linear bond-conformation can reversibly be modified to metastable bent Mn-NO geometry by laterally moving the closely placed gold scanning tunneling microscope (STM) tip in either constant tunneling current or constant tip-height mode. Interestingly, along with this conformational change between linear and bent conformations, one can efficiently switch-off (S = 0) and on (S = 1) the spin-moments of the MnP. Moreover, non-equilibrium Green's function (NEFG) based transmission calculations prominently demonstrate the dependence of

electron and spin-transport characteristics upon the spin-state of the MnP-NO based molecular bridge. In particular, spin-polarized current transport can be switched-off and on reversibly along with the conformational modifications. Furthermore, investigations about the thermoelectric properties of these nano-junctions reveal their potential usage in spin-caloritronic applications. Most importantly, controlled tuning of Fermi level of the system eventually results in generation of pure spin-thermopower without any charge component in this device.

7.2 Computational Details

We perform spin-polarized density functional theory (DFT) based calculations as implemented in Vienna Ab initio Simulation Package (VASP) for the study [22]. Projected augmented-wave (PAW) potentials are used with a plane-wave basis set having a cutoff of 400 eV for all the calculations [23, 24]. Popular Perdew-Burke-Ernzerhof (PBE) functional within the generalized gradient approximation (GGA) is used to include exchange-correlation contributions [25]. We carry out geometry optimizations for all the systems without applying any symmetry constraints and interatomic forces are relaxed up to 0.01 eV/Å. Further, the total energy convergence is considered as 10^{-8} eV for all static calculations. As only GGA functionals are not adequate to describe partially occupied, strongly localized d-orbital containing atoms, we use widely applied GGA + U method [26, 27]. In this method, strong localization of 3d-electrons of TMs are tackled by incorporating Coulomb and exchange corrections, whereas all s- and p-orbitals are described by GGA functionals alone. Except for NO adsorbed MnP molecules, we consider correlation energy (U) as 4 eV and exchange energy (J) as 1 eV, which are well testified for different metalloporphyrin complexes, explored by previous studies [7, 8, 11, 28, 29]. However, as these parameters fail to reproduce experimental ground-state geometry of NO adsorbed MnP, [7, 30] we re-parametrize U and J as U = 2, J = 1 for this particular molecule. We also consider Vosko-Wilk-Nusair modification for spin-polarized calculations to interpolate the correlation energy [31]. Note that good agreement with available experimental data of most of these metalloporphyrin molecules strongly validate our overall computational approach for the present study. To simulate the gold (111) surface, we consider three atomic layers of (8×8) Au where each layer

contains 64 atoms. For all the surface-included calculations, we fix the geometry of surface Au atoms to reduce computational effort. Note that, previous reports on adsorption of MnP on Au(111) with and without performing relaxation of the surface show a negligible difference in geometric, electronic and magnetic properties [32]. To sample the reciprocal space, we use 2×2×1 Monkhorst-Pack k-points. As standard PBE functionals-based DFT calculations can not include the van der Waals interaction between MnP and Au(111) surface properly, we apply DFT-D2 method as suggested by Grimme and implemented in VASP [33]. For electronic transport property calculations, we use NEGF methodology extended for spin-polarized systems, as implemented in the TranSIESTA package [34]. Details of transport calculations can be found in Chapter 6.

7.3 Results and Discussion

7.3.1 Binding of NO with 3d Metalloporphyrins

Geometry optimization reveals that all 3d-TM (V-Co) incorporated porphyrin molecules (i.e. TMP) are planar and TM atoms get accommodated exactly at the middle of the symmetric pore of the porphyrin ring. All these metalloporphyrin molecules exhibit paramagnetic ground-state with the spin-states of S = 3/2, 2, 5/2, 1 and 1/2, where incorporated TMs are V, Cr, Mn, Fe and Co, respectively. Spin density of these molecules predominantly localize at the 3d-orbitals of TM atoms. However, 2p orbitals of each pyrrolic N atom also show minor opposite spin-polarization. Microscopic details about structural, electronic and magnetic properties of these molecules can be found in several previous studies [29, 35]. Note that, two hydrogen atoms of oppositely positioned bridging carbon of the molecule have been substituted by ethynyl groups to make the metalloporphyrin rings suitable for electronic transport measurements (discussed in later part of the chapter). As shown in Fig. 7.1 (MnP as an example), upon exposure to gaseous NO, these metalloporphyrin molecules form stable axial coordinate-bond with nitrogen of NO. The binding can happen in either of two geometries i.e. linear ($TMP - NO_{linear}$) or bent ($TMP - NO_{bent}$). More importantly, relative stability between these two binding modes of TM-NO perfectly agree with Enemark-Feltham's prediction which

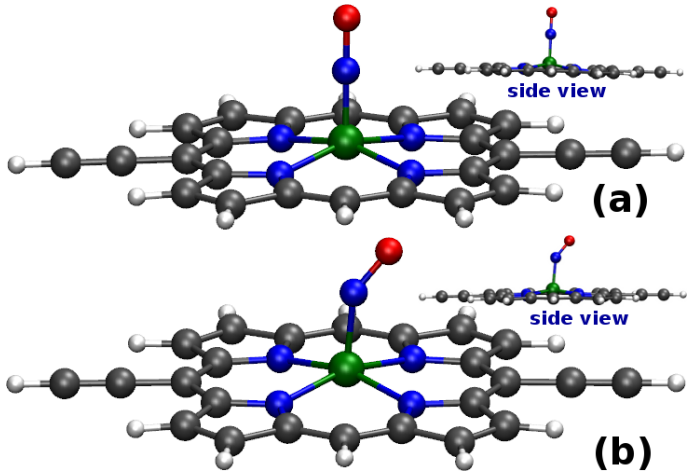

Figure 7.1: Optimized geometry of (a) $MnP - NO_{linear}$ and (b) $MnP - NO_{bent}$. Side view of the structures are shown in inset. White, black, blue, red and green atoms represent H, C, N, O and Mn, respectively.

correlates the total number of d-electrons in TM and π^* orbital-electrons of NO to the TM-N-O angle [36, 37]. Metalloporphyrins of early transition metals i.e. VP, CrP and MnP form almost perfect linear TM-N-O bonding ($\angle TM-N-O \approx 180°$). Whereas CoP (i.e. late transition metal containing porphyrin) gets stabilized in proper bent conformation ($\angle Co - N - O \approx 122°$). FeP shows an intermediate value of Fe-N-O bond angle i.e. $\approx 143°$. As V, Cr and Mn atoms have low-lying singly occupied $3d_\pi$ orbitals (i.e. $3d_{xz}$ and $3d_{yz}$), orbital of NO forms d_π-p_π back-bonding with these metal atoms, resulting in linear binding between TM and NO (see Fig. 7.2 (a)). However, for CoP where metal $3d_\pi$ orbitals are completely filled, non-bonded $3d_{z^2}$ orbital only remains as singly occupied molecular orbital. Thus, the p_π^* orbital of NO creates in-phase σ-type bonding with $3d_{z^2}$ orbital of Co, resulting in bent Co-NO bond in $CoP - NO_{bent}$ (see Fig. 7.2 (b)). Now, as shown in Fig. 7.1 (d), in case of FeP, p_π^* orbital of NO weakly overlaps with $3d_{z^2}$ orbital of Fe and consequently forms bonding molecular orbital where an unpaired electron gets accommodated. Furthermore, the p_π^* orbitals of NO hybridize with partially occupied $3d_\pi$ orbitals of Fe as well (see Fig. 7.1 (c)). Thus, due to the involvement of both $3d_{z^2}$ and $3d_\pi$ orbitals towards NO binding, an intermediate Fe-N-O bond angle (i.e. 143°) appears in this case. This Fe-N-O bond is also quite flexible in nature where linearly bonded (i.e. $\angle Fe - N - O \approx 180°$) FeP-NO is only

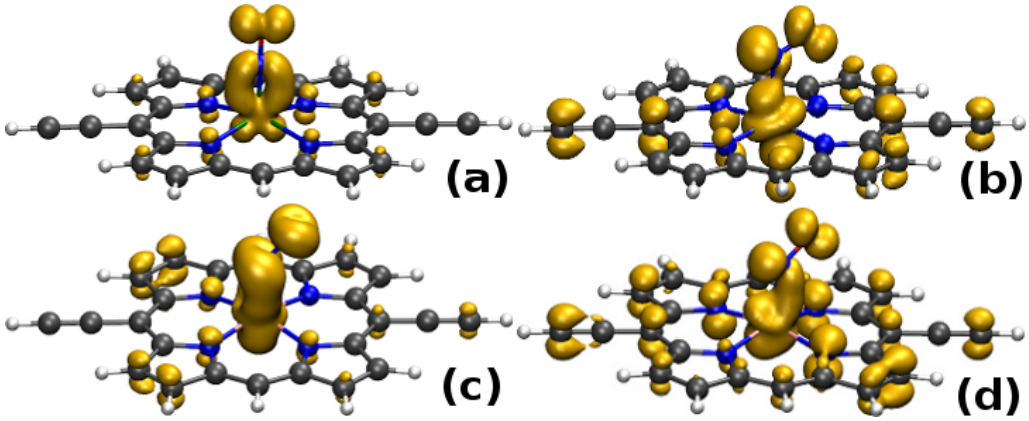

Figure 7.2: Partial charge densities of (a) d_{π}-p_{π}* orbital of $MnP-NO_{linear}$ (b) $3d_{z^2}$-p_{π}* orbital of $CoP-NO$, (c) d_{π}-p_{π}* orbital and (d) $3d_{z^2}$-p_{π}* of $FeP-NO$ The isosurface value is considered as 0.025 e $\mathring{A}^{-3}$ for all charge densities.

0.13 eV higher in energy than the ground state bent geometry [38]. Interestingly, the energy barrier between linear and bent conformers of MnP-NO also appears to be small. The ground state i.e. $MnP-NO_{linear}$ remains energetically more stable by 34 meV than the intermediate bent geometry ($\angle Mn-N-O \approx 143°$). Thus, the bent conformation can be considered as a metastable equilibrium point in the potential energy surface with respect to bending distortion. Most importantly, the spin-state of MnP which shows low-spin configuration i.e. S = 0 due to linear NO binding, switches on the spin-moment and stays in an intermediate spin-state i.e. S = 1 as binding mode changes to bent conformation. However in case of Fe, note that, experimentally [39] as well as theoretically [38] observed paramagnetic nature of FeP-NO (i.e. S = 1/2) remains unaffected with respect to the change in Fe-NO binding conformation. In the present study, as we are interested on the complete spin-switching of metalloporphyrin by precisely controlling the TM-NO binding mode, MnP-NO appears to be most appropriate one to consider. Note that, though V-porphyrin also shows prominent conformation-induced spin-switching, we are excluding it from our discussion due to its poor stability in VP form [40]. Thus, in the following sections, we focus on the microscopic reasons behind the spin-switching of this molecule upon conformational change of Mn-NO bond.

7.3.2 Binding of NO with MnP

Binding energies of NO to MnP in its linear and bent conformations are evaluated as -1.56 eV and -1.52 eV, respectively. This certainly indicates strong coordination bond formation between Mn and N of NO. Moreover, the axial coordination causes minor structural modifications to the MnP molecule. Most notably, Mn atom goes out of the porphyrin ring plane (defined by the four pyrrolic nitrogen atoms) by 0.32 Å (0.29 Å) for linear (bent) binding mode. This out-of-plane movement of metal upon uniaxial coordination can also be observed for other metalloporphyrin systems [28, 37]. Moreover, forceful impose of the planarity (i.e. keeping Mn atom inside porphyrin core) on $MnP-NO_{linear}$ ($MnP-NO_{bent}$), destabilizes the molecule by an energy of 0.52 eV (0.32 eV). As Mn-NO bond forms due to the significant $3d_{\pi}$-p_{π}* (for linear conformer, Fig. 7.3 (a) and Fig. 7.2 (a)) as well as $3d_{z^2}$-p_{π}* (for bent conformer, Fig. 7.3 (b) and Fig. 7.3 (c,d)) orbital overlaps, Mn atom lifts-up from the core of the cavity to ease these hybridizations. The out-of-plane shift of Mn also assists the core of porphyrin ring to reduce the in-plane electron-accumulation, which arises due to double (for linear conformer) or single (for bent conformer) occupation of non-bonding d_{xy} orbital of Mn. Note that, stronger $3d_{\pi}$-p_{π}* orbital overlap and complete occupancy of in-plane d_{xy} orbital for linear binding mode results in higher out-of-plane shift of Mn atom than the other one.

Comparing optimized structures of $MnP-NO_{linear}$ and $MnP-NO_{bent}$, it's apparent that conformational modification only alters the $Mn-N_{NO}$ bond length and keeps rest of the MnP geometry almost unchanged. Now question arises, why does the Mn-N(NO) bond length changes with this conformational change? As shown in Fig. 7.2 (a) and Fig. 7.3 (a), linearly bonded NO acts like a π-acid ligand where along with σ-donation, π-back-donation also occurs through d_{π}-p_{π}* bonding, resulting in partial double bond character of $Mn-N_{NO}$ bond. However, for bent conformation, just as an anionic π-ligand, NO forms only a single σ-bond with $3d_{z^2}$ of Mn (Fig. 7.3 (b)) and severely weaken the back-donation. Thus, $Mn-N_{NO}$ bond-length remain longer in bent conformation than that of linear one.

Most importantly, though conformational modification in Mn-NO binding mode exerts an insignificant effect upon the overall structures of MnP-NO conformers, it can efficiently switch off/on the molecular spin moment. In Fig. 7.3 (a), partial density of states (pDOS) for 3d-orbitals of Mn and 2p-orbitals of NO of $MnP-NO_{linear}$

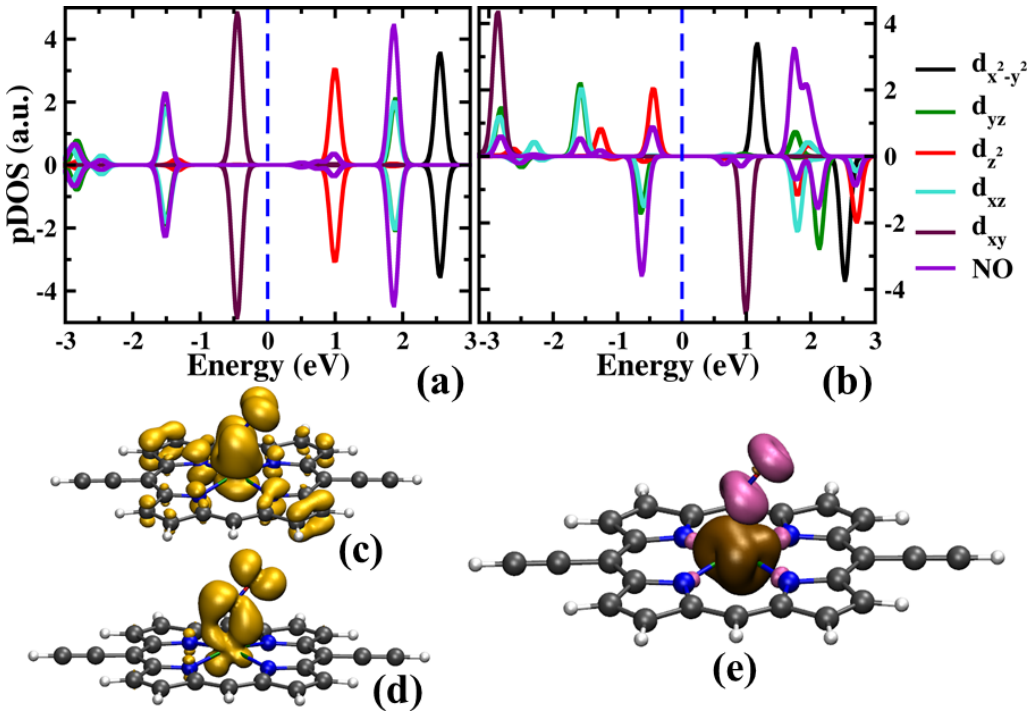

Figure 7.3: Partial density of states (pDOS) of (a) $MnP-NO_{linear}$ and (b) $MnP-NO_{bent}$ molecules. (c) d_{π}-p_{π}* orbital, (d) $3d_{z^2}$-p_{π}* orbital and (e) spin density plot for $MnP-NO_{bent}$. The isosurface values are considered as 0.015 and 0.05 e $\mathring{A}^{-3}$ for charge and spin density, respectively.

depict that spin-degenerate $3d_{\pi}$ orbitals of Mn overlap with π* orbitals of NO and form spin unpolarized d_{π}-p_{π}* back-bonded molecular states. Further, comparing pDOS for 3d-orbitals of Mn in MnP (not shown in present thesis) and $MnP-NO_{linear}$ (Fig. 7.3 (a)) evidently demonstrates that upon axial ligation to linear NO, $3d_{z^2}$ and $3d_{x^2-y^2}$ orbitals shift to higher energy region due to strong crystal field splitting. This alteration in 3d orbital-ordering results in an increased electron population in non-bonding $3d_{xy}$ and bonded $3d_{\pi}$-p_{π} orbitals, however this makes $3d_{z^2}$ and $3d_{x^2-y^2}$ orbitals completely empty. Thus, in the linear binding mode, π-acid ligand NO acts as a strong field ligand and pairs up all initially unpaired electrons, exhibiting a spin crossover from high-spin state (S = 5/2) to low-spin state (S = 0). This reduction of spin-moment in MnP upon exposing it to gaseous NO has already been demonstrated experimentally by observing absence of X-ray magnetic circular dichroism (XMCD) signals [7]. On the other hand, in bent conformation,

majority-spin $3d_{z^2}$ and minority-spin $3d_{\pi}$ orbitals of Mn mainly overlap with π*-orbitals of NO (Fig. 7.3 (b)). Whereas, electrons from majority-spin $3d_{\pi}$ and $3d_{xy}$ orbitals remain almost inert to the NO binding and result in appearance of a finite magnetic moment which arises from ≈ 2.5 spin-1/2 objects of the Mn atom. Furthermore, as minority-spin density gets localized on bent NO, the total magnetic moment of $MnP - NO_{bent}$ reduces to 2 spin-1/2. Spin density in Fig. 7.3 (e), also clearly shows major localization of oppositely polarized spins over Mn and NO. Therefore, in its bent geometry, NO acts as σ-donor weak-field ligand and keeps 3d-orbitals partially filled. Experimentally, upon conformational change in Mn-NO binding, XMCD-based spectroscopic study can prominently exhibit the reappearance of characteristic spectral signature which indicates the stability of magnetically active state of $MnP - NO_{bent}$.

7.3.3 Effect of Au(111) surface

As mentioned earlier, generally metalloporphyrin molecules get chemisorped or physisorped on the well defined metallic surfaces (magnetic or non-magnetic) and exhibit a number of substrate-assisted exciting properties [7, 8, 10, 41]. However, as the present study is majorly focused on the modulation of molecular electron and heat transport characteristics upon conformation-induced spin-state switching of MnP-NO, a weakly interacting surface should be a perfect choice. Thus, we consider non-magnetic Au(111) plane as supporting surface to deposit the MnP molecules. Several studies already have demonstrated an almost planar geometry for pristine as well as substituted metalloporphyrine molecules, adsorb on Au(111) with relatively weak molecule-surface interaction [10, 29, 42]. Here, we choose three different highly possible adsorbing sites i.e. on-top, bridge and hollow-sites of Au(111) plane to place the centre of mass of MnP i.e. Mn atom. Interestingly, relaxing the geometry of surface-adsorbed MnP on these different sites, we find quite similar binding energy for all of them (difference in energy is of few meV). This site-unspecific interaction between MnP and Au surface indicates characteristic weak surface-molecule overlap. However, after relaxation, Mn atom gets shifted from porphyrine plane by 0.23 Å towards metallic surface, whereas whole molecule remains 3.11 Å away from the surface. Further, axially coordinating NO in its different conformations (i.e. linear and bent), we optimize the MnP-NO on Au surface. Here also, we

keep Mn of MnP-NO in those three different adsorbing sites (see Fig. 7.4 (a) for $MnP - NO_{linear}$ on-top) and find a negligible site-specificity of adsorption. The axial coordination of NO to MnP does not alter the MnP-Au(111) distance (i.e. 3.07 Å) also. Focusing on electronic structure, it's evident that in presence of Au surface states, narrow molecular states of MnP-NO become broadened (see the molecular DOS in Fig. 7.4 (b)) which indicate a weak molecule-surface coupling, without formation of any strong chemical bonds. Binding energies between NO and MnP for their linear and bent conformations appear as -1.19 eV and -1.16 eV, respectively. Linear (bent) Mn-NO binding energy in presence of Au surface become weaker by 0.37 eV (0.36 eV) due to the competitive binding of surface Au atoms with Mn in trans-position with respect to NO. Note that, as NO coordinates much strongly with Mn in either of its conformations than the Au surface, Mn atom moves out of the porphyrin plane by $\approx$ 0.2 Å towards NO. Most importantly, conformation induced spin-state switching of MnP-NO remains unchanged even in the presence of Au surface. After adsorbing to Au surface, $MnP - NO_{linear}$ and $MnP - NO_{bent}$ still remain in the spin-state of S = 0 and S = 1, respectively. As shown in Fig. 7.4 (c), spin-density plot for $MnP - NO_{bent}$ on Au(111) surface clearly depicts that only 3d-orbitals of Mn and 2p-orbitals of NO remain spin-polarized by majority and minority spins, respectively. The initially non-magnetic Au(111) surface does not show any signature of induced spin-polarization due to weak interaction with adsorbate molecule. Thus, unlike other magnetic surfaces, Au surface remain completely inactive towards spin-spin interaction at molecule-surface interface. As Au(111) surface does not have any significant influence on various properties of MnP-NO molecules, we can safely exclude the presence of this inert adsorbent for further calculations.

7.3.4 STM-tip induced conformational change

To reversibly manipulate the conformation of MnP-NO between linear and bent form, we propose the use of an atomically sharp nonmagnetic gold STM tip [43]. STM tip is widely used to precisely modify the conformation as well as magnetic, electronic, mechanical properties at a single molecular level [14, 17, 43, 44]. Particularly, lateral motion of the tip along a predefined path has been implemented to induce precise changes in the molecular geometry [43, 45]. Moresco *et. al.* successfully achieved reversible conformational switching in a substituted CuP molecule by

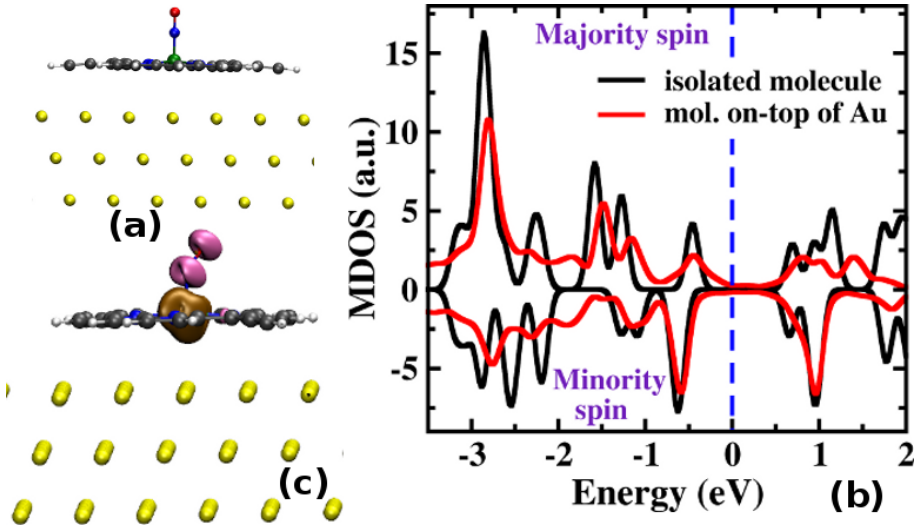

Figure 7.4: (a) Side view of optimized geometry of $MnP - NO_{linear}$ on-top of Au(111) surface. (b) Molecular DOS for isolated $MnP - NO_{bent}$ and at on-top of Au(111) surface. (c) Spin density plot for $MnP - NO_{bent}$ on-top of Au(111). Isosurface is considered as 0.05 e $\mathring{A}^{-3}$.

lateral STM-tip induced manipulation [17]. Very recently, Saywell *et. al.* also manipulated the conformation of single organometallic chain with the same approach [45]. These observations strongly support our computational approach to achieve the controlled conformational switching of MnP-NO.

We model the gold tip by taking pyramidal cluster, containing 4 Au atoms in it. This bare Au_4 cluster geometry has been optimized without any constraint and kept fixed for further calculations. This cluster model has successfully been used in several earlier studies to mimic the effect of STM tip [46, 47]. We also optimized the Au_4 coordinates along with MnP-NO molecules but do not find any major difference in the results. Further test calculations considering larger Au cluster with 10 Au atoms eventually produces the same results.

We propose the following scheme to realize STM-tip assisted spin-switching in MnP-NO: initially, metalloporphyrin molecule can be deposited on the Au(111) surface at low temperature and ultrahigh-vacuum condition as suggested by several previous reports [9, 10]. Then gaseous NO molecules can be exposed to the adsorbed MnP. In the ground-state, NO binds to Mn centre in linear mode as discussed earlier. Now, using the STM-imaging, Mn-NO bond can be exactly located. At cryogenic temperature, the STM tip should be placed so close to O of NO that tip-apex Au

atom (Au_{tip}) can exerts a chemical binding force on oxygen [43]. Further, lateral movement of the tip in constant height mode efficiently modifies the binding of Mn-NO from ground-state linear to metastable bent conformation and vice versa. Lastly, tip can be removed from the vicinity of Mn-NO after achieving the desired molecular geometry as both the conformers are quite stable at low temperature.

To find the characteristic threshold tip height (i.e. the tip-ON distance where the interaction is strong enough for mechanical manipulation) [43], we relaxed the isolated Au_4-ON cluster and consider the required height same as optimized Au-O bond length i.e. 2.18 Å. Further, to simulate the STM-tip assisted conformational change, we firstly optimize the geometry of $MnP - NO_{linear}$ by keeping the STM-tip ($MnP - NO_{linear}$-Au_4) fixed at the threshold height. NO remains almost linearly bonded to Mn i.e. $\angle Mn - N - O \approx 168^\circ$ (see Fig 7.5 (a)). Binding energy between $MnP - NO_{linear}$ and Au_4 also appears to be weak i.e. 0.08 eV only. Further, we shift the tip laterally by 1 Å through the middle of two $Mn - N_{pyrrole}$ bond. With this precise manipulation, Mn-NO bond modifies its geometry to the bent conformation. As shown in Fig. 7.5 (b), in $MnP - NO_{bent}$-Au_4, we find $\angle Mn - N - O \approx 132^\circ$ and interaction between tip and NO becomes much stronger as the binding energy is calculated as 0.58 eV. Most importantly, as binding between Mn and NO is much more stronger than the interaction between tip and NO, this tip-induced manipulation is too weak to break Mn-NO bond. However, it is evident that along with the structural changes, spin-state which remains as S = 0 for $MnP - NO_{linear}$-Au_4, becomes S = 1 for $MnP - NO_{bent}$-Au_4. Moreover, even if the tip is removed , the MnP-NO structure remains in its bent metastable state where $\angle Mn - N - O \approx 143^\circ$ and spin-state S = 1. Thus, by mechanically bending the linear Mn-N-O bond, one can switch the spin-state of MnP-NO from off to on state.

7.3.5 Electron Transport Properties

In the following section, we explore how the electron transmission gets modified along with the conformational change in MnP-NO. At this point, firstly, we make sure that localized-orbital basis-set incorporated code, SIESTA (used for further calculations)[48], qualitatively reproduces the VASP calculated electronic and magnetic properties of MnP-NO. Further, as discussed earlier, to calculate the molecular

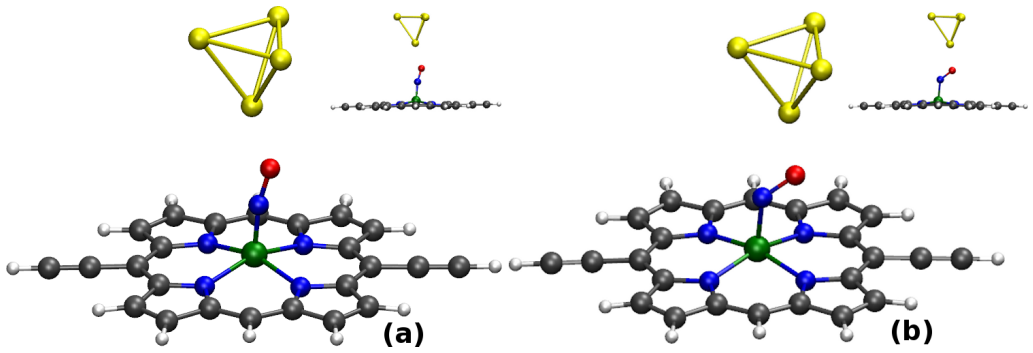

Figure 7.5: Optimized geometry of (a) MnP − NO_{linear}-Au_4 and (b) MnP − NO_{bent}-Au_4. Side view of the structures are shown in inset.

transmission, we sandwich the MnP molecule in between two semi-infinite gold electrodes and name them as E-M-E. Each of these electrodes are modeled by considering a non-magnetic 4×4×4 bulk gold (Au (111) plane), containing 48 gold atoms. To have strong coupling between molecule and electrodes, we substitute the hydrogen of ethynyl group with thiol (-SH) in either side of metalloporphyrin molecule. Following the same sequence of steps as discussed in Chapter 6, we optimize E-M-E.

As shown in Fig. 7.6 (a,b), the transmission function near the E_F gets modified substantially as STM-tip induces conformational change in MnP-NO. Notably, the transmission function which is spin-independent for MnP − NO_{linear} based molecular bridge, switches on strong spin-polarized nature in its bent conformation. To gain a microscopic understanding about these conformation-induced modifications of transmission spectra, we analyze the DOS and molecular pDOS of E-M-E system. As shown in Fig. 7.6 (a-d), positions of transmission peaks at both the conformations exhibit a prominent correlation with the peaks appearing in molecular pDOS spectra. Fundamentally, transmission peaks appear only when narrow molecular states resonate with the states of electrodes. Now, for MnP − NO_{linear}, as all the molecular states are spin-independent (i.e. either completely filled or completely empty), transmission through these states obviously remain spin-unpolarized. Further, near to the E_F, the transmission spectra shows prominent resonating peaks i.e. peak 1 and 2. As depicted in Fig. 7.7 (a,b), the charge density of the states of corresponding transmission peaks are totally delocalized over the whole molecular bridge and form suitable resonating channel for carrier transmission between two electrodes. Along with π-orbitals of conjugated porphyrin ring, $3d_{xy}$ and $3d_{z^2}$

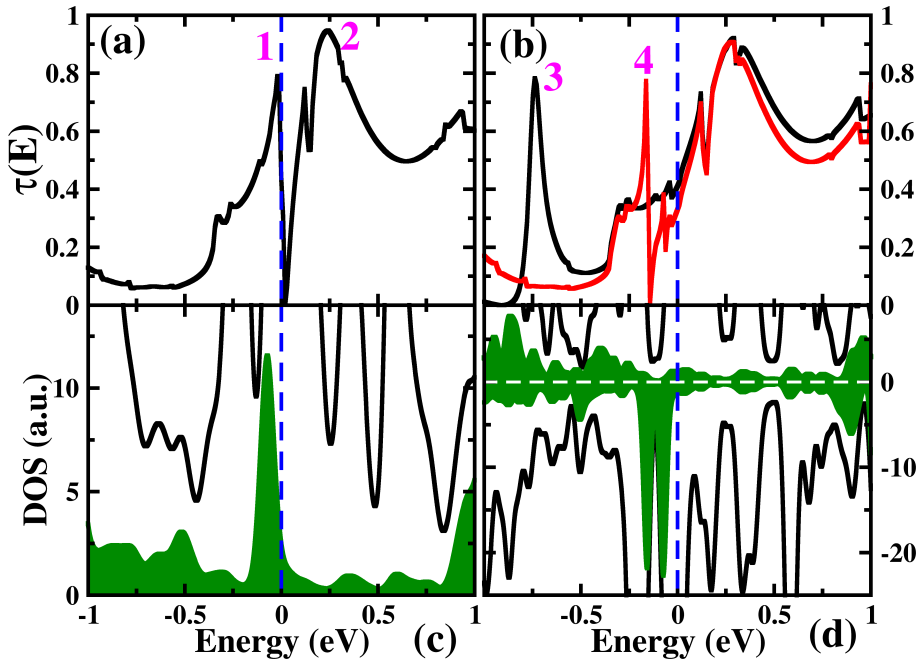

Figure 7.6: Top panel: zero-bias transmission functions for (a) Au-[MnP $-$ $NO_{linear}(S_2)$]-Au (spin-unresolved) and (b) Au-[MnP $-$ $NO_{bent}(S_2)$]-Au (spin-resolved). Solid black and red lines represent majority and minority-spin transmission function. Major transmission peaks are numbered as 1-4. Bottom panel: DOS for (c) Au-[MnP $-$ $NO_{linear}(S_2)$]-Au (spin-unresolved) and (d) Au-[MnP $-$ $NO_{bent}(S_2)$]-Au (spin-resolved). Solid green portions depict the pDOS of molecular bridges of E-M-E systems.

orbitals of Mn contribute significantly to these transport-active molecular channels. Other occupied molecular orbitals stay far from the E_F and consequently remain quite inactive towards molecular transport. Most importantly, as the eigenstates at the E_F remain significantly localized over the electrodes, the transmission spectra shows a sharp deep at that energy.

On the other hand, transmission spectra for $MnP-NO_{bent}$ bridged junction exhibits quite distinct nature between major and minor spin channels just below the E_F. In Fig. 7.6 (b), minority (majority) spin channel shows sharp transmission peak i.e. peak 4 (peak 3) at -0.16 eV (-0.74 eV). Like linear geometry, completely delocalized charge densities of the eigenstates results in the major peaks in transmission spectra. As shown in Fig. 7.7 (c) (Fig. 7.7 (d)), charge density for the corresponding state of peak 3 (peak 4) has dominant contributions from the conjugated π-orbitals of porphyrin and majority spin-orbitals of $3d_{xy}$ and $3d_{z^2}$ (minority spin-orbital of $3d_{xy}$, $3d_{yz}$ and $3d_{z^2}$) of Mn. Thus, in bent Mn-NO conformation, spin-split 3d-orbitals of Mn result in spin-polarization of electron transmission spectra. More importantly, as transmission through $MnP-NO_{linear}$ is spin independent i.e. $\tau_S = 0$, spin-polarization of transmission can be switched off/on just by modulating binding mode. As the real molecular devices operate under finite bias, we calculate the

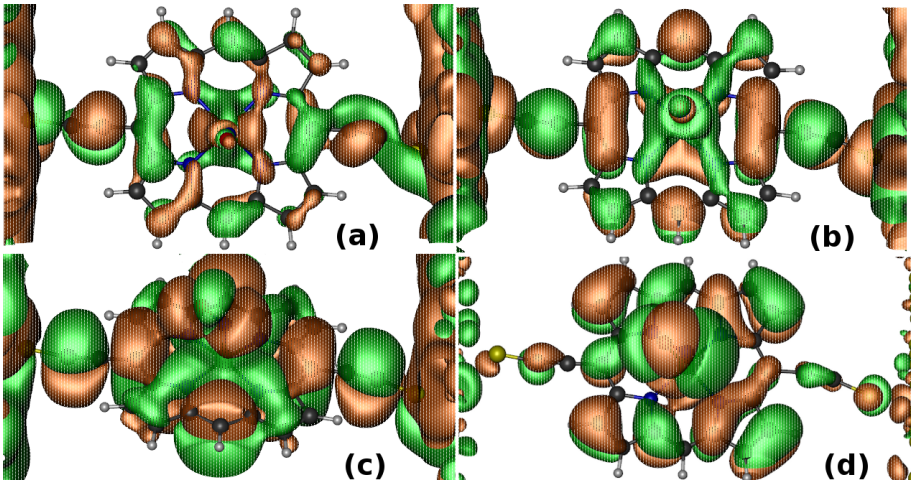

Figure 7.7: (a-d) Wave function plot of the states which corresponds to the transmission peaks (1-4) of Fig. 7.6. The isosurface value is considered as 0.01 e $\mathring{A}^{-3}$.

current (I) through molecular junction by varying source-drain bias voltage (V_{SD}). As shown in Fig. 7.8 (a), total current through this molecular junction remains

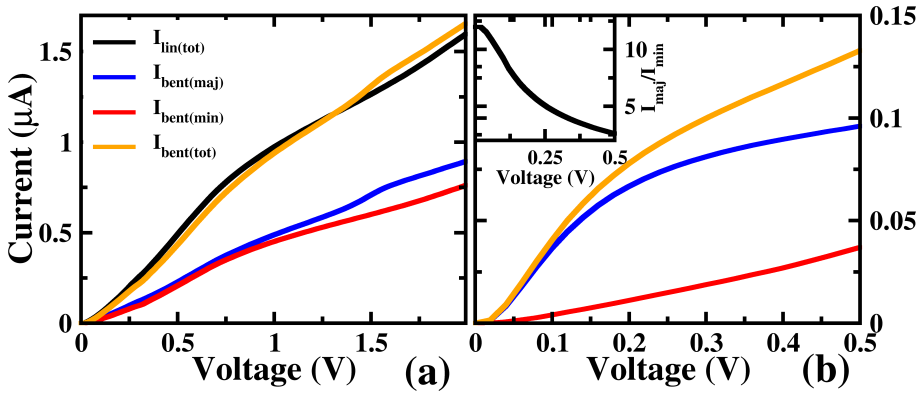

Figure 7.8: (a) I-V characteristics for Au-[MnP – $NO_{linear}(S_2)$]-Au and Au-[MnP – $NO_{bent}(S_2)$]-Au. (b) I-V characteristics for Au-[MnP – $NO_{bent}(S_2)$]-Au after shifting the electrode E_F to -0.737 eV. $(I_{maj})/(I_{min})$ is shown in the inset of (b)

almost unchanged in two different Mn-NO binding conformations. Further, in bent conformation, as majority and minority-spin current remain almost equal to each other, the net transmitted current shows spin-unpolarized behavior. However, for this conformer, shifting the E_F of E-M-E to -0.737 eV, spin-polarized current appears. As depicted in Fig. 7.8 (b), majority spin current (I_{maj}) evidently dominates over the minority spin current (I_{min}) at low voltage (i.e. $0 \leqslant V \leqslant 0.5$). Further, $(I_{maj})/(I_{min})$ reaches up to ≈12 at infinitesimal voltage and reduces with increase in applied bias voltage (see inset of Fig. 7.8 (b)). Fundamentally, as peak 3 appears at -0.737 eV, majority spin channel predominantly gets activated for transport upon alignment of the E_F at that energy state. And consequently, the molecular junction becomes highly efficient spin-polarized current generator at low voltage regime. Same kind of spin-polarized current can be generated by precisely aligning system's E_F to other spin-polarized transmission peaks also.

7.3.6 Thermoelectric Properties

In this section, using the previously applied methodology (see Chapter 6), we explore the thermoelectic properties of the presently investigated molecular bridge.

7.3.6.1 Temperature Induced Current

First, we calculate the current ($I_{thermo,linear/bent}$) for both metalloporphyrin-based molecular bridges as a function of source-electrode temperature (T_S) (100 K $\leqslant T_S \leqslant$ 400 K) at different source-drain temperature difference (T_{SD}). As shown in Fig. 7.9 (a), total charge current ($I_{thermo,linear}$) through $MnP - NO_{linear}$ bridge increases with the increment in T_S for a constant T_{SD} value. Current also increases in presence of higher temperature-bias i.e. T_{SD} as already has been found in experiments [49]. Fundamentally, the magnitude and sign of $I_{thermo,linear}$ at low-bias regime is determined by two terms, (1) relative difference in the Fermi distributions of two electrodes i.e. $[f_S(T_S, E) - f_D(T_D, E)]$ and (2) transmission function (i.e. τ_σ) of molecular junction near the E_F. Due to the temperature difference, electrons (holes) of source (drain) electrode with energy higher (lower) than E_F get transported to drain (source). And consequently, device exhibits negatively (positively) signed electron (hole) current I_e (I_h) which flows from drain to source electrode. Now, the transmission spectrum in Fig. 7.6 (a) and current spectrum (i.e. $J(E) = \tau_\sigma[f_S(T_S, E) - f_D(T_D, E)]$ in Fig. 7.9 (b,c) clearly shows that transmitting states below E_F is major contributor of hole-dominating current in this junction. Thus, the resultant positively signed current flows from source to drain for this bias-region. Further, as shown in Fig. 7.9 (a-c), increase in either of T_S and T_{SD} eventually results in activation of more transport channels below the E_F and that increases the magnitude of $I_{thermo,linear}$. Interestingly, Fig. 7.9 (a) shows negligible amount of current at T_S = 100 K ($I_{thermo,linear}$ < - 0.004μA), where the device remains in off-state. Now if we increase the T_S maintaining certain T_{SD}, device switches on as measurable amount of current starts flowing through the junction. At $T_S \approx$ 400 K and T_{SD} = 80 K, the I_{on}/I_{off} ratio reaches as high as 10^5 for the charge current (Fig. 7.9 (d)). Thus, the device can be demonstrated as a temperature controlled high-performance-switch. In fact, as discussed earlier, for $T_{SD} > 0$, $f_S(T_S, E) - f_D(T_D, E) \neq 0$ and current can flow in the device only if $\tau_{maj/min}(E)$ breaks the electron-hole symmetry within the applied temperature-difference window. Now, at low-bias window (T_S = 100 K), transmission spectrum shows negligible electron-hole asymmetry and consequently device remains in switch-off state. Electron-hole asymmetry becomes prominent only with the application of high T_S where net current-flow appears in the junction and device switches on subsequently. Note that, as this transmission spectrum remains

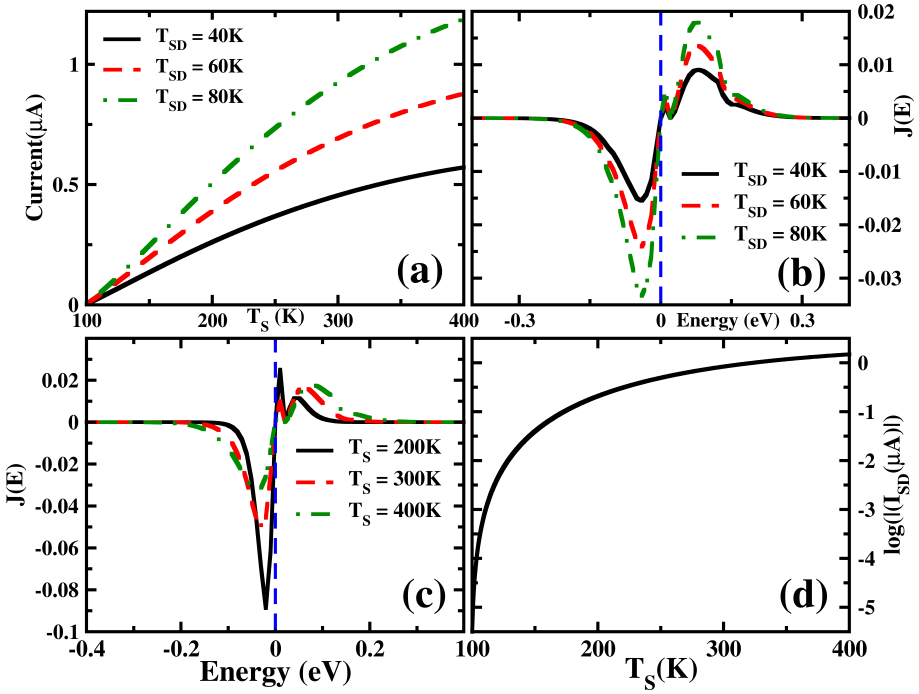

Figure 7.9: (a) $I_{thermo,linear}$ versus T_S with various T_{SD}; J(E) as a function of energy with various (b) T_{SD} (c) T_S; (d) $\log(|I_{SD}|)$ versus T_S plot with T_{SD} = 80 K

spin-degenerate, transported current does not show any spin-polarization.

However, molecular junction of $MnP - NO_{bent}$ exhibits quite distinct features in thermally induced current transport. Most importantly, unlike previous conformation, spin-degeneracy gets lifted in this metalloporphyrin junction, resulting in appearance of spin-polarized current (Fig. 7.10 (a)). Further, $I_{thermo,bent}$ for majority as well as minority spin currents show up a negative sign. The spin-dependent transmission spectra (Fig. 7.6 (b)) and current spectra (see Fig. 7.10 (b) for majority spin current spectrum) demonstrate that for both the spin channels, electrons majorly transport thermal current. Thus, electrons flow from hot source to cold drain electrodes and results in I_e. As plotted in Fig. 7.10 (a), alike previous system, $I_{thermo,bent}$ in either spin channels increase as $T_S(T_{SD})$ increase due to the addition of active electron-dominating transport path in higher source temperature (temperature-bias). Further, at T_S = 400 K and T_{SD} = 80K, majority-spin (minority-spin) channel reaches maximum I_{on}/I_{off} ratio of 10^6 (10^6), which is an order higher than the previously explored device (Fig. 7.10 (c)).

Focusing on spin-polarization of $I_{thermo,bent}$, we find the appearance of minority-spin polarized resultant current in this molecular junction. As shown in Fig. 7.10 (d), resulting spin-polarized current also increases with the increment in $T_S(T_{SD})$. Fundamentally, $I_{thermo,bent}$ is proportional to the area under the active current spectra. Now, in this device, as minority-spin current spectrum has more active region than the majority-spin one, minority-spin polarized thermal current appears predominantly. Hence, this molecular junction can act as a spin-polarized thermally induced current generator also. Further, as $MnP - NO_{linear}$ bridge does not produce spin-polarized thermal current, one can efficiently switch on/off the spin polarization of the thermally induced current here by reversibly tuning the Mn-NO binding geometry.

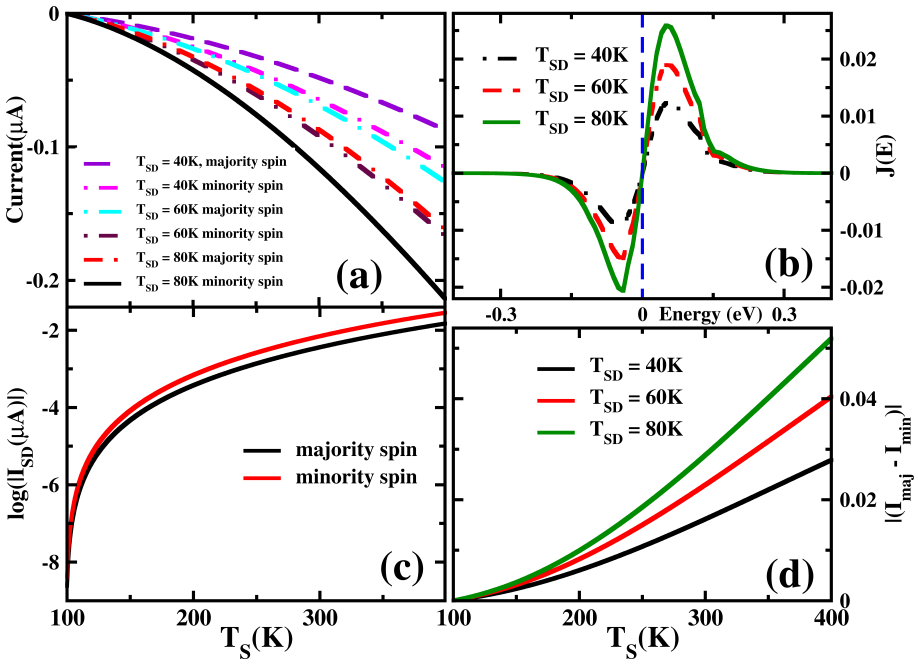

Figure 7.10: (a) $I_{thermo,bent}$ versus T_S with various T_{SD}; J(E) as a function of energy with various (b) T_{SD}; (c) spin-resolved $\log(|I_{SD}|)$ versus T_S plot with $T_{SD} = 80$ K (d) spin polarization of $I_{thermo,bent}$ versus T_S for various T_{SD}.

7.3.6.2 Thermopower

Now, we explore the relationship between charge thermopower i.e. S_C (S_C and spin thermopower i.e. S_S) and chemical potential (μ) of the electrodes for the

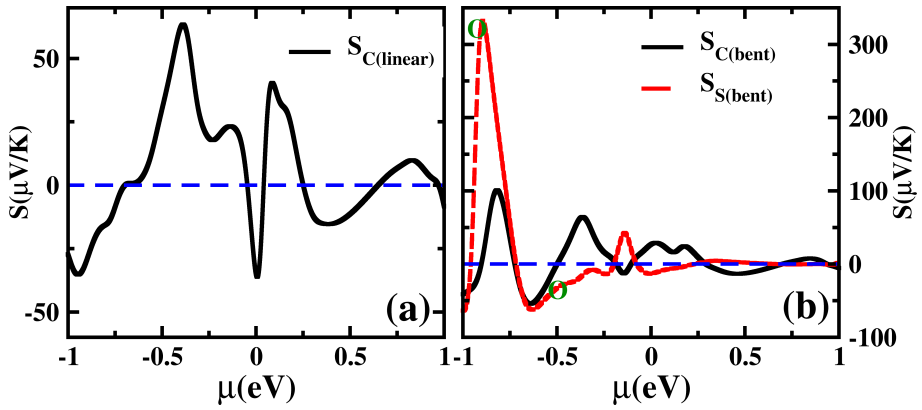

Figure 7.11: (a) $S_{C(linear)}$ and (b) $S_{C(bent)}$ and $S_{S(bent)}$ as a function of μ.

$MnP-NO_{linear}$ ($MnP-NO_{bent}$) bridged molecular junctions. As stated earlier, during the thermopower measurements, $V_{SD} = 0$ and consequently, the chemical potential of electrodes (i.e. μ_L, μ_R) remain aligned to the equilibrium E_F of the system. Further, restricting this present investigation within linear response regime, we keep $T_S \approx T_D \approx 300$ K and vary μ in the range of -1 $\leqslant \mu \leqslant$ 1. Alike current, thermopower generation is also strongly governed by the features of spin-resolved transmission spectra near the E_F. Thus, this nano-device prominently alters S_C and S_S during the conformational change of Mn-NO geometry. Fig. 7.11 (a, b), further demonstrate that (1) due to the presence of electron-hole symmetry, thermopower becomes almost zero at certain energy values, (2) when finite conductance and electron-hole asymmetry appears simultaneously, finite thermopower arises, (3) thermopower changes its sign when μ crosses peaks of transmission spectra as carrier-type changes there. Note that, S becomes negative to positive when carrier changes from electrons to holes. Particularly, at $\mu = 0$, S_C for $MnP-NO_{linear}$ bridged junction ($S_{C(linear)}$) appears as -35 μV/K which indicates an electron dominated thermopower generation (see Fig. 7.11 (a)). Note that, as transmission through $MnP-NO_{linear}$ junction remains spin-degenerate (i.e. $\tau_{maj} = \tau_{min}$), the $S_{S(linear)}$ becomes zero here. Further, in $MnP-NO_{bent}$ conformation, sign as well as magnitude of thermopower change quite distinctly. Importantly, like thermally induced current, spin-polarized Seebeck (S_S) gets switched-on in this device as transmission function becomes spin non-degenerate (i.e. $\tau_{maj} \neq \tau_{min}$). At $\mu = 0$, S_S and $S_{C(bent)}$ appear as -13.2 μV/K and 26.6 μV/K, respectively. Thus, device shows the

generation of hole-mediated charge thermopower at zero bias where both majority and minority spin-channels have holes as dominant carrier. Most importantly, Fig. 7.11 (b) demonstrates that at -0.95eV $\leqslant \mu \leqslant$ -0.77eV and -0.68eV $\leqslant \mu \leqslant$ -0.44eV, S_S becomes much larger than S_C. Fundamentally, in these regions, totally spin-polarized majority-spin holes and minority-spin electrons participate in thermopower generation which results in smaller magnitude of S_C while much larger value of S_S. Particularly, at $\mu \approx$ -0.9 eV and $\mu \approx$ -0.5 eV where $S_C = 0$ but $S_S =$ -327 μV/K and -32.6 μV/K, respectively (see the green circles in Fig. 7.11 (b)), we can generate pure spin-thermopower without any charge component.

7.4 Conclusions

To conclude, in this chapter, we demonstrate the conformation-induced spin-state switching in NO adsorbed MnP molecule, adsorbed on Au(111) surface. The low-spin (S = 0) ground state of linearly bonded NO containing MnP switches on its spin-state to S = 1 when Mn-NO bonding moves to metastable bent conformation. The mechanical manipulation of closely spaced gold STM-tip can precisely modify this Mn-NO bonding conformation in a reversible way. Electronic transport as well as thermoelectic properties of this molecular junction also gets significantly modified upon the conformational change. Most importantly, spin-polarized nature of voltage- or temperature-induced current can reversibly be switched off/on by the structural manipulation. By precisely controlling the chemical potential of this molecular junction in its bent conformation, one can find pure spin-thermopower which is highly demanding in the field of spin-caloritronics. As the present theoretical calculations are performed within the constraint of well-developed experimental set up, we strongly believe that exciting results of this study can be verified experimentally.

Bibliography

[1] L. Bogani and W. Wernsdorfer, Nat. Mater. **7**, 179 (2008).

[2] R.-Q. Wang, L. Sheng, R. Shen, B. Wang, and D. Xing, Phys. Rev. Lett. **105**, 057202 (2010).

[3] L. Zhou, S.-W. Yang, M.-F. Ng, M. B. Sullivan, V. B. Tan, and L. Shen, J. Am. Chem. Soc **130**, 4023 (2008).

[4] T. Miyamachi, M. Gruber, V. Davesne, M. Bowen, S. Boukari, L. Joly, F. Scheurer, G. Rogez, T. K. Yamada, P. Ohresser, *et al.*, Nat. Commun. **3**, 938 (2012).

[5] D. Ghosh, P. Parida, and S. K. Pati, Appl. Phys. Lett. **106**, 193105 (2015).

[6] W. Auwärter, D. Écija, F. Klappenberger, and J. V. Barth, Nat. Chem. **7**, 105 (2015).

[7] C. Wäckerlin, K. Tarafder, D. Siewert, J. Girovsky, T. Hählen, C. Iacovita, A. Kleibert, F. Nolting, T. A. Jung, P. M. Oppeneer, *et al.*, Chem. Sci. **3**, 3154 (2012).

[8] H. Wende, M. Bernien, J. Luo, C. Sorg, N. Ponpandian, J. Kurde, J. Miguel, M. Piantek, X. Xu, P. Eckhold, *et al.*, Nat. Mater. **6**, 516 (2007).

[9] C. Wäckerlin, D. Chylarecka, A. Kleibert, K. Müller, C. Iacovita, F. Nolting, T. A. Jung, and N. Ballav, Nat. Commun. **1**, 61 (2010).

[10] H. Kim, Y. H. Chang, S.-H. Lee, Y.-H. Kim, and S.-J. Kahng, ACS Nano **7**, 9312 (2013).

[11] J. Girovsky, K. Tarafder, C. Wäckerlin, J. Nowakowski, D. Siewert, T. Hählen, A. Wäckerlin, A. Kleibert, N. Ballav, T. A. Jung, *et al.*, Phys. Rev. B **90**, 220404 (2014).

[12] R. D. Jones, D. A. Summerville, and F. Basolo, Chem. Rev. **79**, 139 (1979).

[13] J. Buchler, The Porphyrins **1**, 389 (2012).

[14] B. W. Heinrich, L. Braun, J. I. Pascual, and K. J. Franke, Nano Lett. **15**, 4024 (2015).

[15] B. A. Friesen, B. Wiggins, J. L. McHale, U. Mazur, and K. Hipps, J. Am. Chem. Soc **132**, 8554 (2010).

[16] H. Kondo, J. Nara, and T. Ohno, J. Phys. Chem. C **115**, 6886 (2011).

[17] F. Moresco, G. Meyer, K.-H. Rieder, H. Tang, A. Gourdon, and C. Joachim, Phys. Rev. Lett. **86**, 672 (2001).

[18] W. J. Cho, Y. Cho, S. K. Min, W. Y. Kim, and K. S. Kim, J. Am. Chem. Soc **133**, 9364 (2011).

[19] G. Sedghi, V. M. Garc´ia-Suárez, L. J. Esdaile, H. L. Anderson, C. J. Lambert, S. Mart´in, D. Bethell, S. J. Higgins, M. Elliott, N. Bennett, *et al.*, Nat. Nanotechnol. **6**, 517 (2011).

[20] V. A. Dediu, L. E. Hueso, I. Bergenti, and C. Taliani, Nat. Mater. **8**, 707 (2009).

[21] C. Wäckerlin, K. Tarafder, J. Girovsky, J. Nowakowski, T. Hählen, A. Shchyrba, D. Siewert, A. Kleibert, F. Nolting, P. M. Oppeneer, *et al.*, Angew. Chem. Int. Ed. **52**, 4568 (2013).

[22] G. Kresse and J. Hafner, Phys. Rev. B **47**, 558 (1993).

[23] P. E. Blöchl, Phys. Rev. B **50**, 17953 (1994).

[24] G. Kresse and D. Joubert, Phys. Rev. B **59**, 1758 (1999).

[25] J. P. Perdew, K. Burke, and M. Ernzerhof, Phys. Rev. Lett. **77**, 3865 (1996).

[26] V. I. Anisimov, F. Aryasetiawan, and A. Lichtenstein, J. Phys. Condens. Matter. **9**, 767 (1997).

[27] S. Dudarev, G. Botton, S. Savrasov, C. Humphreys, and A. Sutton, Phys. Rev. B **57**, 1505 (1998).

[28] P. M. Panchmatia, B. Sanyal, and P. M. Oppeneer, Chem. Phys. **343**, 47 (2008).

[29] K. Leung, S. B. Rempe, P. A. Schultz, E. M. Sproviero, V. S. Batista, M. E. Chandross, and C. J. Medforth, J. Am. Chem. Soc **128**, 3659 (2006).

[30] W. R. Scheidt, K. Hatano, G. Rupprecht, and P. Piciulo, Inorg. Chem. **18**, 292 (1979).

[31] S. Vosko, L. Wilk, and M. Nusair, Can. J. Phys. **58**, 1200 (1980).

[32] M. E. Ali, B. Sanyal, and P. M. Oppeneer, J. Phys. Chem. C **113**, 14381 (2009).

[33] S. Grimme, J. Comput. Chem. **27**, 1787 (2006).

[34] M. Brandbyge, J.-L. Mozos, P. Ordejón, J. Taylor, and K. Stokbro, Phys. Rev. B **65**, 165401 (2002).

[35] M.-S. Liao and S. Scheiner, J. Chem. Phys. **117**, 205 (2002).

[36] R. D. Feltham and J. H. Enemark, in *Structures of Metal Nitrosyls* (2009) pp. 155–215.

[37] G. R. Wyllie and W. R. Scheidt, Chem. Rev. **102**, 1067 (2002).

[38] A. Ghosh, Acc. Chem. Res **38**, 943 (2005).

[39] W. R. Scheidt, H. F. Duval, T. J. Neal, and M. K. Ellison, J. Am. Chem. Soc **122**, 4651 (2000).

[40] J. G. Erdman, V. G. Ramsey, N. W. Kalenda, and W. E. Hanson, J. Am. Chem. Soc **78**, 5844 (1956).

[41] M. Bernien, J. Miguel, C. Weis, M. E. Ali, J. Kurde, B. Krumme, P. M. Panchmatia, B. Sanyal, M. Piantek, P. Srivastava, *et al.*, Phys. Rev. Lett. **102**, 047202 (2009).

[42] Y. He, T. Ye, and E. Borguet, J. Am. Chem. Soc **124**, 11964 (2002).

[43] J. A. Stroscio and D. Eigler, Science **254**, 1319 (1991).

[44] A. Zhao, S. Tan, B. Li, B. Wang, J. Yang, and J. Hou, Phys. Chem. Chem. Phys. **15**, 12428 (2013).

[45] A. Saywell, W. Gren, G. Franc, A. Gourdon, X. Bouju, and L. Grill, J. Phys. Chem. C **118**, 1719 (2013).

[46] K. Tao, V. Stepanyuk, W. Hergert, I. Rungger, S. Sanvito, and P. Bruno, Phys. Rev. Lett. **103**, 057202 (2009).

[47] W. Hofer, A. Fisher, R. Wolkow, and P. Grütter, Phys. Rev. Lett. **87**, 236104 (2001).

[48] J. M. Soler, E. Artacho, J. D. Gale, A. Garc´ia, J. Junquera, P. Ordejón, and D. Sánchez-Portal, J. Phys. Condens. Matter. **14**, 2745 (2002).

[49] J. R. Widawsky, P. Darancet, J. B. Neaton, and L. Venkataraman, Nano Lett. **12**, 354 (2011).

Chapter 8

Electron Transport through Heterocyclic Molecules: A Quantum Many-body Approach*

8.1 Introduction

Molecular electronics, the investigation about the electronic properties of circuits, made of individual molecules, have gained a huge research attention in past few decades [1, 2]. Appearance of efficient switching [3], negative differential conductance (NDC) [4], rectification [5], spin-transport[6], spin-filtration [7], thermoelectric effect [8] in various molecular junctions evidently show the potential of these nano-devices to be used as alternative of conventional silicon-based semiconductor electronics. Among all these fascinating properties, particularly rectification and NDC characteristics have been explored quite thoroughly from very beginning of this field. A number of molecules strongly attached to the bulk electrodes have shown the efficient rectification and/or NDC, mainly due to (1) molecular asymmetric nature (donor-acceptor molecules) [5] (2) different electrode-molecule coupling strengths (asymmetric anchoring groups or electrodes) [5] (3) different spatial potential profiles [4] etc. Although these phenomena mainly appear for covalently

*Works reported in this chapter is a manuscript under preparation: D. Ghosh, P. Parida and S. K. Pati,(2016)

bonded molecule-electrode systems (i.e. coherent tunneling regime), recent experimental and theoretical investigations demonstrated them for weakly coupled molecular junctions also (sequential tunneling regime) [4, 9]. Small molecules (such as benzene), double quantum dots (like GaAs-based QDs) which are coupled weakly to metallic electrodes have shown their prominent rectification and NDC properties, due to various factors, such as, internal charge transfer, intrinsic molecular asymmetries, interference effects, Pauli spin-blocking etc. [4, 10–12].

Theoretical modelling of these weakly coupled devices show that coherent non-equilibrium Green's function (NEGF) [13, 14] formalism coupled with self-consistent field (SCF) approach is not adequate to reproduce experimental findings even in qualitative level. Unlike strongly coupled systems, in these devices charging energies of molecules/QDs are much higher than electrode coupling and plays a major role [15, 16]. Consequently, these devices remain in Coulomb blockade (CB) regime where integral charge transfer dominates the electron transport through molecular junctions. The mostly used formalism to describe the molecular transport in CB regime is the quantum master or rate equation approach [17, 18]. This formalism efficiently describes electron transport through many-body eigenstates of molecular systems. Since in this limit, charging energy is much higher than the molecule/dot electrode coupling, in the kinetic equation method, we do not explicitly consider the electrode or its coupling with the molecule/dot device. We discuss the formalism in detail in Models and Methods section of the chapter.

Using this approach, Hettler *et. al.* have demonstrated the large NDC behaviour in weakly coupled benzene-based molecular junctions [10]. Here, under finite bias, the radiative relaxation of electrons populate a particular many-body state which blocks the transport of current, resulting in the NDC in the device. Darau *et. al.* revisited the same system with generalized master equation approach, where strong interference effect appears to be the reason for the observed NDC behavior [19]. Apart from molecules, donor-acceptor QDs in weak coupling regime also have been investigated thoroughly for their various non-linear transport characteristics. Parida *et. al.* used similar kinetic equation approach to investigate transport characteristics in donor-acceptor double QD systems [11]. In this study, the authors find increased population in the non-conductive triplet state with increase in bias voltage and consequent reduction in the current transport, exhibiting a prominent

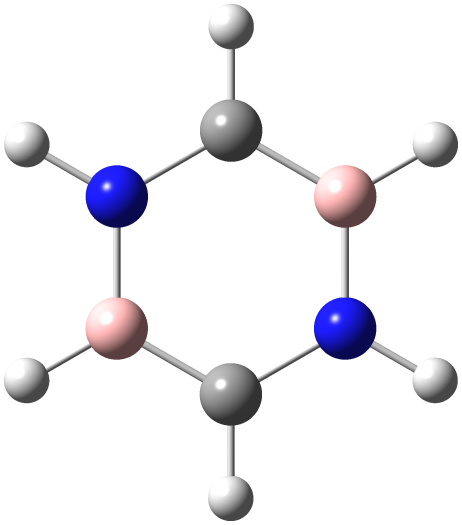

Figure 8.1: A schematic representation of a $B_2C_2N_2H_6$ molecule. Hydrogen, boron, carbon and nitrogen are represented by white, lime, gray and blue coloured spheres.

NDC feature. Murulidharan *et. al.* demonstrated the criterion to find NDC in these double QDs in terms of transition rates for populating and depopulating energetically transport-active many-body states [16]. Song *et. al.* have shown the appearance of rectification in I-V characteristics for weakly coupled spatially separated donor-acceptor systems [20]. Different coupling strengths of these sites to the electrodes result in the rectification effect in these molecular junctions. In this chapter, we consider heterocyclic benzene i.e. $B_2C_2N_2H_6$ (see Fig. 8.1) as the molecular bridge which is weakly coupled to the metallic electrodes in either side. Thus, the molecular junction is effective in Coulomb blockade regime. Here, B, C and N sites act as acceptor, bridge and donor (from the electron point of view), respectively due to their intrinsic chemical nature. This molecule can efficiently be modelled as two identical donor-bridge-acceptor half-rings (B-C-N) connected to each other in end-on manner by covalent bonds. Following several previous works, we construct the interacting isolated molecular Hamiltonian considering localized $2p_z$ orbitals of B, C and N atoms as only participating orbitals [10, 19]. This is to describe its low energy properties, the the σ orbitals have much higher energy scale. Depending on the sites, which form electrode-molecule coupling, we find various non-linear current-voltage characteristics, such as, prominent NDC, strong

rectification, Coulomb staircase in this two-terminal molecular device. The bias-dependent probability analyses of many-body states evidently show that population and depopulation of various low-energy molecular states result in bias-dependent blockade/conduction of electron-flow through these molecular states. The origin of conducting or blocking nature of many-body states towards current transport has be understood by looking at the charge distributions at all atomic sites for each of these low-lying transport-active channels.

8.2 Model and Methods

We undertake the quantum master-equation approach to explore transport characteristics of $B_2C_2N_2H_6$ (see the schematic Fig. 8.1) in the sequential tunneling i.e. Coulomb blockade regime. This approach properly formulates the carrier transport through a correlated system, having many-body eigenstates. In this present approach, the occupation probabilities of many-body states are calculated from their corresponding wave functions. Note that, the rate equation problem is solved by neglecting the off-diagonal coherence for the present study.

We model $B_2C_2N_2H_6$ molecule with 6 sites points by considering Hubbard description. Taking into account the on-site electron-electron interactions and hopping between nearest neighbour sites, we write down the most general form of the Hamiltonian as follows,

$$H = \sum_{i=1}^{6} (\epsilon_i - eV_g) a_i^{\dagger} a_i + \sum_{i\sigma} -t(a_{i\sigma}^{\dagger} a_{i+1\sigma} + h.c.) + U \sum_{i=1}^{N} n_{i\uparrow} n_{i\downarrow} \tag{8.1}$$

where t is hopping strength between nearest neighbour sites with identical spin, ϵ_i are the on-site energies for different atomic sites and U is the Hubbard interaction, V_g represents the external gate bias. For hopping parameters, we consider only nearest neighbours and for each of them the magnitude is considered as 2.4 eV [10, 21]. Note that, B-C, C-N and B-N hopping is considered the same (2.4eV) as exactly as the C-C hopping strength in benzene. Here, we neglect the small differences among the hopping parameters what may appear due to different chemical nature of C, B and N atoms. For Hubbard parameters, we obtain Hubbard on-site energy as the difference between 1st ionization potential and electron affinity of each of the

atomic species. Thus, the Hubbard on-site parameters are evaluated to be 8.02 eV, 9.67 eV and 14.46 eV for B, C and N, respectively [22]. The site-energy term in the Hamiltonian corresponds to negative of 1st ionization potential for each atomic species. And these turns out to be -8.30 eV, -11.26 eV and -14.53 eV for B, C and N, respectively.

To compute the transport properties in the sequential tunneling limit, we diagonalize the system Hamiltonian, H, considering the total number of electron and total z-component of spin, as these two commute with H. Diagonalization of H give many-body eigenstates $|s>$ with the corresponding eigenenergies, E_s, and their total z-component spin S_s. Followed by that, we introduce a master equation approach to calculate the occupation probabilities, P_s, in the steady state of the system. The transition rate, $W_{s'\to s}$, from many-body state of the molecule s' to s, differing by single electron, is calculated up to linear order in Γ (i.e. the bare electron tunneling rate between the molecule and the left/right electrodes), using the Fermi's golden rule. The transition rate is as follows,

$$W^{L+}_{s'\to s} = \Gamma f_L(E_s - E'_s) \sum_\sigma | < s|a^\dagger_{1\sigma}|s' > |^2$$

$$W^{R+}_{s'\to s} = \Gamma f_R(E_s - E'_s) \sum_\sigma | < s|a^\dagger_{N\sigma}|s' > |^2 \tag{8.2}$$

The corresponding equation for $W^{L-}_{s\to s'}$ and $W^{R-}_{s\to s'}$ are formulated by replacing $f_{L,R}(E_s - E'_s)$ by $(1 - f_{L,R}(E_s - E'_s))$, where $f_{L,R}$ is the Fermi function for left and right electrodes. Here, $+/-$ represents the creation/annihilation of an electron inside the molecule due to electron movement from/to left (L) or right (R) electrodes. $C^\dagger_{1\sigma}$ and $C^\dagger_{N\sigma}$ are the creation operators for electrons with spin, σ, at the 1^{st} and N^{th} lattice sites, respectively. We also have assumed that the creation and annihilation happen only at the sites which are directly connected to the electrodes. The total transition rate is then formulated as, $W_{s\to s'} = W^{L+}_{s\to s'} + W^{R+}_{s\to s'} + W^{L-}_{s\to s'} + W^{R-}_{s\to s'}$. The non-equilibrium probability, P_s, of occurrence of each many-body state, s, can be

represented by the rate equation:

$$\dot{P}_s = \sum_{s'} (W_{s' \to s} P_{s'} - W_{s \to s'} P_s). \tag{8.3}$$

At the steady state, the population of the different many-body states (P_s) can found by solving the above rate equation (Eq. (8.3)). At this state, the Eq. (8.3) becomes

$$\dot{P}_s = \sum_{s'} (W_{s' \to s} P_{s'} - W_{s \to s'} P_s) = 0. \tag{8.4}$$

The Eq. (8.4) can be written in an expanded form that results in a homogeneous linear system (AX=0) of the size of the many-body space:

$$\begin{pmatrix} -\sum_s (W_{1\to s}) & W_{2\to 1} & \cdots & W_{(N-1)\to 1} & W_{N\to 1} \\ W_{1\to 2} & -\sum_s (W_{2\to s}) & \cdots & W_{(N-1)\to 2} & W_{N\to 2} \\ \vdots & \vdots & \vdots & \vdots & \vdots \\ W_{1\to (N-1)} & W_{2\to (N-1)} & \cdots & -\sum_s (W_{(N-1)\to s}) & W_{N\to (N-1)} \\ W_{1\to N} & W_{2\to N} & \cdots & W_{(N-1)\to N} & -\sum_s (W_{N\to s}) \end{pmatrix} \begin{pmatrix} P_1 \\ P_2 \\ \vdots \\ P_{N-1} \\ P_N \end{pmatrix} = 0 \tag{8.5}$$

Since AX = 0 can not be solved, we make use of $\sum_{\mathrm{s}} \mathrm{P_s} = 1$ to eliminate one row/column, thus reformulating the eigenvector problem into an inhomogeneous linear system (AX=B), which can be solved using well-known linear algebraic methods [23]. Thereafter, the current in the left and right electrodes is calculated via

$$I_\alpha = \frac{e}{\hbar} \sum_{s,s'} (W^{\alpha+}_{s' \to s} P_{s'} - W^{\alpha-}_{s \to s'} P_s) \tag{8.6}$$

where $\alpha = L/R$. At steady state, the current at two terminal is same, $I_L(t) = I_R(t) = I(t)$.

As we are investigating the transport characteristics for a donor-bridge-acceptor molecular circuit in weak-coupling regime, the coupling strength between molecule and electrodes are considered to be very weak in magnitude. To be specific, we simulate the molecular junction at room-temperature, T = 300K and consider Γ to be the molecule-electrode coupling i.e. 0.25 meV. The coupling parameter is much smaller than the charging energy of the molecule, a condition which must be followed

for every weakly coupled system. We apply the exact diagonalization (ED) method to diagonalize the 6-site Hamiltonian, described in equation Eq. (8.1), where total number of basis is 6^4 i.e.4096.

Several previous investigations established the fact that asymmetric coupling strengths for left and right electrode-molecule junction give rise to NDC or rectification in these weakly coupled molecular junctions [16, 18]. However, we consider symmetric electrode-molecule coupling for the presently studied junctions. For our case, asymmetry in the system is inherent and appears due to very different chemical nature of constituent atoms.

8.3 Results and Discussion

To begin with, we first investigate about the stability of different charge states of the molecule under applied gate voltage (V_G). Thus, we plot number of electrons of the molecular state with lowest energy under various gate bias values, keeping source-drain bias (V_{SD}) zero (see Fig. 8.2). This plot eventually depicts the energies needed to charge the molecule with different number of electrons or holes. As can be seen in Fig. 8.2, the six electron molecular state has widest plateau, indicating this charge state as the ground state of the present molecule.

As the molecule is cyclic in nature, we can connect the electrodes to it in different possible conformations such as ortho, meta or para positions. Some of the representative conformations are given in Fig. 8.3. Note that, as the calculations are in weak coupling limit, electrodes can be connected through weakly interacting anchoring groups or through a long thiol chain. These approaches make the molecular site-electrode coupling negligible.

To calculate the current through these differently connected molecular junctions, the Fermi energy is chosen from the gate voltage value which results in the six-electron ground state as ground state of molecule at $V_{SD} = 0$ (shown in Fig. 8.2). We further fix the Fermi energy in such a way that small V_{SD} bias can transform the molecule from 6-electron ground state to 7-electron ground state i.e. anionic state with one more electron. Note that, in this chapter, we are investigating the I-V characteristics of the device keeping molecule in neutral and negatively charged states.

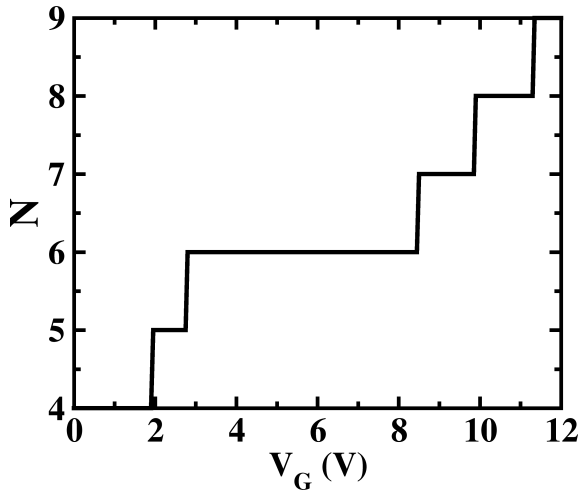

Figure 8.2: The number of electrons (N) in the molecule with variation of gate voltage (V_G) of the device. The widest plateau in the plot appears for the charge sector where molecule is with six-electrons. We have not included the spin sector in the present plot.

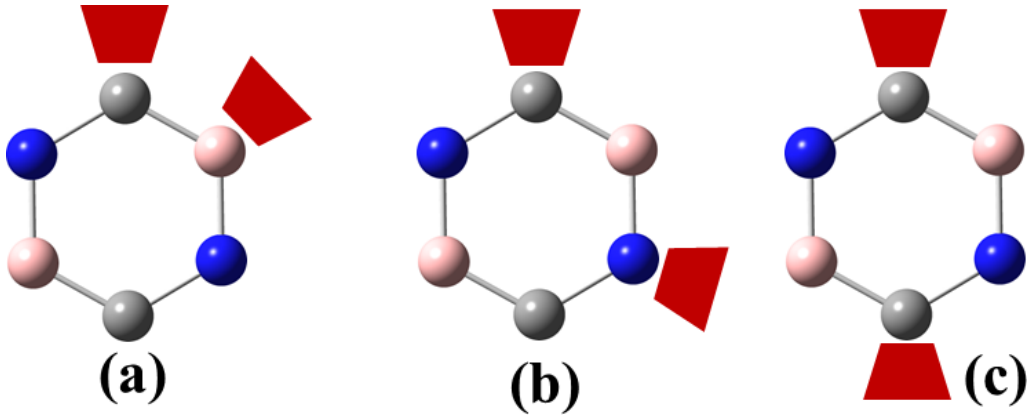

Figure 8.3: Schematic diagram of the molecular devices with different molecule-electrode connections. (a) carbon and boron in ortho position, (b) carbon and nitrogen in meta position and (c) two carbon atoms in para position, weakly connected to electrodes (shown in red blokes), are presented. Hydrogen atoms are removed as they are not modelled for the present study.

8.3.1 Negative Differential Resistance

First, we consider the particular device where both para-positioned B atoms are weakly connected to the electrodes. Properly setting E_F, we have calculated the current by varying the V_{SD} at room temperature and plotted the I-V characteristic in Fig. 8.4 (a-c). As can be seen in Fig. 8.4 (a), the I-V characteristic of this device is identical with opposite sign for both positive and negative bias directions i.e. I(V_{SD}) = I (-V_{SD}). It is quite obvious as the molecule-electrode coupling geometry and strength are symmetric in nature. This symmetric nature of I-V characteristic has already been found for benzene and double quantum dot systems. [10, 16] Taking the advantage of this symmetry, here we discuss the I-V characteristics, focusing only on positive bias regime. As shown in Fig. 8.4 (b), at low bias i.e. $V_{SD} < 1.0V$, the current appears to be very small, of the order of pA only. However, most important feature of this nano-junction appears at the bias range of $1.0 < V_{SD} < 2.2V$, where it shows a sharp rise and fall in current with increase in V_{SD}, exhibiting a strong NDC behaviour (see Fig. 8.4 (a, c)). Applying high bias i.e. $V_{SD} > 2.80V$, the transporting current steeply increases and continues the growth. To find the reason behind the appearance of NDC in this molecular junction, we focus on the non-equilibrium occupation probabilities of transport-active many-body states and find how they get modified along with the change in V_{SD}. As shown in Fig. 8.5, at $0.0 < V_{SD} < 0.2V$, the 6-electron ground-state remains almost completely populated, leaving all other states nearly empty. In this bias region, the applied V_{SD} is not enough to charge the molecule with an extra electron i.e. formation of anion is not favoured. Thus, as the molecule is stable in neutral 6-electron state and there is no other state(s) within this energy scale, the current does not flow through the molecular bridge. Consequently, the device remains in Coulomb blockade regime. As V_{SD} increases, 7-electron ground state becomes energetically accessible and transition of electrons from 6-electron ground state to 7-electron ground state starts occurring (see Fig. 8.5). However, unlike other molecules explored previously [10], the current flowing due to this particular transition, appears to be very small, in the order of a few pA, as mentioned earlier. It simply depicts that 7-electron ground-state is not suitable for electronic transport through the present molecule. Increasing the V_{SD} above a certain threshold bias-voltage, i.e. $V_{SD} > 1.15V$, the 7-electron first excited state comes to the bias-window and consequently starts getting populated.

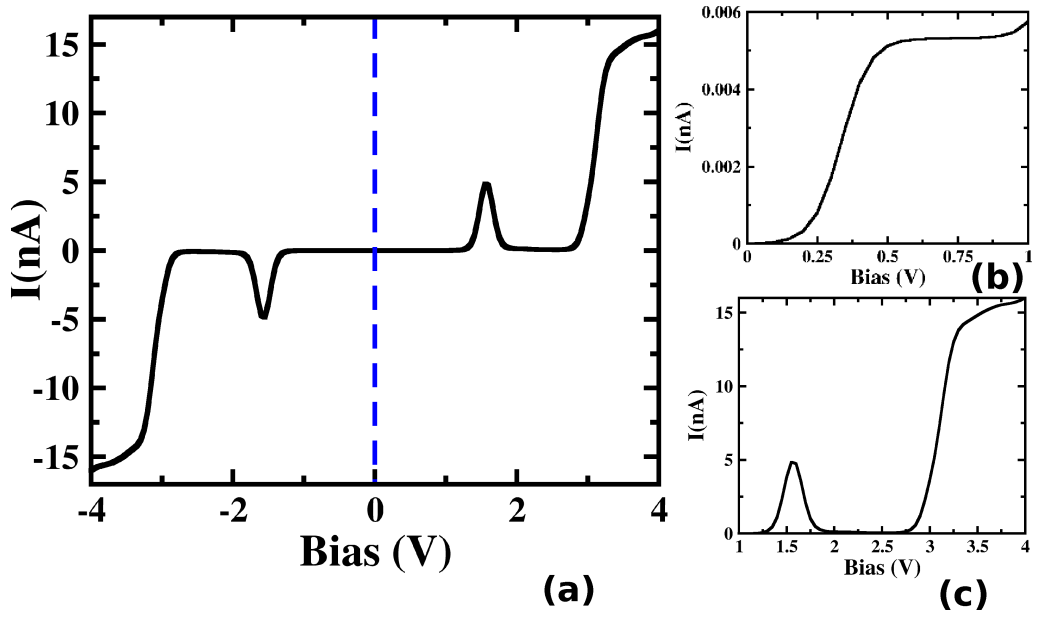

Figure 8.4: Current (I) - source-drain voltage (V_{SD}) characteristics of the boron - boron connected device. The I-V plot for (a) both positive and negative voltages, (b) for bias-range $0.0 < V_{SD} < 1.0V$ and (c) $1.0 < V_{SD} < 2.2V$ are given. Blue dash line in (a) represents the $V_{SD} = 0.0$.

This in turn exhibits sharp increase in resulting current for $V_{SD} > 1.30V$ (see Fig. 8.5). Importantly, here, the magnitude of current appears in the order of nA, much higher than the current due to 6-electron ground state to 7-electron ground state transition. However, at $V_{SD} > 1.60V$ the probability of this conducting 7-electron 1st excited state reduces, causing sharp drops in the current. Thus, the bias-induced population and depopulation of conducting 7-electron 1st excited state in a particular bias range, gives rise to prominent NDC in the presently investigated molecular junction.

Now, we need to understand the atomistic reason behind the different nature of 7-electron many-body states towards the electron transport in sequential tunneling regime. In Fig. 8.6, we represent the charge density of every sites of the molecule considering their different low-energy transport active many-body states. As shown in Fig. 8.6, quite obviously, boron and nitrogen atoms in 6-electron ground state remain electron deficient and rich, respectively, due to their intrinsic electronegativity. Interestingly, 7-electron ground state also follows same kind of electron density

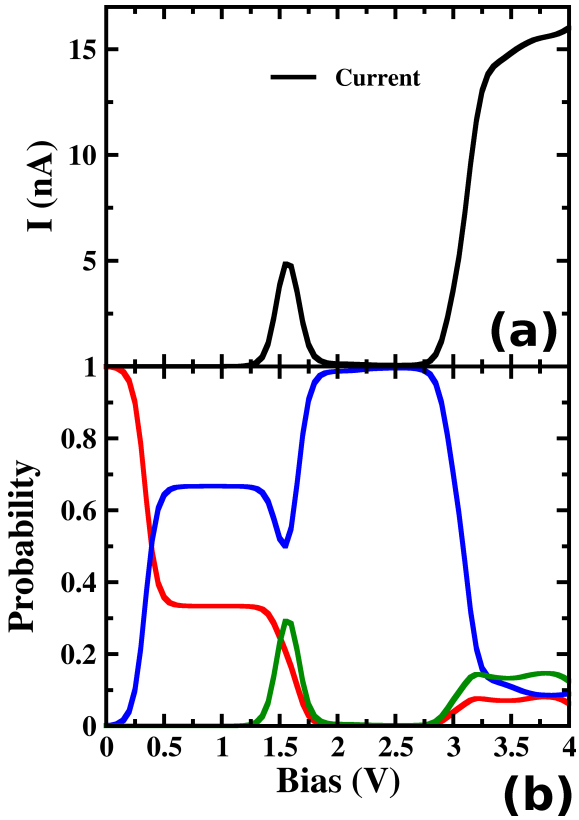

Figure 8.5: The variation of (a) current (I) (b) occupation probability of the 6-electron ground state, 7-electron ground state and 7-electron 1st excited state with V_{SD} for device where both boron atoms are connected to electrode. In (b), red, blue and green solid lines depict the occupation probability of the 6-electron ground state, 7-electron ground state and 7-electron 1st excited state, respectively. We have used same colour coding for other probability plots later on in the chapter.

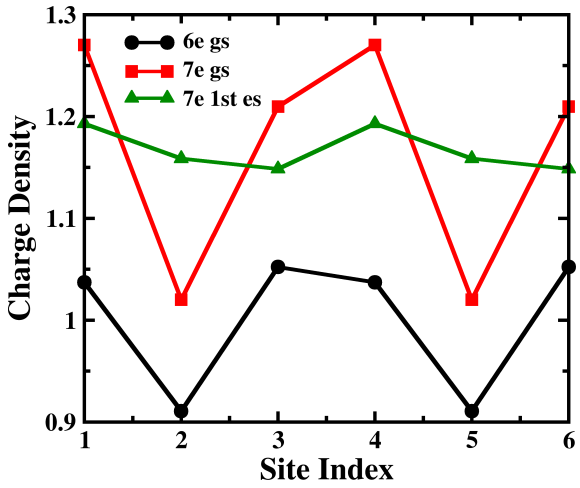

Figure 8.6: The charge density distribution of the 6-electron ground state, 7-electron ground state and 7-electron 1st excited state over the sites of $B_2C_2N_2H_6$.

distribution where the state remains largely polar due to charge localization over nitrogen and charge depletion on boron sites. Now, as the electrodes are connected to the boron atoms, which are electron deficient in both transport-active many-body states, transition of molecule from 6-electron ground state to 7-electron ground state at finite bias does not raise the electron-density at the electrode-molecule coupling region. And consequently, it results in very weak current flow through molecular junction. This explains the negligible current flow in the bias range of $0.0 < V_{SD} < 1.3V$ in the junction as shown in Fig. 8.5. On the other hand, in the 7-electron 1st excited state, electrons remain almost equally distributed over all the atomic sites. Thus, when the higher-energy state gets populated at particular bias, the electron densities at B atoms increase appreciably. And consequently, the current of few a nA, flows through this molecular junction. This flow of electron gets quenched when the higher bias populates the charge localized 7-electron ground state once again. At much higher bias i.e. $V_{SD} > 2.80V$ many more excited states from other charge sectors appear as transport-active channels. Consequently, rapid growth of current can clearly be found in Fig. 8.5(a).

Thus, the population and depopulation of anionic ground state and 1st excited state of $B_2C_2N_2H_6$ where charge distribution patterns are quite different and decisive for current flow, results in exciting non-linear behaviour of current-voltage plot.

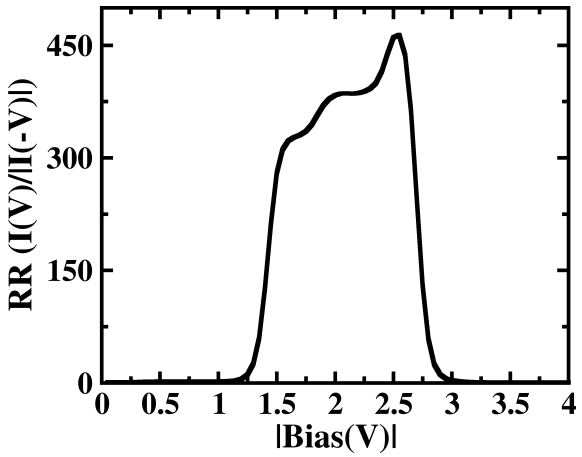

Figure 8.7: The rectification ratio for the C and B connected device with varying V_{SD}.

8.3.2 Rectification

Considering the device where electrodes are connected to energetically asymmetric C and B atoms (see Fig. 8.3 (a)), a prominent rectification of current appears in the I-V characteristics, as plotted in Fig. 8.8. Although in positive bias regime, nA current flows through the device, in the negative bias regime, the current magnitude is nearly zero up to $V_{SD} = -2.80V$. The current shoots up through the device only at $V_{SD} > -2.80V$. To have quantitative idea about rectification, we calculate rectification ration (RR) which is defined as the ratio between the absolute current-values at positive and negative voltages,

$$RR(V) =\mid I(V)/I(-V) \mid \tag{8.7}$$

The rectification ratio is plotted in the Fig. 8.7. As can be seen, the RR(V) is as high as 463.9 at 2.55 V. The probability analysis of many-body states shows that at positive bias, major transition occurs between 6-electron ground state to 7-electron excited state resulting in flow of current at $V_{SD} > 1.25V$ (see Fig. 8.8). On the other hand, applying negative bias to this molecular junction, transition happens from 6-electron ground state to 7-electron ground state. And consequently, the current remain negligible until $V_{SD} > 2.80V$. After this threshold voltage, current starts flowing due to the population of higher energy conducting states. To find the fundamental reason for different conducting nature of these many-body anionic

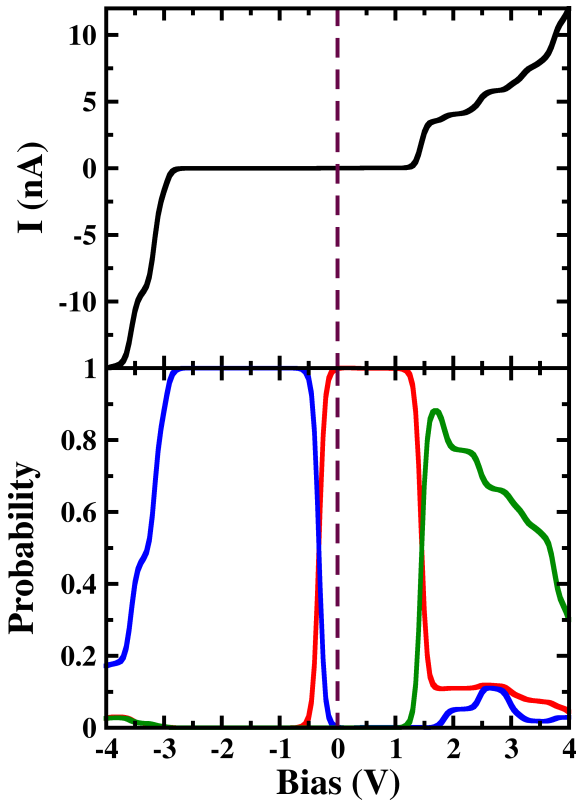

Figure 8.8: The variation of (a) current (I) (b) occupation probability of the 6-electron ground state, 7-electron ground state and 7-electron 1st excited state with V_{SD} for the device where ortho positioned C and B are attached to electrodes.

states, we look back at the charge density distribution per sites, as shown in Fig. 8.6. It is evident that the boron site, attached with one of the electrode, is electron deficient for 7-electron ground state. Thus, the population of 7-electron ground state eventually gives rise to unfavourable electron transport through this molecular junction. However, for the 7-electron excited state both the connecting sites i.e. C and B are electron rich in nature and consequently appears to be suitable for electron transport. So, the population/depopulation of these states at positive or negative bias, results in negligible or prominent current flow in the device.

8.3.3 Staircase

Next, we focus on the molecular junctions where electrodes are connected to two carbon atoms which are in para-position to each other and energetically symmetric

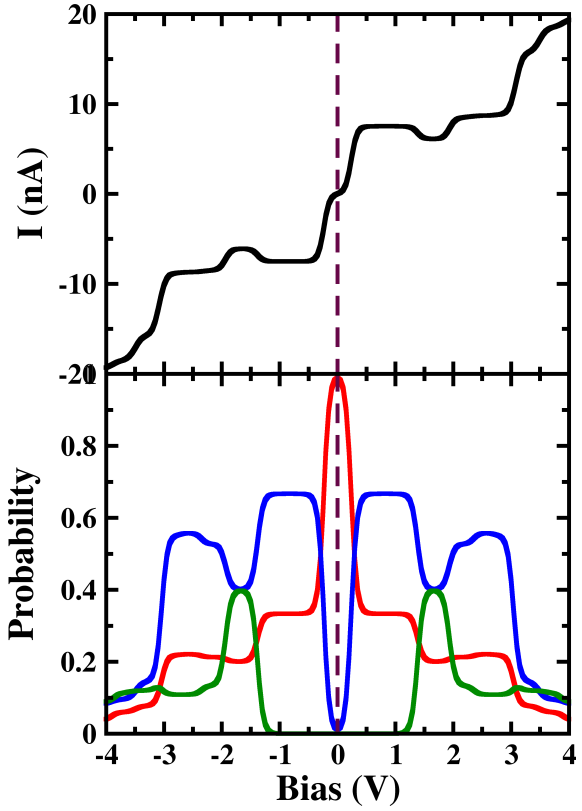

Figure 8.9: The variation of (a) current (I) (b) occupation probability of the 6-electron ground state, 7-electron ground state and 7-electron 1st excited state with V_{SD} for the device where para positioned two C atoms are attached to electrodes.

(see Fig. 8.3 (c)). As shown in Fig. 8.9, the I-V characteristic of this particular device shows step-like feature which is quite common for the junctions where sequential tunneling is the major mechanism for electron transport. As discussed previously, in this sequential tunneling regime, the charging energy for molecules is quite high and needs to be overcome by applying certain V_{SD}. Before that threshold V_{SD}, we find Coulomb blockade regime in the device (see Fig. 8.9). For the present case, as we choose the Fermi level very close to 6-electron to 7-electron transition, the Coulomb blockade regime appears to be small. Further, with increment in V_{SD}, 7-electron ground state starts filling up and electrons start flowing through the junction. With increment in V_{SD}, other excited states of different charge and spin sectors start appearing in the active bias-window. And this, results in the steps in the I-V plot for present molecular junction. Importantly, for this particu-

lar device, as the electrodes are connected to two carbon atoms (see Fig. 8.3 (c)) which are electron-rich in nature for 7-electron ground state, we find electron-flow through the molecular junctions as increased V_{SD} populate this state. Small dip in the current for the bias range of $1.1V < V_{SD} < 2.0V$ appears due to the population of 7-electron 1st excited state which is less favourable towards electron transport in the present device. Lesser electron density at the electrode-connected carbon-sites, reduces the conducting nature of 7-electron 1st excited state than that of 7-electron ground state.

8.4 Conclusions

In this chapter, we have discussed the transport characteristics of cyclic molecular systems in sequential tunneling regime, applying well known kinetic equation approach. We chose our system to be a six-site molecule where donor, bridge and acceptor get arranged in a cyclic manner. Results clearly indicate that I-V character of presently investigated molecule strongly depend on the atomic nature of the sites, which are connected to the electrodes. When two different chemical species form the electrode-molecule coupling, prominent rectification of current appears. Importantly, when both B atoms are used as connecting sites, we find appearance of NDC in the device. All these exciting non-linear properties emerge due to the V_{SD} dependent population and depopulation of low-lying excited states, which are quite different in terms of charge distribution pattern and electron conduction nature. Fundamentally, the unequal charge distributions at different-sites of the molecule for these transport active many-body states determine the I-V characteristic. Particularly, the charge densities at the connecting sites to the electrode mainly control the current conduction through the molecular junction. Thus, in this chapter, we have successfully demonstrated various non-linear transport behaviour appear for an intrinsically asymmetric heteronuclear cyclic molecule containing nano-junction.

Bibliography

[1] J. R. Heath and M. A. Ratner, *Molecular electronics* (2003).

[2] G. Cuniberti, G. Fagas, and K. Richter, *Introducing molecular electronics: A brief overview* (Springer, 2006).

[3] J. L. Zhang, J. Q. Zhong, J. D. Lin, W. P. Hu, K. Wu, G. Q. Xu, A. T. Wee, and W. Chen, Chem. Soc. Rev. **44**, 2998 (2015).

[4] B. Xu and Y. Dubi, J. Phys.: Condens. Matter **27**, 263202 (2015).

[5] R. M. Metzger, Chem. Rev. **115**, 5056 (2015).

[6] A. R. Rocha, V. M. Garcia-Suarez, S. W. Bailey, C. J. Lambert, J. Ferrer, and S. Sanvito, Nat. Mater. **4**, 335 (2005).

[7] D. Aravena and E. Ruiz, J. Am. Chem. Soc. **134**, 777 (2011).

[8] Y. Dubi and M. Di Ventra, Rev. Mod. Phys. **83**, 131 (2011).

[9] J. Park, A. N. Pasupathy, J. I. Goldsmith, C. Chang, Y. Yaish, J. R. Petta, M. Rinkoski, J. P. Sethna, H. D. Abruña, P. L. McEuen, *et al.*, Nature **417**, 722 (2002).

[10] M. Hettler, W. Wenzel, M. Wegewijs, and H. Schoeller, Phys. Rev. Lett. **90**, 076805 (2003).

[11] P. Parida, S. Lakshmi, and S. K. Pati, J. Phys.: Condens. Matter **21**, 095301 (2009).

[12] K. Ono and S. Tarucha, Phys. Rev. Lett. **92**, 256803 (2004).

[13] C. Caroli, R. Combescot, D. Lederer, P. Nozieres, and D. Saint-James, J. Phys. C **4**, 2598 (1971).

[14] A. Rocha and S. Sanvito, Phys. Rev. B **70**, 094406 (2004).

[15] B. Muralidharan, A. Ghosh, and S. Datta, Phys. Rev. B **73**, 155410 (2006).

[16] B. Muralidharan and S. Datta, Phys. Rev. B **76**, 035432 (2007).

[17] B. Muralidharan, A. W. Ghosh, S. K. Pati, and S. Datta, IEEE Trans. Nanotechnol. **6**, 536 (2007).

[18] M. H. Hettler, H. Schoeller, and W. Wenzel, Europhys. Lett. **57**, 571 (2002).

[19] D. Darau, G. Begemann, A. Donarini, and M. Grifoni, Phys. Rev. B **79**, 235404 (2009).

[20] B. Song, D. A. Ryndyk, and G. Cuniberti, Phys. Rev. B **76**, 045408 (2007).

[21] Y. A. Pati and S. Ramasesha, J. Phys. Chem. A **118**, 4048 (2014).

[22] J. E. Sansonetti, W. Martin, and S. Young, Carbon **100**, 1634 (2005).

[23] E. Anderson, Z. Bai, C. Bischof, S. Blackford, J. Dongarra, J. Du Croz, A. Greenbaum, S. Hammarling, A. McKenney, and D. Sorensen, *LAPACK Users' guide*, Vol. 9 (Siam, 1999).

Chapter 9

Summary and Future Outlook

In this chapter, we present a brief summary of all the salient results obtained in complete thesis. We also outline a few future directions of research, which emerges from the thesis. To begin with, a general introductory chapter, covering the basics of nanomaterials and fundamental models and methods used in the thesis are given. Following that, the thesis broadly concentrates on two topics, (1) structural, electronic, magnetic and optical properties of various low-dimensional systems which are explored in second to fifth chapters and (2) electron, spin and heat transport through molecular nano-junctions, investigated in last three chapters.

In the second and third chapters, we have demonstrated different ways to insert extended line defects (ELDs) in controlled manner at grain boundaries of different layered systems such as graphene, boron nitrides, in-plane hybrid of them, silicene etc. We predict the possibility of several new kinds of stable extended line defects (8-8-8, 7-4-7, and 4-ELD) at the heterojunction of in-plane hybrid of graphene and boron nitride nanoribbons. The reconstruction processes in these systems mainly depend upon the atoms present at and near to the line defect, simulation temperature etc. Furthermore, depending upon the interfacial structures, these systems show a wide range of electronic and magnetic properties ranging from semiconducting to spin polarized metallic behaviours. Interestingly, for some of the systems, magnetic ground state, where magnetic moments are ferromagnetically ordered and strongly localized at the line-defect, creates an one-dimensional spin-channel. Note that, these spin channels are quite stable because, unlike the edge of nanoribbons, structural reconstruction or contamination cannot destroy the ordering of magnetic

moments. Highlighting the controlled formation of ELDs and consequent emergence of technologically important properties in these systems, we propose new routes to realize nanomaterial-based nanoelectronic and spintronic devices.

In fourth chapter, we have investigated electronic, magnetic and optical properties of experimentally synthesized 3d-transition metal embedded graphitic carbon nitride sheets with and without graphene support. Transition metal inclusion makes all the systems metallic in nature. Particularly, for graphene supported systems, due to the charge-transfer, we find graphene layer hugely n-doped in nature. Importantly, Cr, Fe, Co, and Ni embedded systems show long-range ferromagnetic coupling among metal atoms in their ground state. The magnetic ordering appears due to suitable ferromagnetic dp exchange interaction, which is absent in paramagnetic V- and Mn-embedded sheets. The Curie temperatures of some of these systems appear to be quite higher than room temperature, exhibiting promising usage towards magnetic storage application. Last chapter of this part of the thesis, is dedicated to the study of various nitrogen substituted point-defects containing graphene sheet for their potential application towards selective trapping of pollutant gases such as HF, HCN, $CHClF_2$ and CHF_3. Moderately strong hydrogen-bond formation between the hydrogen atom of the gas molecules and nitrogen of defect-sites stabilizes the trapped pollutant molecules on these sheets even at room temperature. Importantly, these defect-sites, which strongly repel the non-polar N_2 and O_2 gases, appear to be very much selective towards the polar gas molecules. Further, increasing the defect concentration of N-doped defects in the graphene, we find the increase of gas adsorption capacity of these adsorbents.

As some open directions, one can focus on the in-silico investigation of various kinds of line defects, which may be included in some controlled manner in the newly emerging two-dimensional materials, such as, transition metal dichalcogenide (MX_2, M=Mo, W, X= S, Se, Te), layers of ternary carbides and nitrides i.e. MAXene, homo-elemental layers (silicene, phosphorene, germanene etc.) and their various hybrid structures. Further, these defect-induced systems can be found to have promising electronic and spintronic device applications, efficient for different catalytic processes etc. On the other hand, mono dispersed transition metal embedded monolayer systems can be explored for their application towards various kinds of catalytic reactions, such as, oxygen reduction reaction, water splitting etc.

These two-dimensional sheets can also be explored in the field of magnetic-storage devices as these systems can have very stable magnetic ground state. Further, spin-phonon interaction in these systems and their effect on the magnetic nature of these low dimensional systems are also very interesting and relatively unexplored field of research. Moreover, research on interfaces between these two dimensional systems and various metallic substrates, are being hugely explored due to their promising applications towards electronics, spintronics, thermoelectrics, catalysis etc. Preliminary studies evidently showed that these properties strongly depend on the atomic details of the interface. However, experimental difficulties to gain an atomistic picture of these interfaces appear as a serious bottleneck for the development of this field. Consequently, ab-initio simulation based reliable modeling of these interfaces is in high demand. Gaining the fundamental understanding about various kinds of interactions, playing major role to control the properties of the interfaces is an active field of research now. These atomistic understanding can predict the ways to make these interfaces more efficient for some particular desired applications.

In the last three chapters of the thesis, we have investigated various kinds of single-molecular junctions to find their potential applications towards nano-electronics, molecular spintronics and thermoelectrics. Exploring both i.e. coherent and sequential tunneling regimes of the molecular junctions, we have used two different methodologies, non-equilibrium Green's function approach coupled with density functional theory (DFT) and many-body master (rate) equation approach, respectively. In strong coupling limit, the spin-dependent transport and thermoelectric properties of spin-crossover molecule based nano-junction has been explored. A large magnetoresistance, efficient conductance-switching, and spin-filter activity in this molecule-based two-terminal device has been demonstrated. The spin-crossover process also modulates the thermoelectric entities. It can efficiently switch the magnitude as well as spin-polarization of the thermocurrent. Moreover, it also substantially affects the thermopower and consequently, the device shows extremely efficient spin-crossover magnetothermopower generation. Furthermore, by tuning the chemical potential of electrodes into a certain range, a pure spin-thermopower can be achieved for the high-spin state. On the other hand, in the sequential tunneling i.e. weak coupling regime, we find that the chemical nature of site, attached to electrodes, can influence the response of this nano-system to an external source-drain bias. Depending on

attachment of electrodes at various atomic sites, we have been able to obtain a host of exotic current-voltage characteristics, from negative differential conductance to rectification to Coulomb blockade behaviors.

To go further in this field, thermoelectric devices which are promising technology towards waste-heat management, power generation, cooling systems etc., can be explored. This particular field strongly suffer from low conversion efficiency due to various fundamental limitations. Very recently, several approaches have been demonstrated, such as, incorporating disorder, nano-structuring (quantum-dot superlattice, nanowires etc.), band structure engineering, using molecules etc. to increase the heat-to-voltage conversion efficiency. Research to gain theoretical understanding about various strongly influencing factors, such as, phonon-phonon/phonon-defect/phonon-grain boundary scattering, density, mobility and anisotropy of active carrier etc. in these newly emerged systems by using suitable ab-initio methods is a rapidly growing field now. With clear understanding, one can further predict the possible ways to improve the performance of existing thermoelectric materials as well as can suggest different new potential thermoelectric materials.

Furthermore, spintronics i.e. application of spin degree-of-freedom along with charge in nanomaterials has introduces a new concept for next-generation energy-efficient, spin-logic and data-storage devices. The lattice vibrations, presence of defects and other disorder, dimensionality of transport channels in these devices are found to have huge influences towards the performances. Lack of fundamental understanding about the spin-dynamics in these non-ideal situations strongly limits its practical device application. In this regard, the investigation of different phenomena associated with the spin-dynamics in real nanomaterials such as scattering, switching, interactions with orbitals, relaxation, dephasing of spin-moments in fundamental level is very much essential.